Doctoral Dissertation
博士論文

Ultrafast transient absorption spectroscopy using attosecond soft X-ray pulses in the water window

（「水の窓」領域のアト秒軟X線パルスを用いた
超高速過渡吸収分光）

A Dissertation Submitted for
the Degree of Doctor of Philosophy
December 2019
令和元年１２月博士（理学）申請

Department of Physics, Graduate School of Science,
the University of Tokyo
東京大学大学院理学系研究科物理学専攻

Nariyuki Saito
齋藤 成之

Abstract

Eighteen years have passed since the birth of attosecond spectroscopy in 2001, and its technology has made significant progress. One notable advance is the development of soft X-ray (SX, 200-2000 eV) attosecond science. The first attosecond pulse was generated by high-harmonic generation (HHG) with a femtosecond Ti:sapphire (Ti:Sa) laser, and its photon energy was around 100 eV, in the extreme ultraviolet (XUV) region (10-200 eV). Recently, by using infrared (IR, 1-3 μm) or mid-infrared (MIR, 3-10 μm) optical parametric amplifiers (OPAs) and optical parametric chirped-pulse amplifiers (OPCPAs) as drive sources, the photon energy of high harmonics (HHs) has been significantly extended. So far, the highest photon energy of 1.6 keV was demonstrated in 2012. Such attosecond pulses can be utilized for element-specific X-ray spectroscopy at various absorption edges in the SX region. Especially, HHG-based X-ray absorption spectroscopy (XAS) in the "water window" region, which ranges from the C K-edge (284 eV) to the O K-edge (543 eV), is intensively investigated. The water window region contains the K-edges of C, N, and O. If attosecond spectroscopy at these edges becomes possible, fundamental dynamics of various important materials such as biomolecules, organic solar cells, and photocatalysis is expected to be revealed. However, until now, HHG-based time-resolved XAS, or X-ray transient absorption spectroscopy, has only been established up to the C K-edge. Compared to the highest photon energy of 1.6 keV, this photon energy (284 eV) is much lower. This is because transient absorption spectroscopy requires much more SX photons than a static XAS measurement; in a transient absorption measurement, many absorption spectra have to be measured for many pump-probe delays. Since the photon flux of IR- or MIR-driven HHG is more than $\sim$3 orders of magnitude lower than that of Ti:Sa-driven HHG, it is not easy to obtain sufficient photons for transient absorption spectroscopy.

In this dissertation, the realization of HHG-based transient absorption spectroscopy at the N K-edge (400 eV) in the water window is presented. This is achieved by the combination of a powerful IR light source, an efficient HHG scheme, and a robust and stable transient absorption beamline. From the measured transient absorption spectra of nitric oxide (NO) and nitrous oxide (N_2O), electronic, vibrational, and rotational dynamics is successfully extracted, which demonstrates the versatility of HHG-based transient absorption in the SX region. Moreover, novel ultrafast phenomena such as intramolecular position-specific electronic dynamics and molecular alignment of cations are revealed. We believe that these results will deepen the understandings of photoinduced molecular dynamics, and will be a base to apply transient absorption measurements to more complex systems such as liquids or solids.

The dissertation comprises eight chapters. In Chapter 1, a general introduction is given to clarify the motivation and the purpose of the research. In Chapter 2, a detailed

theoretical and experimental background is described. In Chapter 3, the IR light source employed in the research is presented. It is a BiB_3O_6-based OPCPA system, which delivers intense, phase-stable, 10-fs pulses at 1.6 μm. In addition to the description of the light source, a new waveform characterization method of IR pulses is presented. In Chapter 4, the details of the HHG and the transient absorption beamline are described. The HHG setup consists of a semi-infinite HHG gas cell and a two-stage differential pumping system, which enables efficient SX generation. The transient absorption beamline is equipped with an attosecond delay stabilization system to achieve high delay controllability required for transient absorption spectroscopy using attosecond pulses. In Chapter 5, measured properties of the generated SX HHs are presented. In Chapters 6 and 7, the results of transient absorption experiments at the N K-edge are presented. First, in Chapter 6, NO is used as the target of transient absorption. From the measured transient absorption spectra, signatures of electronic dynamics, vibrational dynamics, and rotational dynamics is extracted. Second, in Chapter 7, N_2O is used as the target. Different from NO, N_2O has two absorption edges at the N K-edge which originate from two nitrogen atoms in the molecule. In the measured transient absorption spectra, different absorption changes in the two edges are found, implying the existence of intramolecular position-specific electronic dynamics. Moreover, rotational dynamics of both neutral N_2O and N_2O^+ cation is simultaneously observed. The rotational dynamics of the cation is found to be largely dependent on the anisotropy in the strong-field ionization process, which manifests the importance of the coupling between electron and nuclear dynamics. Chapter 8 states the conclusion of the research as well as the future prospect.

List of Publications

Publications included in this dissertation are marked with asterisks.

1. *N. Saito, H. Sannohe, N. Ishii, T. Kanai, N. Kosugi, Y. Wu, A. Chew, S. Han, Z. Chang, and J. Itatani, "Real-time observation of electronic, vibrational, and rotational dynamics in nitric oxide with attosecond soft x-ray pulses at 400 eV," Optica, **6**, 1542-1546 (2019). (included in Chapters 4-6)

2. P. Rupp, C. Burger, N. G. Kling, M. Kübel, S. Mitra, P. Rosenberger, T. Weatherby, N. Saito, J. Itatani, A. S. Alnaser, M. B. Raschke, E. Rühl, A. Schlander, M. Gallei, L. Seiffert, T. Fennel, B. Bergues, and M. F. Kling, "Few-cycle laser driven reaction nanoscopy on aerosolized silica nanoparticles," Nat. Commun. **10**, 4655 (2019).

3. *N. Saito, N. Ishii, T. Kanai, and J. Itatani, "All-optical characterization of the two-dimensional waveform and the Gouy phase of an infrared pulse based on plasma fluorescence of gas," Opt. Express **26**, 24591-24601 (2018). (included in Chapter 3)

4. N. Saito, P. Xia, F. Lu, T. Kanai, J. Itatani, and N. Ishii, "Observation of selection rules for circularly polarized fields in high-harmonic generation from a crystalline solid," Optica **4**, 1333-1336 (2017).

5. N. Saito, N. Ishii, T. Kanai, S. Watanabe, and J. Itatani, "Attosecond streaking measurement of extreme ultraviolet pulses using a long-wavelength electric field," Sci. Rep. **6**, 35594 (2016).

Contents

Abbreviations

ADK Ammosov-Delone-Krainov

AR Anti-Reflection

BBO β-BaB_2O_4 (Beta Barium Borate)

BIBO BiB_3O_6 (Bismuth Borate)

BPF Band-Pass Filter

BSM Band Stop Mirror

CCD Charge-Coupled Device

CMOS Complementary Metal–Oxide–Semiconductor

CEP Carrier-Envelope Phase

CM Chirped Mirror

CPA Chirped-Pulse Amplification

DFG Difference Frequency Generation

DFT Density Functional Theory

DXAFS Dispersive XAFS

EXAFS Extended X-ray Absorption Fine Structure

FROG Frequency Resolved Optical Gating

FS Fused Silica

FWHM Full Width at Half Maximum

HCO Half-Cycle Cutoff

HH High-Harmonic

HHG High-Harmonic Generation

HOMO Highest Occupied Molecular Orbital

HWP Half-Wave Plate

HX Hard X-ray

IR Infrared

ISRS Impulsive Stimulated Raman Scattering

LUMO Lowest Unoccupied Molecular Orbital

MIR Mid-Infrared

OPA Optical Parametric Amplification/Amplifier

OPCPA Optical Parametric Chirped-Pulse Amplification/Amplifier

PFA Perfluoroalkoxy Alkane

PMT Photomultiplier Tube

PSD Power Spectrum Density

QWP Quarter-Wave Plate

SFA Strong Field Approximation

SH Second Harmonic

SOMO Singly Occupied Molecular Orbital

SX Soft X-ray

TDSE Time-Dependent Schrödinger Equation

THG Third Harmonic Generation

TIPTOE Tunneling Ionization with a Perturbation for the Time-domain Observation of an Electric Field

Ti:Sa Ti:sapphire

TMP Turbomolecular Pump

UV Ultraviolet

VIS Visible

VND Variable Neutral Density Filter

VUV Vacuum Ultraviolet

WFAT Weak-Field Asymptotic Theory

XAFS X-ray Absorption Fine Structure

XANES X-ray Absorption Near Edge Structure

XAS X-ray Absorption Spectroscopy

XFEL X-ray Free-Electron Laser

XUV Extreme Ultraviolet

Chapter 1

Introduction

Since the invention of a ruby laser in 1960 [1], laser technology has made a significant impact on a wide range of scientific and industrial fields. Especially, in science, ultrafast pump-probe spectroscopy has been one of the most successful applications of lasers. This is represented by the Nobel Prize in chemistry in 1999, which was awarded to Zewail for his pioneering works on femtosecond (10^{-15} s) pump-probe spectroscopy [2]. In a pump-probe measurement, a sample is irradiated by a pump laser pulse to initiate dynamics, then it is irradiated by a probe laser pulse with a delay. By observing the interaction between the sample and the probe pulse (e.g., absorption, reflection, and photoemission), the real-time evolution of the photoinduced dynamics can be tracked.

Until the 1990's, the temporal resolution of pump-probe spectroscopy was in the femtosecond region, where the intrinsic limit of the temporal resolution arises from the duration of visible (VIS) laser pulses. As one optical cycle of VIS light is a few femtoseconds, it is difficult to obtain laser pulses with temporal duration of less than one femtosecond.

A breakthrough in this situation was the discovery of high-harmonic generation (HHG) [3,4]. HHG is a highly nonlinear process where an intense laser pulse is strongly focused into gas atoms to generate an extreme ultraviolet (XUV, 10-200 eV) high-harmonic (HH) pulse (Fig. 1.1). The required laer intensity is typically $\sim 10^{14}$ W/cm^2. As shown in the next chapter, the temporal duration of the generated HH pulse is naturally in the attosecond (10^{-18} s) region.

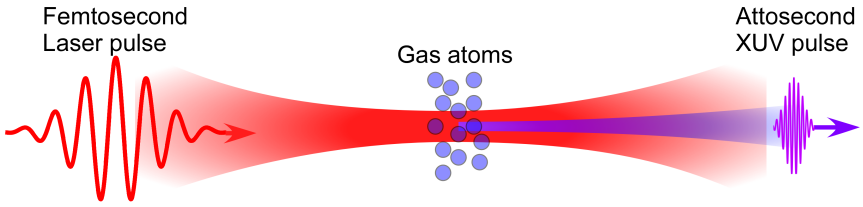

Figure 1.1: Schematic of the HHG process.

Although the first HHG experiments were conducted with picosecond drive lasers, femtosecond Ti:sapphire (Ti:Sa) lasers were soon found to be more efficient for HHG. Ti:Sa is one of the most ideal laser media for high power ultrashort pulse generation because of its broad gain bandwidth and high thermal conductivity [5]. The chirped-pulse

amplification (CPA) technique [6], which received the Nobel Prize in physics in 2018, was combined with the Ti:Sa technology to push the peak power of Ti:Sa laser pulses to the sub-terawatt region [7]. Furthermore, the emergence of spectral broadening techniques [8], precise pulse compression techniques [9], and phase stabilization techniques [10] enabled the generation of few-cycle, phase-controlled, intense laser pulses.

In 2001, by using Ti:Sa-based HHG, the first attosecond pump-probe measurements were performed [11, 12]. Since then, attosecond spectroscopy has been widely conducted to investigate various dynamics with an unprecedented temporal resolution. While the picosecond to the femtosecond region is the typical time scale of nuclear rotation or vibration, the attosecond region is a characteristic time scale of electron motions. Therefore, electron dynamics, including Auger decay [13], photoionization [14–18], charge migration [19], electron correlation [20], and electron excitation and coherence in solids [21–25], has been revealed.

Now, eighteen years have passed since the birth of attosecond spectroscopy, and tremendous technological progress has been made. Attosecond pulses with various characteristics can now be generated. For example, the shortest pulse duration has reached 43 attoseconds [26], and the polarization control of HHG has become possible [27, 28]. Intense attosecond pulses for XUV nonlinear optics have also been developed [29, 30].

Among many branches of attosecond technology, the extension of the cutoff energy of HHs to the soft X-ray region (SX, 200-2000 eV) is one of the hot topics. As shown in the next chapter, the cutoff energy $\hbar\omega_{\mathrm{cutoff}}$ and the wavelength of the drive laser λ_{laser} are related as

$$\hbar\omega_{\mathrm{cutoff}} \propto \lambda_{\mathrm{laser}}^{1.6-1.7}. \tag{1.1}$$

Therefore, by using long-wavelength infrared (IR, 1-3 μm) or mid-infrared (MIR, 3-10 μm) lasers, the cutoff energy can be significantly extended. For example, the typical cutoff energy of HHG driven by a Ti:Sa laser ($\lambda_{\mathrm{laser}} \sim 0.8$ μm) is < 150 eV, but it can be extended to ∼450-500 eV by using an IR light source with $\lambda_{\mathrm{laser}} \sim 1.6$ μm. The development of such long-wavelength light sources has been challenging because of the lack of appropriate laser media in the IR or MIR regions. Recently, however, advances in nonlinear wavelength conversion techniques such as optical parametric amplification (OPA) and optical parametric chirped-pulse amplification (OPCPA) have enabled the generation of intense, femtosecond IR or MIR pulses [31–40]. By using these light sources, HHG in the SX region has been demonstrated [41–51]. In 2012, the highest cutoff energy of 1.6 keV was reported by using an MIR OPCPA system ($\lambda_{\mathrm{laser}} \sim 3.9$ μm) [52]. As shown in Fig. 1.2, OP(CP)A-based HHG has now become a standard laser-based SX source, which is complementary to X-ray free-electron lasers (XFELs) or synchrotron facilities. Furthermore, compared to these accelerator-based SX light sources, HHG has unique properties such as ultrashort pulse duration, table-top size, and excellent spatial and temporal coherence.

One of the most expected applications of OP(CP)A-based HHG is X-ray absorption spectroscopy (XAS) at various absorption edges. An absorption edge is a photon energy which is required to excite a core shell electron to unoccupied orbitals. Because the position of an absorption edge is specific to each element, XAS can provide element-specific information of various samples. XAS has been mainly conducted in synchrotron facilities because most of the absorption edges exist in the SX or in the hard X-ray (HX) regions, but now, HHG sources can also be utilized. So far, HHG-based XAS has been

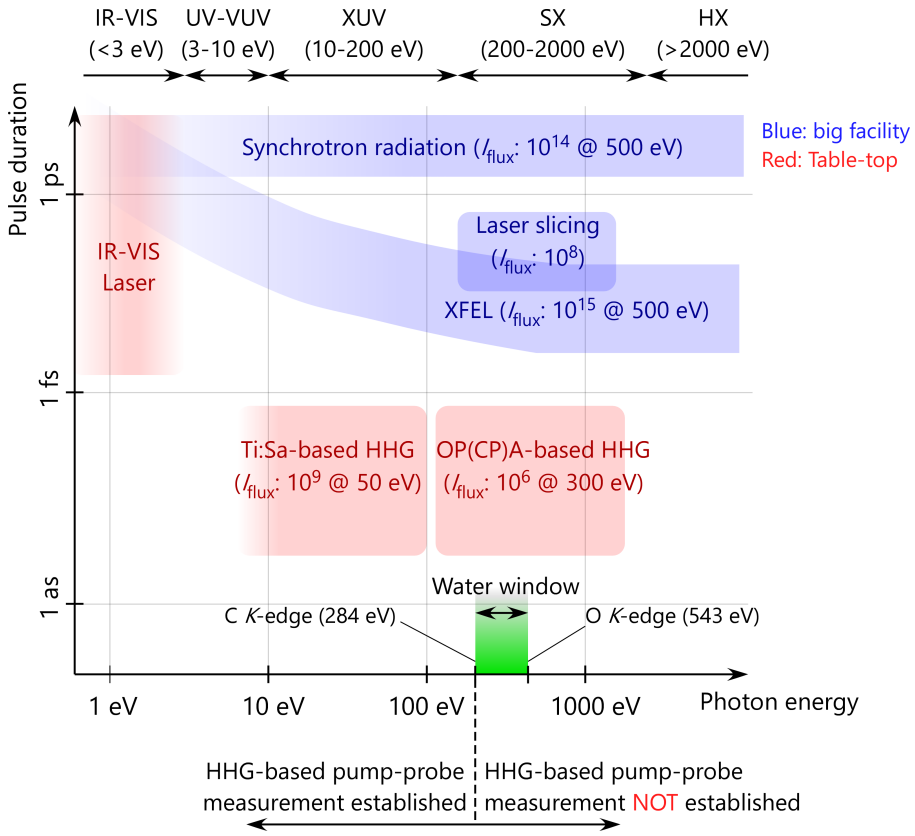

Figure 1.2: Comparison of light sources from the IR to the SX regions. I_{flux} is the photon flux presented in photons/s/1%bandwidth. The data in the figure are based on refs. [30, 46, 50, 53–56].

demonstrated at the C K-edge (284 eV) [45, 48, 57–59], the N K-edge (400 eV) [60], the Sc L-edge (400 eV) [61], the O K-edge (543 eV) [50], and the Fe L-edge (710 eV) [61]. Especially, XAS measurements in the water window region, which ranges from the C K-edge to the O K-edge, are intensively studied because the water window contains absorption edges of important elements such as C, N, and O.

However, there is still a challenge in OP(CP)A-based SX HHG: pump-probe measurements using OP(CP)A-based SX HHG sources are much more difficult than those using Ti:Sa-based XUV HHG sources. In fact, the first HHG-based pump-probe spectroscopy in the SX region was realized at the C K-edge in 2017 [58, 62–64], but it was nine years after the first demonstration of OPA-based HHG at the same photon energy [42]. Moreover, until now, the maximum photon energy of published HHG-based pump-probe X-ray spectroscopy has still been limited to the C K-edge. Although there is a preprint which reports an attosecond time-resolved pump-probe measurement at the Ti L-edge (460 eV) [65], there is still an argument over its reproducibility.

The reason why pump-probe measurements are difficult is the low photon flux of IR- and MIR-driven HHG. Actually, as shown in the next chapter, the HHG photon flux $I_{\mathrm{HH\,flux}}$ scales with the drive laser wavelength λ_{laser} as

$$I_{\mathrm{HH\,flux}} \propto \lambda_{\mathrm{laser}}^{-(8-7.4)}. \tag{1.2}$$

Indeed, the photon flux of IR-OP(CP)A-based HHG at 300 eV is ∼8-9 orders of magnitude lower than that of XFEL or synchrotron radiation, and ∼3 orders of magnitude lower than that of Ti:Sa-based HHG at 50 eV (Fig. 1.2). This low photon flux is a big problem when performing pump-probe measurements. For example, in a pump-probe XAS measurement, an X-ray absorption spectrum has to be recorded for each delay between the pump and the probe pulse. Therefore, assuming that the number of the delay points is ∼100, the required total SX photon number is ∼100 times higher than that in a static XAS measurement.

Considering this, in order to extend the photon energy limit of the pump-probe measurements beyond the C K-edge, an efficient SX HHG system driven by a powerful IR light source, and a stable beamline for a long-time data acquisition are required.

Purpose and achievement of research

This study aims to realize HHG-based pump-probe XAS, or X-ray transient absorption spectroscopy, at the N K-edge (400 eV) in the water window. Because a nitrogen atom is contained in various organic/inorganic materials and biomolecules, the realization of transient absorption spectroscopy at the N K-edge has an important meaning for materials science, chemistry, and biology.

In the experiment, a BiB_3O_6-based OPCPA (BIBO-OPCPA) system is employed as an HHG drive source. It delivers phase-stable, intense (1.5 mJ in pulse energy) IR pulses at 1.6 μm with 10-fs pulse duration at a repetition rate of 1 kHz [57]. The author has developed an SX beamline for HHG and transient absorption spectroscopy. The beamline is equipped with an semi-infinite HHG gas cell and a differential pumping system for efficient SX HHG. Moreover, a vibration isolation and an active delay feedback system

are developed to realize attosecond stability of the delay between the pump and the probe pulses for several hours.

By using the developed beamline, ultrafast transient absorption spectroscopy of NO is demonstrated to capture its electronic, vibrational, and rotational dynamics. Transient aborption spectroscopy of N_2O is also conducted, and novel ultrafast phenomena such as intramolecular position-specific electronic dynamics and molecular alignment of ions are revealed.

Chapter 2

Background of research

In this chapter, we present the theoretical and experimental background of this research. First, we describe the mechanism of HHG and derive how the properties of HHs scale with the wavelength of the drive laser. Second, we describe the principles of XAS and X-ray transient absorption spectroscopy, and review some of the previous studies of ultrafast HHG-based transient absorption spectroscopy. Third, we review previous studies of NO and N_2O molecules, which are the targets of our transient absorption measurements. Finally, we describe ultrafast X-ray light sources other than HHG, such as XFELs and laser-slicing sources.

2.1 Mechanism of HHG and scaling laws

2.1.1 Semi-classical three-step model

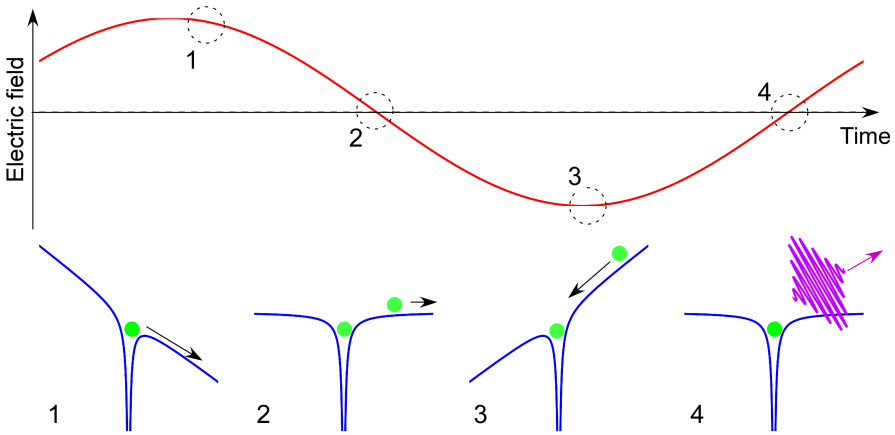

Figure 2.1: Concept of the three-step model. 1: Tunnel ionization. 2, 3. Acceleration by the laser electric field. 4. Recombination and emission of an HH photon.

HHG is a wavelength conversion process where an intense femtosecond laser pulse is focused into gas atoms and attosecond XUV/SX pulses are generated. The mechanism of HHG can be semi-classically explained by the three-step model proposed by Corkum [66]. As shown in Fig. 2.1, the model comprises the following steps:

1. The valence electron of an atom is tunnel-ionized.
2. The ionized electron is accelerated away from the parent ion by the laser field. After the direction of the laser field is inverted, the electron is accelerated towards the parent ion.
3. The accelerated electron is recombined with the parent ion, and the sum of the ionization potential and the kinetic energy of the electron is converted into an XUV or an X-ray photon.

In the following, we describe the details of each step.

As for the first step, the Keldysh parameter γ which is defined as

$$\gamma = \frac{\omega\sqrt{2I_\mathrm{p}}}{E} \tag{2.1}$$

is an important parameter in the ionization process [67]. Here, ω, I_p, and E are, in atomic units, the angular frequency of the laser field, the ionization potential, and the laser electric field amplitude, respectively. If γ is greater than $\sim$1, the ionization process is well-described as multiphoton ionization, where an atom absorbs multiple laser photons to be ionized. On the other hand, if γ is less than $\sim$1, which is the case in typical HHG experiments using intense ($\sim 10^{14}$ W/cm^2) near-IR or IR lasers, the tunnel ionization picture becomes valid. In tunnel ionization, the Coulomb potential of an atom is distorted by a quasi-static strong laser field, and the electron wave packet is transmitted through the distorted potential barrier.

To mathematically formulate the ionization process, several models [67,68] have been proposed. Among them, the Ammosov-Delone-Krainov (ADK) model [69] is widely used in simulating tunnel ionization. In the ADK model, the tunnel ionization rate w_ADK is expressed in atomic units as

$$w_\mathrm{ADK} = |C_{n^*l^*}|^2 G_{lm} I_\mathrm{p} \left(\frac{2E_0}{E}\right)^{2n^*-|m|-1} \exp\left(-\frac{2E_0}{3E}\right). \tag{2.2}$$

Here, n^*, m, $C_{n^*l^*}$, and G_{lm} are constants which are specific to atomic species, I_p is the ionization potential, E is electric field amplitude, and E_0 is defined as $(2I_\mathrm{p})^{3/2}$. In Eq. (2.2), the tunnel ionization rate depends on the exponential of the inverse of the electric field amplitude, indicating that the tunnel ionization rate has a high nonlinearity. Therefore, if a strong AC electric field is applied to an atom, the electron is mostly ionized at the local maxima of the oscillating field, as shown in Fig. 2.2.

As for the second and the third step, the acceleration and the recombination of the electron can be described by a classical equation of motion. Let $E\cos\omega_0 t$ and t_0 be a laser electric field and the time of ionization, respectively. The velocity of the ionized electron $v(t)$ obeys the following equation:

$$\frac{\mathrm{d}v(t)}{\mathrm{d}t} = -E\cos\omega_0 t. \tag{2.3}$$

Here, atomic units are used. By solving this equation, we obtain

$$v(t) = -\frac{E}{\omega_0}\left[\sin\omega_0 t - \sin\omega_0 t_0\right] \tag{2.4}$$

$$x(t) = \frac{E}{\omega_0^2}\left[\cos\omega_0 t - \cos\omega_0 t_0\right] + \frac{E}{\omega_0}(t-t_0)\sin\omega_0 t_0. \tag{2.5}$$

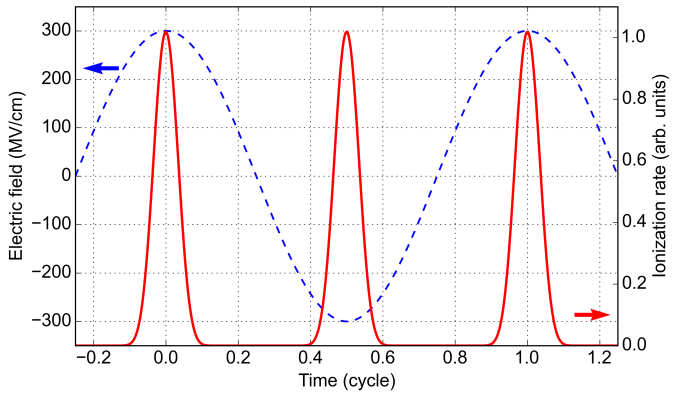

Figure 2.2: Calculated tunnel ionization rate of Ne (red curve) irradiated by an AC electric field with a peak electric field of 300 MV/cm or an intensity of 1.2×10^{14} W/cm^2 (blue dashed curve).

Here, $x(t)$ represents the position of the electron. The position and the velocity of the electron at t_0 are assumed to be zero. By introducing the recombination time t_1, the kinetic energy of the recombining electron is expressed as $v(t_1)^2/2$. Therefore, the photon energy of the emitted HH photon ω_{X} is

$$\omega_{\mathrm{X}} = I_{\mathrm{p}} + \frac{E^2}{2\omega_0^2}\left[\sin\omega_0 t_1 - \sin\omega_0 t_0\right]^2 = I_{\mathrm{p}} + 2U_{\mathrm{p}}\left[\sin\omega_0 t_1 - \sin\omega_0 t_0\right]^2, \tag{2.6}$$

where I_{p} is the ionization potential, and U_{p} is the ponderomotive energy defined as $U_{\mathrm{p}} = E^2/4\omega_0^2$. Figure 2.3 plots the calculated electron trajectories with various ionization times and their recombination energies. In Fig. 2.3(b), it is visible that the maximum

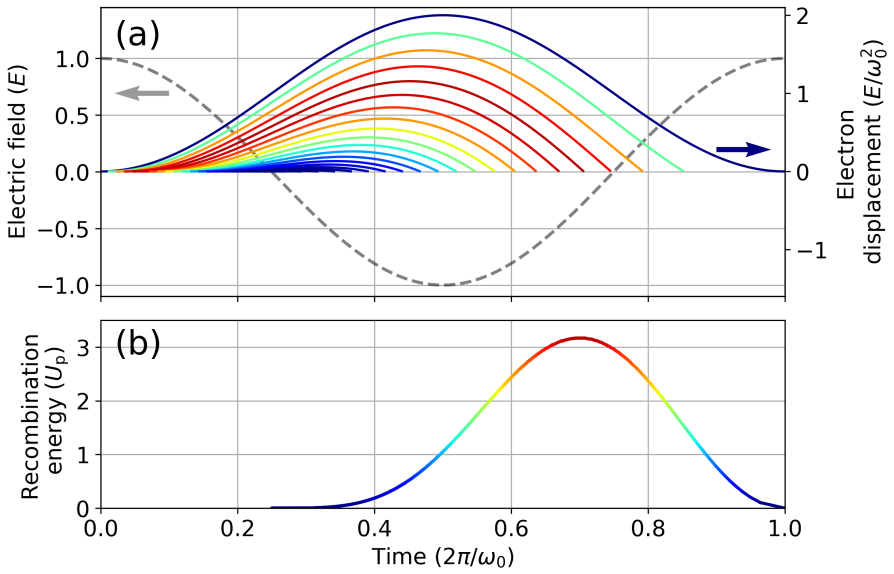

Figure 2.3: (a) Calculated trajectories of the ionized electron with various ionization times (solid curves). The laser electric field is plotted as a dashed gray curve. (b) Recombination energy as a function of the recombination time.

recombination energy is about $3.17U_{\mathrm{p}}$. Therefore, the cutoff energy of HHG ω_{cutoff} is expressed as

$$\omega_{\mathrm{cutoff}} = 3.17U_{\mathrm{p}} + I_{\mathrm{p}}. \tag{2.7}$$

Because the ionization, the acceleration, and the recombination of the electron are repeated every half cycle of the laser pulse, HHs are emitted at a period of half the laser cycle. Therefore, HHs usually form an attosecond pulse train.

2.1.2 Quantum mechanical model

In order to describe the HHG process more quantitatively, a quantum mechanical formulation is required. In this section, the Lewenstein model [70], which is one of the most simple and widespread quantum mechanical models of HHG, is presented.

In the Lewenstein model, an electron wave function $|\psi(\boldsymbol{x},t)\rangle$ irradiated by a laser field $\boldsymbol{E}(t)$ obeys the following time-dependent Schrödinger equation (TDSE):

$$i\frac{\mathrm{d}}{\mathrm{d}t}|\psi(\boldsymbol{x},t)\rangle = \left[-\frac{\Delta}{2} + V(\boldsymbol{x}) + \boldsymbol{E}(t)\cdot\boldsymbol{x}\right]|\psi(\boldsymbol{x},t)\rangle. \tag{2.8}$$

Here, $V(\boldsymbol{x})$ is the Coulomb potential of the parent ion, and atomic units are used. To solve Eq. (2.8), the following approximations (Strong Field Approximation; SFA) are introduced.

1. The bound excited states are ignored.
2. The unbound states (continuum states) do not feel the Coulomb potential of the parent ion.

These approximations are valid when the laser field is strong and the kinetic energy of the ionized electron is sufficiently higher than the ionization potential. By using SFA, Eq. (2.8) can be analytically solved.

The HHs are treated as dipole radiations from the atom. The dipole $x_{\boldsymbol{n}}(t)$ ($\boldsymbol{n}$: a unit vector which specifies the direction of the dipole) is defined as

$$x_{\boldsymbol{n}}(t) = -\langle\psi(\boldsymbol{x},t)|\boldsymbol{x}\cdot\boldsymbol{n}|\psi(\boldsymbol{x},t)\rangle. \tag{2.9}$$

By substituting the solution of the TDSE (Eq. (2.8)) for Eq. (2.9), we obtain

$$\begin{aligned} x_{\boldsymbol{n}}(t) &= i\int_{-\infty}^{t}\mathrm{d}t'\int\mathrm{d}^3\boldsymbol{p}\left[\boldsymbol{n}\cdot\boldsymbol{d}^*(\boldsymbol{p}+\boldsymbol{A}_(t))\right] \\ &\quad\times\left[\boldsymbol{E}(t')\cdot\boldsymbol{d}(\boldsymbol{p}+\boldsymbol{A}(t'))\right]\exp[-iS(\boldsymbol{p},t,t')] + c.c. \end{aligned} \tag{2.10}$$

Here, $\boldsymbol{p}$ is the momentum of the ionized electron and $\boldsymbol{A}(t)$ is the vector potential of the laser field. The momentum is defined as $\boldsymbol{p} = \boldsymbol{v} - \boldsymbol{A}(t)$, where $\boldsymbol{v}$ is the velocity of the electron. $\boldsymbol{d}(\boldsymbol{v}) = \langle\boldsymbol{v}|\,\boldsymbol{x}\,|0\rangle$ is the atomic dipole matrix element for the transition between the ground state $|0\rangle$ and the continuum state $|\boldsymbol{v}\rangle$. $S(\boldsymbol{p},t,t')$ is the classical action which is defined as

$$S(\boldsymbol{p},t,t') = \int_{t'}^{t}\mathrm{d}t''\left[\frac{1}{2}(\boldsymbol{p}+\boldsymbol{A}(t''))^2 + I_{\mathrm{p}}\right]. \tag{2.11}$$

Equation (2.10) can further be simplified by using the saddle point approximation as

$$x_{\boldsymbol{n}}(t) = i\int_{-\infty}^{t} \mathrm{d}t' \left(\frac{\pi}{\epsilon + i(t-t')/2}\right)^{3/2} [\boldsymbol{n}\cdot\boldsymbol{d}^*(\boldsymbol{p}_{\mathrm{st}} + \boldsymbol{A}(t))] \times [\boldsymbol{E}(t')\cdot\boldsymbol{d}(\boldsymbol{p}_{\mathbf{st}} + \boldsymbol{A}(t'))] \exp[-iS(\boldsymbol{p}_{\mathrm{st}}, t, t')] + c.c., \tag{2.12}$$

where

$$\boldsymbol{p}_{\mathrm{st}} = -\frac{\int_{t'}^{t} \mathrm{d}t'' \boldsymbol{A}(t'')}{t-t'}. \tag{2.13}$$

The physical interpretation of Eq. (2.12) can be associated with the semi-classical three-step model. Firstly, $[\boldsymbol{E}(t')\cdot\boldsymbol{d}(\boldsymbol{p}_{\mathbf{st}} + \boldsymbol{A}(t'))]$ represents the tunnel ionization at time t'. Secondly, $\exp[-iS(\boldsymbol{p}_{\mathrm{st}}, t, t')]$ corresponds to the acceleration of the ionized electron from t' to t. At the same time, $((\pi/(\epsilon + i(t-t')/2))^{3/2}$ represents the spreading of the electron wave packet during the acceleration process. Lastly, $[\boldsymbol{n}\cdot\boldsymbol{d}^*(\boldsymbol{p}_{\mathrm{st}} + \boldsymbol{A}(t))]$ represents the recombination of the accelerated electron to the parent ion.

The HH spectrum $I_{\mathrm{HHG}}(\omega)$ is calculated from the dipole as

$$I_{\mathrm{HHG}}(\omega) \propto \left|\omega^2 \int x_{\boldsymbol{n}}(t) e^{i\omega t} \mathrm{d}t\right|^2. \tag{2.14}$$

2.1.3 Half-cycle cutoff and isolated attosecond pulse generation

By using the models presented in the previous sections, we can discuss the mechanism of the generation of isolated attosecond pulses by HHG.

When the pulse duration of a laser pulse is sufficiently short, its waveform dramatically changes within one or two half cycles. Because the cutoff energy of HHG is proportional to the laser intensity according to Eq. (2.7), it means that different half cycles have different cutoff energies [71, 72]. The cutoff energy for each half cycle of the laser pulse is called the "half-cycle cutoff" (HCO) [72]. Figure 2.4 plots the calculated HH spectra generated by a sub-two-cycle laser pulse (temporal duration: 10 fs FWHM, wavelength: 1.7 μm, peak intensity: 1×10^{14} W/cm^2), clearly showing the HCO structures. Here, the Lewenstein model is employed for the calculation.

In order to obtain isolated attosecond pulses, it is important that the carrier-envelope phase (CEP) of the laser pulse is set to an appropriate value. The CEP is defined as the phase of the carrier wave with respect to the maximum of the envelope. When the laser electric field is expressed as $E_0(t)\cos(\omega_0 t + \phi)$, $E_0(t)$ is the envelope, $\cos(\omega_0 t + \phi)$ is the carrier wave, and ϕ is the CEP. The left and right columns of Fig. 2.4 show HH spectra generated by a laser pulse with a "cosine-like" CEP (ϕ=0) and a "sine-like" CEP ($\phi = \pi$/2), respectively. In the case of the cosine-like CEP, only one HCO is present around 100 eV. Therefore, isolated HH pulses are obtained around this energy region. However, in the case of the sine-like CEP, two HCOs coexist around 100 eV, resulting in double HH pulses.

Figure 2.5 shows experimentally recorded CEP-dependent HH spectra driven by a Ti:Sa laser [72]. For each HH spectrum, there are several "hump" structures in it. These humps correspond to the HCOs. Recently, CEP-dependent HCO structures have also been observed in the SX region [44–46, 48–50].

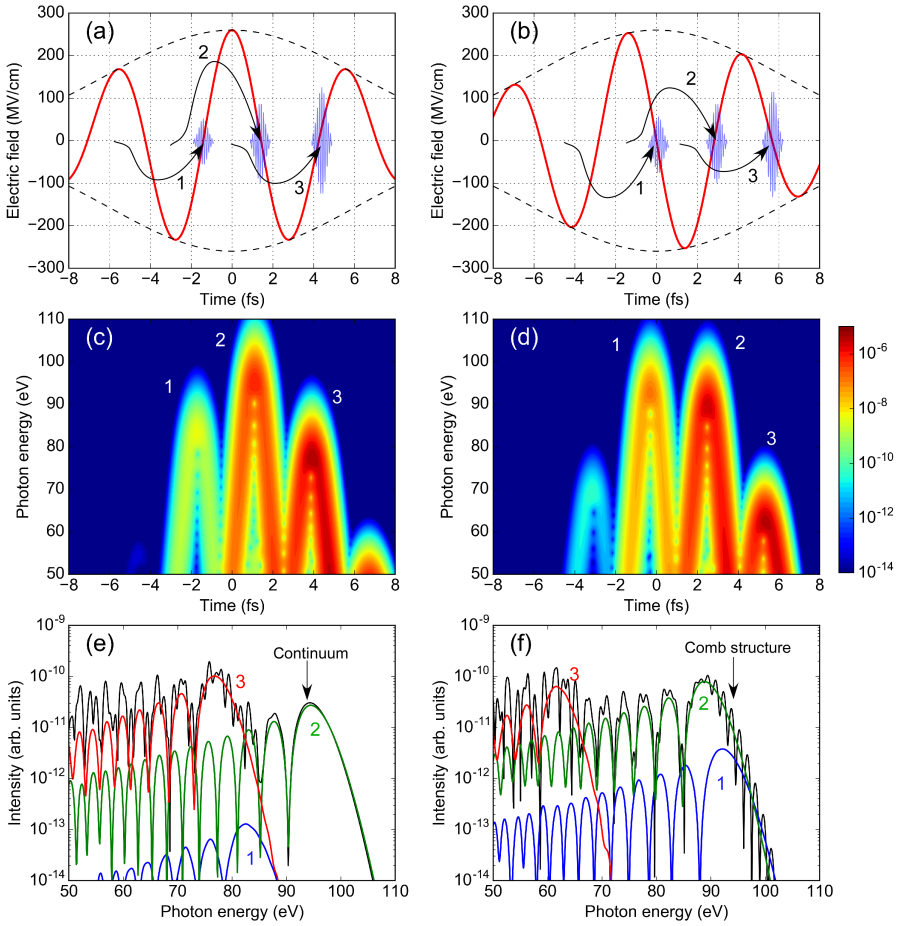

Figure 2.4: Mechanism of the generation of an isolated attosecond pulse. (a, b) The electric fields of the drive laser pulse (c, d) Time-frequency plots of the generated HH spectra obtained by a short-time Fourier transform with a 0.66-fs-FWHM-wide Gaussian window. (e, f) Total HH spectra (black curves) and the HH spectrum from each laser half cycle (colored curve). The CEP of the drive laser pulse is set to cosine-like in (a, c, e) and sine-like in (b, d, f).

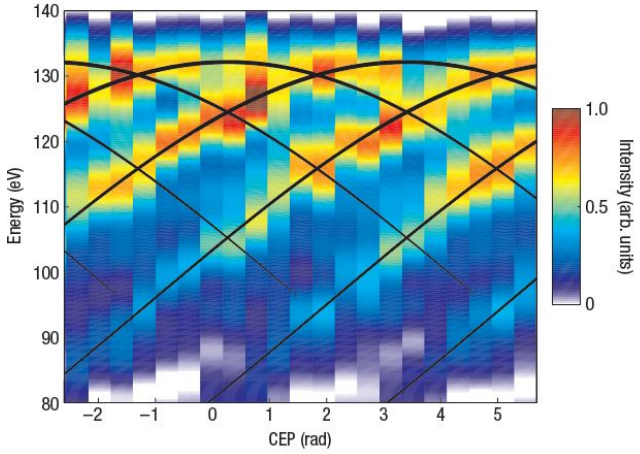

Figure 2.5: Experimentally observed CEP-dependent HCO structures [72].

2.1.4 Scaling laws of HHG

One of the important implications of the three-step model and the Lewenstein model is the scaling laws of HHG with respect to the laser wavelength. In this section, we review two important scaling laws. Note that we fix the laser intensity and the ionization potential in the following discussion.

First, according to Eq. (2.7), if the cutoff energy is sufficiently higher than the ionization potential, the cutoff energy is proportional to the ponderomotive energy. Because the ponderomotive energy is proportional to λ^2 (λ: laser wavelength), the cutoff energy scales with λ^2.

Second, the photon flux ($\propto$ spectral intensity) of HHs also scales with the wavelength. According to Eq. (2.12), the diffusion of the accelerated electron wave packet is represented as $((\pi/(\epsilon + i(t-t')/2))^{3/2}$ (t': ionization time, t: recombination time). Because $t - t'$ is proportional to λ, the diffusion of the wave packet is proportional to $\lambda^{-3/2}$. Therefore, in the photon flux, the effect of the diffusion scales as λ^{-3}. Moreover, because the cutoff energy scales as λ^2, the photon flux, which is proportional to the number of photons per unit photon energy, scales as λ^{-2}. Considering these two effects, the photon flux is expected to scale as λ^{-5}. In TDSE calculations [73] and experiments [74], it has been shown that the actual scaling law is $\lambda^{-(6.5-5.5)}$.

2.1.5 Phase matching of HHG and modified scaling laws

In the previous sections, the HHG process in a single atom is described. However, in actual experiments, HH emissions from many atoms are superimposed to form a macroscopic HH beam. In order to obtain bright HHs, it is important that these emissions are coherently added without any destructive interferences. Let k_1 and k_q be the wave numbers of the drive laser and the q-th harmonic, respectively. If $k_q = qk_1$, the phase velocity of the drive laser and that of the harmonic beam become the same, and the harmonic emission at each position is added constructively. This condition is called the phase-matching condition. By introducing the phase mismatch $\Delta k = k_q - qk_1$, the phase-matching condition can be expressed as $\Delta k = 0$.

For simplicity, we describe phase matching along the one-dimensional axis which is parallel to the laser propagation direction. In this case, the phase mismatch Δk can be written as the sum of the following four components [75, 76]:

$$\Delta k = \Delta k_{\mathrm{gouy}} + \Delta k_{\mathrm{atomic}} + \Delta k_{\mathrm{neutral}} + \Delta k_{\mathrm{plasma}}. \tag{2.15}$$

Each component is defined as

$$\begin{aligned} \Delta k_{\mathrm{gouy}} &= \frac{q}{z_{\mathrm{R}}\left(1 + (z/z_{\mathrm{R}})^2\right)}, \quad \Delta k_{\mathrm{atomic}} = \frac{2\alpha I_0 z}{\left(1 + (z/z_{\mathrm{R}})^2\right)^2 z_{\mathrm{R}}^2}, \\ \Delta k_{\mathrm{neutral}} &= -\frac{q\omega_0}{c} P(1-p)(n_a - 1), \quad \Delta k_{\mathrm{plasma}} = \frac{q\omega_0}{c}\frac{e^2}{2\epsilon_0 m_e}\frac{N_0 P p}{\omega_0^2}. \end{aligned} \tag{2.16}$$

Here, z is the position; z_{R} is the Rayleigh length of the drive laser; α is the derivative of the phase of the HH emission with respect to the laser intensity; I_0 is the maximum laser intensity; ω_0 is the angular frequency of the drive laser; c is the speed of light in vacuum;

P is the pressure of the gas medium; p is the ionization fraction; n_a is the refractive index of a 1-bar gas medium; e is the elementary charge; ϵ_0 is the dielectric constant of vacuum; m_e is the mass of an electron; N_0 is the number density of a 1-bar gas medium. Δk_{gouy} represents the increase of the phase velocity of the drive laser by the Gouy phase; $\Delta k_{\mathrm{atomic}}$ arises from the dipole phase of the HHs; $\Delta k_{\mathrm{neutral}}$ and $\Delta k_{\mathrm{plasma}}$ represent the decrease and increase of the phase velocity of the drive laser by the refractive index of neutral gas and free electrons, respectively.

If the phase-matching condition is required to be fulfilled, it imposes several restrictions on the experimental parameters such as the laser intensity and the gas pressure, thus modifies the scaling laws of HHG. The discussions below are based on ref. [77]. Note that we focus on the phase-matching condition around the cutoff energy.

First, the scaling of the cutoff energy is modified as follows. If the laser intensity is very high, the ionization fraction p becomes very large. In this case, due to large $\Delta k_{\mathrm{plasma}}$, the phase-matching condition cannot be fulfilled. Practically, the laser intensity is limited to a range which satisfies $|\Delta k_{\mathrm{plasma}}| < |\Delta k_{\mathrm{neutral}}|$. The maximum cutoff energy within this intensity range is called the phase-matching cutoff energy. Because of the $1/\omega_0^2$ term in $\Delta k_{\mathrm{plasma}}$, the limit of the ionization fraction p scales as λ^{-2}. Therefore, as the laser wavelength becomes longer, the intensity limit becomes smaller. Figure 2.6 shows the calculated scaling of the phase-matching cutoff energies for various gas species. The ADK model is used to calculate the ionization fraction. Different from the single atom response, the phase-matching cutoff energy scales as $\lambda^{1.6-1.7}$.

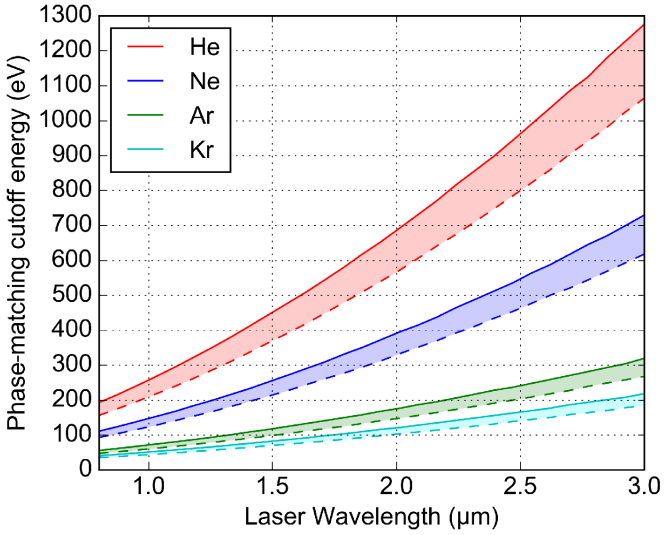

Figure 2.6: Calculated phase-matching cutoff energies as a function of the laser wavelength for He (red), Ne (deep blue), Ar (green), and Kr (light blue). The solid curves and the dashed curves represent the calculation results for two- and eight-cycle laser pulses, respectively.

Second, because of the above-mentioned intensity limit, the scaling law of the photon flux is affected. Although we skip the details here, it is shown from numerical simulations that the scaling law becomes $\lambda^{-(8-7.4)}$ [77].

Lastly, the optimum gas pressure for HHG also scales with the laser wavelength. The gas pressure P is included in the $\Delta k_{\mathrm{neutral}}$ and the $\Delta k_{\mathrm{plasma}}$ terms. Considering the fact

that $\omega_0 \propto \lambda^{-1}$ and $q \propto \omega_{\mathrm{HH}}/\omega_0 \propto \lambda^3$ (ω_{HH}: angular frequency of the HHs which scales with λ^2), it can be derived that $\Delta k_{\mathrm{neutral}}, \Delta k_{\mathrm{plasma}} \propto P\lambda^2$. On the other hand, because $z_{\mathrm{R}} \propto \lambda^{-1}$ and $\alpha \propto \lambda^3$ [78], $\Delta k_{\mathrm{gouy}}, \Delta k_{\mathrm{atomic}} \propto \lambda^4$. Therefore, in order to fulfill $\Delta k = 0$, the pressure should scale as λ^2.

Table 2.1 summarizes the scaling laws of the microscopic (single atom) and the macroscopic HHG processes. It is evident that, when the laser wavelength becomes longer, the cutoff energy can be significantly extended. However, at the same time, the photon flux also dramatically decreases. Moreover, the required gas pressure for efficient HHG becomes high.

Table 2.1: Scaling laws of HHG

	Cutoff energy	Photon flux	Optimum gas pressure
Single-atom response	λ^2	$\lambda^{-(6.5-5.5)}$	-
Macroscopic response	$\lambda^{1.6-1.7}$	$\lambda^{-(8-7.4)}$	λ^2

Experimentally, these scaling laws have been qualitatively confirmed. Figure 2.7 shows measured HH spectra from He obtained with various drive laser wavelengths [52]. The cutoff energy for each drive laser wavelength roughly agrees with the predicted value in Fig. 2.6. As for the gas pressure, Fig. 2.8 shows experimentally measured optimum gas pressures in HHG from He at various wavelengths. It is visible that the measured optimum gas pressures roughly follow the scaling law.

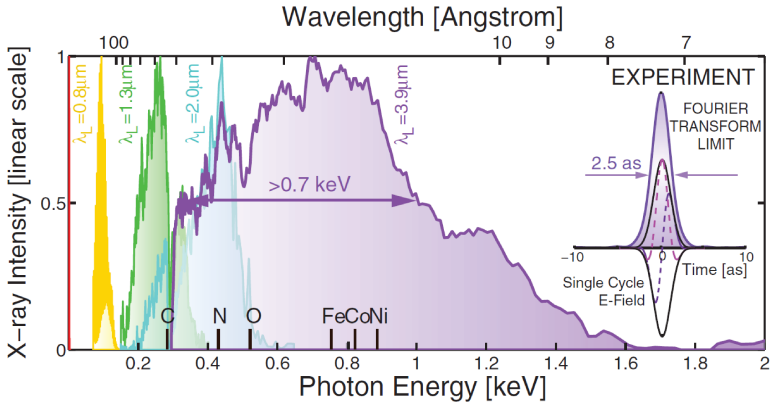

Figure 2.7: HH spectra from He obtained with various drive laser wavelengths [52].

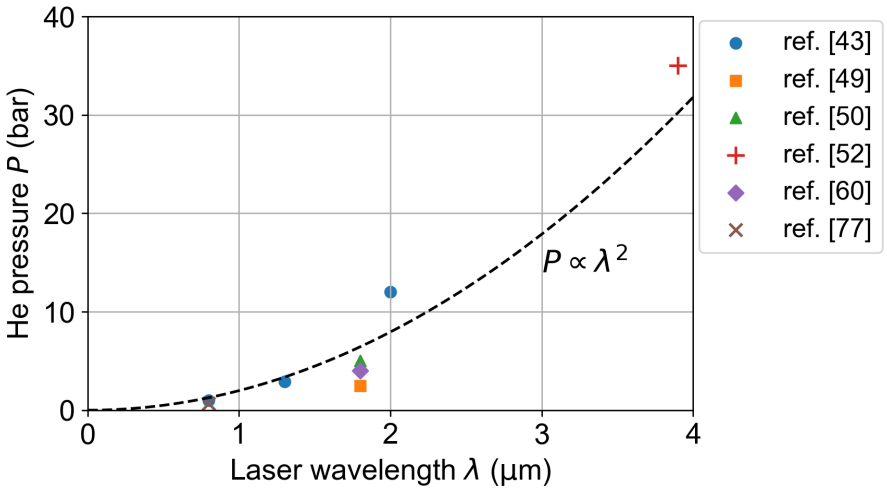

Figure 2.8: Experimentally measured optimum gas pressures in HHG from He at various laser wavelengths [43, 49, 50, 52, 60, 77]. Black dashed curve is a guide for the eye, showing the quadratic scaling law.

2.2 X-ray absorption spectroscopy (XAS)

XAS is one of the most powerful techniques to investigate local electronic and structural information of matter. Figure 2.9 depicts the principles of XAS. In an X-ray absorption spectrum, there are steep rising edges called absorption edges. The photon energy of an absorption edge corresponds to the transition energy of a core shell electron to unoccupied orbitals or continuum states.

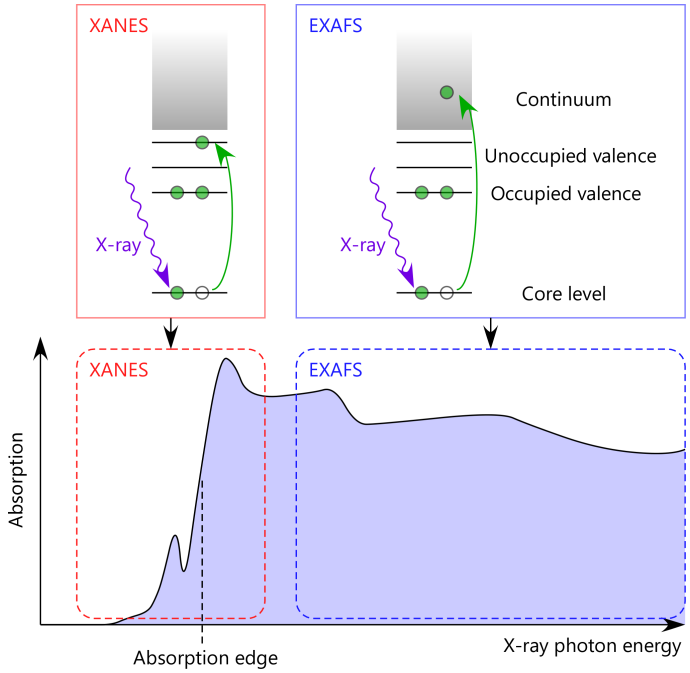

Figure 2.9: Schematic of the concept of XAS (XANES and EXAFS).

A spectral structure around an absorption edge is called X-ray absorption fine-structure (XAFS), and it is classified to X-ray absorption near edge structure (XANES, or NEXAFS) and extended X-ray absorption fine structure (EXAFS). XANES exists around the absorption edge ($\sim$10-20 eV), and it corresponds to the transitions from a core shell to unoccupied valence orbitals. XANES is sensitive to local electronic structures such as electron population, chemical bonding and valence number. On the other hand, EXAFS spans several hundreds of electron volts from an absorption edge, and it corresponds to the transitions from a core shell to continuum states. EXAFS is sensitive to local lattice structures.

An important aspect of XAS is element specificity. Because each element has characteristic absorption edges, one can investigate a specific element by tuning the X-ray photon energy to an appropriate absorption edge. Element specificity is especially helpful when the target matter has a complex structure and many elements coexist in it.

Figure 2.10 shows the list of absorption edges in the SX region. Between 100 and 600 eV, there are K-edges (transitions from 1s shells) of light elements, L-edges (transitions from 2p or 2s shells) of light elements and some transition metals. The region between the C K-edge (284 eV) and the O K-edge (543 eV) is called the "water window," where X-rays are transmitted through water but absorbed by carbon-containing molecules. The

water window region is important because it contains K-edges of carbon, nitrogen, and oxygen. These elements are fundamental components of many materials such as oxides, photocatalytic systems, and organic molecules including biomolecules. Furthermore, because water is transparent in this region, XAS of aqueous solution is possible in the transmission mode.

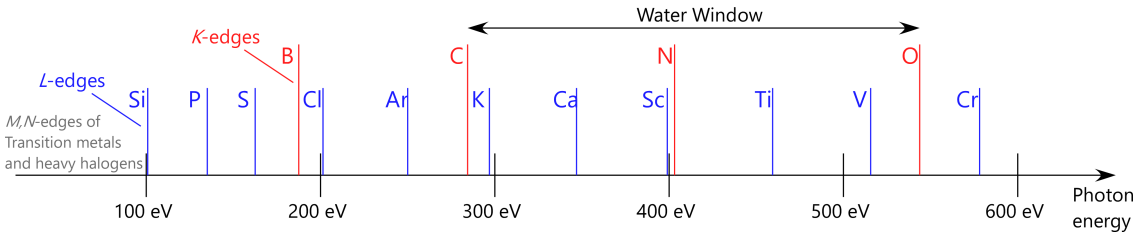

Figure 2.10: Absorption edges in the SX region.

XAS is one of the most suitable techniques for HHG-based attosecond SX spectroscopy. As explained below, this is because of the low photon flux and the ultrashort pulse duration of HHs. For example, HHG-based X-ray emission spectroscopy is difficult because it requires high photon flux. In the case of X-ray photoelectron spectroscopy, X-ray has to be monochromatized before irradiated to a sample, but it significantly elongates the pulse duration of the X-ray as well as reduces the photon flux. However, in the case of XAS, these problems can be solved by irradiating non-monochromatized X-ray to a sample and dispersing its spectrum after the sample. This measurement method is called dispersive XAFS (DXAFS) [79]. In DXAFS, the short pulse duration of HHs is preserved on the sample. Furthermore, an absorption spectrum can be measured without scanning anything, thus the measurement time can be shortened. Note that DXAFS is different from usual XAS measurements in synchrotron, where monochromatized X-ray beam is irradiated to the sample and the total (partial) photoelectron or fluorescence yield is detected while scanning the X-ray photon energy.

Mathematical formulation of XANES

The X-ray absorption process can be analytically formulated as follows. The X-ray absorption cross section σ_x of the transition from an initial state $|i\rangle$ can be written as [80],

$$\sigma_x = \sum_f \frac{4\pi^2 e^2}{m^2 c\omega} |\langle f|\boldsymbol{e}_x \cdot \boldsymbol{p}|i\rangle|^2 \rho_f(E), \tag{2.17}$$

where $|f\rangle$ is a final core-excited state, e is the elementary charge, m is the mass of an electron, c is the speed of light in vacuum, ω is the angular frequency of the X-ray, $\boldsymbol{e}_x$ is the polarization vector of the X-ray, $\boldsymbol{p}$ is the momentum operator, and $\rho_f(E)$ is the energy density of the final state. The actual absorption spectrum is broadened by a few hundreds of milli-electron volts from that obtained by Eq. (2.17) due to the finite lifetime of the core-excited states.

In the case of XANES of atoms or molecules, $\rho_f(E)$ is proportional to $(1-n)\delta(E - E_f + E_i)$ (n: electron population in the unoccupied orbital, E_f: total energy of the final state, E_i: total energy of the initial state). Considering the above discussions, XANES of atoms or molecules can provide the following information:

1. The electron population in the unoccupied orbital n [81].
2. The transition energy $E_f - E_i$.
3. The transition dipole moment $|\langle f|\boldsymbol{e}_x \cdot \boldsymbol{p}|i\rangle|^2$.

Here, it is known that the transition energy and the transition dipole moment contain the information of chemical bondings and the orientation of molecules, respectively [82, 83].

2.3 X-ray transient absorption spectroscopy

A major advantage of using HHs for XAS is that ultrafast pump-probe measurements can be performed. Pump-probe XAS is called X-ray transient absorption spectroscopy. Figure 2.11 shows a schematic of transient absorption spectroscopy. A pump laser pulse and a probe X-ray pulse are irradiated to a sample with a delay, and the spectrum of the absorbed X-ray pulse is observed by a spectrometer. By scanning the delay, one can track the dynamics of the sample via the change of the absorption spectrum.

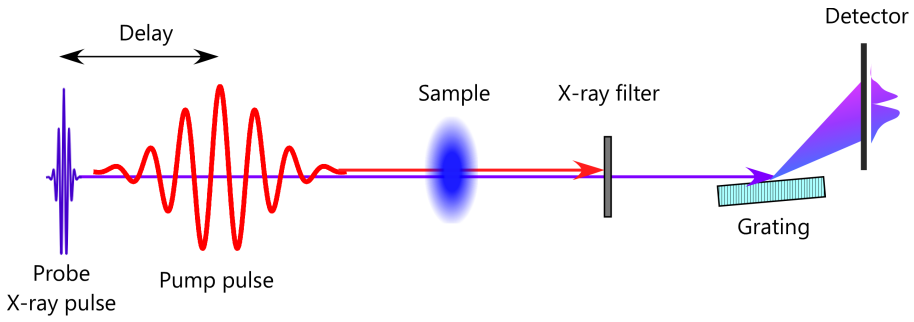

Figure 2.11: Concept of X-ray transient absorption spectroscopy.

Based on the formulation of XANES in the previous section, an X-ray transient absorption spectrum of atoms and molecules can provide the following information:

1. The change of the electron (or hole) population in unoccupied orbitals due to electron excitation, ionization, or core-hole decay.
2. The change of the transition energy $E_f - E_i$ due to nuclear motions or Stark shift.
3. The change of the transition dipole moment $|\langle f|\boldsymbol{e}_x \cdot \boldsymbol{p}|i\rangle|^2$ due to nuclear motions.
4. The emergence of new final states due to photoionization, chemical reaction, or the appearance of laser-dressed states.

Here, we add supplementary explanations for the second and the third information. Regarding the second one, as the nuclei in a molecule move, the total potential energy of a molecule changes because of the change of the repulsion and attraction force among the nuclei and electrons, thus $E_f - E_i$ changes. Aside from nuclear motions, laser-induced AC Stark shift can also change $E_f - E_i$. As for the third one, $|\langle f|\boldsymbol{e}_x \cdot \boldsymbol{p}|i\rangle|^2$ changes as the nuclei move because of the change of the molecular wave functions. Also, it is

expected to be sensitive to molecular rotation with respect to the polarization of the X-ray because of the $\boldsymbol{e}_x \cdot \boldsymbol{p}$ term in the transition dipole moment.

In addition to the above information, if there is coherence between two electronic states, it can also be probed via the oscillation of the intensity of the absorption peaks [84].

2.3.1 Previous studies of XUV transient absorption spectroscopy

Until now, HHG-based transient absorption experiments in the XUV region have been widely performed to investigate various photoinduced dynamics. In this section, several representative experiments are reviewed.

First, Fig. 2.12 shows the result of transient absorption spectroscopy of IBr which reveals its femtosecond molecular dissociation and vibration dynamics. [85]. Here, IBr is pumped by a few-femtosecond VIS laser pulse, and probed by an attosecond XUV pulse at the I N-edge and the Br M-edge. Around 0 fs, the absorption peaks of unpumped IBr (48-51 eV and 68-70 eV) decrease due to photoexcitation. Instead, new absorption peaks appear below them, which correspond to IBr molecules in their excited states. From 0 to 100 fs, the positions and the intensities of these new absorption peaks gradually change. This is due to the change of the internuclear distance in the dissociation process. At the same time, it is visible that the absorption peaks of unpumped IBr have oscillatory structures with a period of $\sim$100 fs. This is because of molecular vibration initiated by impulsive stimulated Raman scattering. After 100 fs, the dissociation process is completed and the absorption peaks converge to those of the final products, atomic I and Br.

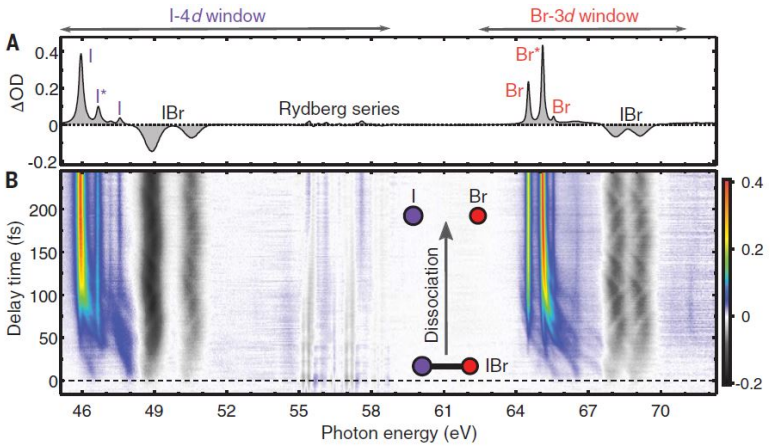

Figure 2.12: Transient absorption spectroscopy of IBr molecules at the I N-edge and the Br M-edge [85]. (A) Absorption spectrum of the dissociation products. (B) Transient absorption spectrum.

Second, examples of attosecond transient absorption spectroscopy are shown in Fig. 2.13. Figure 2.13(a) shows an attosecond transient absorption spectrum of He atoms pumped by a few-femtosecond Ti:Sa laser pulse. The photon energy of the probe pulse is set around the ionization potential of He, so there are many absorption lines corresponding to the transitions from the valence orbital to the Rydberg orbitals. Around 0 fs, these Rydberg peaks are significantly modulated, and it oscillates with a period of half the laser

cycle of the pump pulse (1.3 fs). The modulations of the peaks are due to AC Stark shift and the emergence of laser-dressed states. The coherence among these states results in the fast oscillation. Figure 2.13(b) shows an attosecond transient absorption spectrum of Xe atoms. Xe is pumped by again a few-femtosecond Ti:Sa laser pulse and probed by an attosecond pulse at the Xe N-edge. The emergence of new absorption peaks around 0 fs ($5p_{1/2}^{-1}$ and $5p_{3/2}^{-1}$ peaks) is due to the generation of Xe^+ ion by strong-field ionization. The 1.3-fs-period oscillation in these peaks reflects sub-optical-cycle hole population dynamics during the ionization process.

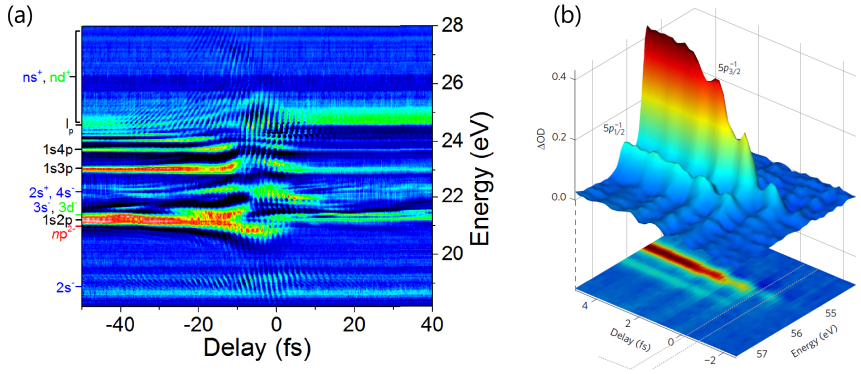

Figure 2.13: (a): Attosecond transient absorption spectrum of He atoms around the ionization threshold [86]. The assignment of the absorption peaks is shown along the left axis. (b): Attosecond transient absorption spectrum of Xe atoms at the Xe N-edge [18].

The above examples clearly demonstrate that transient absorption spectroscopy is a powerful tool to observe nuclear and electron dynamics with femtosecond-to-attosecond temporal resolution. Other than these examples, various transient absorption measurements have been conducted to reveal molecular vibration [87–89], dissociation [89–91], electron-nuclear coupling [92,93], autoionization [20,94], tunnel ionization [16,95], and electronic coherence [84,89,95]. Moreover, recently, transient absorption measurements have been extended to solids [21–25,96].

2.3.2 Previous studies of SX transient absorption spectroscopy

Recently, the development of the OP(CP)A-based HHG technology has enabled transient absorption spectroscopy in the SX region. Figure 2.14 shows representative results.

In 2017, Pertot *et al.* demonstrated HHG-based transient absorption spectroscopy at the C K-edge for the first time [62] (Fig. 2.14(a)). In their study, femtosecond dissociation of CF_4 was observed. In the same year, femtosecond transient absorption spectroscopy of cyclohexadiene (C_6H_8) molecules at the C K-edge was reported [63]. Here, a photoinduced ring opening reaction was observed. After that, femtosecond transient absorption spectroscopy at the C K-edge has been applied to various molecules such as acetylacetone ($C_5H_8O_2$), furfural (C_4H_3OCHO), chloroiodomethane (CH_2ClI), and dimethyl disulfide (CH_3SSCH_3) [97].

As for attosecond transient absorption spectroscopy in the SX region, there are two previous studies. The first demonstration was in 2018 [98] (Fig. 2.14(b)), and Chew *et al.* observed field-induced electron dynamics of Ar at the Ar L-edge (250 eV). The other

study is transient absorption spectroscopy of TiS_2 at the Ti L-edge (460 eV) [65] (Fig. 2.14(c)). They observed electron motions driven by an IR laser pulse in the conduction band of TiS_2. However, this result has not been published in a peer-reviewed journal, and there is still an argument over its reproducibility.

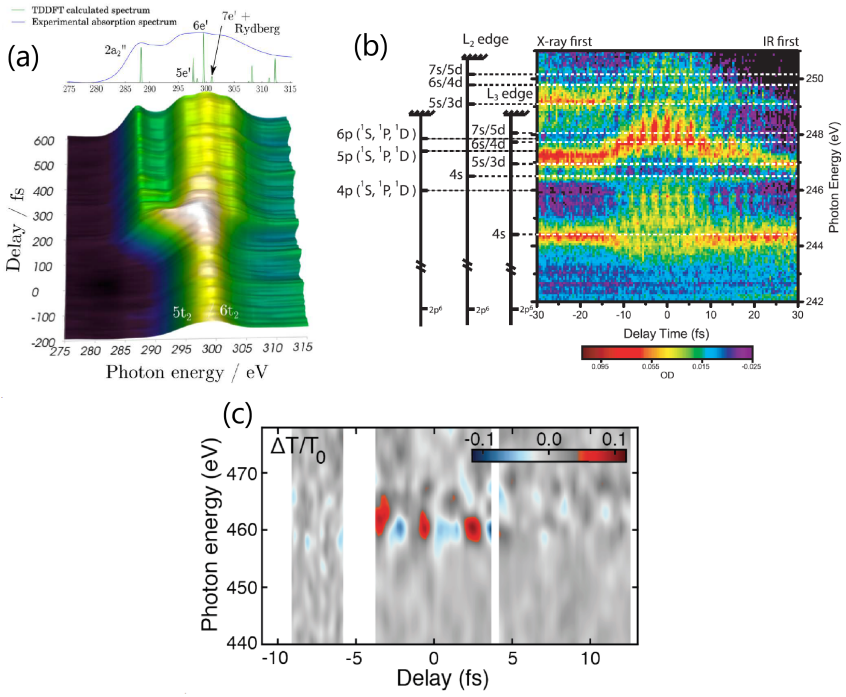

Figure 2.14: (a) Femtosecond transient absorption spectrum of CF_4 at the C K-edge [62]. (b) Attosecond transient absorption spectrum of Ar at the Ar L-edge [98]. (c) Attosecond transient absorption spectrum of TiS_2 at the Ti L-edge [65].

2.4 Previous studies of NO and N_2O

In this section, we review previous studies of NO and N_2O as these molecules are the targets of our transient absorption measurements. Especially, we focus on static XAS experiments in synchrotron facilities and laser-based experiments on ultrafast molecular dynamics.

XAS

XAS measurements of NO and N_2O at the N K-edge were conducted by Kosugi *et al.* [99] and Adachi *et al.* [100], respectively, as shown in Figs. 2.15 and 2.16. In these measurements, synchrotron radiation was used. For both absorption spectra, peak assignments were performed based on ab initio calculations. As for NO, the strong peak at 400 eV corresponds to the transition from the N 1s orbital to the 2π orbital. The weak peaks above 405 eV correspond to the transitions from the N 1s orbital to the Rydberg orbitals. As for N_2O, two strong peaks exist at 401 eV and 404.5 eV. These peaks correspond to the transitions from the 1s orbitals of the two nitrogen atoms to the

3π orbital. As in the case of NO, the weak peaks in the higher energy region correspond to the transitions from the 1s orbitals to the Rydberg orbitals.

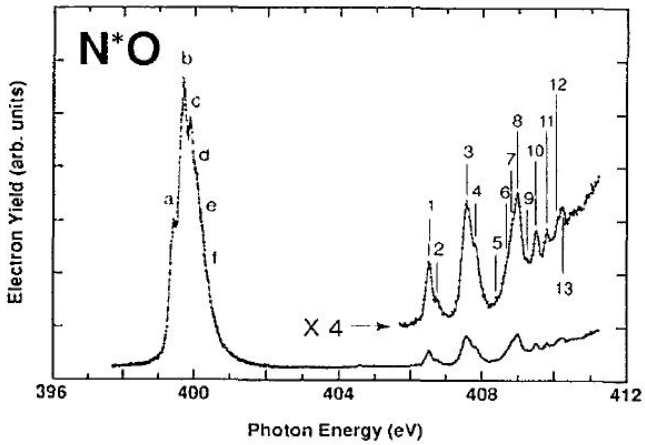

Figure 2.15: XANES of NO at the N K-edge measured in the total electron yield mode [99].

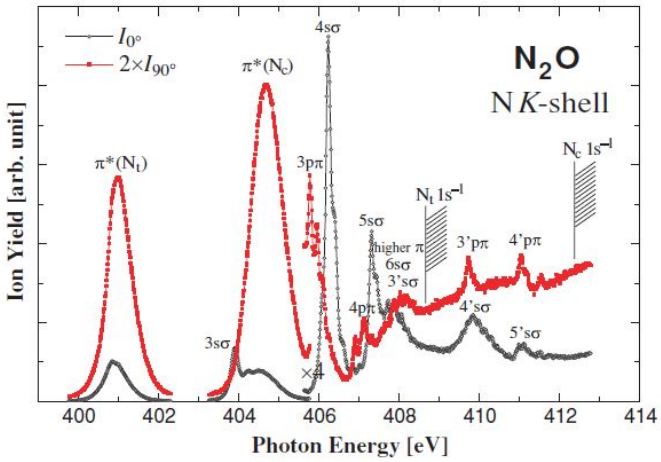

Figure 2.16: XANES of N_2O at the N K-edge [100]. Red and black curves show absorption spectra measured by collecting photoions emitted parallel and perpendicular to the polarization of the SX beam, respectively. The total absorption spectrum is obtained by taking the sum of the two curves.

Observations of ultrafast dynamics

Until now, ultrafast dynamics of NO and N_2O has been experimentally investigated by various techniques.

As for NO, there are several studies which investigated its laser-induced non-adiabatic rotational dynamics. References [101–103] utilized photoion spectroscopy, high-harmonic

spectroscopy, and photoelectron spectroscopy, respectively, to observe the rotational dynamics. Especially, refs. [102] and [103] observed a coupling between the rotational dynamics and the electronic coherence.

As for N_2O, its dissociation dynamics initiated by an XUV pulse was investigated by a photoion-photoion coincidence measurement [104]. Another study by Huppert *et al.* observed attosecond delays in photoionization of N_2O irradiated by an XUV pulse [105]. They employed the reconstruction of attosecond beating by interference of two-photon transitions (RABBITT) technique.

For both molecules, however, to the best of our knowledge, ultrafast transient absorption spectroscopy in the XUV or the SX region has not been performed so far.

2.5 Ultrafast SX light sources other than HHG

In this section, we review ultrafast light sources other than HHG.

Accelerator-based femtosecond SX light sources, such as XFELs or laser-slicing sources, are now available [106, 107]. Also, laser-based plasma sources [108, 109] provide femtosecond to picosecond X-ray pulses in a table-top manner.

Ultrafast spectroscopy using these sources have been widely conducted. For example, femtosecond transient absorption spectroscopy has been performed by using XFELs [110–112] and laser-slicing sources [113]. Figure 2.17 shows a transient absorption spectrum of thymine molecules at the O K-edge (543 eV) measured with an XFEL. Absorbance changes at a time scale of $\sim$100 fs are clearly resolved. Other than transient absorption spectroscopy, time-resolved X-ray magnetic circular dichroism (XMCD) [114], X-ray diffraction [115, 116], and photoelectron spectroscopy [117] have been successfully demonstrated.

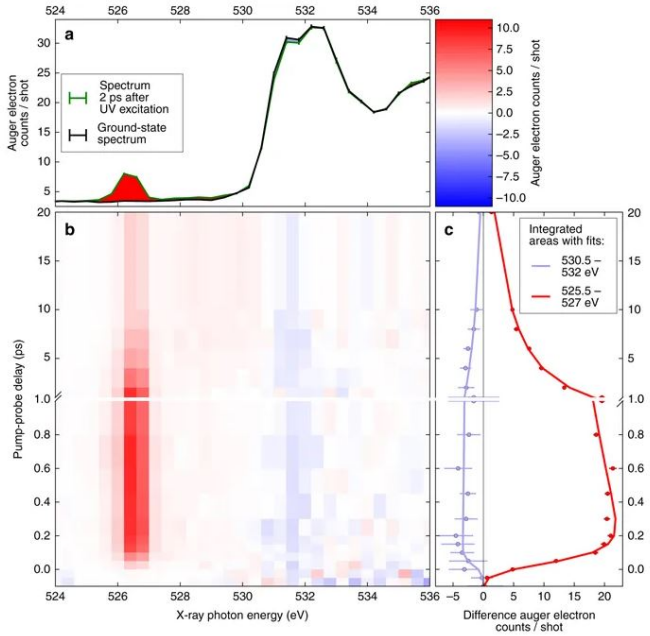

Figure 2.17: X-ray transient absorption spectrum of thymine molecules at the O K-edge measured with an XFEL [111].

As shown in Fig. 1.2, XFELs or laser-slicing sources have higher photon flux than HHG, and also cover a wide range of the SX region. However, in terms of temporal resolution, HHG-based ultrafast spectroscopy is still advantageous. Although the generation of attosecond pulses in XFELs was recently reported [118, 119], attosecond pump-probe measurements in XFELs are still challenging due to the difficulty in the precise synchronization between pump and probe pulses.

Chapter 3

IR light source and its characterization

In this chapter, we present the BIBO-OPCPA system which is employed in the HHG and the transient absorption experiments as a drive laser. Firstly, the principles of OPCPA and the broadband degenerate OPA by a BIBO crystal are briefly described. Secondly, the technical details of the BIBO-OPCPA system are presented. Finally, the characterization of the temporal waveform of the output pulses of the BIBO-OPCPA system is presented.

3.1 Principles of OPCPA

OPCPA [120] is a technique to obtain intense ultrashort light pulses by combining OPA [121] and CPA [6]. A schematic of the setup of OPA is shown in Fig. 3.1(a). A strong pump beam and a weak signal beam are incident on a nonlinear crystal to obtain an amplified signal beam. Here, another beam, called an idler beam, is generated. The photon energy of the idler beam is equal to the difference between the photon energy of the signal beam and that of the pump beam. Figure 3.1(b) depicts the microscopic OPA process. A pump photon is split into a signal and an idler photon via virtual excited states in the nonlinear crystal. Because of the energy conservation law, $\omega_{\mathrm{pump}} = \omega_{\mathrm{signal}} + \omega_{\mathrm{idler}}$ is satisfied. In OPCPA (Fig. 3.1(c)), the temporal duration of the signal pulse is stretched before OPA, and it is compressed after OPA. By doing so, even if the fluence of the pump pulse is high, damages in the nonlinear crystal can be avoided.

OPCPA has several advantages over conventional light amplification by laser crystals. First, because of the broad gain bandwidth of OPA, it is relatively easy to generate ultrashort pulses without extra spectral broadening. Second, because the energy of a pump photon is fully converted into those of signal and idler photons, the heat accumulated in a nonlinear crystal is much smaller than that in a laser crystal. Therefore, OPCPA is scalable to high average power systems.

3.2 Degenerate OPA in a BIBO crystal

For efficient OPA, the wave numbers of the pump (k_p), the signal (k_s), and the idler (k_i) beams have to fulfill the following phase-matching condition:

$$k_p \simeq k_s + k_i. \tag{3.1}$$

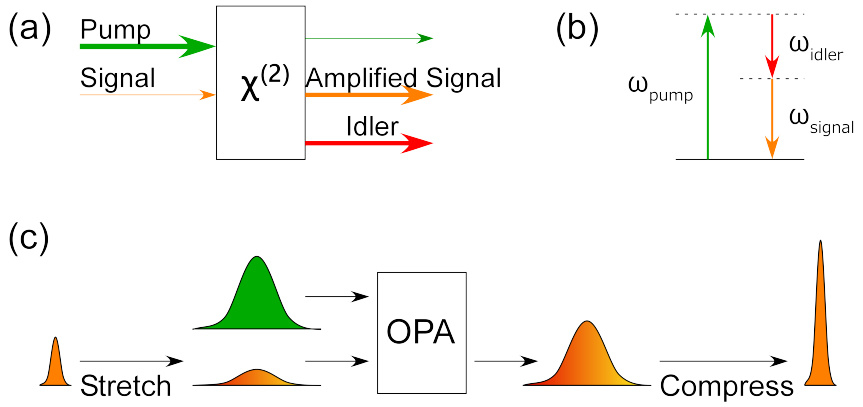

Figure 3.1: Schematics of (a, b) OPA and (c) OPCPA.

Intuitively, if the phase-matching condition is not fulfilled, the relative phases of the three beams are shifted as they propagate in the nonlinear crystal, resulting in a destructive interference of the amplified signal beam. Phase matching can be evaluated by the phase mismatch Δk which is defined as

$$\Delta k = k_p - k_s - k_i. \tag{3.2}$$

To realize efficient and broadband OPA, the phase mismatch has to be small for a wide range of the spectrum. However, because the refractive index of a material is dependent on wavelength, the phase mismatch is also usually largely dependent on wavelength.

The phase mismatch in OPA can be analytically modeled as follows. We assume that the bandwidth of the pump pulse is narrow and its wavenumber k_p can be regarded as constant. The signal and the idler pulses are assumed to be broadband, and their central frequencies are represented as ω_{s0} and ω_{i0}, respectively. Let $\omega_s = \omega_{s0} + \Delta\omega$ be a frequency component of the signal pulse. According to the energy conservation law, the corresponding frequency component of the idler pulse is $\omega_i = \omega_{i0} - \Delta\omega$. In this case, the wave numbers of the signal and the idler pulses, k_s and k_i can be expressed as

$$k_s(\omega_{s0} + \Delta\omega) = k_s(\omega_{s0}) + \frac{\mathrm{d}k}{\mathrm{d}\omega}\Big|_{\omega=\omega_{s0}} \Delta\omega + \frac{1}{2}\frac{\mathrm{d}^2k}{\mathrm{d}\omega^2}\Big|_{\omega=\omega_{s0}} \Delta\omega^2 + \cdots \tag{3.3}$$

$$k_i(\omega_{i0} - \Delta\omega) = k_i(\omega_{i0}) - \frac{\mathrm{d}k}{\mathrm{d}\omega}\Big|_{\omega=\omega_{i0}} \Delta\omega + \frac{1}{2}\frac{\mathrm{d}^2k}{\mathrm{d}\omega^2}\Big|_{\omega=\omega_{i0}} \Delta\omega^2 - \cdots . \tag{3.4}$$

The phase mismatch is then calculated as

$$\begin{aligned}\Delta k = {} & k_p - k(\omega_{s0}) - k(\omega_{i0}) \\ & - \left(\frac{\mathrm{d}k}{\mathrm{d}\omega}\Big|_{\omega=\omega_{s0}} - \frac{\mathrm{d}k}{\mathrm{d}\omega}\Big|_{\omega=\omega_{i0}}\right)\Delta\omega \\ & - \frac{1}{2}\left(\frac{\mathrm{d}^2k}{\mathrm{d}\omega^2}\Big|_{\omega=\omega_{s0}} + \frac{\mathrm{d}^2k}{\mathrm{d}\omega^2}\Big|_{\omega=\omega_{i0}}\right)\Delta\omega^2 \\ & - \frac{1}{6}\left(\frac{\mathrm{d}^3k}{\mathrm{d}\omega^3}\Big|_{\omega=\omega_{s0}} - \frac{\mathrm{d}^3k}{\mathrm{d}\omega^3}\Big|_{\omega=\omega_{i0}}\right)\Delta\omega^3 - \cdots .\end{aligned} \tag{3.5}$$

The first term of the right hand side of Eq. (3.5) is the phase mismatch at the central frequency, and it can be tuned to zero by adjusting the cut angle of the nonlinear crystal. The other terms cannot usually be compensated. However, if the central frequencies of the signal and the idler pulses are the same (i.e., $\omega_{s0} = \omega_{i0}$), all terms with odd powers of $\Delta\omega$ vanish, thus the phase mismatch becomes small for a broad range of the spectrum. This condition is called degenerate OPA. Moreover, if $\mathrm{d}^2k/\mathrm{d}\omega^2$ is zero at ω_{s0} (= ω_{i0}), the $\Delta\omega^2$ term also vanishes. Because $\mathrm{d}^2k/\mathrm{d}\omega^2$ is the group velocity dispersion, such a wavelength is called a zero-dispersion wavelength.

In the case of BIBO, the zero-dispersion wavelength is around 1600 nm. Therefore, if the pump wavelength is 800 nm and the signal and the idler wavelengths are 1600 nm, ultrabroadband degenerate OPA can be realized. Here, the signal wavelength of 1600 nm is favorable for HHG in the water window. Furthermore, the pump pulse at 800 nm can be generated with the highly matured Ti:Sa technology.

The gain curve of BIBO pumped by an 800 nm, 10 GW/cm^2 pulse is shown in Fig. 3.2. A broad gain spectrum ranging from 1100 nm to the MIR region is obtained. Note that, because BIBO has strong absorption above ∼2200 nm, the effective gain bandwidth is approximately one octave (1100-2200 nm).

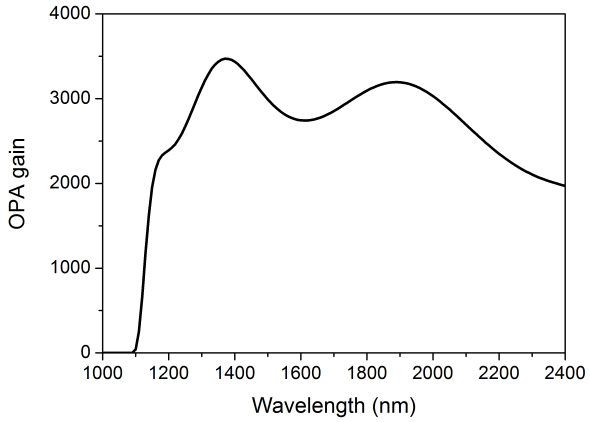

Figure 3.2: Calculated OPA gain spectrum of a 5-mm-thick BIBO crystal pumped by a 800 nm, 10 GW/cm^2 pulse.

3.3 BIBO-OPCPA system

Figure 3.3 depicts a schematic of the BIBO-OPCPA system. This system was designed and developed by Dr. Nobuhisa Ishii [36, 57].

For the generation of the pump and the seed (unamplified signal) pulses of OPCPA, Ti:Sa CPA systems are employed. First, the output from a Ti:Sa oscillator (Femtolasers, INTEGRAL element, 450 mW, < 10 fs) is split into two arms: seed and pump arms.

First, we describe the details of the seed arm. The pulses from the Ti:Sa oscillator are stretched by a grating pair, then amplified by a Ti:Sa regenerative amplifier (1 kHz), and compressed by a transmission grating pair (1250 l/mm) [122]. The pulse energy and the temporal duration of the output pulses are 1 mJ and 45 fs FWHM, respectively.

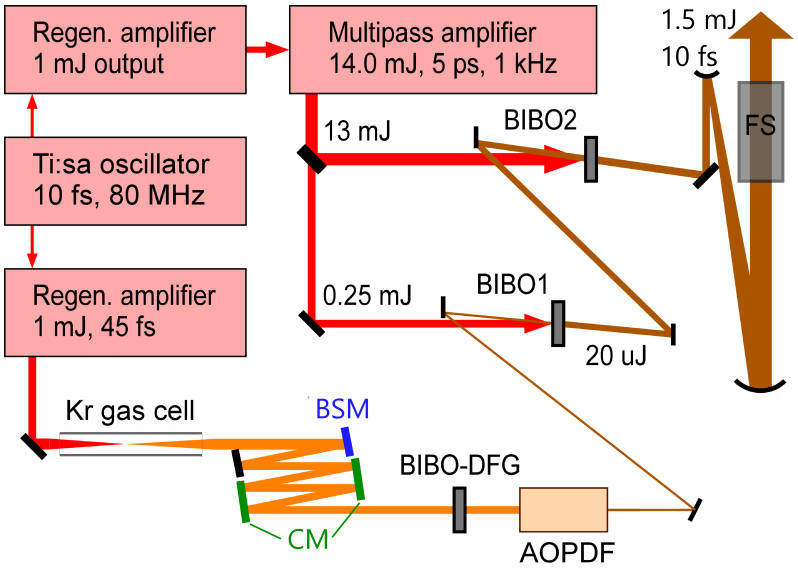

Figure 3.3: Schematic of the BIBO-OPCPA system (BSM: band stop mirror, CM: chirped mirrors, BIBO-DFG: 1-mm-thick BIBO crystal for difference frequency generation, AOPDF: acousto-optic programmable dispersive filter, BIBO1: 4-mm-thick BIBO crystal, BIBO2: 6-mm-thick BIBO crystal, FS: 15-cm-long fused silica).

These pulses are loosely focused to a gas cell filled with 1 bar of Kr, where the spectrum is broadened by self-phase modulation. The broadened white light pulses are reflected by a band stop mirror (BSM, custom fabricated by Tokai Optical) to remove the central part of its spectrum around 800 nm. Then they are compressed by a pair of chirped mirrors (CMs) and focused into a 1-mm-thick BIBO crystal by a concave mirror (f = 250 mm). Here, by the difference frequency generation (DFG) process between the short and the long wavelength components of the white light, IR seed pulses with a central wavelength of 1600 nm are generated. In the DFG process, the CEP of the seed pulses is passively stabilized [123, 124]. The mechanism of the CEP stabilization can be explained by a frequency comb picture of DFG. Let $f_n = nf_{\mathrm{rep}} + f_{\mathrm{CEO}}$ be the n-th longitudinal mode of the white light pulses (f_{rep}: repetition rate, f_{CEO}: carrier offset frequency). Then, the difference frequency between the n-th and m-th modes can be calculated as $f_n - f_m = (n-m)f_{\mathrm{rep}}$. In this way, the carrier offset frequency of the DFG pulses becomes zero, and their CEP is stabilized. After DFG, the seed pulses are transmitted through an acousto-optical programmable dispersive filter (AOPDF, Fastlite, Dazzler HR45-1200-2200) [125]. In the Dazzler, the seed pulses are diffracted by a grating structure generated by acoustic waves. The spectral phase, including the CEP and the group delay, of the diffracted seed pulses can be arbitrarily controlled by changing the patterns of the acoustic waves. In our system, the seed pulses are positively chirped and stretched to $\sim$4 ps in the Dazzler.

Next, we describe the details of the pump arm. The output pulses of the Ti:Sa oscillator are stretched and amplified in a regenerative amplifier as in the seed arm. After that, the pulses are further amplified by a three-stage multipass amplifier to 17.5 mJ. The amplified pulses are compressed by a pair of transmission gratings (1740 l/mm) [122]. Here, by adjusting the spacing between the gratings, the compressed pulses are slightly negatively

chirped and their pulse duration is adjusted to ∼5 ps. By doing so, the pulse durations of the pump and the seed pulses become almost the same, and efficient OPA is realized. The pulse energy of the pump pulse is 14 mJ after the compressor.

Because the seed and the pump Ti:Sa beams are amplified in independent regenerative amplifiers, the timing drift between the two beams might be a problem. If the timing drift is very large, it leads to the instability of the output from the BIBO-OPCPA system. In order to check the timing drift, a balanced optical cross correlation measurement [126] is performed. Two beams from the pump and the seed arms are picked up for cross-correlation: a Ti:Sa beam which is transmitted through a BIBO crystal in the first stage of the OPCPA and a Ti:Sa beam which is transmitted through the BSM. The two beams are fed into a balanced optical cross correlator shown in Fig. 3.4(a). The measured timing drift between the two beams for 700 minutes is plotted in Fig. 3.4(b). The drift is a few tens of femtoseconds, which is much smaller than the pulse duration of the pump and the seed pulses (∼ 5 ps). Therefore, the timing drift does not so much affect the stability of the OPCPA.

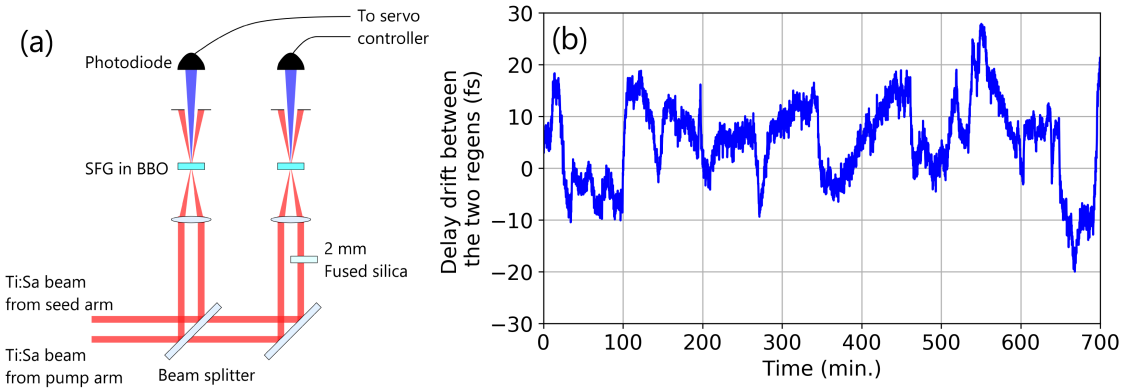

Figure 3.4: (a) Setup of the balanced optical cross correlator. (b) Measured timing drift between the pump and the seed arms.

In the OPCPA, the seed pulses are amplified in two stages. In the first stage, the pulse energy of the pump pulse is set to 250 µJ. The thickness of the BIBO crystal is 4 mm, and the cut angle is 11.4° (type I phase matching). The amplified signal pulse has ∼20 µJ pulse energy. In the second stage, the pulse energy of the pump pulse is 13 mJ. The thickness of the BIBO crystal is 6 mm, and the cut angle is the same. The amplified signal pulse is transmitted through a 15-cm-long fused silica (FS) block, where its positive chirp is compensated by the negative dispersion of FS. The pulse energy of the compressed output pulse is 1.5 mJ. The spectral phase and the CEP of the output pulse can be finely tuned by changing the settings of the Dazzler.

The temporal shape of the output pulse is characterized by the third harmonic generation frequency resolved optical gating (THG-FROG) technique [127], as shown in Fig. 3.5. The pulse duration is measured to be 10.1 fs. The central wavelength in Fig. 3.5 is around 1700 nm, which is longer than the designed value (1600 nm). The central wavelength depends on the daily alignment of the OPCPA system, and it is typically from 1600 to 1700 nm.

The CEP stability of the BIBO-OPCPA system is evaluated by the single-shot f-to-$2f$ interferometry. A fraction of the output beam is focused into a 5-mm-thick fused silica

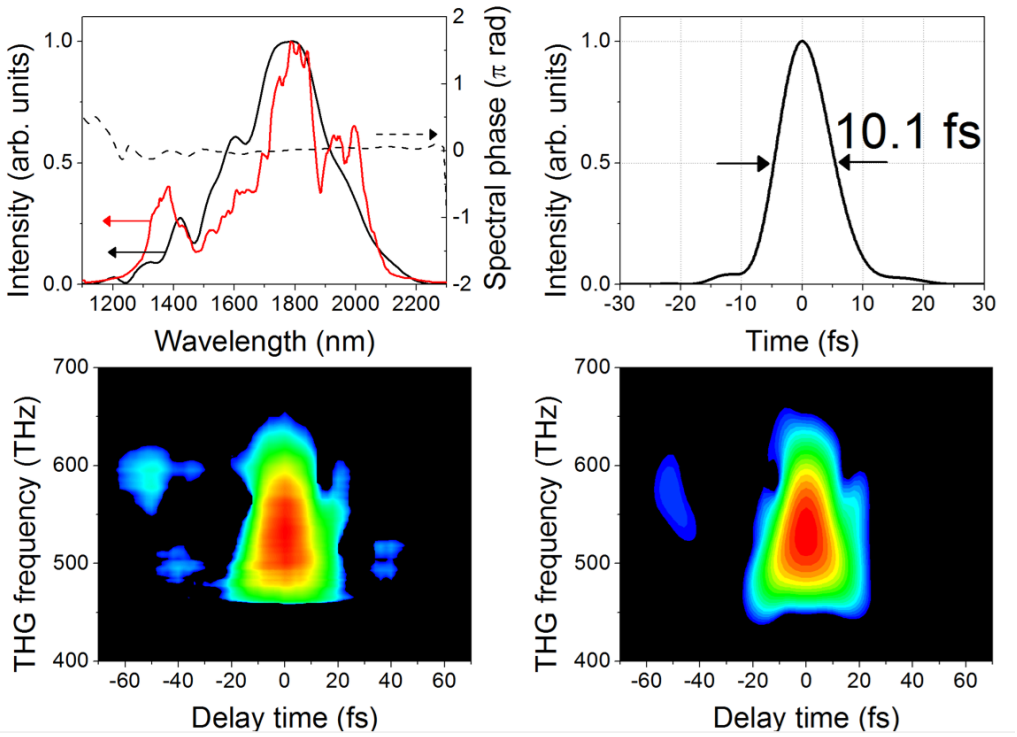

Figure 3.5: THG-FROG measurement of the output of the BIBO-OPCPA system [57]. (Upper left) Measured (red solid curve) and reconstructed (black solid curve) spectral intensities together with the reconstructed spectral phase (black dashed curve). (Upper right) Reconstructed pulse shape. (Lower left) Measured FROG trace. (Lower right) Reconstructed FROG trace.

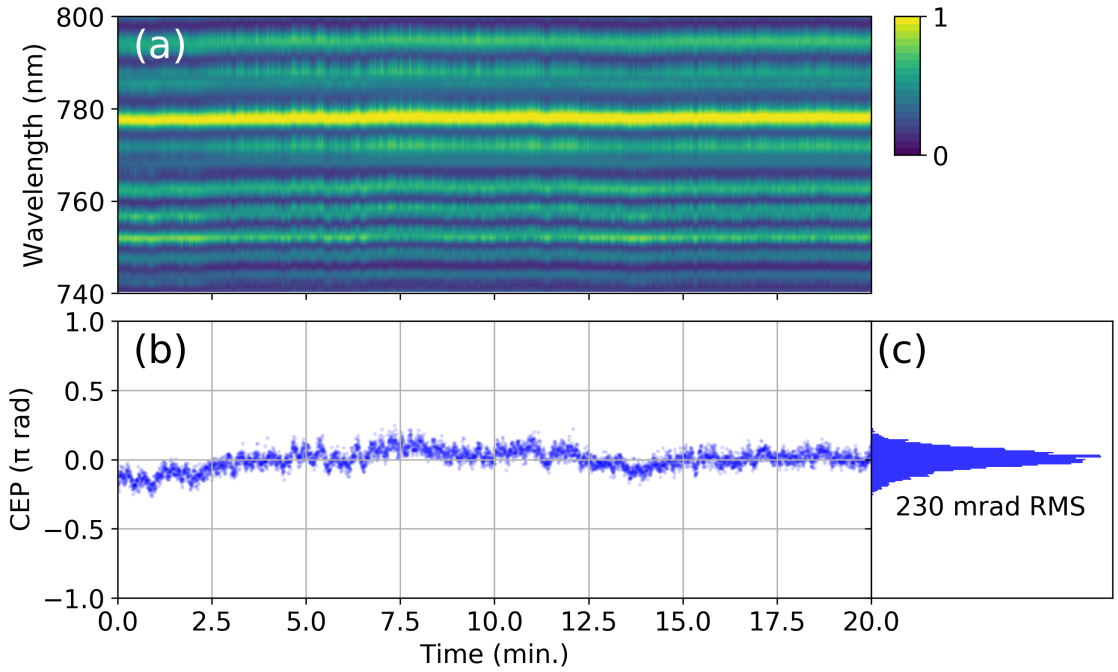

Figure 3.6: *f*-to-2*f* measurement of the output pulses of the BIBO-OPCPA. (a) Measured spectral interference fringes. (b) Relative CEPs extracted from the interference fringes. (c) Distribution of the measured relative CEPs.

plate to generate a white light. The beam is then refocused into a 100-µm-thick β-BaB_2O_4 (BBO) crystal to generate the second harmonic (SH). The spectral interference between the white light and the SH is measured by a spectrometer. The data acquisition time of the spectrometer is set to 1 ms to realize a single-shot measurement. Here, we do not synchronize the spectrometer to the accurate repetition rate of the laser, so sometimes we have two shots or zero shot in a measured spectrum, which we discard when analyzing the data. The spectra are recorded for 20 minutes with a 200-ms interval between each data acquisition. Figure 3.6 shows the result. The measured CEP stability is 230 mrad RMS for 20 minutes. As for the long-term CEP stability, another (not a single-shot) *f*-to-2*f* measurement is performed, and the drift of the CEP is measured to be 240 mrad RMS for 12.8 hours.

3.4 Waveform characterization of IR pulses using plasma fluorescence

3.4.1 Motivation

In the previous section, the temporal shape of the BIBO-OPCPA output pulse is measured by THG-FROG. However, although the THG-FROG measurement provides the information on the pulse envelope, it cannot measure the carrier wave including the absolute CEP. This missing information is important for strong field physics, where electron dynamics is dramatically affected by a small change of CEP. Therefore, it is desirable to measure

the complete temporal waveform rather than the pulse envelope alone.

Until now, various waveform characterization techniques have been demonstrated, including attosecond streaking [128], petahertz optical oscilloscope [129], attosecond resolved interferometric electric-field sampling (ARIES) [130], XUV spatial interferometry [131], and frequency-resolved optical gating capable of carrier-envelope phase determination (FROG-CEP) [132]. However, these techniques require either XUV optics or numerical retrieval procedures, which complicates the waveform measurements.

Recently, a technique called TIPTOE (tunneling ionization with a perturbation for the time-domain observation of an electric field) has been demonstrated to solve this problem [133]. A schematic of the TIPTOE measurement is depicted in Fig. 3.7. A strong, CEP-locked, few-cycle "probe" pulse and a weak, CEP-locked "signal" pulse are focused into a gas medium. The ion current from the tunnel-ionized gas medium is measured as a function of the delay between the probe and the signal pulses, as shown in the gray dashed frame in Fig. 3.7. This ion current (= tunnel ionization yield) directly reflects the waveform of the signal pulse [134, 135]. In this approach, the measurement can be performed without a vacuum setup and the waveform can be obtained without a numerical retrieval procedure.

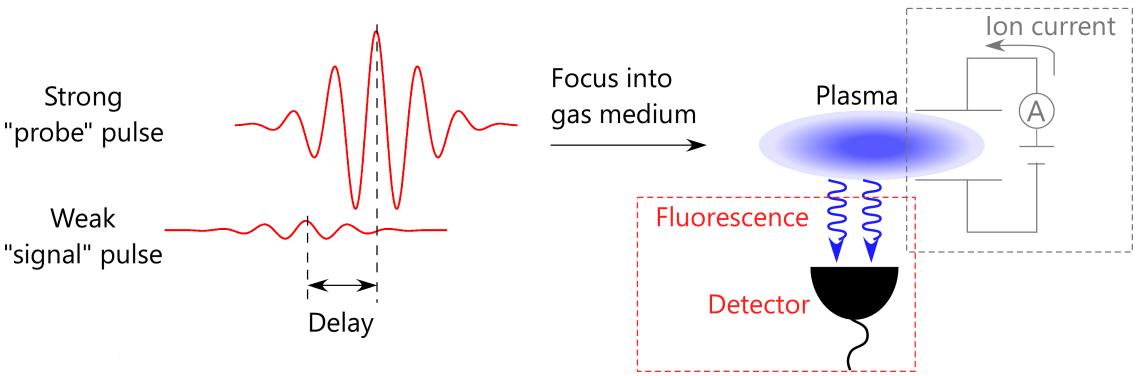

Figure 3.7: Schematic of the waveform characterization. In TIPTOE, the ion current is measured as a function of the delay between the probe and the signal pulses (gray dashed frame), but our method detects the fluorescence from the plasma instead of the ion current (red dashed frame).

One drawback of TIPTOE is that metal electrodes for collecting the ion current have to be inserted near the focus of the laser. For example, if one would like to perform other experiments at the same focus, these electrodes might interfere with other experimental setups (e.g., a gas cell for HHG). Therefore, it is convenient if waveforms can be measured from a remote position without disturbing the focal region of the laser. For this, we have developed a new TIPTOE method. In this method, instead of the ion current, the fluorescence from the ionized gas molecules is measured by a detector, as shown in the red dashed frame in Fig. 3.7. Such fluorescence is called "plasma fluorescence" [136]. The intensity of the plasma fluorescence is expected to be proportional to the tunnel ionization yield, thus waveforms can be measured as in the ion current measurement.

3.4.2 Measurement principle

The mechanism of the waveform measurement can be mathematically formulated as follows. Let $\boldsymbol{E}_p(t)$ and $\boldsymbol{E}_s(t)$ be the electric field vectors of the strong probe pulse and the weak signal pulse, respectively, and $w(E)$ be the tunnel ionization rate at a static field amplitude E. Note that the probe pulse is linearly polarized and its envelope has a peak at $t = 0$; also note that the signal pulse has an arbitrary polarization. The ionization probability $P(\tau)$ under the irradiation by the probe and the signal pulses with a delay of τ can be written as

$$\begin{aligned} P(\tau) &= \int w(|\boldsymbol{E}_p(t) + \boldsymbol{E}_s(t+\tau)|)\mathrm{d}t \\ &\simeq \int \frac{\mathrm{d}w}{\mathrm{d}E}\Big|_{E=|\boldsymbol{E}_p(t)|} \frac{\boldsymbol{E}_p(t)\cdot\boldsymbol{E}_s(t+\tau)}{|\boldsymbol{E}_p(t)|}\mathrm{d}t + \mathrm{const.} \\ &= \int \frac{\mathrm{d}w}{\mathrm{d}E}\Big|_{E=|\boldsymbol{E}_p(t)|} E_{s\,proj}(t+\tau)\mathrm{d}t + \mathrm{const.} \end{aligned} \tag{3.6}$$

Here, $E_{s\,proj}(t)$ is the projection of the signal electric field along the polarization direction of the probe pulse. In Eq. (3.6), we assume that the signal pulse is sufficiently weaker than the probe pulse and extract only the first-order term of $\boldsymbol{E}_s(t+\tau)$. Furthermore, we ignore the depletion of the ground state. Note that, in our experiment, we use N_2 as a target gas medium and use a 1600-nm, 1.28×10^{14}-W/cm^2, 11-fs laser pulse as a probe pulse. In such a situation, as shown below, the ionization probability is calculated to be less than 1%. Thus, the assumption of the low ground state depletion is reasonable in our case. Tunnel ionization is highly nonlinear and mostly confined to the regions in which $|\boldsymbol{E}_p(t)|$ becomes maximal (i.e., the peaks in the probe field occurring every half cycle). Therefore, if the carrier wave of the probe electric field is proportional to $\cos(\omega t)$, the ionization probability can further be approximated as

$$P(\tau) \simeq \sum_n a_n E_{s\,proj}(\tau + \frac{n\pi}{\omega}) + \mathrm{const}, \tag{3.7}$$

where a_n is a constant representing the derivative of the ionization rate with its sign alternating between adjacent half cycles of the probe pulse. If the probe pulse is short enough and its waveform is cosine-like, the component at $n = 0$ becomes dominant in the summation in Eq. (3.7), and $E_{s\,proj}(\tau)$ becomes proportional to the modulation of the ionization probability $P(\tau)$. In this way, the signal waveform can be directly measured from the tunnel ionization yield. Note that the Keldysh parameter is 0.5 in our experiment, which is calculated from the ionization potential of N_2 (15.58 eV) and the wavelength and the peak intensity of the probe pulse (1600 nm and 1.28×10^{14} W/cm^2). Therefore, the tunnel ionization picture is valid in our experiment.

To verify the validity of the above formulation, a simulation of the waveform measurement is performed. The probe pulse used in the simulation is a Gaussian pulse with a central wavelength of 1600 nm, a peak electric field of 310 MV/cm (1.28×10^{14} W/cm^2), and a pulse duration of 11 fs. First, the time evolution of the ionization probability of a nitrogen molecule irradiated by only the probe pulse is calculated (Fig. 3.8(a)). In the calculation, the molecular ADK model [137] for randomly oriented nitrogen molecules is used. Figure 3.8(a) indicates that the ionization is mostly confined to the central part

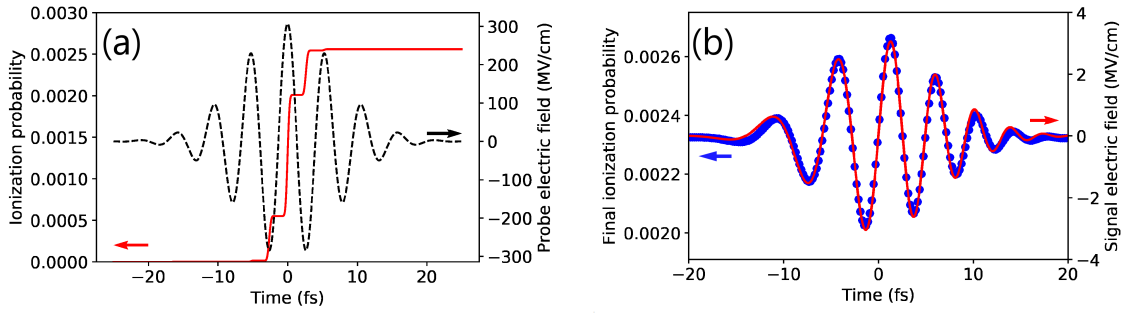

Figure 3.8: (a) Calculated temporal evolution of the ionization probability of N_2 (red solid curve) irradiated by a strong probe pulse (black dashed curve). The peak intensity of the probe pulse is set to 1.28×10^{14} W/cm^2. (b) Calculated final ionization probability (blue circles) as a function of the delay between the probe pulse (red solid curve in (b)) and the signal pulse (red solid curve). The peak intensities of the probe and the signal pulses are set to 1.28×10^{14} W/cm^2 and 1.20×10^{10} W/cm^2, respectively.

of the probe pulse. Next, a signal pulse is superimposed on the probe pulse and the ionization modulation is simulated. The central wavelength and the temporal duration of the signal pulse are the same as those of the probe pulse; however, the peak electric field amplitude is reduced to 3 MV/cm (1.20×10^{10} W/cm^2) and a linear chirp is added. The polarization of the signal pulse is set to the same as the probe pulse. The calculated ionization modulation and the waveform of the signal pulse are almost perfectly matched as shown in Fig. 3.8(b).

3.4.3 Experiment

Figure 3.9(a) shows a schematic of the experimental setup of the waveform measurement. The IR pulses from the BIBO-OPCPA system are split into two arms by a hole-drilled mirror. The reflected beam serves as the probe beam. It passes through a half-wave plate (HWP, Thorlabs AHWP10M-1600), a variable neutral density filter (VND), and a 2-mm-thick FS plate for dispersion compensation. The transmitted beam serves as the signal beam. It passes through a pair of FS wedges for CEP control, a VND, a quarter-wave plate (QWP, Thorlabs AQWP10M-1600), and an iris. The temporal delay between the two beams is controlled by a delay stage in the probe arm. The two beams are recombined by another hole-drilled mirror and focused into a nitrogen gas cell by a concave mirror (f = 375 mm). The pressure of nitrogen is set to 50 mbar to suppress nonlinear propagation. The fluorescence is collected by a BK7 lens, filtered through a band-pass filter (BPF, Edmund Optics #65-189) and an iris, then detected by a photomultiplier tube (PMT, Hamamatsu H10720-210). The BPF transmits only the 337-nm line (2P(0, 0)) in the fluorescence spectrum (Fig. 3.9(b)), which corresponds to the transition from the lowest vibration level of the $C^3\Pi_u$ state to the lowest vibration level of the $B^3\Pi_g$ state in a neutral nitrogen molecule [138]. The electric current from the PMT is measured by a lock-in amplifier. For lock-in detection, the repetition rate of the signal pulse is reduced to 500 Hz by a chopper.

For accurate waveform measurements, it is important that the CEP of the probe pulse is set to cosine-like. To detect the CEP of the probe pulse, the SH of the IR pulse is

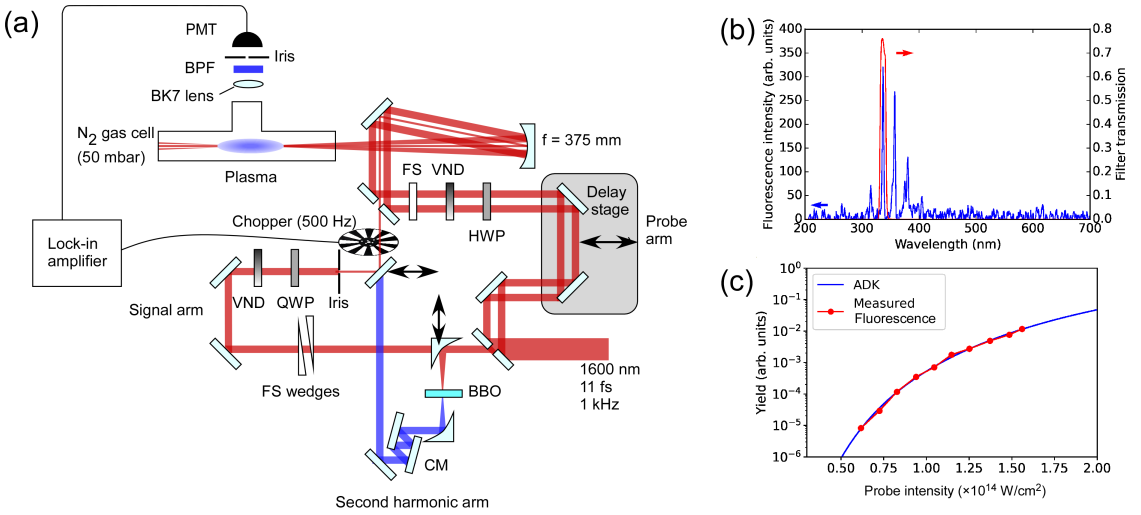

Figure 3.9: (a) Experimental setup of the waveform measurement. (b) Spectrum of the plasma fluorescence from nitrogen gas (blue curve) and the transmission of the BPF (red curve). (c) Dependence of the plasma fluorescence yield on the laser intensity (red circles) and the tunnel ionization yield calculated using the molecular ADK model (blue curve).

introduced as a signal pulse and the intensity of the plasma fluorescence is measured as a function of the delay between the probe and the SH pulses as described in [133]. In our setup, the signal arm can be replaced with the SH arm that comprises a BBO crystal to generate the SH and a CM pair for pulse compression. In this way, the CEP of the probe pulse can be detected with an error of $\sim 0.04\pi$ rad. Then, the CEP is fixed to cosine-like using the Dazzler.

Unlike the ion current, it is not trivial that the fluorescence intensity is proportional to the tunnel ionization yield. To verify this, the laser intensity dependence of the 2P(0, 0) fluorescence yield is measured under irradiation with only the probe beam (Fig. 3.9(c), red circles). Note that the absolute intensity in Fig. 3.9(c) is calibrated to match the calculated ion yield using the ADK model for randomly-oriented nitrogen molecules (Fig. 3.9(c), blue curve). The calibrated laser intensity agrees with the intensity estimated based on the pulse energy, pulse duration, and spot size within a factor of two. The agreement between the measured intensity dependence and the ADK calculation indicates that the plasma fluorescence is almost proportional to the ionization yield, and thus can be utilized to measure optical waveforms.

3.4.4 Results

Figure 3.10(a) plots a typical waveform measured with a long delay scan. The estimated peak electric fields of the probe and the signal pulses are 310 MV/cm (1.28×10^{14} W/cm^2) and 3 MV/cm (1.20×10^{10} W/cm^2), respectively. The spectral intensity and the phase obtained from the Fourier-transform of the measured waveform are plotted in Fig. 3.10(b) as the red and the black circles, respectively. The spectral intensity measured by a grating-based spectrometer is also shown as the blue curve. The good agreement between the two spectral intensities indicates that the waveform measurement covers a broad spectrum spanning nearly one octave.

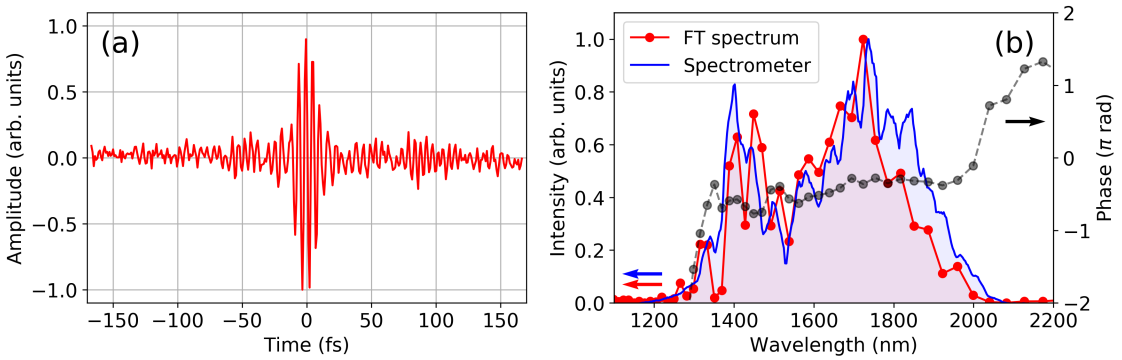

Figure 3.10: (a) A waveform measured by a long delay scan and (b) its spectral intensity (red circles) and phase (black circles). The spectral intensity measured by a spectrometer is shown as a reference (blue curve).

In order to check that the measured spectral phase is reliable, a 2-mm-thick FS plate is inserted in the signal arm, and the waveform is measured. Figures 3.11(a) and (b) plot the measured waveforms without and with the FS plate. With the FS plate, it is visible that the waveform is negatively chirped and the pulse duration is elongated. By extracting the spectral phases of the two waveforms and taking their difference, the spectral phase induced by the FS plate can be obtained (Fig. 3.11(c), blue circles). The obtained phase agrees well with the calculated phase of the FS plate by using the Sellmeier equation [139] (red curve). This result indicates that our method can correctly measure spectral phases.

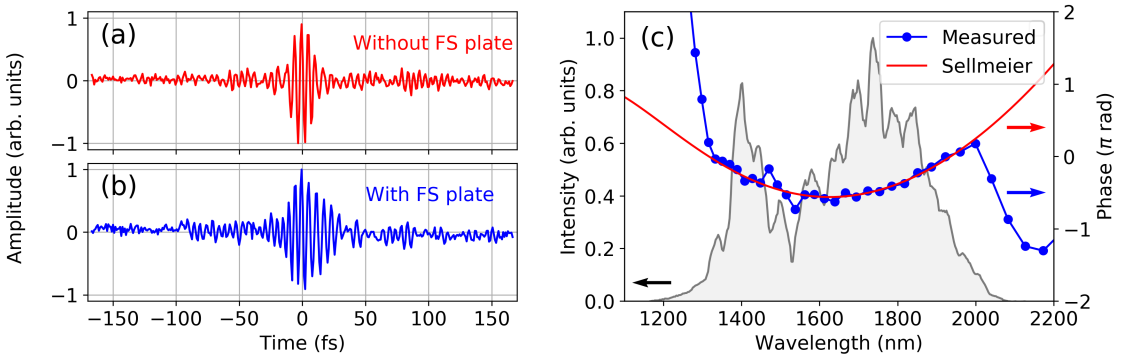

Figure 3.11: Measured waveforms (a) without and (b) with a 2-mm-thick FS plate inserted in the signal arm. (c) Spectral phase difference between the two waveforms in (a) and (b) (blue circles). Calculated spectral phase of the FS plate (red curve) and the spectral intensity of the signal pulse (gray curve) are also shown.

CEP-dependent waveforms are also measured (Fig. 3.12). In the measurement, the insertion of the FS wedge in the signal arm is adjusted to change the CEP of the signal pulse. The red and blue circles in Fig. 3.12 represent two measured waveforms with a CEP difference of π rad. The solid curves represent the smoothed data after Fourier filtering and the dashed curves are their envelopes. As expected, the carrier waves are inverted while their envelopes are almost unchanged. From the waveform measurements, the temporal duration of the signal pulse is estimated to be 11 fs FWHM.

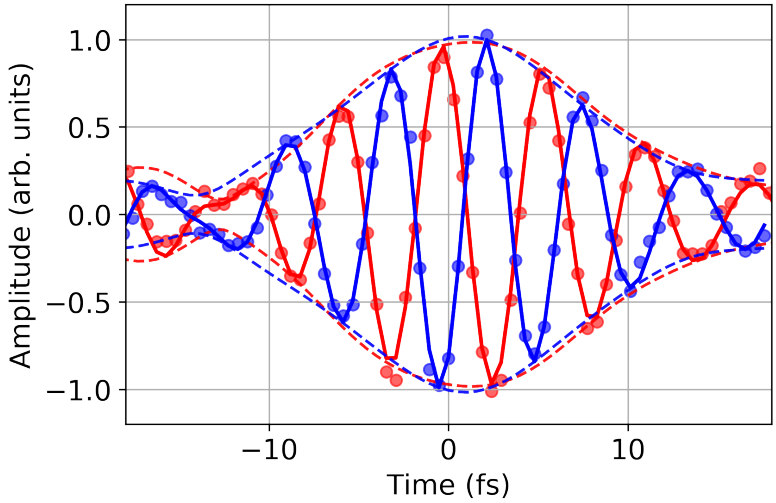

Figure 3.12: CEP-dependent waveforms; the red and blue circles represent the data measured with a CEP difference of π rad. The solid curves are the smoothed data and the dashed curves are their envelopes.

3.4.5 Discussions

The above results show that the output of the BIBO-OPCPA system has an almost flat spectral phase and an ultrashort pulse duration of $\sim$10 fs, which is also observed in the THG-FROG measurement (Fig. 3.5). Furthermore, the controllability of the CEP is directly confirmed. This is especially important for the generation of isolated attosecond pulses.

A difference between the results of the THG-FROG and the TIPTOE measurements is the spectral phases around the edges of the laser spectrum. In the TIPTOE measurement, the spectral phase is deviated from the flat phase around $\sim$1200 nm and $\sim$2000 nm while it is relatively flat in the THG-FROG measurement. This might be due to different optimization of the spectral phase of the BIBO-OPCPA system, as the two measurements are conducted in different days. Another reason might be large errors in determining the spectral phase around the edges of the laser spectrum in THG-FROG and TIPTOE.

Different from the ion current measurement, the spatial distribution of the ionization yield can be easily obtained in the fluorescence measurement. Although we skip the details here, by using a CCD camera as a fluorescence detector, we demonstrate that the information on the spatial properties of the IR beam such as the Gouy phase can also be retrieved [140]. Moreover, the space-resolved fluorescence detection can be applied to a single-shot waveform measurement. Using cylindrical focusing, the probe pulse can generate a sheet-like plasma distribution. If a large, collimated signal pulse is superimposed on the probe pulse with a small tilt, the delay between the two pulses can be mapped to the position in the beam. Thus, by measuring the spatial distribution of the fluorescence with a CCD camera, the waveform can be retrieved from a single image. This method would be highly beneficial for low-repetition-rate and high-power few-cycle lasers.

Chapter 4

Development of HHG and transient absorption beamline

In this chapter, we present the HHG and the transient absorption beamline which the author has developed during the doctoral course. Firstly, an overview of the beamline is briefly explained. Secondly, the details of each vacuum chamber in the beamline are described. Finally, the implementation of an attosecond delay stabilization system is presented.

4.1 System overview

The beamline consists of four vacuum chambers: HHG chamber, toroidal chamber, sample chamber, and grating chamber, as shown in Fig. 4.1.

The IR pulses obtained from the BIBO-OPCPA system (1.6 μm, 10 fs, ∼1.5 mJ, 1 kHz) are split into pump and probe arms by a broadband beam splitter (custom fabricated by OptoSigma). We use two kinds of beam splitters: R:T = 10:90 and R:T = 20:80. The choice of the beam splitter depends on the required pump pulse energy in a transient absorption measurement.

The IR beam which is transmitted through the beam splitter goes to the probe arm, where the IR pulses are focused by an AR-coated CaF_2 lens (f = 500 mm, f/33) into an HHG gas cell filled with He or Ne to generate SX HHs. Here, the f-number is calculated from the focal length and the $1/e^2$ beam diameter of the IR beam at the lens. The CaF_2 lens is mounted on a linear translation stage, so its position along the laser propagation axis can be adjusted. A two-stage differential pumping system after the gas cell using two dry pumps (500 l/minute) reduces the gas pressure in the subsequent vacuum chambers in the beamline. The SX pulses are transmitted through an Al (150 nm) and FS (1 mm) double filter to remove the fundamental IR component and focused into a sample gas cell by a gold-coated toroidal mirror ($4f$ = 2 m, fabricated by Kiyohara Optics). The SX pulses are then sent to an X-ray spectrometer consisting of a slit (50 or 200 μmwide), an Al filter (150 nm, Lebow Company), a flat-field grating (2400 l/mm, Shimadzu 30-003), and a Peltier-cooled X-ray CCD camera (ANDOR Newton DO940P-BN-FH).

The IR beam which is reflected by the beam splitter goes to the pump arm. In the pump arm, the IR pulses are transmitted through an AR-coated 3-mm-thick FS plate and an AR-coated 3-mm-thick CaF_2 plate for dispersion compensation, and then transmitted

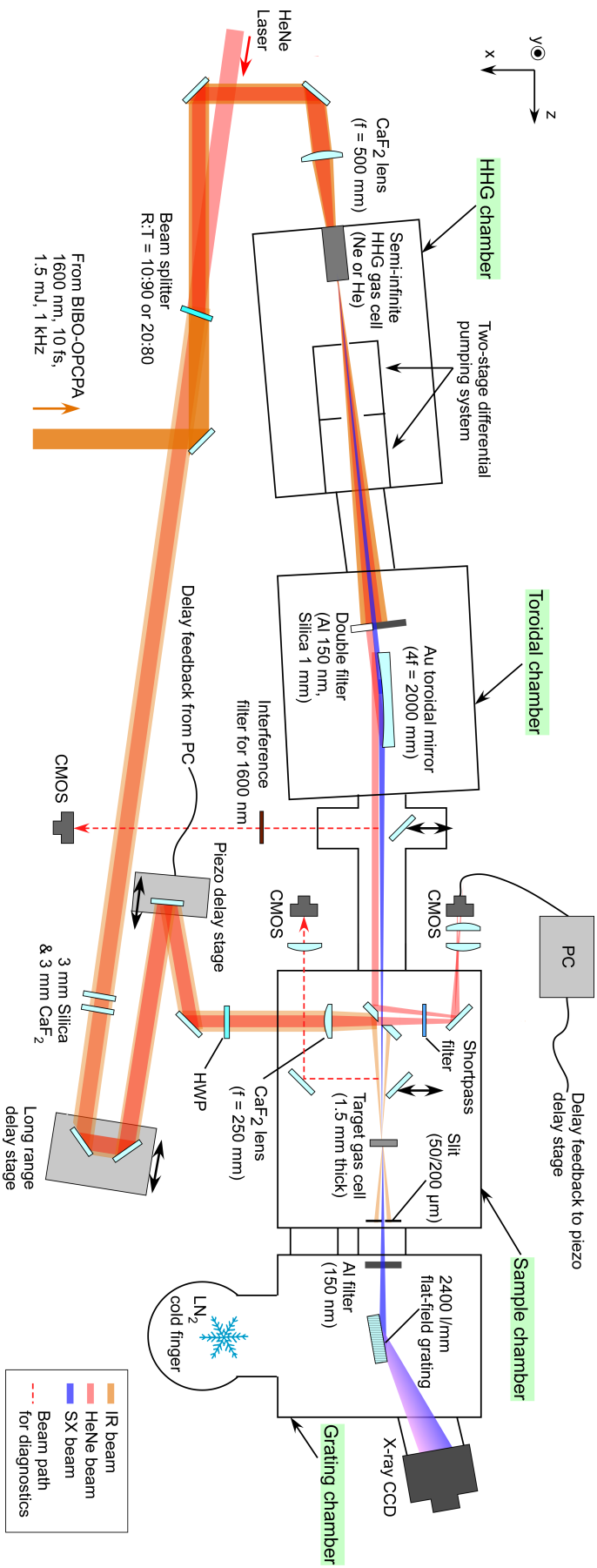

Figure 4.1: Schematic of the HHG and the transient absorption beamline viewed from the top (from the Y direction).

through an HWP (Thorlabs AHWP10M-1600) for polarization control. Then, the pump IR pulses are transmitted through an uncoated CaF_2 lens (f = 250 mm, f/17). Again, the f-number is calculated from the focal length and the $1/e^2$ beam diameter of the pump IR beam at the lens. The pump IR pulses are recombined with the probe SX pulses by a gold-coated flat mirror with a rectangular hole at the center (custom fabricated by Optosigma). The $1/e^2$ beam diameter of the pump IR beam at this mirror is 15 mm. The pump IR pulses and the probe SX pulses are collinearly focused into the sample gas cell.

The delay between the probe SX and the pump IR pulses is scanned either by a piezo stage (Physik Instrumente P-621.1CD and E-665.CR) or a long range delay stage (Sigmatech FS-1020PX) in the pump arm. The piezo stage is employed when a high delay stability is required or when the delay scan range is short. By a feedback system using a HeNe laser which is propagated in the pump and the probe arms, the piezo stage can reach a delay stability of a few tens of attoseconds. On the other hand, the long range delay stage is not compatible with the feedback system, but its scan range is over 100 ps.

4.2 Details of beamline components

4.2.1 HHG chamber

Figure 4.2(a) presents a schematic of the HHG chamber. The HHG chamber consists of two parts: the HHG gas cell and the differential pumping system.

First, the IR beam is focused into the HHG gas cell by a CaF_2 lens (f = 500 mm, f/33) to generate HHs. The pulse energy of the IR beam at the HHG gas cell is typically 1.1-1.2 mJ without using the beam splitter, 1.0-1.1 mJ with the 10:90 beam splitter, and 0.9-1.0 mJ with the 20:80 beam splitter. Note that these values are lower than those calculated from the original output pulse energy of the BIBO-OPCPA system (1.5 mJ), but this is due to the loss of the metallic mirrors for beam handling. Figure 4.3 shows the beam profile of the focused IR beam measured with a CMOS camera using two-photon absorption. In the beam profile measurement, the IR beam is significantly weakened by neutral density filters before focusing and also the 1500-nm-component of the IR beam is selected by an interference filter. The focused beam profile is almost Gaussian with a $1/e^2$ diameter of 61 μm. Considering the two-photon absorption process, the true beam diameter is estimated to be $\sqrt{2} \times 61 = 86$ μm.

Our HHG gas cell (deep blue region in Fig. 4.2(a)) is so-called a "semi-infinite" cell [63, 141–143], which was developed by Prof. Zenghu Chang's group. The semi-infinite gas cell is much longer (22 cm) than the confocal parameter of the IR beam (shorter than 1 cm). The IR beam enters the gas cell through the entrance window and is focused around the exit pinhole (∅250 μm, 1 mm thick) to generate HHs. The semi-infinite gas cell design has several practical advantages over a conventional finite gas cell because a semi-infinite gas cell has only one exit pinhole while a finite gas cell has two entrance and exit pinholes. First, it is easy to align the laser beam to pass through the gas cell. Second, the amount of the gas flow from the cell is reduced by half, thus the gas load for the vacuum pumps is relaxed.

In our gas cell design, the position of the exit pinhole can be adjusted by an XY motorized stage using picomotors (for the definition of X, Y, and Z, see the upper part of Fig. 4.2(a)). For this purpose, the front part and the rear part of the cell is connected

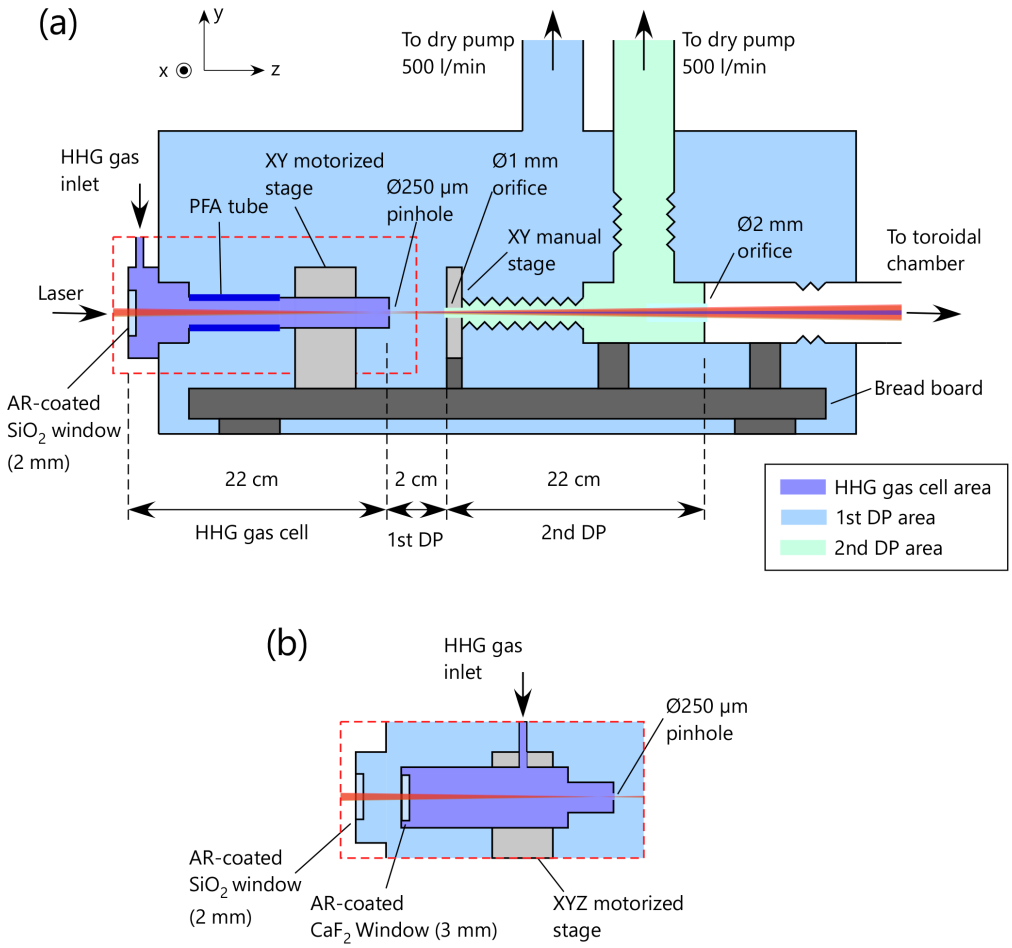

Figure 4.2: Schematic of the HHG chamber viewed from the side (from the X direction). (a) Overview of the system. Wavy lines represent vacuum bellows. Each differential pumping area is distinguished by its filling color. (b) Design of the improved HHG gas cell.

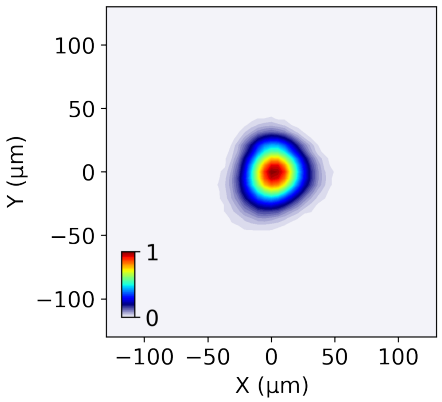

Figure 4.3: Spatial profile of the focused IR beam measured with a CMOS camera using two-photon absorption.

by a flexible perfluoroalkoxy alkane (PFA) tube. Later, an improved version of the semi-infinite gas cell (Fig. 4.2(b)) has also been installed. In the original version of the cell, the entrance window is attached to the wall of the HHG chamber. However, in the new version (Fig. 4.2(b)), the entrance window is isolated from the HHG chamber, so the gas cell can be moved along the Z axis as well as the X and Y axes. This enables us to optimize the position of the focus of the SX beam around the sample gas cell of transient absorption. The new gas cell gives almost the same HHG photon flux as the original cell.

After passing through the gas cell, the SX beam goes to the two-stage differential pumping system which was mainly designed by Mr. Hiroki Sannohe. This differential pumping stage is necessary because the pressure inside the HHG gas cell is significantly high in the case of IR-driven HHG according to the scaling law. In order to operate turbomolecular pumps (TMPs) in the toroidal, sample, and grating chambers, it is required to pump out the large gas flow from the HHG gas cell using roughing pumps.

The first stage of the differential pumping system is the HHG chamber itself, which is pumped by a dry pump (500 l/min). The second stage is made of NW16 bellows and NW25 pipes, and is also pumped by a dry pump (500 l/min). The entrance and the exit of the second stage are ∅1-mm and ∅2-mm orifices, respectively. The entrance orifice is mounted on an XY manual stage, so its position can be finely adjusted to the beam.

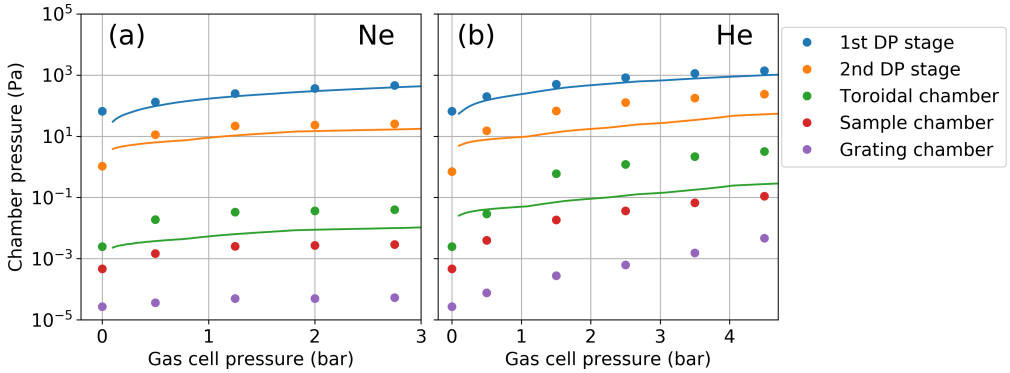

Figure 4.4: Pressure in each chamber as a function of the pressure in the HHG gas cell in the case of (a) Ne and (b) He. Circles are the measured data, and solid curves are the calculations.

The performance of the differential pumping system is evaluated by measuring the vacuum pressure in each chamber in the beamline as a function of the pressure inside the HHG gas cell. Figure 4.4 shows the result. The circles are the measured data and the solid curves are calculations based on the conductance of the orifices and the pumping speed of the dry pumps. For both Ne and He, the pressures in the toroidal chamber, the sample chamber, and the grating chamber do not exceed 10 Pa, thus the TMPs in these chambers can be safely operated. Note that in actual HHG experiments, the HHG gas cell pressure is typically set below 2 bar and 4 bar for Ne and He, respectively. It is not clear why the calculated pressures are deviated from the measured values, but it might be due to the errors in the estimation of the calculation parameters (e.g., the conductances of the orifices in the differential pumping system).

The reabsorption of the SX beam after the gas cell is also estimated from the measured pressures and the literature values of the SX absorption cross section of Ne and He [144]

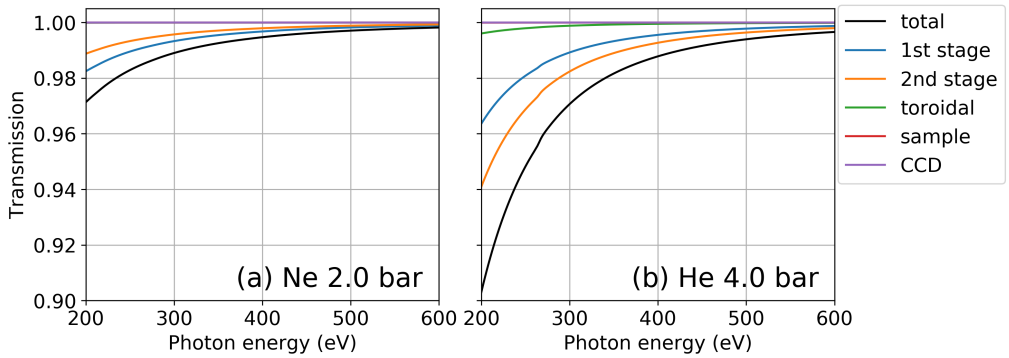

Figure 4.5: Calculated transmission spectra of the residual gas in the beamline in the case of (a) Ne, 2.0 bar and (b) He, 4.0 bar. The black curves and the colored curves represent the transmission through the overall beamline and each component, respectively.

(Fig. 4.5). The reabsorption by the residual gas in the beamline is smaller than 10% for both Ne (2.0 bar) and He (4.0 bar) above 200 eV.

4.2.2 Toroidal chamber

The generated HHs are sent to the toroidal chamber, where the fundamental IR beam is blocked by X-ray filters and the HHs are focused by a toroidal mirror. Figure 4.6(a) shows a schematic of the toroidal chamber.

The HH beam from the HHG chamber is first transmitted through two filter wheels. The filter wheels are aluminium disks on which several metal filters can be mounted. The wheels can be rotated by picomotors to switch the filters. One wheel contains an Al and FS double filter (Fig. 4.6(b)), and the other wheel contains a Ti filter (Lebow Company) and a C filter (Lebow Company). The transmission spectra of these filters are plotted in Fig. 4.7. Note that the actual transmission is reduced to 86% of the plotted values because of Ni wire meshes which support the filter surfaces.

The double filter consists of an Al thin film (t = 150 nm) and an FS plate (t = 1 mm), as shown in Fig. 4.6(b). This filter is made from a commercial Al filter (Lebow Company) by peeling a half of the Al surface by a scotch tape and attaching an FS plate using Torr Seal and adhesive carbon tapes. In attosecond time-resolved transient absorption measurements, the double filter is used to separate the SX beam from the fundamental IR beam. The central part of the IR+SX beam hits the Al filter part, where only the SX component is transmitted. A part of the outer IR beam and the co-propagating HeNe beam are transmitted through the FS plate. The HeNe beam is sent to the sample chamber and used for active stabilization of the pump-probe delay. The role of the FS plate is to shift the timing between the transmitted IR beam and the SX beam so that the transmitted IR beam does not interfere with the pump IR beam at the sample gas cell of transient absorption.

The Ti (t = 150 nm) and C (t = 300 nm) filters are optionally inserted for calibration of the spectrometer because they have sharp absorption edges at 284 and 460 eV. Moreover, in femtosecond or picosecond transient absorption measurements, the Ti filter is sometimes used to separate the SX and the IR beam instead of the Al double filter. This is because

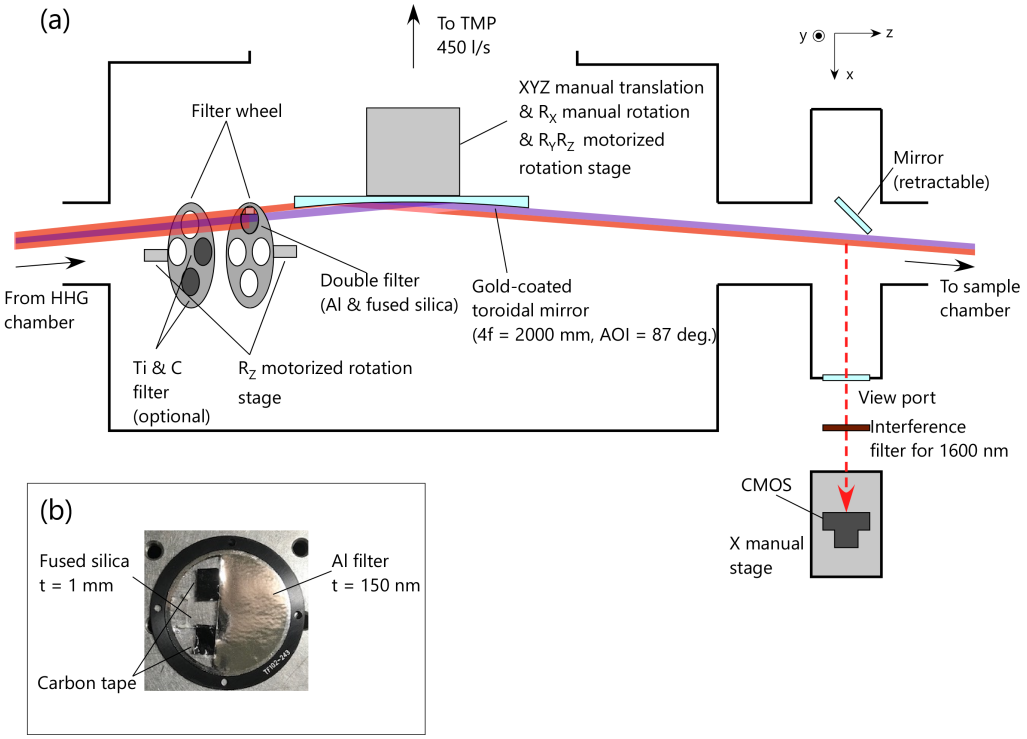

Figure 4.6: (a) Schematic of the toroidal chamber viewed from the top (from the Y direction). (b) Photo of the Al and FS double filter.

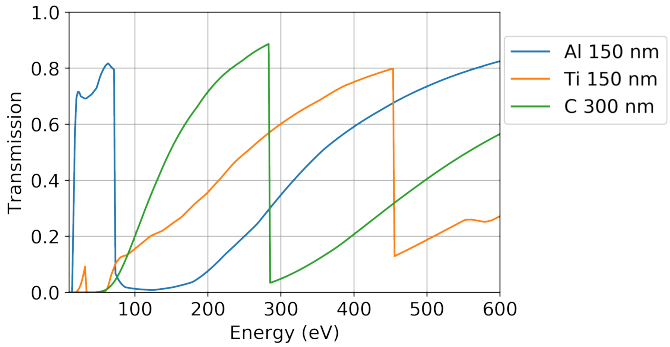

Figure 4.7: Transmission spectra of various X-ray filters [144].

femtosecond or picosecond measurements do not require the active delay stabilization system, and also because Ti has slightly higher transmission than Al below 460 eV.

After the filter wheels, the SX beam is reflected by a gold-coated toroidal mirror (Kiyohara Optics, $4f = 2000$ mm, angle of incidence = 87 deg.). The distance between the HHG source and the toroidal mirror and that between the toroidal mirror and the sample gas cell are both set to 1 m. The width and the height of the toroidal mirror are 180 mm and 15 mm, respectively (corresponding to 10×15 mm beam size). As shown in the next section, the beam divergence of the HH beam is below 5 mrad (corresponding to $\varnothing 5$ mm beam diameter at the toroidal mirror), so the size of the toroidal mirror is large enough to reflect the HH beam. The toroidal mirror is mounted on a translational and rotational stage. The XYZ translational position, and the rotation around the X-axis (R_X) can be manually adjusted. The rotation around the Y and Z-axis (R_Y and R_Z) can be adjusted by picomotors. Here, the definition of the X, Y, and Z axes is shown in the upper part of Fig. 4.6(a).

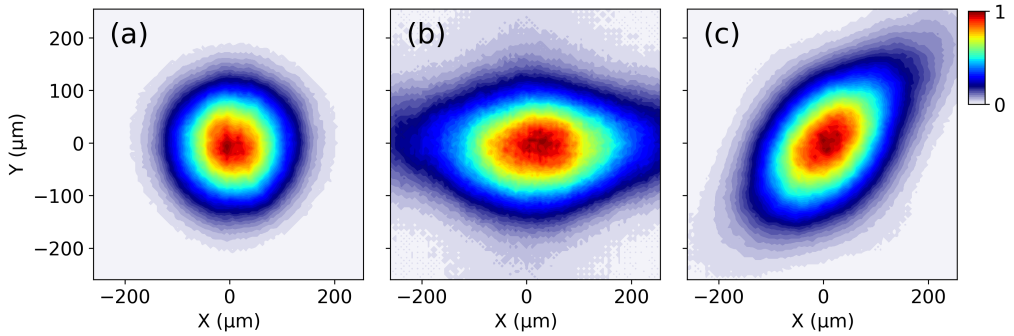

Figure 4.8: IR beam profiles measured by the CMOS camera when the toroidal mirror is (a) perfectly aligned, (b) misaligned in the R_Y direction, and (c) misaligned in the R_Z direction.

For alignment of the toroidal mirror, the X-ray filters are removed from the beam path, and a retractable flat mirror is inserted to send the IR beam to a CMOS camera (Thorlabs DCC1545M) outside the chamber. The CMOS camera is mounted on a manual translation stage so that the beam profile in front of and behind the focal position can be tracked. The alignment is performed by adjusting the R_Y and R_Z rotations of the toroidal mirror to obtain a round beam profile around the focus. Figure 4.8 shows typical beam profiles measured by the CMOS camera. When the alignment of the toroidal mirror is perfect, the beam profile becomes almost round. However, when the alignment is not perfect, the profile is elongated in a certain direction due to astigmatism.

4.2.3 Sample chamber and X-ray spectrometer

After the toroidal chamber, the SX beam goes to the sample chamber, where the SX beam interacts with the target sample of transient absorption. The SX beam is then sent to the grating chamber and an X-ray CCD camera to observe its spectrum. A schematic of the sample chamber and the grating chamber is depicted in Fig. 4.9(a).

The probe SX beam and the pump IR beam are recombined by a gold-coated hole-drilled mirror (Fig. 4.9(b)), where the probe SX beam passes through the rectangular

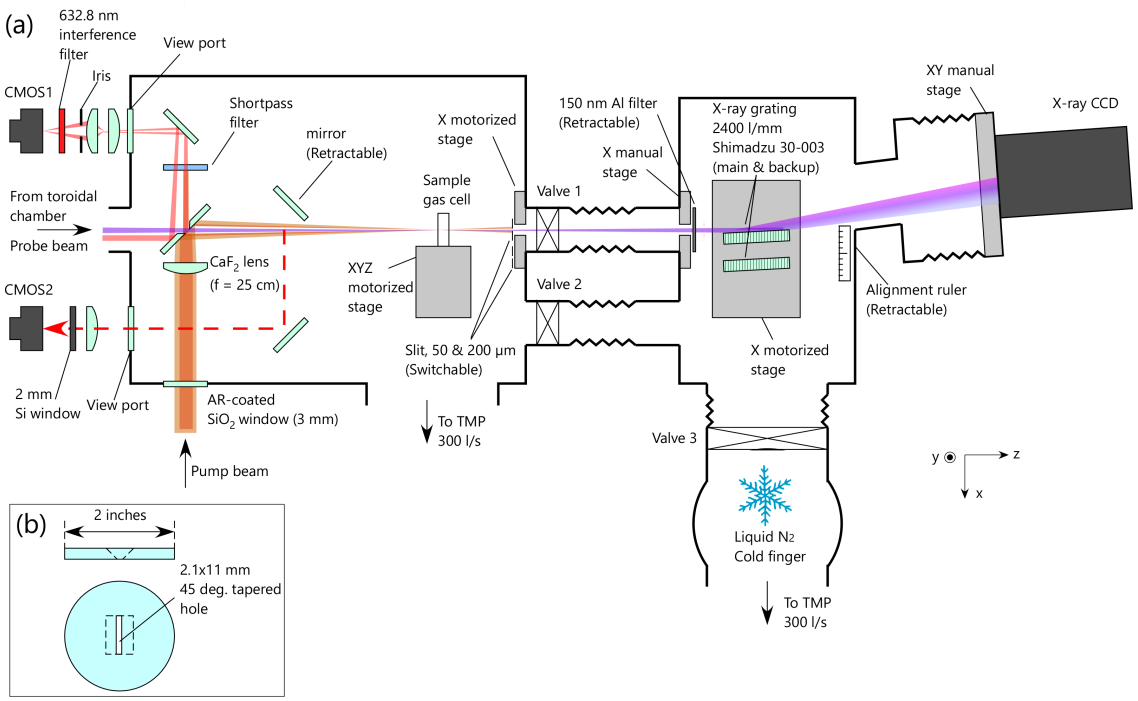

Figure 4.9: (a) Schematic of the sample chamber and the grating chamber viewed from the top (from the Y direction). (b) Schematic of the hole-drilled mirror.

hole and the pump IR beam is reflected. The hole is tapered at 45 degrees so that the central part of the pump IR and the HeNe beams can pass through the hole for the active delay stabilization. This passed pump IR and HeNe beams are recombined with the IR and HeNe beams from the probe arm which are reflected by the surface of the mirror. These two beams are filtered by a short-pass filter (Thorlabs FGS900) to remove the IR component and focused into a CMOS camera (CMOS1 in Fig. 4.9(a), Thorlabs DCC1545M) to observe interference fringes by the two HeNe beams (more details are given in Section 4.3).

The probe SX beam and the reflected pump IR beam are focused into the sample gas cell filled with the target gas of transient absorption. The typical pulse energy of the reflected pump IR beam is 70 µJ when using the 10:90 beam splitter, and 140 µJ when using the 20:80 beam splitter. Figure 4.10 shows the beam profile of the focused pump IR beam measured by a CMOS camera using two-photon absorption. The profile is almost round, but there is a small side peak. This side peak appears because the central part of the pump IR beam is clipped by the rectangular hole in the hole-drilled mirror. The $1/e^2$ diameter of the beam profile in Fig. 4.10 is 38 µm. This corresponds to the actual diameter of 54 µm considering the two-photon absorption process. Note that the IR beam is significantly attenuated before focused into the camera by using neutral density filters.

A photo of the sample gas cell is shown in Fig. 4.11(a). The sample cell can hold solid samples as well as gas samples, but we only use gas samples in this study. Its cross-sectional view is shown in Fig. 4.11(b). The sample gas is provided from a stainless tube which is attached to the body of the cell by Torr Seal. The SX and the IR beams pass through mechanically drilled two pinholes in the gas cell. The diameter of the pinholes

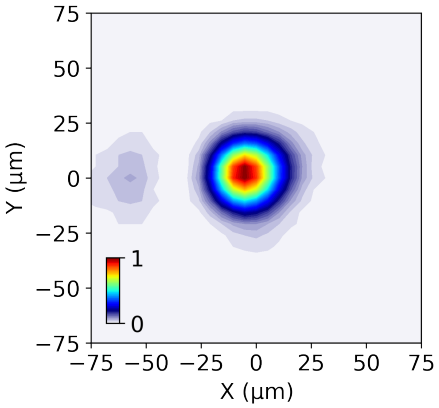

Figure 4.10: Spatial profile of the focused pump IR beam measured with a CMOS camera using two-photon absorption. Note that the pixel size of the CMOS camera is 5.2 µm, and the image is smoothly interpolated.

is set to 100 µm. This is sufficiently large to pass both the pump IR (∅54 µm) and the probe SX (∅78 µm) beams. Note that if the diameter of the pinholes is too large (e.g., > 200 µm), it becomes difficult to ensure the spatial overlap between the pump and the probe beams because the spatial overlap is confirmed by the fact that both beams pass through the pinholes. The thickness of the gas cell (1.5 mm) is chosen so that it matches the confocal parameter of the pump IR beam (1.2 mm).

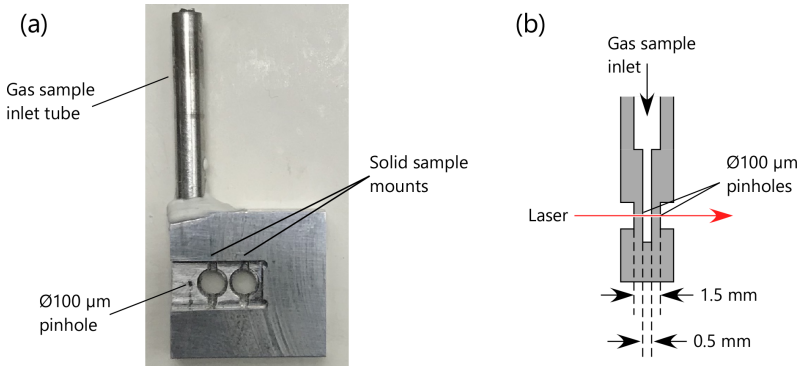

Figure 4.11: (a) Photo of the front view of the sample gas cell. (b) Cross-sectional view of the sample gas cell.

The gas cell is mounted on a motorized X, Y, and Z translational stage. Here, the definition of the X, Y, and Z axes is shown in the lower part of Fig. 4.9(a). The Y and Z directions are adjusted by picomotors, while the X direction is adjusted by a NewStep actuator (Newport). The alignment procedure of the gas cell is as follows. Firstly, the tilt angle of the gas cell is adjusted so that the entrance and the exit pinholes are aligned parallel to the IR beam from the probe arm. This procedure is conducted manually at the atmospheric pressure. Secondly, the beamline is evacuated and filled with ∼100 Pa of Kr gas. Then, the gas cell is retracted from the beam path and its Z position is adjusted to match the Z position of the plasma filament formed by the pump IR beam. Thirdly, the Kr gas is evacuated and the SX HHs are generated. The gas cell is inserted to the beam path,

and the X and Y position of the gas cell is adjusted to maximize the throughput of the SX beam. Finally, the position of the pump IR beam is adjusted so that it passes through the pinholes of the gas cell.

The temporal overlap between the pump and the probe pulses is detected by observing a cross-correlation signal between the two IR pulses from the pump and the probe arms. For that, a retractable flat mirror in the sample chamber is inserted to the beam path to send the two IR beams to a CMOS camera (CMOS2 in Fig. 4.9(a), Thorlabs DCC1545M), where an interference pattern is observed. Here, the X-ray filters in the probe beam path are removed. From the delay dependence of the intensity of a part of the interference pattern, a cross-correlation signal is obtained. Figure 4.12 plots the measured cross-correlation signal. The peak position of the cross-correlation signal indicates the coarse delay origin.

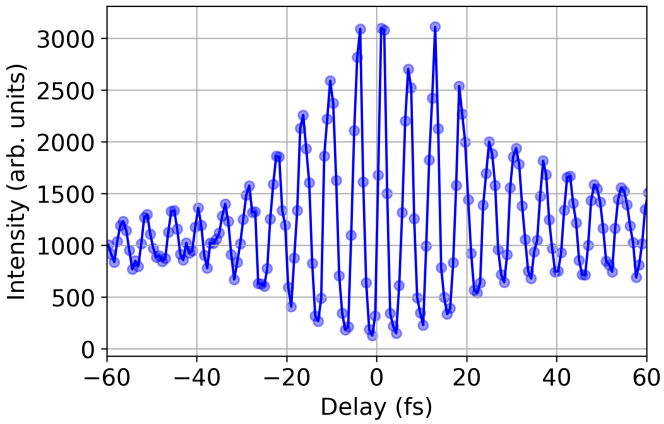

Figure 4.12: Measured cross-correlation signal between the two IR pulses from the pump and the probe arms.

After passing through the sample gas cell, the SX beam passes through a slit. In this slit, most of the pump IR beam is blocked because its beam divergence is much larger than that of the SX beam. Two slits with different widths (50 and 200 µm) can be switched by a motorized translational stage attached to the wall of the chamber. In transient absorption measurements, where the energy resolution of the spectrometer is required to be high, the 50-µm slit is employed. The 200-µm slit is used when the entire SX beam needs to be measured.

The SX beam is then filtered by an Al filter (t = 150 nm, Lebow Company) to remove the residual IR and VIS stray light. This Al filter is mounted on a retractable translation stage attached on the wall of the grating chamber.

After the Al filter, the SX beam is dispersed by a flat-field X-ray grating (2400 l/mm, Shimadzu 30-003). The designed spectral range of the grating is 177-1240 eV (λ = 1-7 nm). The other parameters of the grating are presented in Appendix A. Aside from the main grating, another grating can be mounted as a backup and can be switched by using a motorized translational stage. To obtain the maximum energy resolution of the spectrometer, it is important to adjust the tilt of the grating precisely. For that, in the grating chamber, a ruler is equipped which can be inserted between the grating and an X-ray CCD camera. By using this ruler, one can observe the reflection angle of the HeNe

beam from the probe arm at the grating. While observing the reflection angle, the grating chamber itself is rotated manually to adjust the reflection angle to the designed value.

Finally, the dispersed SX spectrum is observed by an X-ray CCD camera (ANDOR Newton DO940P-BN-FH). The CCD camera has a 27.6×6.9-mm image area with a pixel size of 13.5 μm (2048×512 pixels). The position of the CCD camera can be manually adjusted by an XY translational stage. The CCD camera is cooled to -40°C to suppress thermal noises.

When the CCD camera is cooled, there is a risk that carbon-containing contamination molecules in the chamber get adsorbed to the surface of the CCD camera, resulting in the deterioration of the SX detection efficiency above the C K-edge. To prevent this, a liquid nitrogen cold finger is installed next to the grating chamber. Whenever the CCD camera is cooled, the cold finger is also cooled with liquid nitrogen to catch the contamination molecules. The cold finger can keep the liquid nitrogen temperature for more than twelve hours, which is sufficient for transient absorption measurements.

There are three valves connecting the sample chamber, the grating chamber, and the cold finger (valve 1, 2, and 3 in Fig. 4.9(a)). When an SX measurement is performed, the valves 1 and 3 are opened and the valve 2 is closed. When the measurement is finished, the valves 1 and 2 are opened and the valve 3 is closed to isolate the grating chamber from the cold finger. This is because when the cold finger gets back to room temperature, it emits the adsorbed contamination molecules to the chamber. When the temperature of the cold finger is fully back to room temperature, the valve 3 is opened and the valve 2 is closed. When the sample chamber or the toroidal chamber needs to be vented for alignment, the valve 3 is opened and the valves 1 and 2 are closed. By doing so, the grating chamber can be kept in high vacuum, which is important to avoid the contamination of the gratings and the CCD camera.

4.2.4 Vibration isolation

Because the vibration from the vacuum pumps is one of the largest sources to deteriorate the stability of the pump-probe delay, several vibration isolation systems are installed in the beamline.

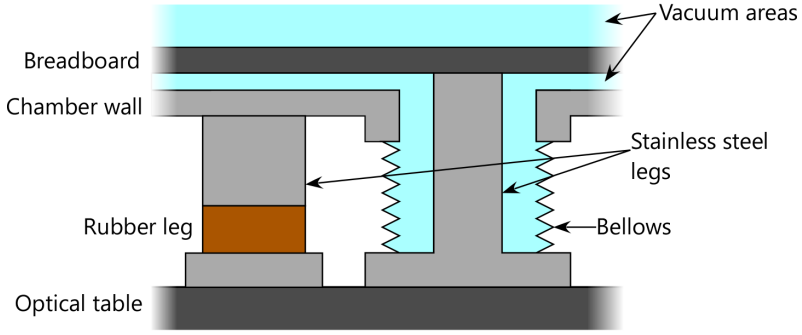

Figure 4.13: Schematic of the mechanism of vibration isolation.

The first one is the vibration isolation of the optical table. In our beamline, the vacuum chambers are mounted on the same optical table as the pump-probe optics, so the isolation between the chambers and the optical table is important. As depicted in the

left side of Fig. 4.13, in order to absorb the vibration from the pumps, rubber legs are inserted between the chambers and the optical table.

The second one is the vibration isolation of the optics inside the vacuum chambers. In the toroidal chamber and the sample chamber, there are some reflective optics for the SX and the IR beams (i.e., the toroidal mirror and the hole-drilled mirror), which are sensitive to vibration. Therefore, these optics are directly mounted on the optical table via solid stainless legs. As depicted in the right side of Fig. 4.13, the stainless legs are connected to the chambers via flexible bellows so that the vibration of the chambers is not transmitted to the optical table. This vibration isolation has another benefit. As our chambers are rectangular, they tend to be slightly distorted when evacuated. By isolating the optics from the chambers, the optics are not affected by this distortion.

4.3 Attosecond stabilization of pump-probe delay

In attosecond time-resolved spectroscopy, it is important that the delay jitter and the drift are sufficiently small compared to the time scale of the observed physical phenomena. For example, in attosecond time-resolved transient absorption measurements, oscillations of absorbance at a period of $\tau/2$ (τ: one cycle of the pump laser electric field) are typically observed [20, 21, 86, 98]. In our case, $\tau/2$ is approximately 2.7 fs. Therefore, if we can stabilize the delay within several hundreds of attoseconds, it is sufficient to observe this type of oscillations. In the following, the details of the active feedback system in our beamline are described.

4.3.1 Delay fluctuation measurement without active stabilization

Before constructing the feedback system, the free-running delay fluctuation is measured to understand the characteristics of the pump-probe delay line.

First, the fast delay jitter (2-2500 Hz) is measured as depicted in Fig. 4.14(a). Two HeNe beams from the pump and the probe arms are noncollinearly focused onto a single-mode fiber and sent to a photodiode. The photodiode signal is recorded by an oscilloscope. The measured signal is shown in Fig. 4.14(b) (deep blue curve). Note that during the measurement, all the vacuum pumps in the beamline are turned on, and the HHG gas cell and the sample gas cell are filled with Ne (1.5 bar) and Ar (50 mbar), respectively. In order to confirm that this signal really reflects the delay jitter, the piezo stage in the pump arm is scanned and the signal is measured again (Fig. 4.14(b), light blue curve). It clearly shows that the delay is directly mapped to the photodiode signal.

In order to investigate the effect of the vibration of the TMPs and the dry pumps, we compare the delay jitters when these pumps are turned on and off. The red and the blue curves in Fig. 4.15(a) are the results. There is no significant change between the two curves, indicating that the vibration of the pumps does not affect the delay stability so much. This is probably because of the vibration isolation systems described in the previous section. The power spectra of the delay jitters (Fig. 4.15(b)) also show that the effect of the pumps is small. The measurements were performed several times, and the root mean square delay jitter is calculated to be 49 ± 2 as when the pumps are on, and 50 ± 5 as when the pumps are off. These values are sufficiently smaller than the required

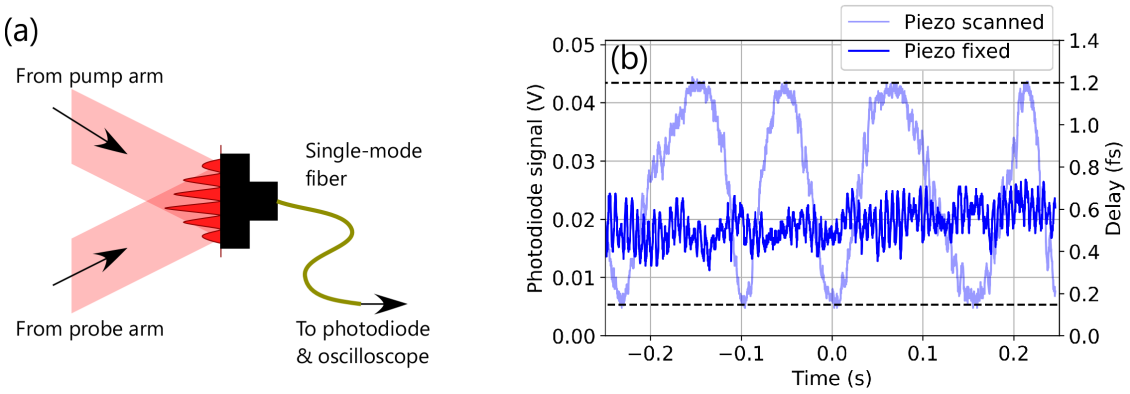

Figure 4.14: Measurement of the fast delay jitter. (a) Schematic of the setup. (b) Measured delay jitter (deep blue curve). Delay jitter when the piezo stage is scanned is also shown as a reference (light blue curve).

delay stability, thus we can conclude that the fast delay jitter is not a problem in our case.

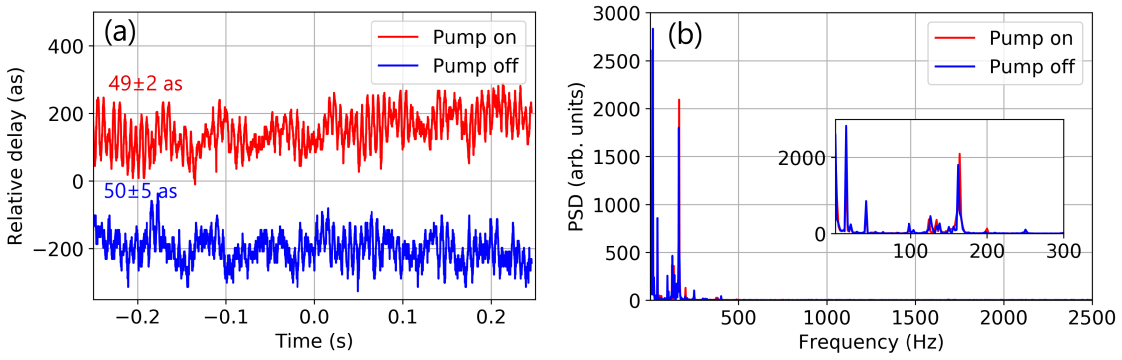

Figure 4.15: (a) Measured fast delay jitters and (b) its power spectra with the vacuum pumps on (red) and off (blue). The inset in (b) shows the magnified power spectra in the low frequency range.

Second, the slow delay drift is measured as depicted in Fig. 4.16(a). Instead of the photodiode and the oscilloscope, a CMOS camera is employed to observe the interference fringes between the two HeNe beams. The signal acquisition rate of the CMOS camera is set to 20 Hz. The contour plot in Fig. 4.16(b) represents the measured interference fringes as a function of time. The delay drift is extracted from the spatial phase of the fringes and plotted as a white curve in Fig. 4.16(b). It shows that the drift is a few femtoseconds over 1500 s. Considering that one transient absorption measurement may take several hours, this drift has to be compensated.

Figure 4.17 plots the power spectrum of the measured slow delay drift (red curve) combined with that of the fast delay jitter (blue curve). It is visible that the major part of the delay fluctuation is concentrated below 10 Hz.

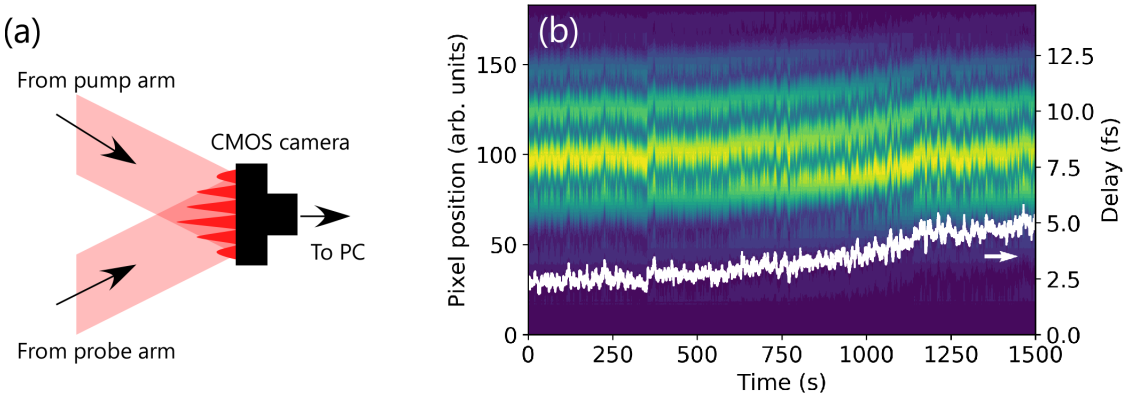

Figure 4.16: Measurement of the slow delay drift. (a) Schematic of the setup. (b) Measured interference fringes as a function of time (contour plot). The delay drift extracted from the fringes is plotted as a white curve.

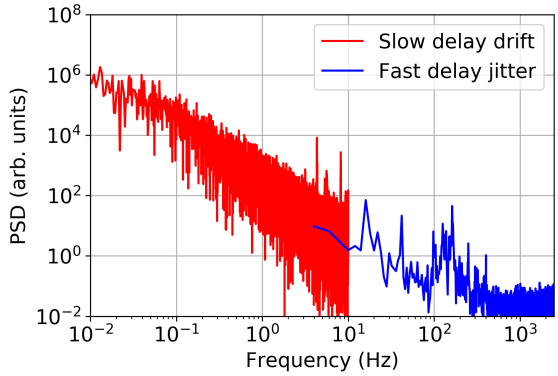

Figure 4.17: Power spectrum of the fast delay jitter (blue) and the slow delay drift (red) measured with a photodiode and a CMOS camera, respectively. The two measurement results are smoothly connected around 10 Hz.

4.3.2 Implementation of delay stabilization system

There are several ways to stablize the delay with a sub-femtosecond precision. Some methods utilize CMOS cameras to detect interference fringes [145, 146], while other ones utilize photodiodes [143, 147, 148]. The CMOS-camera method is easy to implement, but the feedback bandwidth is limited by the acquisition rate of the camera. In our case, as discussed above, the delay fluctuation is mostly below 10 Hz and a fast feedback is not needed. Therefore, we adopt the CMOS-camera method.

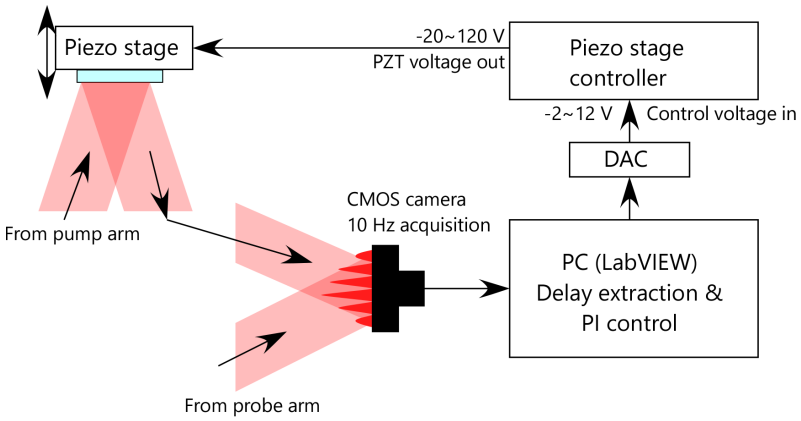

Figure 4.18: Schematic of the delay stabilization system.

A schematic of the setup of the feedback system is depicted in Fig. 4.18. The interference fringes formed by the two HeNe beams from the pump and the probe arms are recorded by a CMOS camera at a 10-Hz acquisition rate. The CMOS image is then sent to a LabVIEW software, where the delay is extracted from the spatial phase of the fringes and a feedback signal is calculated by the PID control toolkit library in LabVIEW. Here, only the proportional (P) and the integral (I) terms are used for the feedback. The feedback signal is converted into an analog voltage by a digital-to-analog converter (National Instruments USB-6002) and sent to the piezo stage controller. The piezo stage controller amplifies the input voltage and sends the amplified voltage to the piezo stage to change the delay.

Typical CMOS images of the HeNe beams during the delay stabilization are shown in Fig. 4.19. As shown in Fig. 4.19(a, b), the beam profiles of the two HeNe beams are very noisy due to unwanted interferences caused by multiple reflections in the transmissive optics in the beamline. However, by properly selecting a region where the two HeNe beams overlap (Fig. 4.19(c)), a clear interference pattern which is sensitive to the pump-probe delay is observed as in Fig. 4.19(d). This interference pattern is used for generating the feedback signal.

Figure 4.20(a) shows the delay fluctuation measured by the CMOS camera with (red curve) and without (blue curve) the delay stabilization. The delay drift is 493 as over 18 minutes without the delay stabilization, but it is reduced to 33 as when the delay stabilization is turned on. Note that these values do not include the fast delay jitter. However, even if the fast delay jitter is taken into account, the total delay stability is expected to be below 100 as, which is sufficient for attosecond time-resolved transient absorption measurements. The power spectra of the delay fluctuations are plotted in Fig.

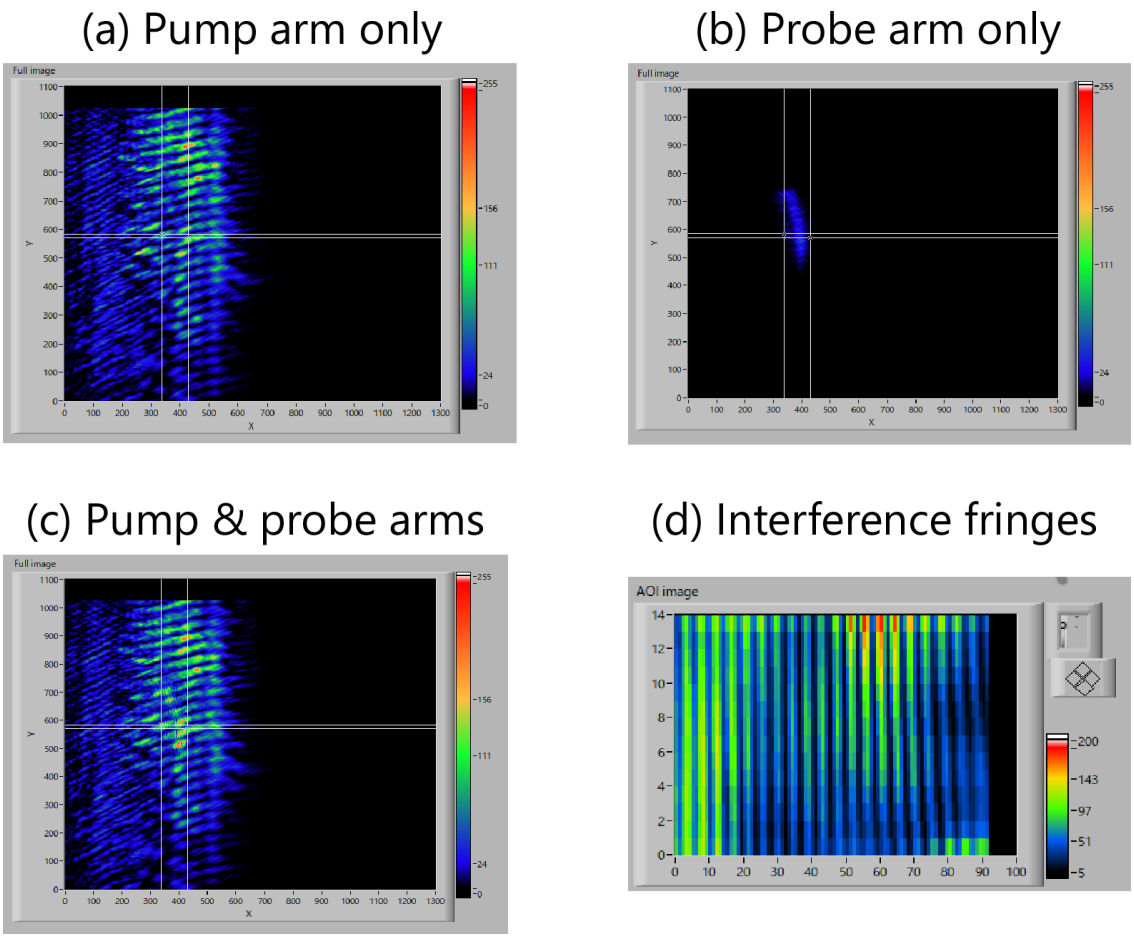

Figure 4.19: Measured CMOS images of the HeNe beams during the delay stabilization. The vertical and horizontal axes represent the pixels of the CMOS camera. Beam profile of the HeNe beam from (a) the pump arm only, (b) the probe arm only, and (c) both pump and probe arms. The rectangular area surrounded by white lines (340-430 pixels in the horizontal direction, and 570-585 pixels in the vertical direction) in (c) is magnified and shown in (d), which contains clear interference fringes.

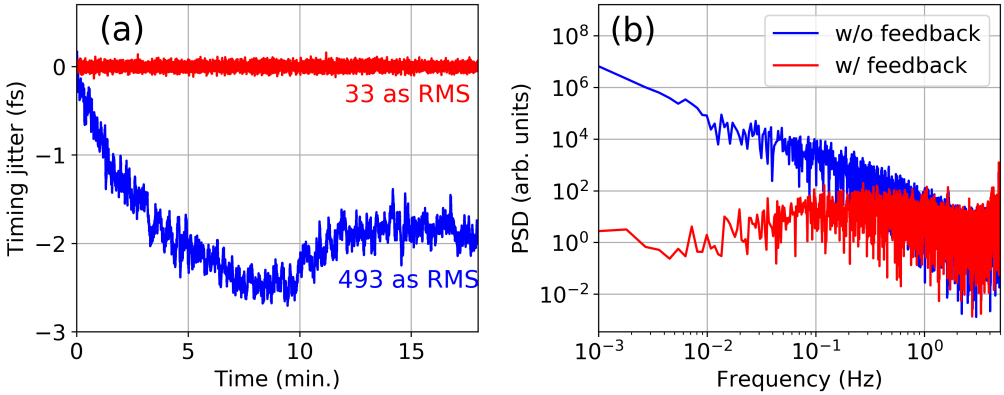

Figure 4.20: (a) Measured delay drifts and (b) their power spectra with (red curve) and without (blue curve) the active delay stabilization.

4.20(b). It is shown that the feedback system successfully suppresses the low frequency noise.

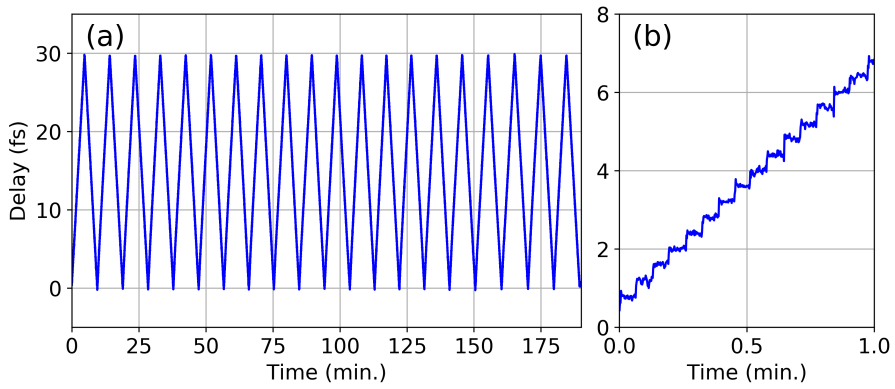

Figure 4.21: (a) Scanned delay for three hours. The delay values are extracted from the spatial phase of the interference fringes of the HeNe beams. (b) The first one minute of (a).

By using the delay feedback system, it is also possible to scan the delay by changing the set point of the PI control. Figure 4.21 shows the scanned delay measured by the CMOS camera for three hours. Here, the delay is swept from 0 to 30 fs with a step of 0.4 fs every 4 seconds.

Chapter 5

Measured characteristics of water window HHs

In this chapter, the measured properties of the HHs are presented. Note that the measurement results in this chapter are obtained with slightly different experimental conditions from the transient absorption measurements. First, the IR beam splitter in the beamline (Fig. 4.1) is removed to use all the pulse energy of the IR beam for HHG because we do not use pump IR pulses in this chapter. Second, the slit width of the X-ray spectrometer is set to 200 µm instead of 50 µm to maximize the throughput of the X-ray spectrometer at the expense of energy resolution. In Section 5.5, however, we set the slit width to 50 µm to measure high-resolution XAS spectra.

5.1 Pressure dependence

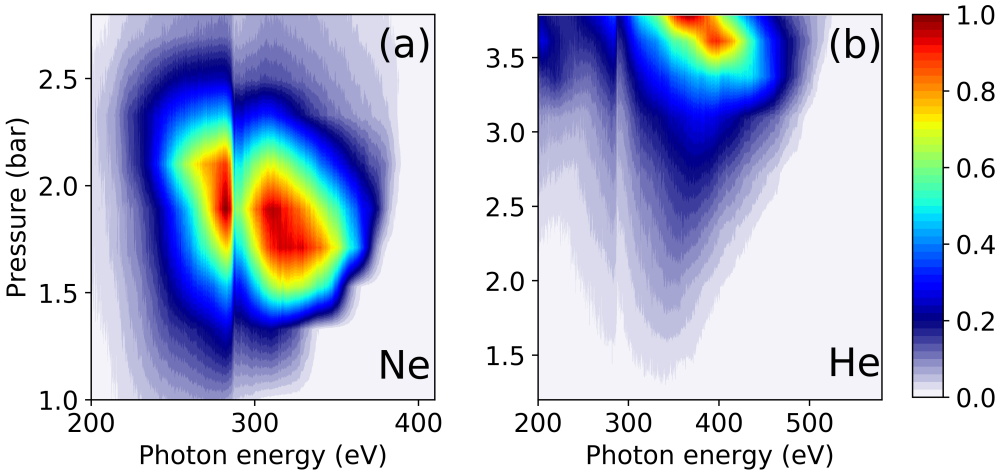

Figure 5.1: Gas pressure dependence of HH spectra from (a) Ne and (b) He. The CEP of the drive laser is randomized in this measurement.

Figure 5.1 shows the measured gas pressure dependence of HHs generated from Ne and He. The dip structure around 284 eV (C K-edge) is due to the carbon-containing contamination in the SX optics. The exposure time of the CCD camera for one pressure

point is set to 10 s (Ne) and 5 s (He). In Fig. 5.1, it is visible that the HH photon fluxes from Ne and He are maximal around 1.5-2.0 bar and 3.4-3.7 bar, respectively. If the phase-matching condition is fulfilled in all pressure regions, the photon flux scales with the square of the gas pressure [149]. The observed gas pressure dependence of HHs is strongly deviated from this scaling, suggesting that the phase-matching condition is fulfilled in the limited pressure regions and it is not fulfilled in the other regions.

Figure 5.2 compares the optimum gas pressure in HHG from He in our experiment (3.6 bar) with those in previous studies [43, 49, 50, 52, 60, 77]. It can be seen that the optimum pressures in our experiment and in the previous studies roughly fit the λ^2 scaling law.

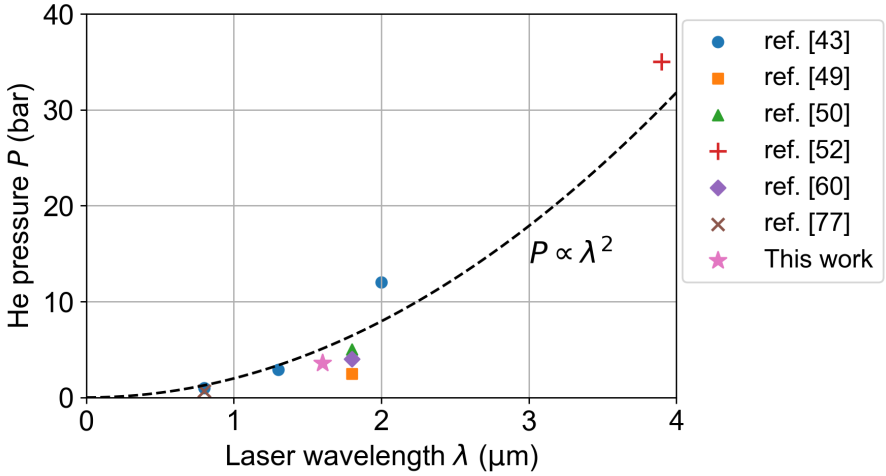

Figure 5.2: Comparison of the optimum gas pressure in HHG from He in our experiment with those in previous studies [43, 49, 50, 52, 60, 77]. Black dashed curve is a guide for the eye, showing the quadratic scaling law.

During the measurement of the gas pressure dependence of HHs, the CEP of the drive laser is increased by 0.1π every laser shot by using the Dazzler. Considering the repetition rate of the laser (1 kHz) and the exposure time of the CCD camera (> 1 s), this CEP sweep can be regarded as the "randomization" of the CEP. The CEP randomization is useful to remove the pressure-dependent HCO structures [150] and to clarify the optimum gas pressures.

Finally, note that the pressure limit in Fig. 5.1(b) (3.7 bar) is due to the fact that the pumping speed of the dry pumps in the differential pumping system at the time of the measurement was smaller (250 l/min.) than that of the current system (500 l/min.). In the current system, we can increase the gas pressure up to ∼4.5 bar.

5.2 HH spectra at optimum pressures and their CEP dependence

Figure 5.3(a) plots the HH spectra at the optimum pressures (Ne: 1.9 bar, He: 3.6 bar). The CEP of the drive laser is randomized as in Fig. 5.1. The exposure time of the CCD camera is 200 s for Ne and 100 s for He. The vertical axis is the photon flux at the CCD

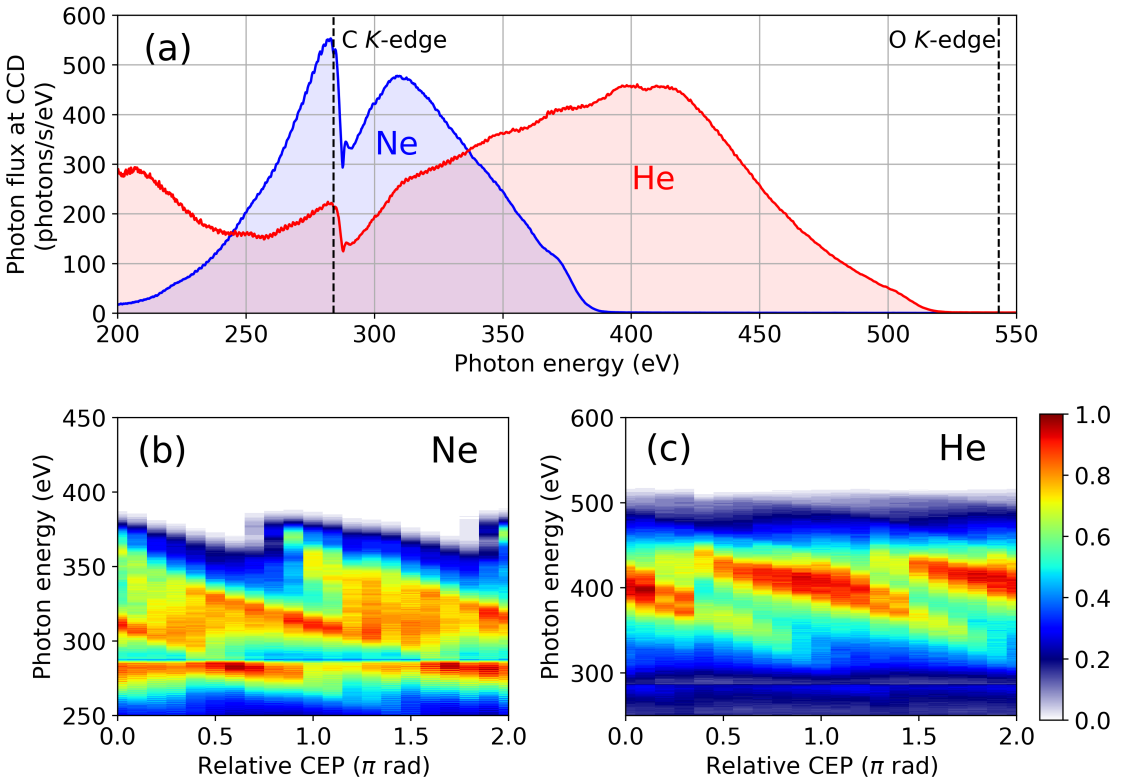

Figure 5.3: HH spectra and their CEP dependence at the optimum gas pressures (Ne: 1.9 bar, He: 3.6 bar). (a) CEP-randomized HH spectra from Ne (blue curve) and He (red curve). CEP-dependent HH spectra from Ne (b) and He (c).

I_{CCD}, which is calculated from the measured CCD count per second in a CCD pixel I_{count}, the quantum efficiency of the CCD camera η, the well depth of the CCD N (the maximum number of electrons which one CCD pixel can accumulate), the ADC resolution of the CCD $2^{n_{\mathrm{ADC}}}$, the number of electrons generated by one X-ray photon in the CCD camera n, the preamp gain of the CCD camera g, and the photon energy interval between adjacent pixels ΔE as $I_{\mathrm{CCD}} = (I_{\mathrm{count}}/\eta) \times (N/2^{n_{\mathrm{ADC}}})/n/g/\Delta E$. Here, $\eta = 0.8$, $N = 100000$, $2^{n_{\mathrm{ADC}}} = 65536$, $n = 0.267\times$(Photon energy (eV)), and $g = 4$. In Fig. 5.3(a), it can be seen that the HHG cutoff energy reaches 520 eV in the case of He, which is significantly lower than the O K-edge.

The CEP dependence of the HH spectra is shown in Fig. 5.3(b) and Fig. 5.3(c) for Ne and He, respectively. Here, the CEP is not randomized, and the CEP is scanned with a step of 0.1π by using the Dazzler. The exposure time of the CCD camera for one CEP is 10 s for Ne and 5 s for He. In Figs. 5.3(b, c), the HCO structures are clearly visible.

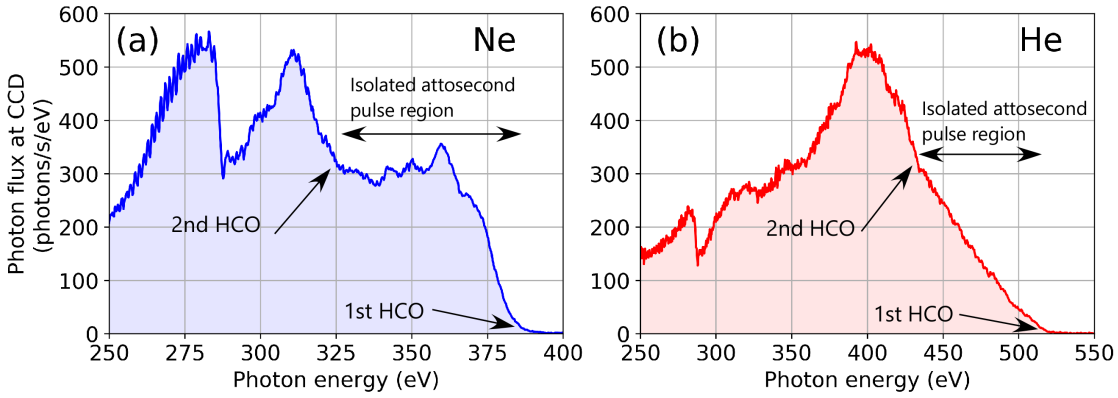

Figure 5.4: HH spectra generated from (a) Ne and (b) He with a fixed CEP (relative CEP of 0 rad in Figs. 5.3(b, c)).

Figure 5.4 plots the HH spectra with a fixed CEP (relative CEP = 0 rad in Fig. 5.3(b, c)). The estimated positions of the HCOs are also shown. Here, note that, to the best of our knowledge, a standard procedure to determine the positions of HCOs is not established. We estimate the positions of the HCOs from the inflection points of the HH spectra. In the energy region between the first and the second HCOs, only one attosecond burst exists, thus an isolated attosecond pulse is expected to be obtained. The energy bandwidth of the isolated attosecond pulse region is estimated to be > 50 eV for both Ne and He. This bandwidth is wide enough to cover an entire XANES structure, thus attosecond transient absorption measurements are possible without using additional gating techniques such as the polarization gating [151].

As for the temporal duration of the isolated attosecond pulse, although we cannot measure the exact value in the current setup, it is estimated to be less than one femtosecond from an SFA calculation (see Section 6.3.2 for details). In the future, the pulse duration should be measured by the attosecond streaking technique [128] by installing a photoelectron spectrometer in the sample chamber.

5.3 Photon flux at HHG source

In the previous section, the photon flux at the surface of the CCD camera I_{CCD} is presented. However, due to the loss in the SX optics in the beamline, this photon flux is much different from that at the HHG source I_{source}. Estimating I_{source} is important for comparing the flux with other experiments, as well as for evaluating the conversion efficiency of the HHG process. I_{source} can be calculated from I_{CCD} as

$$I_{\mathrm{source}} = \frac{I_{\mathrm{CCD}}}{\eta_{\mathrm{grating}} \times \eta_{\mathrm{filter}} \times \eta_{\mathrm{toroidal}} \times \eta_{\mathrm{contamination}}}. \tag{5.1}$$

Here, η_{grating} is the diffraction efficiency of the grating [152], η_{filter} is the transmission of the two Al filters [144], η_{toroidal} is the reflectivity of the toroidal mirror [144], and $\eta_{\mathrm{contamination}}$ is the transmission or reflectivity of the carbon contamination layers on the SX optics. Although the actual source of $\eta_{\mathrm{contamination}}$ is difficult to specify, we assume that it is a thin layer of epoxy ($C_{21}H_{25}ClO_5$). Its thickness is estimated to be 60 nm to match the depth of the dip at the C K-edge in the measured HH spectra. Figure 5.5(a) shows I_{source} (solid curves) and I_{CCD} (dashed curves) for Ne and He. Figure 5.5(b) plots each η employed for the calculation. From the figures, it is evident that I_{source} is 2-3 orders of magnitude higher than I_{CCD} due to the loss of the SX optics.

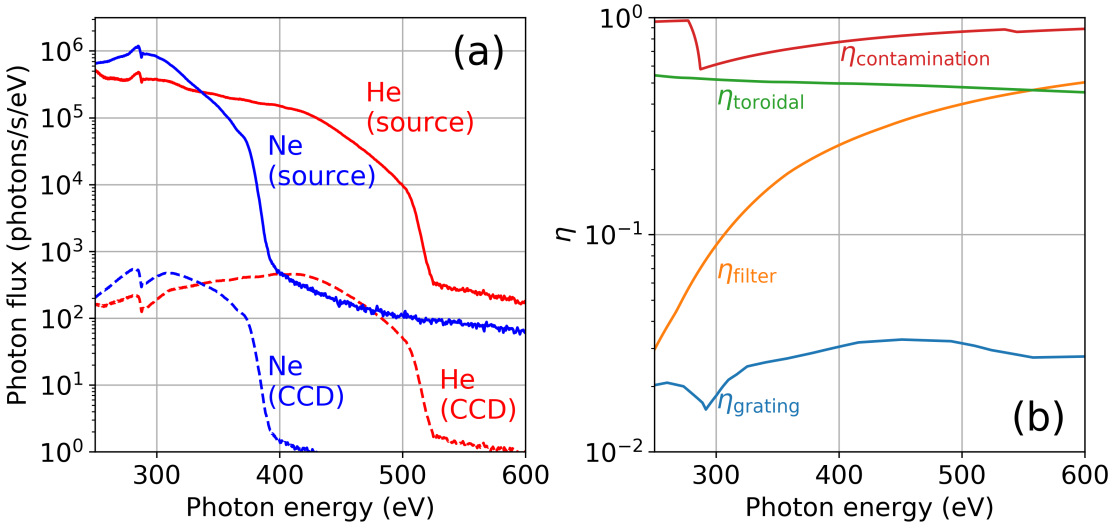

Figure 5.5: Photon flux of the HH beam from (a) Photon flux at the HHG source (solid curve) and the CCD camera (dashed curve) for Ne (blue) and He (red). (b) Efficiency, reflectivity, and transmission curves of the SX optics.

From the obtained I_{source}, the total photon flux of our HHG source in the water window is calculated to be 3.7×10^7 photons/s (1.8 pJ/pulse) for Ne, and 3.6×10^7 photons/s (2.0 pJ/pulse) for He. Considering the fact that the IR pulse energy employed for HHG is 1.1 mJ, the conversion efficiency is estimated to be $\sim2\times10^{-9}$. This number is much lower than the typical conversion efficiency of Ti:Sa-driven HHG ($\sim10^{-6}$) [30, 149], but it is roughly consistent with the $\lambda^{-(8-7.4)}$ scaling of the HHG yield: when the wavelength of the drive laser becomes two times longer, the HHG flux is expected to become $2^{-(8-7.4)} = (4-6)\times10^{-3}$ times lower.

Our photon flux is compared with those obtained in other SX sources in Table 5.1. For both Ne and He, our flux is comparable to the highest HHG flux ever reported [43,46,50]. However, it is interesting to compare the HHG photon flux with XFELs or synchrotron radiation. These accelerator-based SX sources have ∼7-9 orders of magnitude higher photon flux than HHG.

Table 5.1: Comparison of SX photon flux in the water window from various experiments. The data are presented as photons/s/1%bandwidth for 300 eV and 400 eV (the bandwidths for 300 eV and 400 eV are $0.01 \times 300 = 3$ eV and $0.01 \times 400 = 4$ eV, respectively [153]). All the HHG sources except for ref. [43] generate isolated attosecond pulses.

Ref.	SX source	300 eV	400 eV	Entire water window
This work	HHG (Ne)	2.5×10^6	0	3.7×10^7 photons/s (1.8 pJ/pulse)
This work	HHG (He)	1.1×10^6	6.0×10^5	3.6×10^7 photons/s (2.0 pJ/pulse)
[46]	HHG (Ne)	2.8×10^6	-	7.3×10^7photons/s (2.9 pJ/pulse)
[46]	HHG (He)	1.8×10^5	-	0.9 pJ/pulse
[50]	HHG (Ne)	3.0×10^6	5.6×10^4	-
[50]	HHG (He)	1.6×10^5	4.5×10^4	-
[58]	[a]HHG (Ne)	-	-	> 1×10^5 photons/s
[43]	HHG (He)	-	-	6×10^7 photons/s
[53]	XFEL (LCLS)	>10^{15}	>10^{15}	-
[56]	Synchrotron (SPring-8)	>10^{13}	>10^{13}	-

[a] Polarization gating is applied

5.4 Spatial properties

5.4.1 Beam divergence

Figures 5.6(a, b) show the measured divergence of the HH beams from Ne and He. The mean divergence of the entire HH beam is 2.0 mrad FWHM for Ne and 0.9 mrad FWHM for He. In Fig. 5.6(a), there is a horizontal dip, but this is an artifact originating from the Ni wire meshes in the Al filters in the SX beam path. In Fig. 5.6(b), this artifact is small but can still be found around 2 mrad. The position of the artifact is different between Figs. 5.6(a) and (b) because we slightly move the positions of the Al filters between the two measurements.

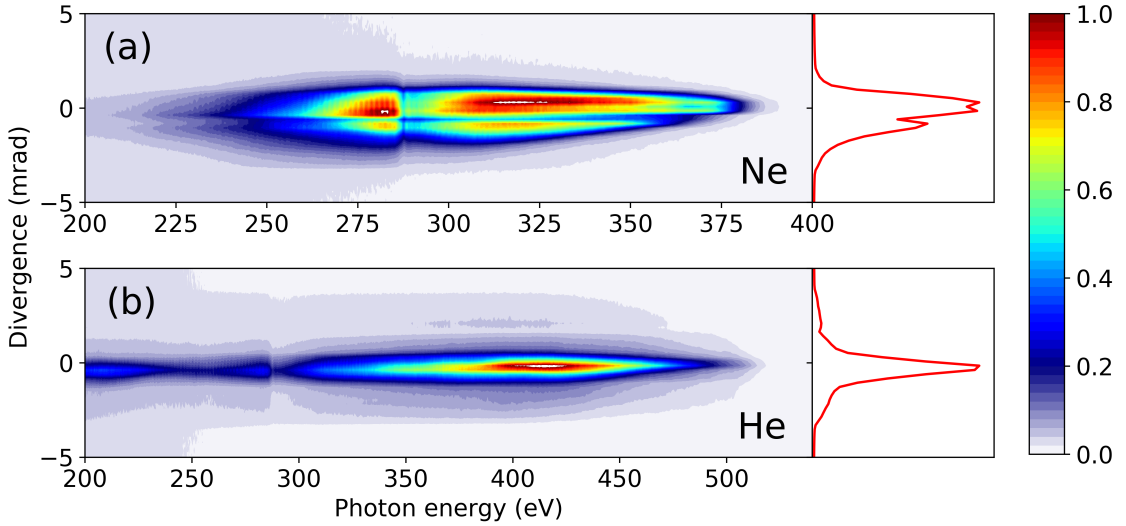

Figure 5.6: Beam divergence of the HHs from (a) 1.9 bar of Ne and (b) 3.6 bar of He. The contour plots show the photon-energy-resolved the beam profiles, and the line plots show the beam profiles integrated over the whole spectrum.

5.4.2 Spot size of focused SX beam

The focal spot size of the SX beam at the sample position is important in transient absorption measurements. This is because if the SX spot size is too large, the pump IR beam cannot cover the entire probed area of the sample, resulting in a decrease of the effective pump intensity. To investigate the SX spot size, we employ the knife edge method. Figure 5.7(a) presents a schematic of the measurement. A razor blade is inserted into the focus of the SX beam generated with He. A fraction of the SX beam is blocked by the blade, and the remaining beam goes to the SX spectrometer. By scanning the X position of the blade and measuring the HH intensity around 400 eV, a knife edge scan trace (blue circles in Fig. 5.7(b)) is obtained. By fitting the measured data with the error function, the spot size of the SX beam is estimated. The knife edge scan is repeated for various Z positions to obtain Fig. 5.7(c). The minimum spot size in Fig. 5.7(c) is 78$\pm$1 µm. This spot size is 1.4 times bigger than that of the pump IR beam (54 µm), so the decrease of the effective pump intensity might occur. However, it is expected that a

large portion of the probed area is still covered by the pump beam. Therefore, we have concluded that transient absorption measurements are possible with these spot sizes.

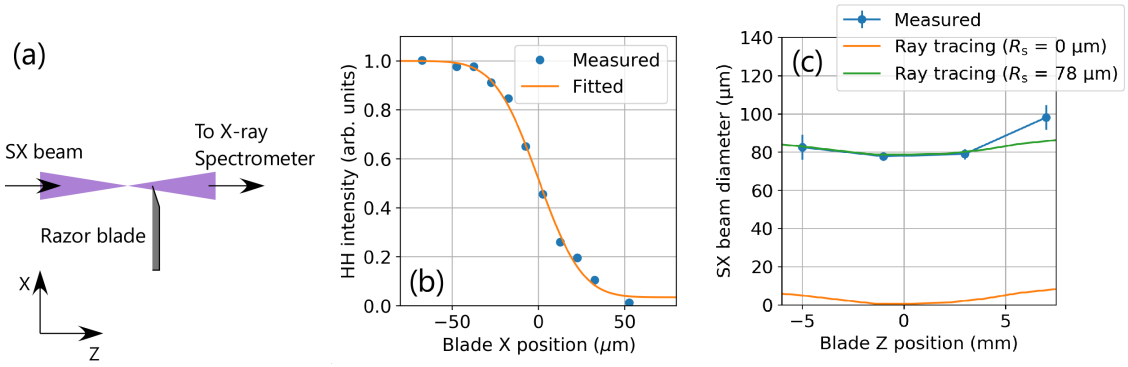

Figure 5.7: Knife edge measurement of the spot size of the SX beam. (a) Schematic of the setup. (b) Typical knife edge scan trace. The circles are the measured data and the curve is the fitting. (c) $1/e^2$ diameters of the SX beam as a function of the Z position of the razor blade. Blue circles are the measured data. Orange and green curves are the calculated data assuming the source size of the SX beam R_s to be 0 μm and 78 μm, respectively.

In Fig. 5.7(c), the measured spot sizes are compared with a calculation by ray tracing. Here, the ray tracing assumes that the SX beam is a top hat beam with a 1 mrad divergence. In our experiment, the source size of the SX beam is unknown, so the source size is treated as a free parameter to obtain a calculation result which fits the experimental data well. It is shown in Fig. 5.7(c) that the calculated beam diameters assuming a source size of 78 μm qualitatively agree with the measured data. Finally, note that our calculation does not consider the imperfect alignment or the limited surface accuracy of the toroidal mirror, which might affect the beam diameters.

5.5 Static XAS measurement

By using the generated HHs, static XAS measurements around the water window region are performed. The target samples of the XAS measurements are Ar gas (at Ar $L_{2,3}$-edge, 250 eV), N_2 gas (at N K-edge, 400 eV), TiO_2 solid (at Ti $L_{2,3}$-edge, 460 eV), and Ti solid (at Ti $L_{2,3}$-edge, 460 eV). The TiO_2 sample is an amorphous thin film deposited by magnetron sputtering on a 100-nm-thick Si_3N_4 membrane (custom fabricated by NTT-AT). The thickness of the TiO_2 layer is estimated to be ∼100 nm. The Ti sample is a commercial X-ray filter with a thickness of 150 nm (purchased from Lebow Company).

HHs from Ne is used for Ar, and HHs from He is used for N_2, TiO_2, and Ti. The slit width of the X-ray spectrometer is set to 50 μm to obtain high energy resolution. The CEP is randomized during the measurements. In the case of Ar and N_2, the sample cell is filled with the gas and the transmitted HH spectrum I_{sample} is measured. After that, the sample cell is emptied and the transmitted HH spectrum I_0 is measured. The absorption spectrum is obtained by $1 - I_{\mathrm{sample}}/I_0$. In the case of the TiO_2 and the Ti films, I_{sample} is measured with the sample inserted to the beam path, and I_0 is measured with the sample retracted from the beam path. Figure 5.8 plots the measured I_{sample} and I_0 for N_2. A

sharp absorption line at the N K-edge is clearly observed. In some energy regions (<390 eV and >460 eV), it is visible that I_{sample} is greater than I_0, but this is due to the intensity fluctuation of the HHs.

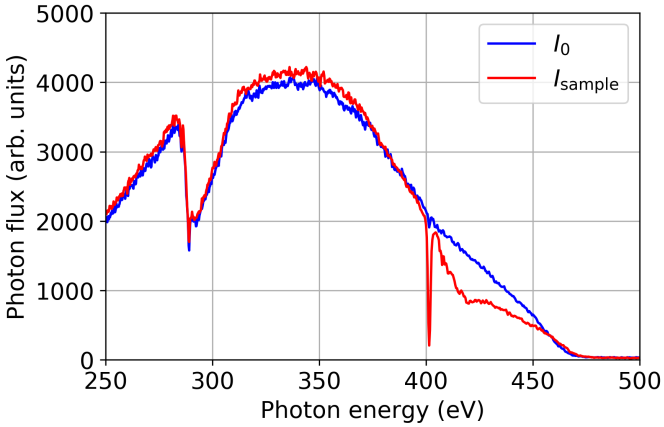

Figure 5.8: Measured I_{sample} and I_0 for N_2.

Fig. 5.9 plots the measured absorption spectra of Ar, N_2, TiO_2, and Ti (blue circles). The red dashed curves are the reference curves obtained with high-resolution spectrometers in synchrotron facilities. The references for Ar, N_2, TiO_2, and Ti are ref. [154] (total electron yield mode), ref. [155] (transmission mode), ref. [156] (total electron yield mode), and ref. [157] (transmission mode), respectively. The reference curves are convoluted with rectangular windows to fit our measured data (red solid curves). The widths of the rectangular windows are 0.35 eV for Ar, (250 eV), 1.0 eV for N_2 (400 eV), 3.0 eV for TiO_2 (460 eV), and 3.3 eV for Ti (460 eV).

The widths of the rectangular windows can be used to determine the energy resolution of the X-ray spectrometer. The red circles in Fig. 5.10 show the obtained energy resolution, which is plotted as $E/\Delta E$, where E is the photon energy and ΔE is the window width in Fig. 5.9.

The energy resolution can also be numerically calculated according to ref. [158]. Assuming that the aberration and slope error of the grating are small enough, the resolvable energy difference ΔE can be obtained as

$$\Delta E = \sqrt{\Delta E_{\text{slit}}^2 + \Delta E_{\text{CCD}}^2}, \tag{5.2}$$

where ΔE_{slit} and ΔE_{CCD} are the smearing of photon energy due to the finite width of the entrance slit and the spatial resolution of the X-ray CCD camera, respectively.

ΔE_{slit} can be calculated as

$$\Delta E_{\text{slit}} = \Delta x_{\text{slit}} \frac{\cos\alpha}{rN\lambda} E, \tag{5.3}$$

where Δx_{slit} is the width of the entrance slit, and α, r, and N are the geometrical parameters of the X-ray grating defined in Fig. A.1 in Appendix A, and λ is the X-ray wavelength. In our experiment, Δx_{slit} is set to 50 μm.

Meanwhile, ΔE_{CCD} can be calculated as

$$\Delta E_{\text{CCD}} = \Delta x_{\text{CCD}} \frac{\cos\beta}{r'N\lambda} E, \tag{5.4}$$

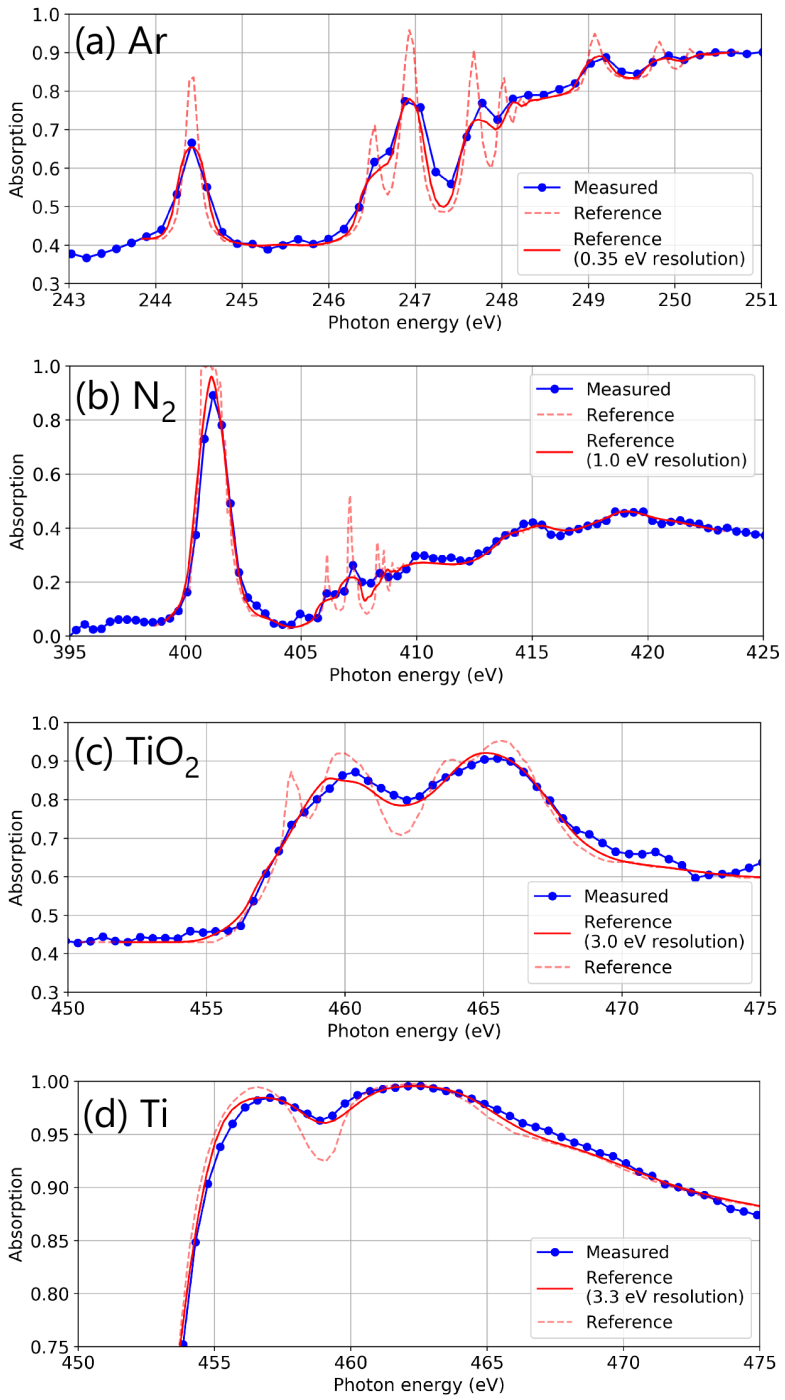

Figure 5.9: X-ray absorption spectra of (a) Ar, (b) N_2, (c) TiO_2, and (d) Ti. The blue circles are the measured data in our beamline, the red dashed curves are the reference data from synchrotron [154–157], and the red solid curves are the reference data convoluted with rectangular energy windows (0.35 eV wide for Ar, 1.0 eV wide for N_2, 3.0 eV wide for TiO_2, and 3.3 eV wide for Ti).

where Δx_{CCD} is the spatial resolution of the X-ray CCD camera, and β and r' are again the geometrical parameters defined in Fig. A.1. Δx_{CCD} is set to 24 µm according to ref. [159].

The blue dashed curve in Fig. 5.10 plots the calculated energy resolution. The agreement between the measurement and the calculation is good at 250 eV. However, above 400 eV, the measured energy resolution is worse than the calculated values. Possible reasons for the disagreement might be small misalignment of the spectrometer, or the aberration and the slope error of the grating.

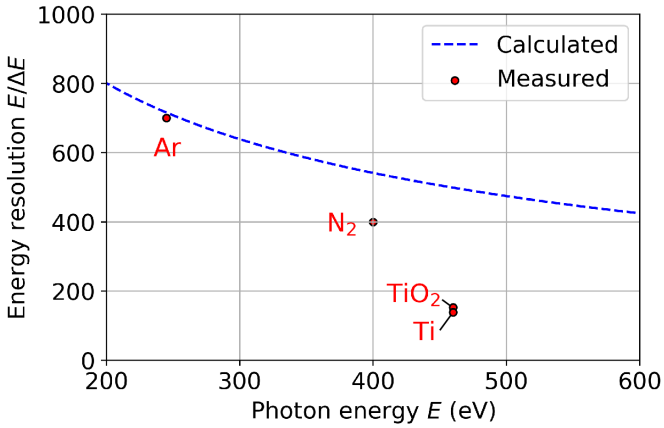

Figure 5.10: Measured (red circles) and calculated (blue dashed curve) energy resolution of the X-ray spectrometer.

Chapter 6

Transient absorption spectroscopy of NO molecules at 400 eV

In this chapter, transient absorption spectroscopy of NO molecules at 400 eV performed in our beamline is presented. This result is, to the best of our knowledge, the first demonstration of HHG-based transient absorption spectroscopy at the N K-edge in the world. Moreover, we simultaneously observe all the electronic, vibrational, and rotational dynamics by transient absorption spectroscopy. These results will pave the way towards complete tracking of photoinduced processes using element-specific SX pulses in the water window with attosecond temporal resolution.

6.1 Motivation

After finishing the development of the beamline, the first thing to do is to demonstrate its capability for transient absorption spectroscopy. Our SX HHG source covers various absorption edges in the water window, namely, the C K-edge (284 eV), the N K-edge (400 eV), the Ca $L_{2,3}$-edge (350 eV), the Sc $L_{2,3}$-edge (400 eV), and the Ti $L_{2,3}$-edge (460 eV). The M-edges of transition metals are also covered. Among these candidates, we choose the N K-edge (400 eV) as our target for the following reasons. One reason is that it is easy to obtain gaseous samples for transient absorption spectroscopy which contain light elements such as nitrogen or carbon (transient absorption measurements of solid samples are much more difficult than gaseous samples because of sample preparation and damage problems). The other reason is that HHG-based transient absorption spectroscopy above the C K-edge has never been performed for gaseous samples (transient absorption spectroscopy at the C K-edge has already been demonstrated by other groups [62, 63]). As a target molecule, we choose NO. NO is one of the simplest nitrogen-containing molecules, so its dynamics is expected to be clear. Therefore, it is an ideal sample for the first demonstration of transient absorption spectroscopy at the N K-edge. Although N_2 is also simple, its ionization energy is much higher than that of NO (N_2: 15.6 eV, NO: 9.26 eV), thus it is relatively difficult to trigger ionization-induced molecular dynamics in N_2.

6.2 Static absorption spectrum of NO

The static absorption spectrum of NO is measured before conducting transient absorption measurements. The HHs from He is used as an SX source, the pressure of NO is set to 0.1 bar, and the thickness of the sample cell is 1.5 mm. The measurement procedure is the same as that in Section 5.5.

Figure 6.1(a) plots the measured (circles) and reference (dashed curve) absorbance spectra of NO. Here, the absorbance is calculated as $-\log_{10}(I_{\mathrm{sample}}/I_0)$ (I_{sample} and I_0 represent the HH intensities which pass through the sample gas cell with and without NO, respectively). Note that Fig. 5.9 in the previous chapter plots "absorption," while Fig. 6.1(a) plots "absorbance." The reference curve is taken from a synchrotron measurement (total electron yield mode) [99]. The assignment of the absorption peaks is also cited from [99] and shown in Fig. 6.1(a). Note that the assignment for some minor absorption peaks is omitted for simplicity. The strong peak at 400 eV corresponds to the transition from the N 1s core shell to the valence 2π orbital (LUMO/SOMO) as depicted in Fig. 6.1(b). The weak peaks around 406-410 eV correspond to the transitions from the N 1s shell to the Rydberg orbitals ($3s\sigma$, $3p\pi$, ...).

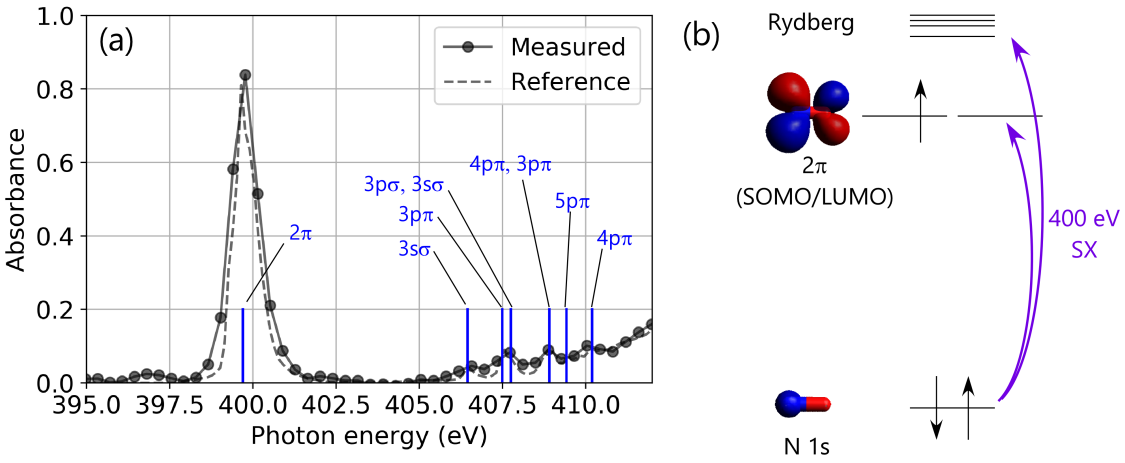

Figure 6.1: (a) Measured (circles) and reference [99] (dashed curve) static absorbance spectrum of NO at the N K-edge. (b) Energy level diagram of NO.

6.3 Experimental conditions and data acquisition procedure

6.3.1 Beamline setup

The experimental conditions for the transient absorption measurements are as follows. The split ratio of the beam splitter for the separation of the pump and the probe beams is R:T = 10:90. The IR beams in the pump and the probe arms contain ~70 μJ and ~1 mJ pulse energies, respectively.

As for the intensity of the pump IR pulse, it is estimated by fitting the simulated molecular-rotation-induced SX absorbance changes to the measured values as described

later in Section 6.4.3. In that simulation, the pump intensity is calculated to be 1.3×10^{14} W/cm^2. Considering possible existence of unknown errors, we round the calculated value to one significant digit, and obtain an estimated pump intensity of 1×10^{14} W/cm^2. The reason why we do not estimate the pump intensity from the pulse energy, spot size, and the pulse duration is that the spatial averaging effect can significantly lower the effective pump intensity, as the spot size of the probe SX beam is larger than that of the pump IR beam. At the pump intensity of 1×10^{14} W/cm^2, the Keldysh parameter is calculated to be $\sim$0.4.

As the HHG gas, He is chosen to generate HHs at 400 eV. The pressure of the NO sample gas cell is set to 0.1 bar. The delay stabilization system is employed in the attosecond time-resolved transient absorption measurement (Section 6.4.1), but it is turned off in other measurements. The CEP of the drive laser is fixed in the attosecond time-resolved measurement to obtain isolated attosecond pulses, but it is randomized in other measurements.

Figure 6.2(a) shows the CEP dependence of the HH spectra recorded with the experimental conditions of the attosecond time-resolved transient absorption measurement. The HH spectrum employed in the attosecond time-resolved transient absorption measurement is shown in Fig. 6.2(b). Here, the NO gas cell is inserted in the SX beam path, so the absorption line of NO is visible. The HH spectrum has the first and the second HCOs at $\sim$450 and $\sim$370 eV, respectively. Therefore, around the absorption line of NO at 400 eV, isolated attosecond pulses are expected to be generated.

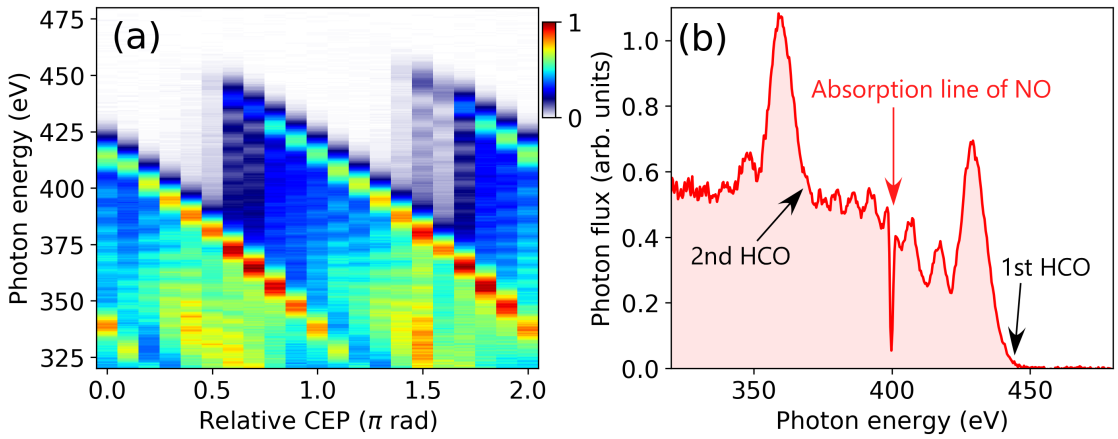

Figure 6.2: (a) CEP-dependent HH spectra. (b) HH spectrum employed in the attosecond time-resolved transient absorption measurement. The sample NO gas cell is inserted in the beam path, so the absorption line of NO at 400 eV is visible.

6.3.2 Estimation of SX pulse duration

The temporal duration of the SX pulse is a critical parameter to determine the temporal resolution of the transient absorption measurement. Although we cannot directly measure the SX pulse duration with the current setup, we perform an SFA (Lewenstein model) simulation to estimate it.

In the simulation, an IR pulse with a peak electric field amplitude of 640 MV/cm, a central wavelength of 1.6 μm, a pulse duration of 10 fs FWHM, and a cosine-like CEP is used as an HHG driver (Fig. 6.3(a)). The ionization potential of a He atom is set to 24.6 eV. The calculated HHs, including both long and short trajectories, are plotted in Fig. 6.3(b) as a time-frequency spectrogram obtained by a short-time Fourier transform. Then, the isolated attosecond pulse region of the HH spectrum (370-450 eV) is extracted, and its pulse shape is plotted in Fig. 6.3(c). The calculated temporal duration of the SX pulse is 820 as FWHM. However, of course, this value may be different from the actual pulse duration as we use many assumptions in the calculation. In the following, we discuss possible factors which can affect the pulse duration.

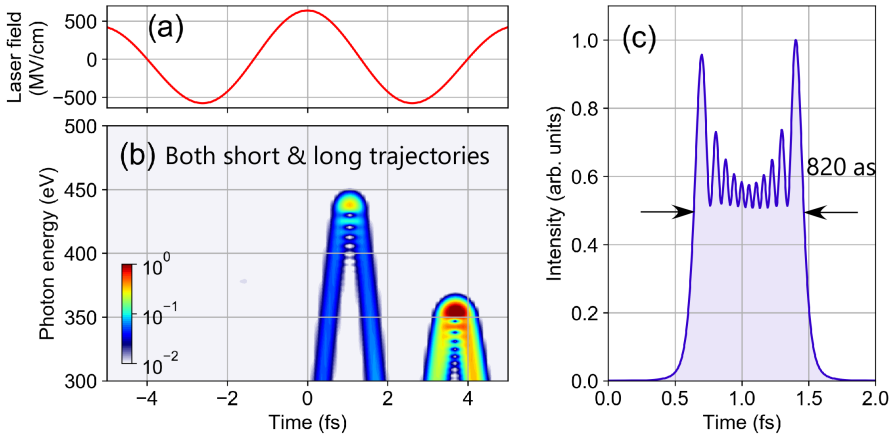

Figure 6.3: Simulation of the SX pulse shape considering both short and long trajectories. (a) Laser electric field employed in the SFA simulation. (b) Time-frequency spectrogram of the simulated HHs. (c) Pulse shape of the simulated HHs in the isolated attosecond pulse region (370-450 eV).

First, we consider the macroscopic response of HHG, namely, the phase matching. An important effect of the phase matching on the SX pulse duration is the selection of the quantum trajectory [160, 161]. In fact, the HH spectrum observed in our experiment in Fig. 6.2(b) shows a signature of the selection of the quantum trajectory. In Fig. 6.2(b), interference fringes with an oscillation period of ∼5-10 eV are visible between the first and the second HCOs. These fringes are due to the interference between the HH radiations emitted from the short and the long trajectories. If the modulation depth of the fringes is 100%, it means that both trajectories equally contribute to the HH spectrum. However, the observed modulation depth is roughly <30%, indicating that one trajectory is dominant. Although we cannot determine which trajectory is dominant in our experiment, it is expected that the SX pulse duration becomes shorter than the calculated value (820 as) as a result of the selection of the trajectory.

Second, we consider the group delay dispersion of the 150-nm-thick Al filter through which the SX beam is transmitted. It is known that the dispersion of such a metal filter affects the SX pulse duration in some cases [58]. We calculate the group delay of the Al filter by using the refractive index of Al in the SX region [144]. Figure 6.4 shows the result. It is visible that the change of the group delay from 300 eV to 500 eV is a few attoseconds, which means the Al filter hardly affects the SX pulse duration in our case.

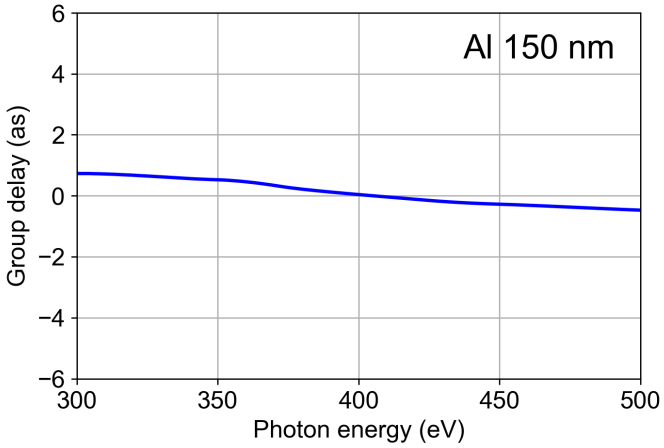

Figure 6.4: Calculated group delay of a 150-nm-thick Al filter around 400 eV.

Finally, we consider the Coulomb potential of the parent ion and the multi-electron effects, which are not considered in the SFA. As for the Coulomb potential of the parent ion, it is not relavant to the SX pulse duration so much. This is because the SFA is highly valid in our HHG scheme as the Keldysh parameter is γ ∼0.3 (wavelength: 1.6 μm, electric field amplitude: 640 MV/cm) and the HH photon energy is much larger than the ionization potential. As for the multi-electron effects, they are not expected to change the pulse duration. This is because the multi-electron effects hardly change the acceleration process of the ionized electron, thus the shapes of the short and long trajectories are not affected.

To summarize, the actual SX pulse duration might be shorter than that estimated by the SFA calculation (820 as), but it is unlikely that the former is longer than the latter. Therefore, we conclude that the SX pulses in our experiment have at least a sub-femtosecond temporal duration.

6.3.3 Data acquisition procedure

The data acquisition procedure of transient absorption is as follows. During the whole measurement, the NO sample gas cell is always inserted to the SX beam path and the pump IR beam is always irradiated to the sample gas cell. Let τ_i ($i = 0, 1, \ldots$) be the delay points. The piezo stage is moved to each τ_i, and the HH spectrum transmitted through the sample gas cell $I_0(E_j, \tau_i)$ ($j = 0, 1, \ldots$, E_j: photon energy at the CCD pixel j) is recorded. Here, the exposure time of the CCD camera at one delay step is set to 3∼5 seconds depending on the HH flux (once the exposure time is determined, it is kept during the whole transient absorption measurement). The delay scan is repeated for a few tens of times to obtain $I_k(E_j, \tau_i)$ ($i, j, k = 0, 1, \ldots$). Then, the averaged HH spectra are calculated as

$$I_{\mathrm{avg}}(E_j, \tau_i) = \frac{1}{N_{\mathrm{scan}}} \sum_k I_k(E_j, \tau_i) \quad (i, j = 0, 1, \ldots), \tag{6.1}$$

where N_{scan} is the number of delay scans. Next, the threshold delay index i_{ref} for the reference HH spectrum is determined. i_{ref} is chosen such that $\tau_{i_{\mathrm{ref}}}$ becomes a delay before

which no molecular dynamics takes place (typically, ∼-100 fs). Then, the reference HH spectrum is calculated as

$$I_{\mathrm{ref}}(E_j) = \frac{1}{i_{\mathrm{ref}}} \sum_{i<i_{\mathrm{ref}}} I_{\mathrm{avg}}(E_j, \tau_i) \quad (j = 0, 1, \ldots). \tag{6.2}$$

The differential absorbance $\Delta A(E_j, \tau_i)$ is then calculated as

$$\Delta A(E_j, \tau_i) = -\log_{10} \frac{I_{\mathrm{avg}}(E_j, \tau_i)}{I_{\mathrm{ref}}(E_j)}. \quad (i, j = 0, 1, \ldots). \tag{6.3}$$

In order to further improve the signal-to-noise ratio by removing the fluctuation of the HH intensity, a background correction procedure is applied to $\Delta A(E_j, \tau_i)$. First, two background energy regions, $E_{j^1_{\mathrm{bg1}}} \sim E_{j^1_{\mathrm{bg2}}}$ and $E_{j^2_{\mathrm{bg1}}} \sim E_{j^2_{\mathrm{bg2}}}$ ($j^1_{\mathrm{bg1}} < j^1_{\mathrm{bg2}} < j^2_{\mathrm{bg1}} < j^2_{\mathrm{bg2}}$) are chosen. These two energy regions should be lower or higher than the XANES region so that they do contain any absorbance change. Typically, they are chosen around 396 eV and 413 eV in the case of NO molecules. Second, two sets of background differential absorbance, $\Delta A^1_{\mathrm{bg}}(\tau_i)$ and $\Delta A^2_{\mathrm{bg}}(\tau_i)$, are calculated as

$$\Delta A^1_{\mathrm{bg}}(\tau_i) = \frac{1}{j^1_{\mathrm{bg2}} - j^1_{\mathrm{bg1}}} \sum_{j^1_{\mathrm{bg2}} \le j < j^1_{\mathrm{bg1}}} \Delta A(E_j, \tau_i) \tag{6.4}$$

$$\Delta A^2_{\mathrm{bg}}(\tau_i) = \frac{1}{j^2_{\mathrm{bg2}} - j^2_{\mathrm{bg1}}} \sum_{j^2_{\mathrm{bg2}} \le j < j^2_{\mathrm{bg1}}} \Delta A(E_j, \tau_i) \quad (i = 0, 1, \ldots). \tag{6.5}$$

Finally, the background-corrected differential absorbance $\Delta A_{\mathrm{cor}}(E_j, \tau_i)$ is obtained as

$$\Delta A_{\mathrm{cor}}(E_j, \tau_i) = \Delta A(E_j, \tau_i) - \frac{E_j - E^1_{\mathrm{bg}}}{E^2_{\mathrm{bg}} - E^1_{\mathrm{bg}}} (\Delta A^2_{\mathrm{bg}}(\tau_i) - \Delta A^1_{\mathrm{bg}}(\tau_i)) \quad (i, j = 0, 1, \ldots). \tag{6.6}$$

Here, E^1_{bg} and E^2_{bg} are defined as $(E_{j^1_{\mathrm{bg2}}} + E_{j^1_{\mathrm{bg1}}})/2$ and $(E_{j^2_{\mathrm{bg2}}} + E_{j^2_{\mathrm{bg1}}})/2$, respectively.

6.4 Results and discussions

Figure 6.5(a) shows the measured transient absorption trace of NO at the N K-edge. The total measurement time is ∼2 hours. The polarizations of the SX and IR pulses are parallel. For reference, the static absorbance spectrum of NO is plotted in Fig. 6.5(b). In the measured transient absorption trace, there are several features originating from ultrafast molecular dynamics.

First, there are weak absorbance modulations in the Rydberg peaks around 408 eV. These modulations are commonly observed in transient absorption spectroscopy of Rydberg states, which can be explained by the emergence of laser-dressed states and AC Stark shift [20, 86, 92, 93, 98]. Here, we do not discuss this phenomenon further.

Second, the absorbance around 400 eV is decreased and the absorbance around 403 eV is increased at the positive delays. According to ab initio configuration-interaction calculation, these energies are assigned to the 1s-2π transitions of NO and NO^+. Therefore, the observed feature indicates that NO molecules are ionized to NO^+ molecular ions

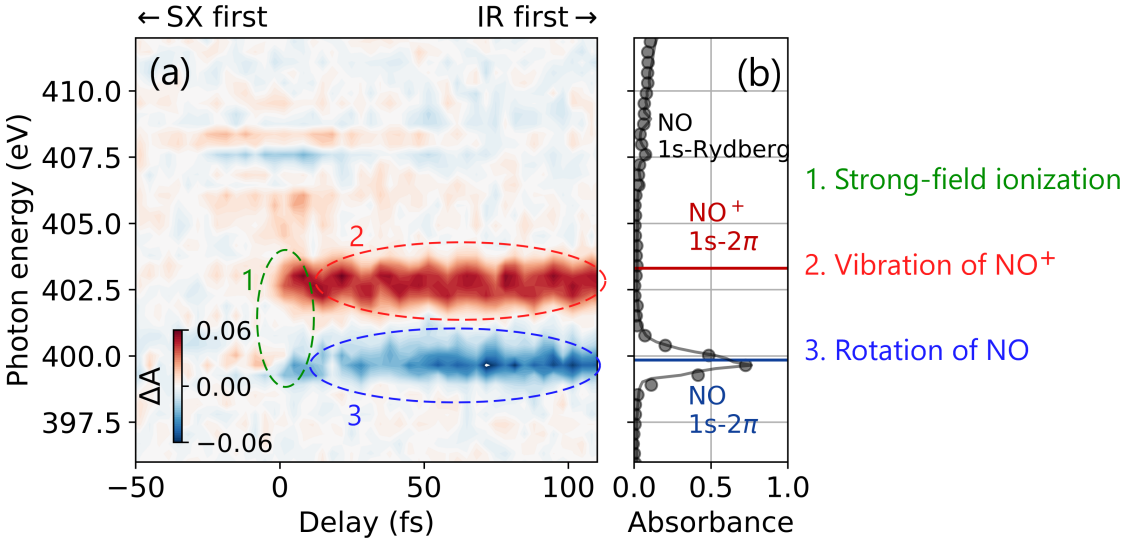

Figure 6.5: (a) Measured transient absorption trace of NO. The dashed ellipses indicate the regions where three different kinds of dynamics are imprinted. (b) Static absorbance spectrum of NO measured in our beamline (circles) and in a synchrotron facility (solid curve) [99].

by strong-field ionization. Here, the ab initio calculation is performed by Prof. Nobuhiro Kosugi by using the GSCF3 software [162,163]. The basis functions are (73/7) contracted Gaussian-type functions with two d-type polarization functions.

Interestingly, from the absorbance changes of these 1s-2π peaks, we can extract three different kinds of dynamics which are associated with different degrees of freedom:

1. Attosecond time-resolved electronic dynamics during strong-field ionization
2. Femtosecond vibrational dynamics of NO^+
3. Sub-picosecond rotational dynamics of NO

These three kinds of dynamics are observed in the dashed regions in Fig. 6.5. In the following sections, each dynamics is discussed in detail.

6.4.1 Attosecond time-resolved electronic dynamics

In this section, the attosecond time-resolved electronic dynamics in the strong-field ionization process is described. Figure 6.6(a) shows the measured attosecond time-resolved transient absorption trace of NO around the delay origin with fine delay steps (400 as). It is visible in the NO and the NO^+ 1s-2π peaks that there are oscillatory structures in addition to the monotonic absorbance decrease or increase. The oscillations become more evident when the differential absorbance of these peaks is shown as a line plot (Fig. 6.6(b)). The period of the oscillation is extracted to be 2.7 fs, which equals half a cycle of the pump IR pulse. This type of oscillation is called "2ω oscillation." Note that there might be other high-frequency oscillations in the measured data, but considering the noise level in our experiment (shaded areas in Fig. 6.6(b) represent the error), it is difficult to discuss

such oscillations. In our results, it is noteworthy that the phase of the 2ω oscillation is opposite for the NO and the NO^+ peaks. This phase relationship can be explained if the origin of the 2ω oscillation is the oscillation of the ion population; when the population of the cations increases, the population of the neutral molecules decreases, and vise versa. Note that the total ion population is estimated to be approximately 3%, which is obtained by deviding the total absorbance decrease of the NO 1s-2π peak averaged from 401.7 to 403.6 eV (0.015, as can be seen in Fig. 6.6(b)) by the static absorbance averaged in the same energy region (0.46).

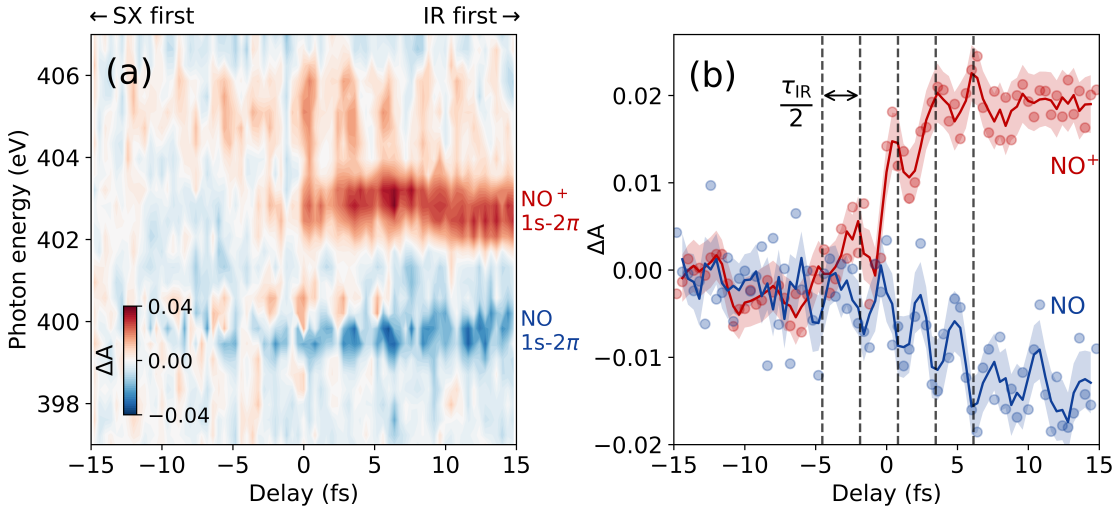

Figure 6.6: (a) Attosecond time-resolved transient absorption trace of NO around the delay origin. (b) Line plot of the differential absorbance of the NO 1s-2π peak (blue circles, averaged from 398.7 to 400.6 eV) and the NO^+ 1s-2π peak (red circles, averaged from 401.7 to 403.6 eV). The solid curves are their 3-point moving averages, and the shaded areas indicate the errors.

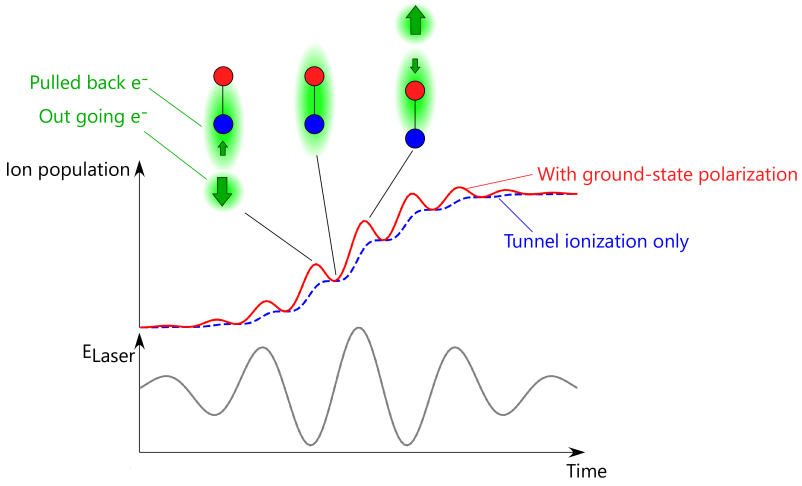

Figure 6.7: Concept of the ground-state polarization effect.

The 2ω oscillation of the ion population during the strong-field ionization process has previously been observed in Xe atoms [18], and called the ground-state polarization

effect. Figure 6.7 depicts its concept. In normal tunnel ionization, the ion population increases stepwise during ionization because the ionization predominantly occurs at the local maxima of the laser electric field (blue dashed curve in Fig. 6.7). However, when the ground-state polarization takes place, a small part of the tunnel-ionized electron wave packet cannot escape from the Coulomb potential of the parent ion and is pulled back to it. As a result, the ion population shows not only monotonic increase but also periodic decrease.

Although the ground-state polarization effect has been reported for atoms, it has never been observed in molecules. Our observation of the signature of ground-state polarization in NO will give a clue to understand sub-cycle electronic dynamics in molecular systems.

6.4.2 Femtosecond vibrational dynamics

Next, the femtosecond vibrational dynamics of NO^+ triggered by strong-field ionization is discussed. The vibration signal is imprinted in the modulation of the peak position of the NO^+ 1s-2π peak as shown in Fig. 6.8(a). By fitting the NO^+ 1s-2π peak with a Gaussian function for each delay and extracting its central photon energy, red circles in Fig. 6.8(b) are obtained. Here, the delay origin is determined by fitting the temporal evolution of the peak height of the NO^+ 1s-2π peak with a sigmoid function and extracting the inflection point of the fitted sigmoid function. The temporal evolution of the extracted central photon energies is fitted with a cosine function plus a Gaussian function (red solid curve in Fig. 6.8(b)). Here, the Gaussian function represents the upper shift of the central photon energies around the delay origin in Fig. 6.8(b). Although the exact reason for the upper shift is not clear, it might be explained by the AC Stark shift of the NO^+ 1s-2π peak or an artifact in the extraction process of the central photon energies due to the existence of the laser-dressed Rydberg states (404–406 eV in Fig. 6.6(a)) above the NO^+ 1s-2π peak. The result of the fitting is shown as a red solid curve in Fig. 6.8(a). From the fitting, the oscillation period of 14.5$\pm$0.1 fs is obtained. This oscillation period agrees well with the literature value of the vibration period of NO^+ (14.23 fs) [164]. Moreover, the initial phase of the vibration is determined to be (0.17$\pm$0.08)π rad, where 0π and 0.5π mean perfect "cosine-like" and "sine-like" phases, respectively. This indicates that the observed molecular vibration is close to "cosine-like."

The mechanism of the observed vibration, including its initial phase, can be explained by the potential energy curves of NO and NO^+ obtained by the ab initio calculation performed by Prof. Nobuhiro Kosugi (Fig. 6.8(c)). After strong-field ionization of NO molecules, a vibrational wave packet is created on the potential energy curve of the electronic ground state of NO^+. Because the equilibrium internuclear distances of NO and NO^+ are different (NO: 1.15 Å, NO^+: 1.06 Å), the created wave packet is displaced from the bottom of the potential energy curve, thus starts vibration. The molecular vibration is directly mapped to the change of the transition energy between the 1s and the 2π levels, as the transition energy monotonically decreases with respect to the internuclear distance. This mechanism [87, 88] is consistent with the experimentally observed "cosine-like" initial phase.

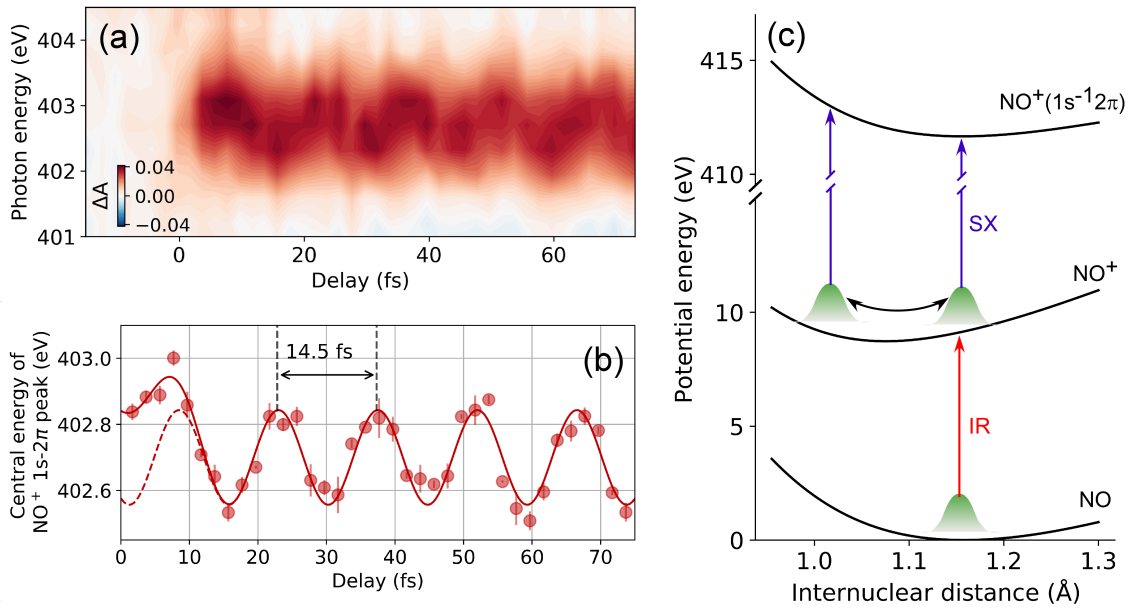

Figure 6.8: (a) Transient absorption trace around the NO^+ 1s-2π peak. (b) Extracted central energy of the NO^+ 1s-2π peak (circles), together with the fitting by a cosine plus a Gaussian function (red solid curve). The red dashed curve is the cosine component of the fitting. (c) Potential energy curves calculated of NO calculated by Prof. Nobuhiro Kosugi and the mechanism of the molecular vibration.

6.4.3 Sub-picosecond rotational dynamics

Finally, the sub-picosecond rotational dynamics of neutral NO molecules is presented. The rotational dynamics can be observed by changing the polarizations of the pump IR and the probe SX pulses. Figures 6.9(a, b) show the measured transient absorption traces with different polarization combinations. It is visible that, when the polarizations of the IR and the SX pulses are parallel, the absorbance of the NO 1s-2π peak decreases around $\sim 1 \times 10^2$ fs. On the other hand, when the polarizations are perpendicular, the absorbance of the NO 1s-2π peak increases around $\sim 1 \times 10^2$ fs.

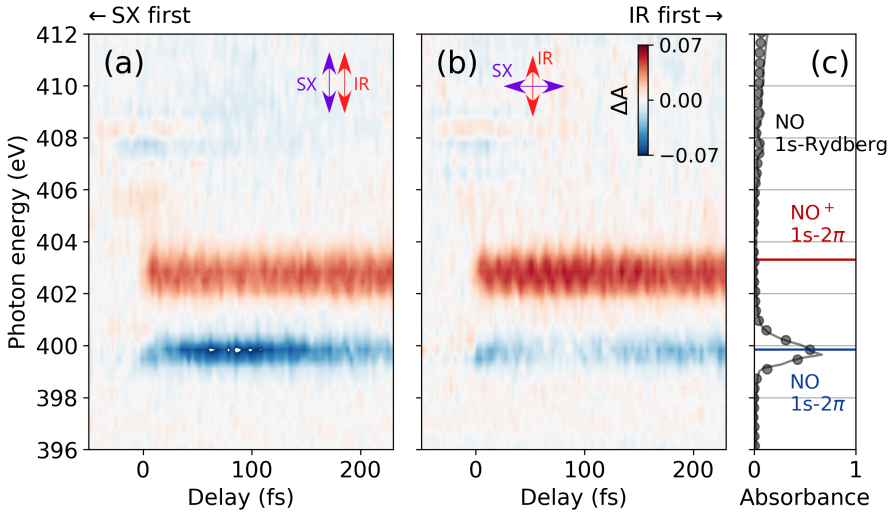

Figure 6.9: Transient absorption traces of NO when the polarizations of the IR and the SX pulses are (a) parallel and (b) perpendicular. (c) Static absorbance spectrum of NO measured in our beamline (circles) and in a synchrotron facility (solid curve) [99].

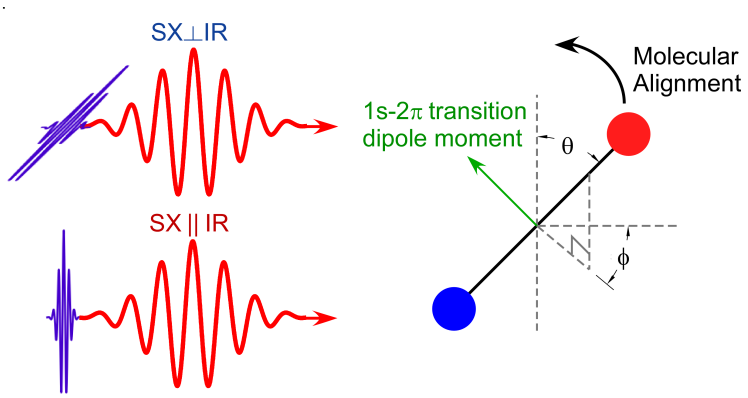

Figure 6.10: Schematic of the mechanism of the SX absorption change upon molecular alignment.

The mechanism of the polarization-dependent absorption change can be explained by the laser-induced molecular alignment process and the relative angle between the SX polarization and the 1s-2π transition dipole moment vector as depicted in Fig. 6.10.

When an NO molecule is irradiated by an IR laser pulse, the molecule begins to align with the IR polarization via the interaction between the induced dipole moment and the laser electric field [165, 166]. In this process, the 1s-2π transition dipole moment, which is perpendicular to the molecular axis, becomes antialigned with the IR polarization. Therefore, when the SX polarization is parallel to the IR polarization, the inner product between the SX polarization and the 1s-2π transition dipole moment decreases as the NO molecules align, resulting in the decrease of the SX absorption. Conversely, when the SX polarization is perpendicular to the IR polarization, the SX absorption increases.

In order to numerically reproduce the observed absorbance change, we perform a TDSE simulation for the molecular alignment dynamics [165]. When a molecule can be regarded as a rigid rotor (i.e., ignore vibronic and electronic excitations) and it interacts with a laser electric field, its Hamiltonian $H(t)$ in atomic units can be written as

$$H(t) = B\boldsymbol{J}^2 - \boldsymbol{\mu}\cdot\boldsymbol{\epsilon}(t) - \frac{1}{2}\epsilon^2(t)\left[(\alpha_\parallel - \alpha_\perp)\cos^2\theta + \alpha_\perp\right]. \tag{6.7}$$

Here, B is the rotational constant, $\boldsymbol{J}$ is the angular momentum operator, $\boldsymbol{\mu}$ is the permanent dipole, $\epsilon(t)$ is the the laser electric field, $\alpha_\parallel$ and $\alpha_\perp$ are the components of the static polarizability which are parallel and perpendicular to the molecular axis, and θ is the angle between the molecular axis and the laser electric field. This Hamiltonian can be simplified using several approximations as follows. First, although $\boldsymbol{\mu}\cdot\boldsymbol{\epsilon}(t)$ is responsible for molecular orientation, it can be ignored when calculating only molecular alignment. Second, the fast oscillation of the carrier wave of $\boldsymbol{\epsilon}(t)$ does not affect the slow molecular alignment process. Therefore, if the envelope function of the laser electric field is $a(t)$, $\epsilon(t)^2$ can be approximated as $a(t)^2/2$. Finally, the second term in the square bracket in Eq. (6.7) does not couple with the alignment angle θ, so it does not affect molecular alignment. By using these approximations, and by introducing $\Delta\alpha$ as $\Delta\alpha = \alpha_\parallel - \alpha_\perp$, the Hamiltonian can be simplified to

$$H(t) = B\boldsymbol{J}^2 - \frac{1}{4}a^2(t)\Delta\alpha\cos^2\theta. \tag{6.8}$$

The TDSE for this Hamiltonian is first solved for the following wave function

$$|\psi_{J_i,M_i}(t)\rangle = \sum_{J\geq|M_i|} c_{J,J_i,M_i}(t)\,|J,M_i\rangle\,, \tag{6.9}$$

where $|J,M_i\rangle$ is a rotational eigenstate. The initial state of this wave function is set to $|J_i,M_i\rangle$ (i.e., $c_{J,J_i,M_i}(0) = 1$ ($J = J_i$) and $c_{J,J_i,M_i}(0) = 0$ ($J \neq J_i$)). This procedure is repeated for every J_i and M_i. Practically, the maximum J_i is set to 50-60. Then, the degree of alignment, $\langle\cos^2\theta\rangle$ is calculated from $|\psi_{J_i,M_i}(t)\rangle$ as

$$\langle\cos^2\theta\rangle = \frac{1}{Z}\sum_{J_i,M_i} e^{-BJ_i(J_i+1)/T}\,\langle\psi_{J_i,M_i}(t)|\cos^2\theta\,|\psi_{J_i,M_i}(t)\rangle\,, \tag{6.10}$$

where T is the temperature of the molecules, and Z is the partition function which is defined as

$$Z = \sum_{J_i,M_i} e^{-BJ_i(J_i+1)/T}. \tag{6.11}$$

The above calculation procedure is applied to NO molecules. The rotational constant and the polarizability anisotropy are set to B = 1.696 cm^{-1} [167] and $\Delta\alpha$ = 0.84 Å^3 [168], respectively. As an excitation IR pulse, we use a Gaussian pulse with a pulse duration of 10 fs FWHM and a peak intensity of 1.3×10^{14} W/cm^2. This peak intensity is chosen such that the calculated absorbance changes fit the experimental data as shown later in Fig. 6.12. The calculated degrees of alignment are plotted in Fig. 6.11 for various temperatures. As the temperature increases, the maximum degree of alignment decreases. This is due to the dephasing among rotational eigenstates with high J_i at high temperatures. In the experiment, the temperature is 300 K because the NO molecules are filled in a room-temperature gas cell.

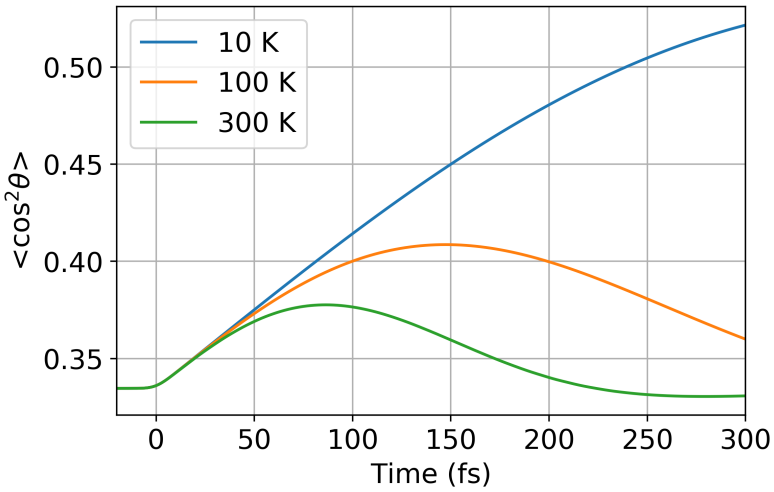

Figure 6.11: Calculated degrees of alignment of NO molecules irradiated with an IR pulse (pulse duration: 10 fs FWHM, peak intensity: 1.3×10^{14} W/cm^2).

The relationship between the degree of alignment $\langle\cos^2\theta\rangle$ and the SX absorption A is formulated as follows. We assume that the transition dipole moment between the inner shell and the valence orbital is perpendicular to the molecular axis, which is the case for the 1s-2π transition in NO. The molecular axis vector $\boldsymbol{r}_{mol}$ and the IR polarization vector $\boldsymbol{e}_{IR}$ can be written as $\boldsymbol{r}_{mol} = (\sin\theta\cos\phi, \sin\theta\sin\phi, \cos\theta)$ and $\boldsymbol{e}_{IR} = (0, 0, 1)$, respectively. Here, note that the definition of the coordinates is different from that in Chapter 4. In this chapter and in the next chapter, it is assumed that the IR polarization axis is fixed to the z axis, and the laser propagation axis is fixed to the y axis. In this coordinate system, if the polarizations of the IR and the SX pulses are parallel, the SX polarization vector $\boldsymbol{e}_{SX}$ can be written as $\boldsymbol{e}_{SX} = (0, 0, 1)$. In this case, the inner product between the transition dipole moment $\boldsymbol{d}$ and the SX polarization vector $\boldsymbol{e}_{\mathrm{SX}}$ is proportional to $\sqrt{1-(\boldsymbol{r}_{mol}\cdot\boldsymbol{e}_{SX})^2} = \sin\theta$. Therefore,

$$A \propto |\boldsymbol{d}\cdot\boldsymbol{e}_{\mathrm{SX}}|^2 = |d|^2\langle\sin^2\theta\rangle = |d|^2(1-\langle\cos^2\theta\rangle). \tag{6.12}$$

On the other hand, if the polarizations of the IR and the SX pulses are perpendicular, the SX polarization vector can be written as $\boldsymbol{e}_{SX} = (1, 0, 0)$. In this case, $\boldsymbol{d}\cdot\boldsymbol{e}_{\mathrm{SX}}$ is

proportional to $\sqrt{1-(\boldsymbol{r}_{mol}\cdot\boldsymbol{e}_{SX})^2} = \sqrt{1-\sin^2\theta\cos^2\phi}$. Therefore,

$$A \propto |\boldsymbol{d}\cdot\boldsymbol{e}_{\mathrm{SX}}|^2 = |d|^2\langle 1-\sin^2\theta\cos^2\phi\rangle \tag{6.13}$$

$$= |d|^2\frac{\int \mathrm{d}\phi(1-\langle\sin^2\theta\rangle\cos^2\phi)}{\int \mathrm{d}\phi} \tag{6.14}$$

$$= |d|^2\frac{1+\langle\cos^2\theta\rangle}{2}. \tag{6.15}$$

To summarize,

$$A \propto \begin{cases} |d|^2(1-\langle\cos^2\theta\rangle) & (\mathrm{SX}\parallel\mathrm{IR}) \\ |d|^2\dfrac{1+\langle\cos^2\theta\rangle}{2} & (\mathrm{SX}\perp\mathrm{IR}). \end{cases} \tag{6.16}$$

At random alignment, $\langle\cos^2\theta\rangle$ = 1/3. Therefore, the absorbance change caused by molecular alignment $\Delta A_{\mathrm{alignment}}$ can be expressed using the static absorbance A_{static} as

$$\Delta A_{\mathrm{alignment}} = \begin{cases} A_{\mathrm{static}}(-\langle\cos^2\theta\rangle+\dfrac{1}{3}) & (\mathrm{SX}\parallel\mathrm{IR}) \\ A_{\mathrm{static}}(\dfrac{1}{2}\langle\cos^2\theta\rangle-\dfrac{1}{6}) & (\mathrm{SX}\perp\mathrm{IR}). \end{cases} \tag{6.17}$$

Figure 6.12 compares the measured (circles) and calculated (solid curves) differential absorbance of the NO 1s-2π peak (averaged from 398.7 to 400.6 eV). The calculation includes two terms: $\Delta A_{\mathrm{alignment}}$ and the absorbance decrease due to strong-field ionization. The former term is obtained by the above calculation procedure. The latter term is obtained by a sigmoid fitting of the sudden absorbance increase of the NO^+ 1s-2π peak around the delay origin. Figure 6.12 clearly shows that the calculation and the measurement are in good agreement.

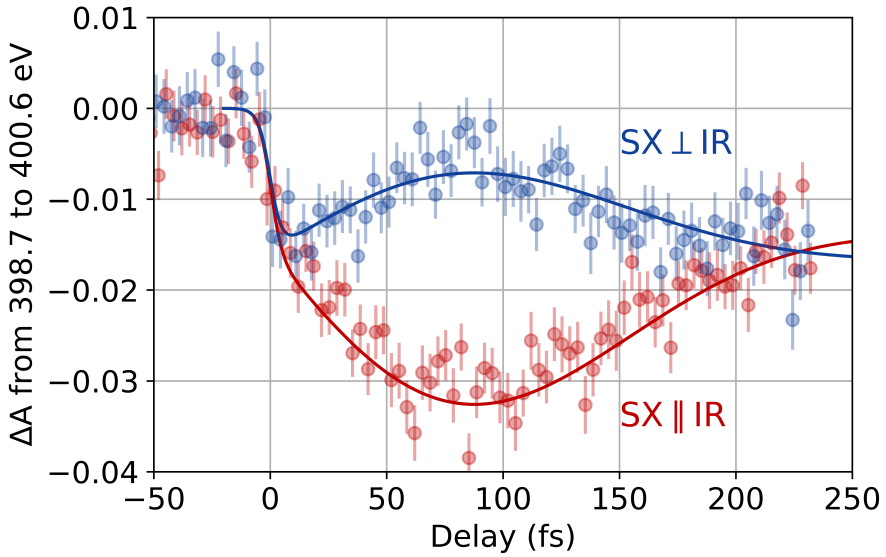

Figure 6.12: Measured (circles) and calculated (solid curves) differential absorbance of the NO 1s-2π peak averaged from 398.7 to 400.6 eV. Blue and red mean that the polarizations of the SX and the IR pulses are perpendicular and parallel, respectively.

To the best of our knowledge, the observation of rotational dynamics by XUV or SX transient absorption spectroscopy using p or d core shells has never been demonstrated so far. One of the possible reasons for this is that p or d core shells are energetically degenerate and the transition dipole moment vector from each degenerate core shell is oriented differently. In this case, $\Delta A_{\mathrm{alignment}}$ from different transitions might partially cancel with each other, resulting in a small alignment signal. However, in our case, the 1s core shell is not degenerate. Therefore, the alignment signal can be clearly observed.

6.5 Summary

In summary, we demonstrate HHG-based transient absorption spectroscopy at the N K-edge. We also demonstrate electronic, vibrational, and rotational dynamics can simultaneously be traced by transient absorption spectroscopy. This result opens up new possibilities for SX transient absorption spectroscopy as a method for the complete tracking of photoinduced chemical or physical reactions. The target sample in our experiment is a prototypical diatomic molecule, NO, but the same technique can be applied to more complex molecules in the gas phase or in solvents, where the element specificity of SX absorption can be fully utilized to understand molecular dynamics that occurs in multiple degrees of freedom at different time scales.

Chapter 7

Transient absorption spectroscopy of N_2O molecules at 400 eV

In this chapter, transient absorption spectroscopy of N_2O molecules at 400 eV is presented. As in the case of NO, electronic, vibrational, and rotational dynamics is simultaneously observed. Furthermore, each dynamics contains more complex physics, which we discuss in detail below.

7.1 Motivation

In the previous chapter, we present transient absorption spectroscopy of a simple diatomic molecule, NO, at the N K-edge. The result clearly shows the capability of our beamline for transient absorption in the water window. The next challenge is to extend the demonstrated technique to more complex systems: polyatomic molecules, liquids, and solids, where element specificity of SX pulses can be fully utilized. As a step toward this goal, we choose a triatomic molecule, N_2O, as a target. Compared to NO, N_2O has complex electronic structures and nuclear degrees of freedom, which provide rich dynamics.

7.2 Static absorption spectrum of N_2O

The static absorption spectrum of N_2O is measured before conducting transient absorption experiments. The molecular structure of N_2O is depicted in Fig. 7.1(a). The two nitrogen atoms in an N_2O molecule are called the "terminal" nitrogen N_t and the "central" nitrogen N_c. Figure 7.1(b) shows the measured (circles) and reference (dashed curve) absorbance spectra of N_2O. The pressure of N_2O is set to 0.1 bar, and the thickness of the sample gas cell is 1.5 mm. The reference curve is taken from a synchrotron measurement (total ion yield mode) [100]. The assignment of the absorption peaks is taken from the same literature. Note that the assignment for some minor absorption peaks is omitted for simplicity. Interestingly, it can be seen that there are two absorption peaks for one valence orbital. This is because N_2O has two nitrogen core shells, and their orbital energies are separated by $\sim$3.5 eV, as shown in Fig. 7.1(c). The strong peaks at 401 eV and 405 eV correspond to the transitions from the N_t 1s orbital and the N_c 1s orbital to the

3π (LUMO) orbital, respectively. The other weak peaks are transitions to the Rydberg orbitals.

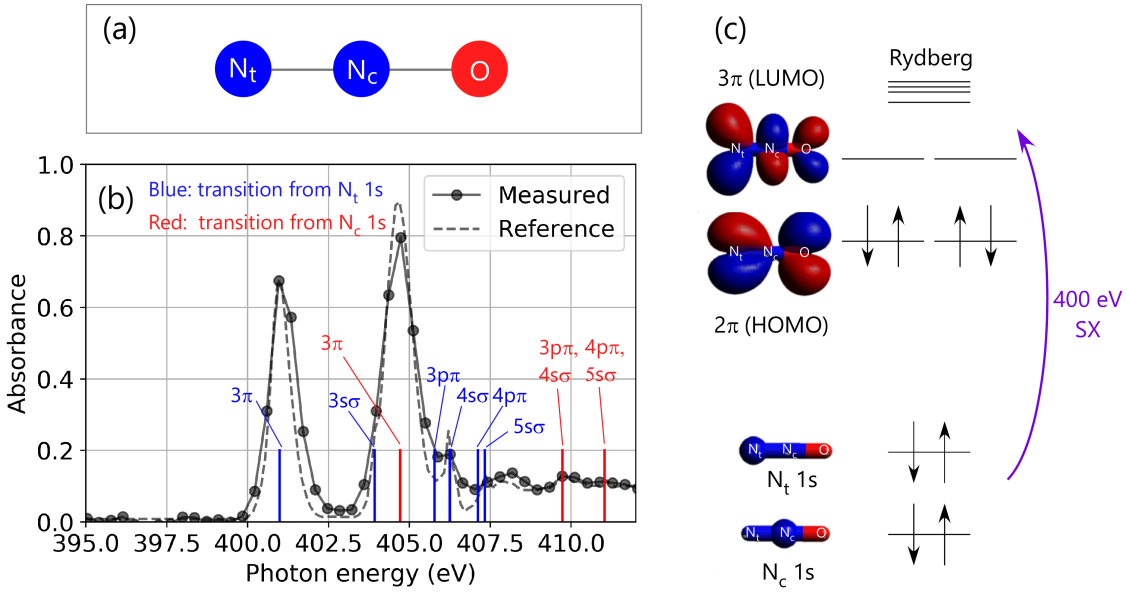

Figure 7.1: (a) Structure of an N_2O molecule. (b) Measured (circles) and reference (dashed curve) static absorbance spectrum of N_2O at the N K-edge [100]. The transition energies from the N_t and N_c 1s core levels are shown as blue and red lines, respectively. (c) Energy level diagram of N_2O.

7.3 Experimental conditions

The experimental conditions are mostly the same as transient absorption spectroscopy of NO. One difference is that the splitting ratio of the beam splitter is changed to R:T = 20:80 from R:T = 10:90 to increase the pump intensity. The pump intensity is estimated to be 2×10^{14} W/cm^2 (rounded to one significant digit) from the molecular-rotation-induced SX absorbance changes as described later in Section 7.4.3. At this intensity, the Keldysh parameter is calculated to be $\sim$0.4. The reason we increase the pump intensity is that the ionization potential of N_2O is higher than that of NO (N_2O: 12.89 eV, NO: 9.26 eV), so N_2O requires more pump intensity to be ionized. The pressure of N_2O inside the sample gas cell is set to 0.1 bar. The data acquisition procedures are the same as those for NO.

7.4 Results and discussions

Figures 7.2(a, b) show the measured transient absorption spectra of N_2O. The polarizations of the SX and the IR pulses are set to parallel in (a) and perpendicular in (b). Figure 7.2(c) plots the static absorbance spectrum of N_2O measured in our beamline (circles) and in a synchrotron facility (solid curve) [100]. The assignment of the absorption peaks is calculated by using the GAMESS software [169]. In the calculation, the molecular orbital energies are obtained by the density functional theory (DFT) with the B3LYP functional

and the 6-311+G(d) basis functions (B3LYP/6-311+G(d)). The same functional and basis functions are used for all the DFT calculations in this chapter. Then, the energy difference between the core and the valence orbitals is calculated to obtain the absorption peak positions. Because of the difficulty in treating the 1s core orbitals in the simulation, the calculated peak positions are shifted by 9.5 eV from the actual values. This shift is corrected to obtain the final peak positions. In Fig. 7.2(c), the calculated peak positions are indicated as blue lines for neutral N_2O and red lines for N_2O^+ cation.

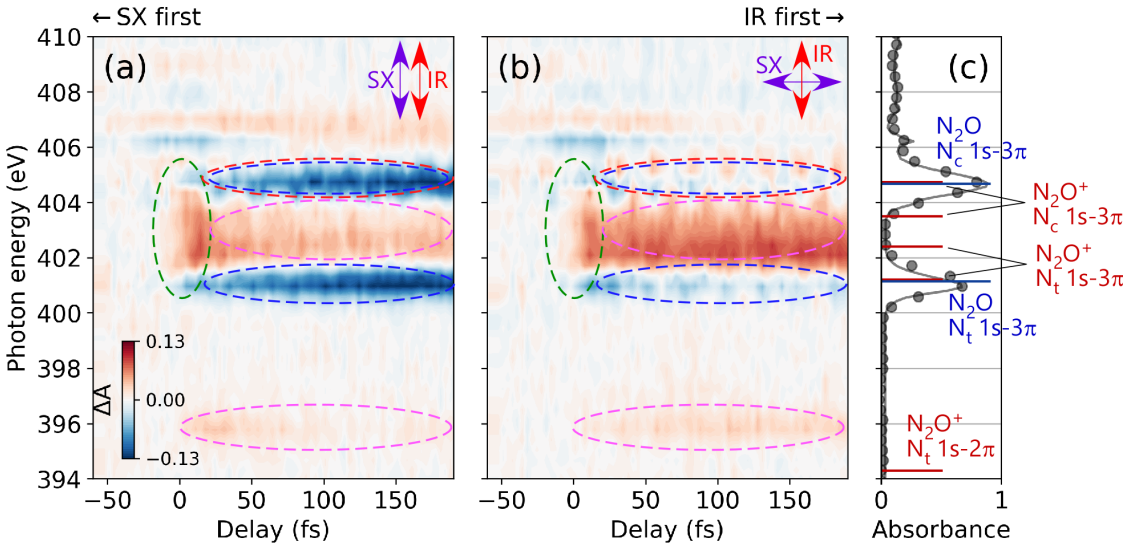

Figure 7.2: (a, b) Measured transient absorption spectra of N_2O. In (a) and (b), the polarizations of the SX and the IR pulses are parallel and perpendicular, respectively. Dashed ellipses indicate the regions where characteristic molecular dynamics is imprinted. (c) Static absorbance spectrum of N_2O measured in our beamline (circles) and in synchrotron (solid curve) [100].

As in the transient absorption spectra of NO, Figs. 7.2(a, b) contain signatures of strong-field ionization. Right after 0 fs, the absorbance of the N_2O N_c, N_t1s-3π peaks decreases, and instead, the N_2O^+ N_c, N_t1s-3π peaks and the N_2O^+ N_t1s-2π peak appears. Note that the N_2O^+ N_c1s-2π peak does not appear. This is because the transition dipole moment between the N_c1s and the 2π orbitals is small; as shown in Fig. 7.1(c), the node of the 2π orbital is located around the N_c atom, so the overlap between the N_c1s orbital and the 2π orbital is small. The ionization fraction is estimated to be 20% by comparing the measured transient absorbance with the static absorbance.

As in the case of NO, electronic, vibrational, and rotational dynamics is observed in the transient absorption spectra. The dashed ellipses in Figs. 7.2(a, b) represent the regions where these three kinds of dynamics are imprinted. In the following sections, we analyze each dynamics in detail.

Again, we do not discuss the modulation of the Rydberg peaks around 405-407 eV.

7.4.1 Attosecond time-resolved electronic dynamics

First, we describe the attosecond time-resolved electronic dynamics. Figure 7.3(a) plots the measured attosecond time-resolved transient absorption spectrum of N_2O around the delay origin. Here, the delay step is set to 400 as and the polarizations of the SX and the IR pulses are set to parallel. As in the case of NO, clear 2ω oscillations are observed. Figure 7.3(b) shows the line plots of the temporal evolutions of the changes in the differential absorbance at the N_2O $N_c1s\text{-}3\pi$ peak (404.9 eV, green), the N_2O $N_t1s\text{-}3\pi$ peak (400.8 eV, blue), and the N_2O^+ N $1s\text{-}3\pi$ peak (402.6 eV, red). Note that the photon energy region from 402 to 404 eV consists of the N_2O^+ $N_t1s\text{-}3\pi$ peak (lower energy part) and the N_2O^+ $N_c1s\text{-}3\pi$ peak (higher energy part). However, there is not a large difference in the 2ω oscillation throughout this region. Therefore, we represent the two peaks as the N_2O^+ N $1s\text{-}3\pi$ peak.

The phase of the 2ω oscillation is opposite for the N_2O^+ N $1s\text{-}3\pi$ peak to that for the N_2O $N_t1s\text{-}3\pi$ peak. This feature is similar to NO, where the phase of the 2ω oscillation is anti-correlated for the NO $1s\text{-}2\pi$ peak and the NO^+ $1s\text{-}2\pi$ peak. This again implies that the possible origin of the observed 2ω oscillation in N_2O is ground-state polarization.

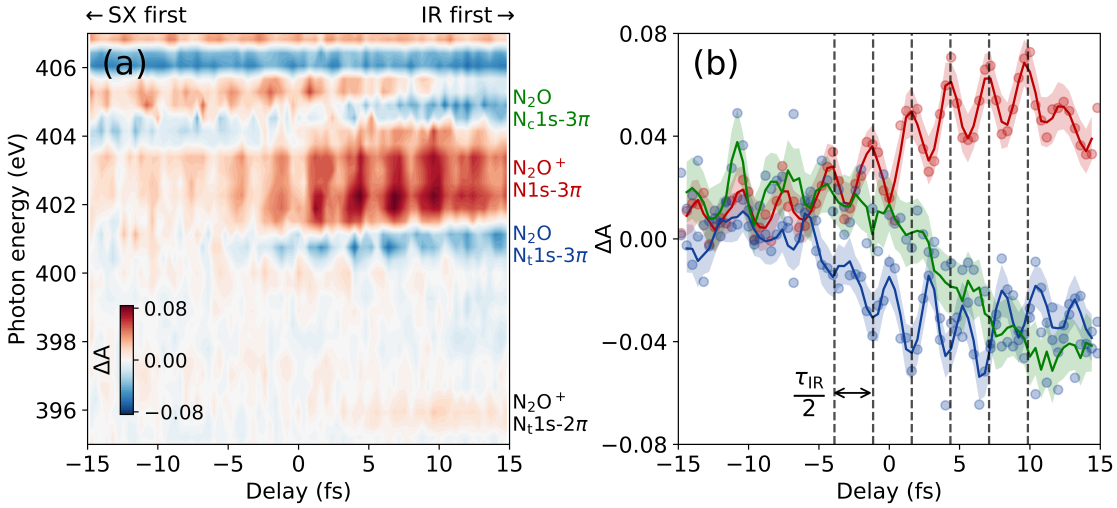

Figure 7.3: (a) Measured attosecond time-resolved transient absorption spectrum of N_2O. The positions of the absorption peaks are noted at the right side of the figure. (b) Temporal evolutions of the changes in the differential absorbance at the N_2O $N_c1s\text{-}3\pi$ peak (404.9 eV, green), the N_2O $N_t1s\text{-}3\pi$ peak (400.8 eV, blue), and the N_2O^+ N $1s\text{-}3\pi$ peak (402.6 eV, red). The circles are the raw data, and the solid curves are the 3-point moving averages. The shaded areas indicate the errors of the solid curves.

In Fig. 7.3(b), it can be seen that the 2ω oscillation exists even before the tunnel ionization process starts, but it can be explained by the fact that the ground-state polarization effect takes place at lower intensities than the tunnel ionization process [18].

Another interesting feature in N_2O is that the 2ω oscillation in the N_2O $N_t1s\text{-}3\pi$ peak and that in the N_2O $N_c1s\text{-}3\pi$ peak are largely different. As can be seen in Fig 7.3(b), the amplitude of the 2ω oscillation is much smaller in the N_2O $N_c1s\text{-}3\pi$ peak compared to the N_2O $N_t1s\text{-}3\pi$ peak. The difference becomes clearer when the 2ω oscillation components of the measured differential absorbance are extracted (Fig. 7.4).

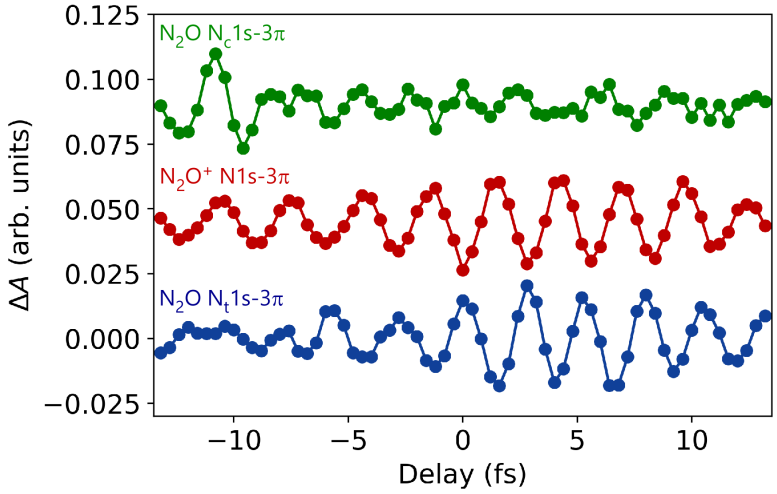

Figure 7.4: 2ω oscillation components of the differential absorbance shown in Fig. 7.3(b). The slow change in the differential absorbance (obtained by the 9-point moving average) is subtracted from the total differential absorbance (3-point moving average).

A possible origin of this phenomenon is that the N_c and the N_t 1s cores are located at different positions in an N_2O molecule; the two cores might probe the electronic dynamics at specific positions. For example, in the ground-state polarization process, it is expected that the change of the hole population is larger at the edge of the molecule than the center of the molecule. In this picture, it is natural that the 2ω oscillation probed by the N_t1s core is larger than that by the N_c1s core. However, this hypothesis is difficult to be proved by the experiment alone. Especially, there are many Rydberg peaks above 404 eV, and these peaks might affect the observed 2ω oscillations. Therefore, TDSE simulations are now in progress to elucidate the origin of the observed features.

Finally, in Fig. 7.3(b), it is visible that the the 2ω oscillations in the N_2O N_t1s-3π and the N_2O^+ N 1s-3π peaks are deviated from the perfect anti-correlation around $\sim$10 fs. Although the reason for this phenomenon is not clear yet, it is possible that a small fraction of N_2O molecules is excited to the bound excited states (e.g. Rydberg states), and it breaks the perfect anti-correlation between the population of N_2O in its ground state and that of N_2O^+.

7.4.2 Femtosecond vibrational dynamics

The molecular vibration signals are observed in the N_c, N_t1s-3π peaks of neutral N_2O. This makes a good contrast with the transient absorption spectra of NO, where the vibration of NO^+ cation, not neutral NO, is observed. This difference can be qualitatively explained by the characteristics of the HOMOs of NO and N_2O. The HOMO of NO has a node in its center, so it is an antibonding orbital. Therefore, if an electron is removed from the HOMO by tunnel ionization, the bonding is stabilized and the bond length shrinks. In fact, the equilibrium bond lengths are 1.15 Å and 1.06 Å for NO and NO^+, respectively. This shrink causes the vibration in the cation. Meanwhile, the HOMO of N_2O has a node in the NO bond, but does not have a node in the NN bond. Therefore, it has both anti-bonding and bonding nature, making it almost nonbonding [170]. Figure 7.5 shows

the equilibrium bond lengths of N_2O and N_2O^+ calculated by DFT using GAMESS. Different from NO, the change of the bond lengths is shorter than 0.01 Å. Therefore, it is expected that the molecular vibration of N_2O^+ is small.

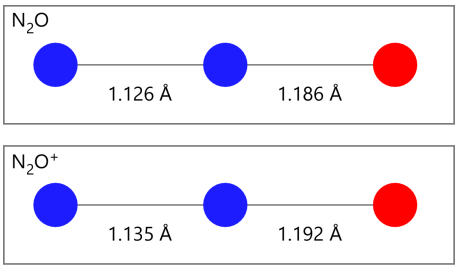

Figure 7.5: Equilibrium bond lengths of N_2O and N_2O^+ calculated by DFT.

To obtain the vibration signals from the N_2O N_c, N_t1s-3π peaks, their central photon energies are extracted using Gaussian fitting. Note that the Gaussian fitting is applied to the total absorbance, which is defined as $A_{\mathrm{static}} + \Delta A$ (A_{static}: static absorbance, ΔA: absorbance change). The obtained vibration signals are Fourier-transformed to identify the vibration modes. The result is shown in Fig. 7.6(b). N_2O has three vibrational modes as shown in Fig. 7.6(a). The observed vibrational mode is υ_1, which is the symmetric stretch between the central nitrogen atom and the oxygen atom. The other modes are not detected within the current signal-to-noise ratio level. Furthermore, it is found that the vibration signal is strong in the N_c1s-3π peak, but weak in the N_t1s-3π peak.

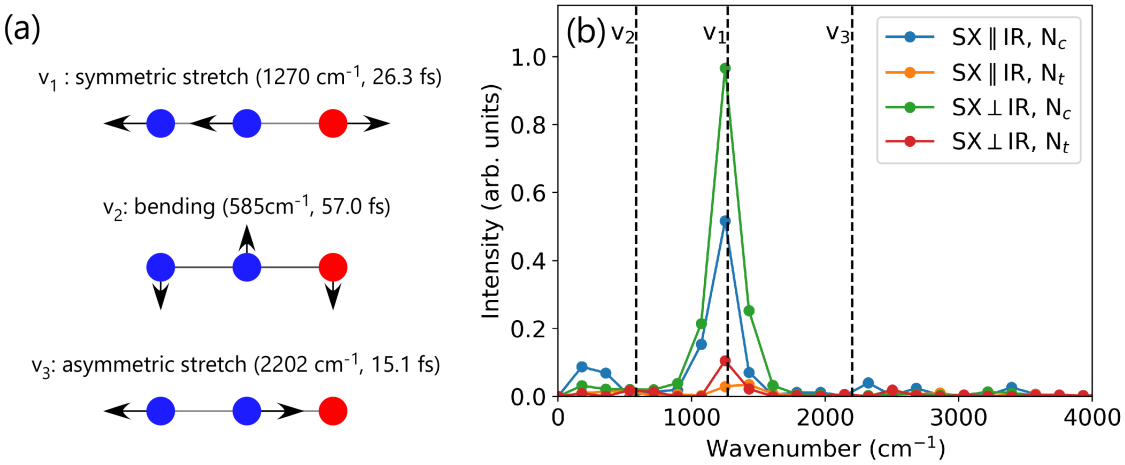

Figure 7.6: (a) Vibrational modes of N_2O [171]. (b) Fourier-transformed vibration signals at the N_c, N_t1s-3π peaks.

Next, in order to obtain the initial phase of the vibration, a cosine fitting is applied to the temporal evolution of the extracted central photon energy of the N_c1s-3π peak. Figure 7.7 plots the result of the fitting. Here, the delay origin is determined by a sigmoid fitting of the temporal evolutions of the peak heights of the N_2O N_c, N_t1s-3π peaks and the N_2O^+ N_c, N_t1s-3π peaks. The initial phase of the vibration is determined to be (0.00±0.07)π rad and (0.17±0.05)π rad for the parallel and perpendicular SX and IR polarizations, respectively. This indicates that the initial phase is close to "cosine-like."

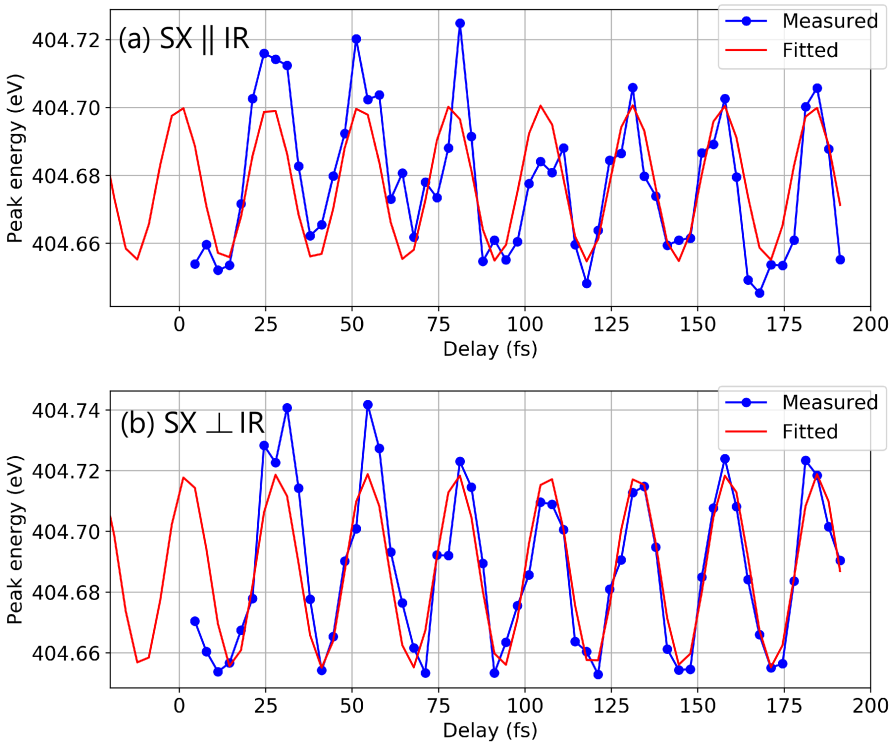

Figure 7.7: Temporal evolutions of the central energies of the N_c1s-3π peak with the polarizations of the IR and the SX pulses (a) parallel and (b) perpendicular. Blue circles are the measured data, and the red curves are the results of cosine fitting.

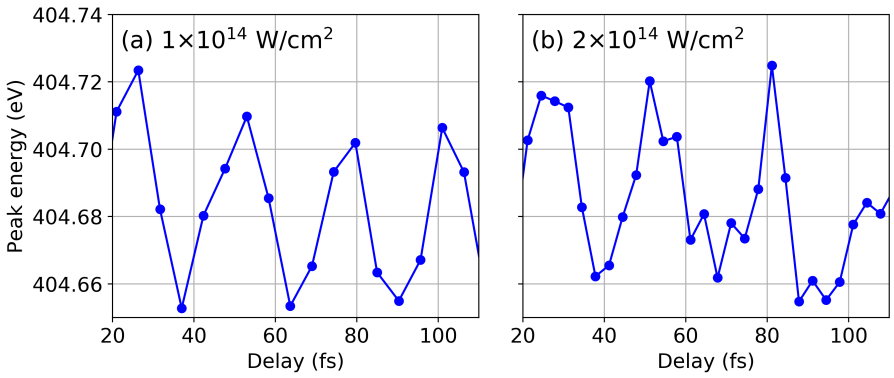

Figure 7.8: Temporal evolutions of the central energies of the N_c1s-3π peak with a pump intensity of (a) 1×10^{14} W/cm^2 and (b) 2×10^{14} W/cm^2. The polarization between the IR and the SX is set to parallel.

The pump intensity dependence of the vibration signal is also investigated by performing a transient absorption measurement with a reduced pump intensity of 1×10^{14} W/cm^2. Figure 7.8 shows the comparison of the vibration signals obtained with 1×10^{14} W/cm^2 and 2×10^{14} W/cm^2 pump intensities. It is observable that, even though the pump intensity is changed by twice, the observed vibration amplitude does not change so much ($\sim$25 meV for both intensities).

Identifying the mechanism of vibration

There are three mechanisms which can trigger molecular vibration in a neutral molecule irradiated by a strong, ultrashort laser pulse: Lochfraß, bond softening, and impulsive stimulated Raman scattering (ISRS) [88]. Figure 7.9 depicts schematics of the three mechanisms. Firstly, Lochfraß is so-called the "R-dependent ionization" mechanism. Because the ionization potential of a molecule is dependent on the bond length, some part of the ground state vibrational wave packet is easy to be ionized while the other part is not. As a result, when the molecule is tunnel-ionized, the wave packet left in the neutral molecule is displaced from its equilibrium position, thus starts vibration. Secondly, in bond softening, the potential energy curve of the neutral molecule is distorted by the strong laser field, and the ground state wave packet moves along the distorted potential energy curve. After the laser pulse is gone, the displaced wave packet starts vibration. Lastly, ISRS is a special case of the stimulated Raman scattering process. The laser photon excites the neutral molecule to a virtual state, and another photon with lower photon energy brings it to a vibrationally excited state. These photons come from one laser pulse, as the laser pulse is ultrashort and its spectrum is broad.

Among these three mechanisms, bond softening and ISRS describe the same phenomenon in different pictures [172]. Bond softening treats the laser pulse as a quasistatic electric field while ISRS treats it as photons. Because ISRS includes only the two-photon process, it is valid only when the laser is not so strong. On the other hand, bond softening is valid for a strong, low frequency laser field.

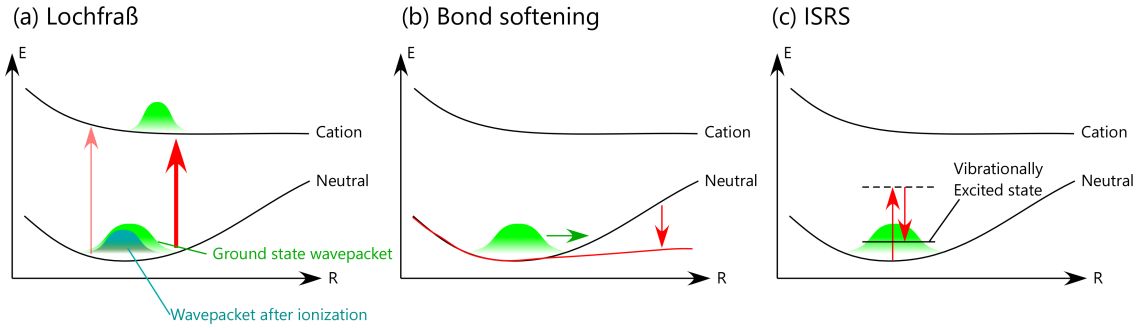

Figure 7.9: Possible mechanisms of vibration in a neutral molecule. (a) Lochfraß, (b) bond softening, and (c) ISRS. R and E represent the bond length and the potential energy, respectively.

The three mechanisms can be distinguished by several characteristics. First, Lochfraß has a "cosine-like" initial phase while bond softening and ISRS have a "sine-like" initial phase. Second, when the pump intensity is increased, the vibration amplitude of bond softening and ISRS increases. However, in the case of Lochfraß, the vibration amplitude

does not necessarily increase [173]. This is because as the pump intensity becomes higher, the ionization potential dependence of the tunnel ionization rate becomes weaker. In our experiment, the observed initial phase is close to "cosine-like." Also, the vibration amplitude does not change so much when the pump intensity is changed. These facts indicate that the mechanism of the vibration is Lochfraß.

To numerically reproduce the experimentally observed vibration, a simulation of Lochfraß is performed. First, the potential energy curve of N_2O $E_{\mathrm{neutral}}(R)$ and that of N_2O^+ $E_{\mathrm{cation}}(R)$ are calculated along the normal coordinate of each vibrational mode R by using DFT. Here, R is scaled so that $E_{\mathrm{neutral}}(R)$ matches the harmonic potential $M\omega_0^2R^2/2$ (M: reduced mass, ω_0: vibration angular frequency) around the equilibrium position. By using $E_{\mathrm{neutral}}(R)$, the probability density of the vibrational ground state of N_2O $P_{\mathrm{gs}}(R)$ is first calculated (blue dashed curves in Figs. 7.10(a-c)). Note that the vibrationally excited states are not populated at room temperature before tunnel ionization. Then, the R-dependent ionization potential is obtained as $I_p(R) = E_{\mathrm{cation}}(R) - E_{\mathrm{neutral}}(R)$ (black dashed curves in Figs. 7.10(a-c)), and the R-dependent ionization rate, $w(R)$ is calculated by using the molecular ADK model [137]. Here, the laser intensity is set to 2×10^{14} W/cm^2. The probability density of the tunnel-ionized vibrational wave packet $P_{\mathrm{ion}}(R)$ is then calculated as $P_{\mathrm{ion}}(R) = P_{\mathrm{gs}}(R)w(R)$ (red curves in Figs. 7.10(a-c)). The wave packet left in the neutral molecule after ionization $P_{\mathrm{left}}(R)$ is calculated as $P_{\mathrm{left}}(R) = P_{\mathrm{gs}}(R) - rP_{\mathrm{ion}}(R)$, where r is a constant to match the ionization fraction to 20%. Then, the centers of mass of $P_{\mathrm{gs}}(R)$ and $P_{\mathrm{left}}(R)$, R_{gs} and R_{left}, are calculated. From these calculations, the spatial displacement of $P_{\mathrm{left}}(R)$ from the equilibrium position is obtained as $\Delta R_{\mathrm{Lf}} = R_{\mathrm{left}} - R_{\mathrm{gs}}$. This ΔR_{Lf} represents the vibration amplitude by Lochfraß. In the actual experiment, because the IR pulse has a finite pulse duration, the vibration is smeared to some extent. Assuming that the intensity of the IR pulse is proportional to $e^{-(t/\tau)^2}$, the smeared vibration amplitude $\Delta R'_{\mathrm{Lf}}$ is calculated as $\Delta R'_{\mathrm{Lf}} = \Delta R_{\mathrm{Lf}} e^{-\tau^2\omega_0^2/4}$, where ω_0 is the angular frequency of the vibration. Here, τ is set to $10/2\ln 2 = 7.2$ fs. In order to compare the measurement and the calculation, it is necessary that the smeared vibration amplitude $\Delta R'_{\mathrm{Lf}}$ is mapped to the SX absorption energy. To do so, the R-dependent central photon energies of the N_c, N_t1s-3π peaks are calculated (Figs. 7.10(d-i)). By using $\Delta R'_{\mathrm{Lf}}$ and the R-dependent central photon energies of the N_c, N_t1s-3π peaks, the amplitude of the vibration of the central photon energy of the N_c1s-3π peak $\Delta E_{\mathrm{Lf,\,c}}$ and that of the N_t1s-3π peak $\Delta E_{\mathrm{Lf,\,t}}$ are obtained.

Table 7.1 summarizes the results of the calculations. As observed in the experiment, the v_1 mode at the N_c1s-3π peak has the largest vibration amplitude. Figure 7.11 plots the ratios of the vibration intensities ($\propto \Delta E^2_{\mathrm{Lf,\,Nc}}$ and $\Delta E^2_{\mathrm{Lf,\,Nt}}$) of the v_1, v_2, and v_3 modes. The calculated intensity ratios agree well with Fig. 7.6(b). Also, the initial phase of the vibration is consistent with the experiment; the vibration starts from the high-photon-energy side. However, compared to the experiment, the calculated vibration amplitude of the v_1 mode at the N_c1s-3π peak is very small. The calculated value is 0.77 meV while the observed value is 25 meV. This large discrepancy indicates that some of the assumptions in the calculations, as listed in the next paragraph, are not valid.

Although we do not identify the correct reason for the discrepancy, there are several possible reasons. First, the modifications of the potential energy curves under the strong electric field may change the vibration amplitudes. To investigate this effect, we calculate $\Delta E_{\mathrm{Lf,\,Nc}}$ of the v_1 mode under a static electric field of 390 MV/cm (corresponding to

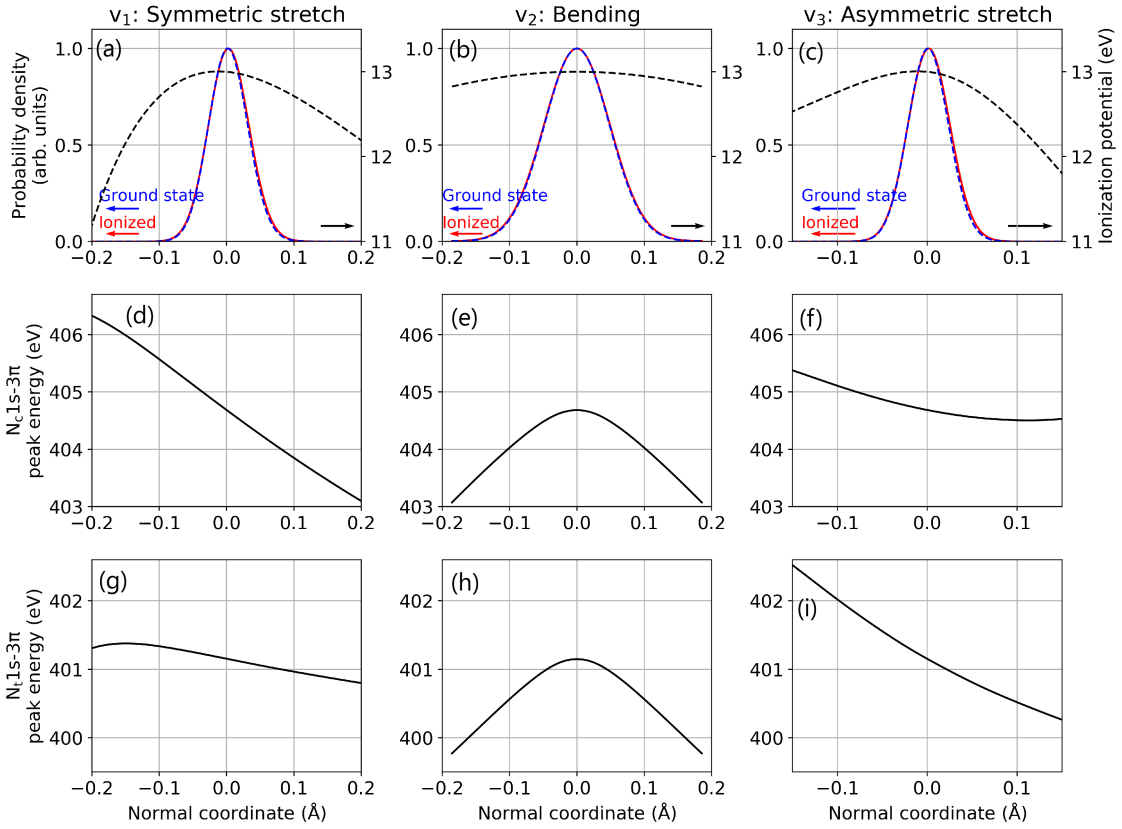

Figure 7.10: Simulation of Lochfraß for the three vibrational modes (v_1, v_2, v_3). (a-c): Ground state wave packets in neutral N_2O (blue dashed curve) and tunnel-ionized wave packets (red solid curve). Ionization potentials are also shown (black dashed curve). (d-f): Central photon energies of the N_c1s-3π peak. (g-i): Central photon energies of the N_t1s-3π peak.

Table 7.1: Calculated vibration amplitudes by Lochfraß. For the v_1 mode, the experimentally measured $\Delta E_{\mathrm{Lf,\,Nc}}$ is also shown.

Vibrational mode	$\Delta R'_{\mathrm{Lf}}$ (pm)	$\Delta E_{\mathrm{Lf,\,Nc}}$ (meV)	$\Delta E_{\mathrm{Lf,\,Nt}}$ (meV)
v_1 Symmetric stretch	-0.0088	0.77 (Experiment: 25)	0.17
v_2 Bending	0	0	0
v_3 Asymmetric stretch	-0.0018	0.057	0.13

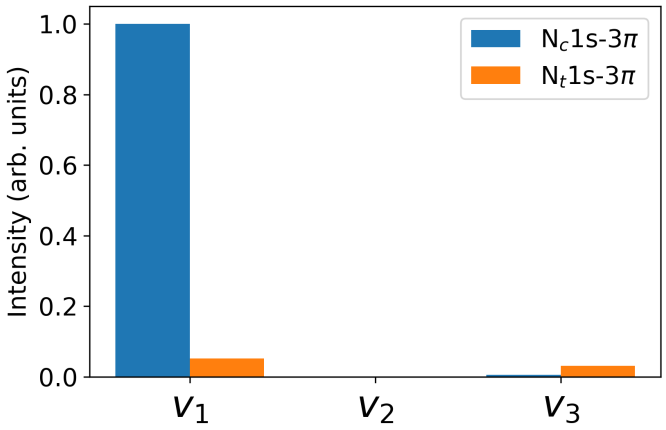

Figure 7.11: Calculated relative intensity of the vibration for each mode.

2×10^{14} W/cm^2 in intensity). The calculation procedure is as follows. First, the potential energy curves of N_2O and N_2O^+ under the static electric field are calculated by using DFT. The angle between the electric field and the molecular axis is set to the average angle of the ionizion anisotropy (37°) calculated by the molecular ADK theory. Then, using the obtained potential energy curves, ΔR_{Lf} is calculated by the same procedure presented above. Finally, ΔR_{Lf} is converted to $\Delta E_{\mathrm{Lf,\,Nc}}$ using the R-dependent central photon energies of the N_c1s-3π peaks. Here, the R-dependent central photon energies of the N_c1s-3π peaks are calculated without applying the static electric field. As a result, $\Delta E_{\mathrm{Lf,\,Nc}}$ under the static electric field is calculated to be 1.2 meV. However, this amplitude is still much smaller than the measured value. Therefore, the modifications of the potential energy curves by the strong electric field is not the main reason for the discrepancy between the measured and the calculated $\Delta E_{\mathrm{Lf,\,Nc}}$. Second, the molecular ADK model might not be accurate enough. Because the ionization potential dependence of the tunnel ionization rate strongly affects the vibration amplitude of Lochfraß, the choice of the tunnel ionization model is important. A more rigorous model such as weak-field asymptotic theory (WFAT) [174] and TDSE might improve the accuracy of the calculation. Finally, the SX transition energy is currently calculated as the difference between the 3π orbital energy and the core orbital energy. However, this transition energy does not necessarily match the energy difference between the ground state and the core-excited state. The core-excited state should be properly treated in the calculation.

7.4.3 Sub-picosecond rotational dynamics

Finally, we describe the rotational dynamics. As in the case of NO, rotational dynamics, or molecular alignment, is reflected in the polarization dependence of the transient absorption spectra. In N_2O, molecular alignment signals are found in both neutral N_2O and N_2O^+ cation.

Molecular alignment of neutral N_2O

First, the molecular alignment dynamics of neutral N_2O is discussed. Circles in Fig. 7.12 plot the measured temporal evolutions of the changes in the differential absorbance

at the N_2O N_c1s-3π peak (averaged from 404.3 to 405.1 eV) and that at the N_2O N_t1s-3π peak (averaged from 400.6-401.3 eV). It is visible that the absorbance changes are clearly dependent on the polarizations. To reproduce the observed transient absorbance, a simulation of molecular alignment is performed. The simulation procedure is the same as that of NO. The polarizability anisotropy and the rotational constant are set to 3.222 Å^3 and 0.4189 cm^{-1}, respectively [175]. The IR pulse used in the simulation has 10-fs FWHM pulse duration. The peak intensity of the IR pulse is chosen to be 2.1×10^{14} W/cm^2 such that the calculated molecular-rotation-induced absorbance changes fit the experimental data. The calculated degrees of alignment are plotted in Fig. 7.13. The calculated absorbance changes are plotted as solid curves in Fig. 7.12.

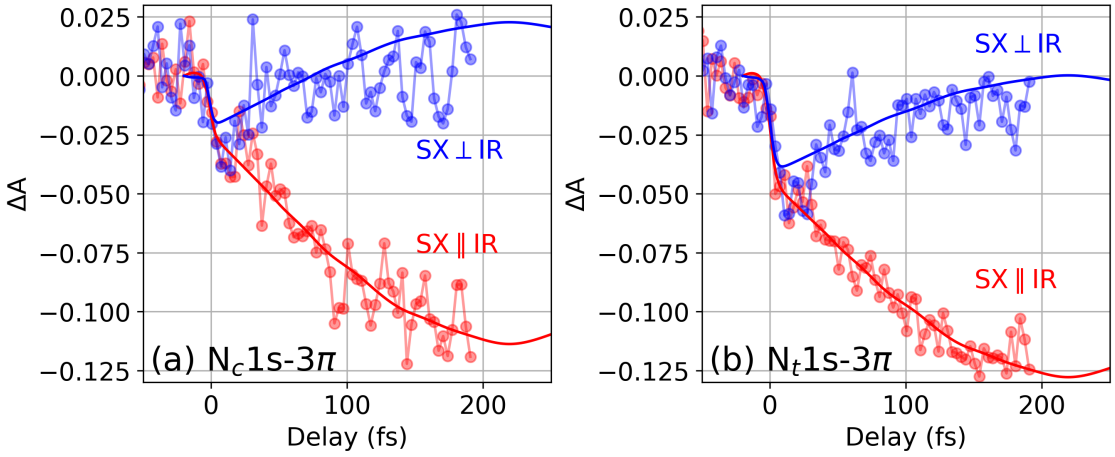

Figure 7.12: Temporal evolutions of the changes in the differential absorbance at (a) the N_2O N_c1s-3π peak (404.3-405.1 eV) and (b) the N_2O N_t1s-3π peak (400.6-401.3 eV). Circles are the measured data and the solid curves are the calculated data. Blue and red mean that the polarizations of the SX and the IR pulses are perpendicular and parallel, respectively.

Molecular alignment of N_2O^+ cation

Figure 7.14 shows the temporal evolutions of the changes in the differential absorbance at the N_2O^+ N 1s-3π peak (averaged from 401.7 to 403.6 eV). As in the case of neutral N_2O, a clear polarization dependence is observed, implying that molecular alignment of N_2O^+ takes place. This polarization dependence is further investigated by a transient absorption measurement with a long delay scan. Figure 7.15 shows the result. The polarization dependence is the largest around 100-200 fs, and then disappears after ∼400 fs. Note that the maximum absorbance change in Fig. 7.15 is smaller than that in Fig. 7.14, but this is due to a small difference in the pump intensity because of a slight misalignment of the beamline.

From the observed alignment signal of N_2O^+ cation, its degree of alignment is estimated to be very high compared to neutral N_2O. For example, in the case of neutral N_2O, the absorbance change caused by molecular alignment is ∼0.1 in the case of the parallel polarization, and it corresponds to ∼25% of the total absorbance. Therefore, the change in the degree of alignment in neutral N_2O is ∼25%. However, in the case

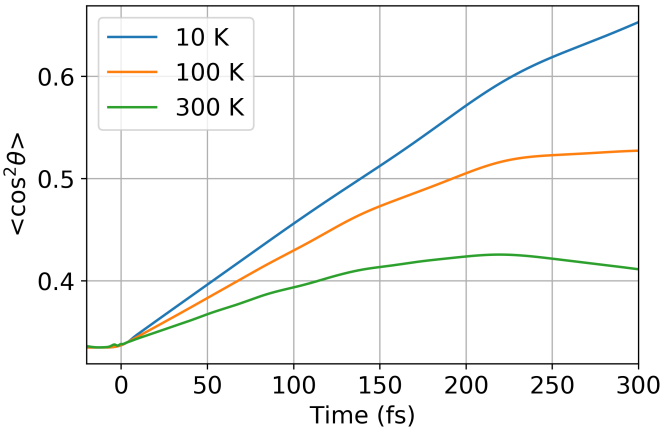

Figure 7.13: Calculated degrees of alignment of NO molecules at various temperatures irradiated with an IR pulse (pulse duration: 10 fs FWHM, peak intensity: 2.1×10^{14} W/cm^2).

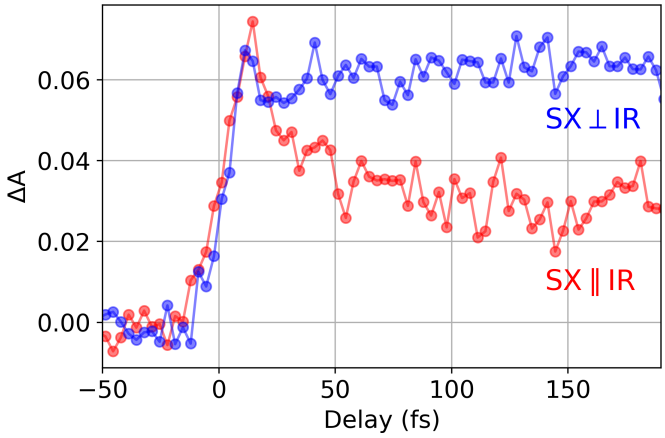

Figure 7.14: Measured temporal evolutions of the changes in the differential absorbance at the N_2O^+ N 1s-3π peak (401.7-403.6 eV).

of N_2O^+ cation, between the parallel and the perpendicular polarizations, the measured absorbance changes differ by up to ∼0.03, and it corresponds to ∼50% of the total absorbance. Therefore, assuming that the polarization dependence of the absorbance changes is purely due to the molecular alignment dynamics, the change in the degree of alignment is estimated to be ∼50%.

In order to explain the observed molecular alignment signal of N_2O^+, a simulation is performed. Different from a neutral molecule, it is expected that the alignment process of a molecular cation is strongly affected by the anisotropy of tunnel ionization. Therefore, a calculation procedure to incorporate the tunnel ionization anisotropy is developed. Figure 7.16 shows the concept of the developed calculation procedure.

First, a rotational state with specific rotational quantum numbers J_i, M_i is prepared (Fig. 7.16(a)). The wave function of this state is a spherical harmonic function $Y_{J_i,M_i}(\theta,\phi)$. Then, the wave function of the tunnel-ionized rotational state $\Psi_{\mathrm{ion},J_i,M_i}(\theta,\phi)$

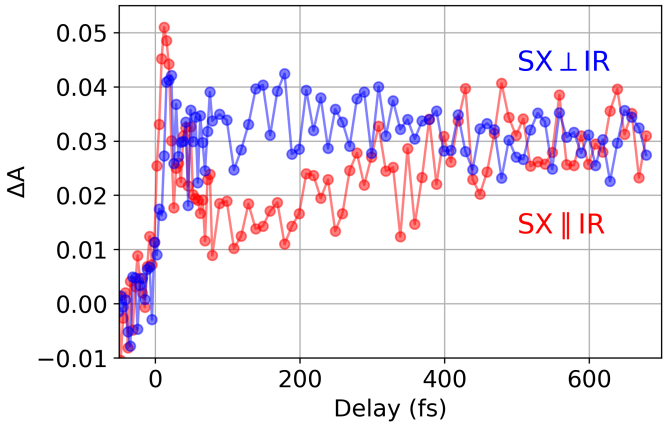

Figure 7.15: Measured temporal evolutions of the changes in the differential absorbance at the N_2O^+ N 1s-3π peak (401.7-403.6 eV) with a long delay scan.

is calculated as

$$\Psi_{\mathrm{ion},J_i,M_i}(\theta,\phi) = \sqrt{w(\theta)}Y_{J_i,M_i}(\theta,\phi), \tag{7.1}$$

with $w(\theta)$ being the angle-dependent tunnel ionization rate calculated by the molecular ADK model. Here, because N_2O is an asymmetric molecule, the tunnel ionization rate is not symmetric; $w(\theta) \neq w(\pi-\theta)$. However, in the current experiment, the laser field does not distinguish this asymmetry for a molecular ensemble. Therefore, in the calculation, $w(\theta)$ is symmetrized as $(w(\theta)+w(\pi-\theta))/2$. The symmetrized tunnel ionization rate for N_2O is shown in Fig. 7.17. $\Psi_{\mathrm{ion},J_i,M_i}(\theta,\phi)$ is then expanded by the spherical harmonics to obtain its state vector (Fig. 7.16(b)):

$$|\Psi_{\mathrm{ion}}\rangle = \sum_{J,M} c_{\mathrm{ion},J_i,M_i,J,M}\,|J,M\rangle\,. \tag{7.2}$$

Then, the TDSE for the Hamiltonian in Eq. (6.8) is solved with $|\Psi_{\mathrm{ion}}\rangle$ as the initial state. Here, the IR pulse drives molecular alignment via the interaction between the induced dipole moment and the laser electric field (Fig. 7.16(c)). In an actual molecule, this process and the tunnel ionization process take place simultaneously, but in the calculation, it is assumed that tunnel ionization occurs first. This assumption is reasonable because the pulse duration of the IR pulse is much shorter than the time scale of the molecular alignment process. When solving the TDSE, the rotational constant of N_2O^+ is set to 0.41158 cm^{-1} [176]. The polarizability anisotropy of N_2O^+ is set to 2.64 Å^3 which is obtained from a DFT calculation in GAMESS (the literature value of the polarizability anisotropy could not be found). The intensity and the pulse duration of the IR pulse are set to 2.1×10^{14} W/cm^2 and 10 fs, respectively. Here, the intensity is set to the same as that in the calculation of the molecular alignment of neutral N_2O. The above procedure is repeated for a sufficiently large set of J_i, M_i (every J_i, M_i with $J_i < 50$), and the degrees of alignment are calculated by using Eq. (6.10).

Figure 7.18 plots the calculated degrees of alignment of N_2O^+ at 300 K. The blue curve takes the ionization anisotropy into account while the orange curve ignores it. It demonstrates that the ionization anisotropy significantly increases the degree of alignment.

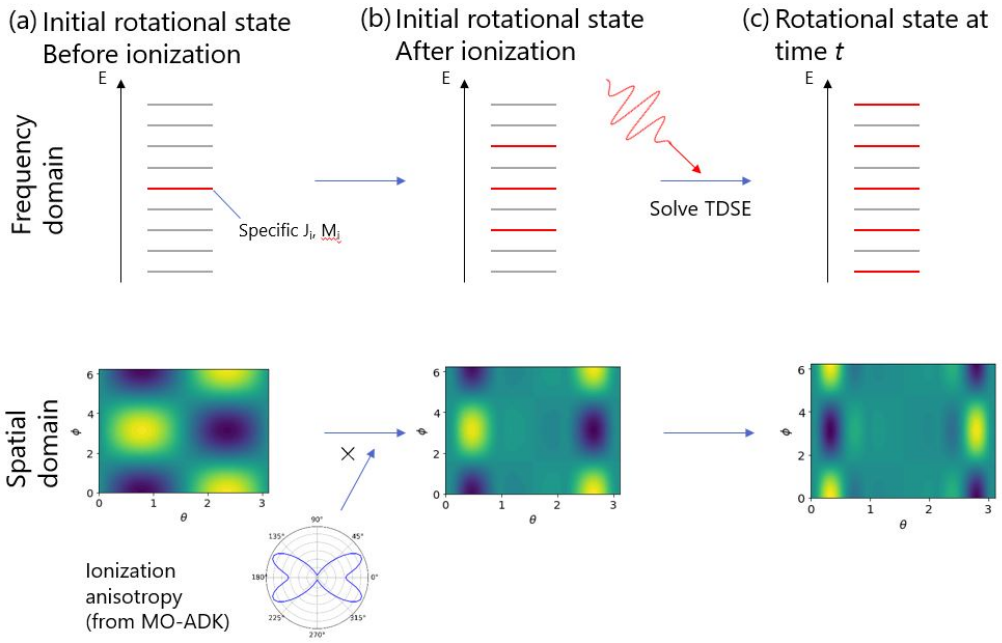

Figure 7.16: Concept of the simulation procedure of the molecular alignment process of a molecular cation incorporating anisotropic tunnel ionization.

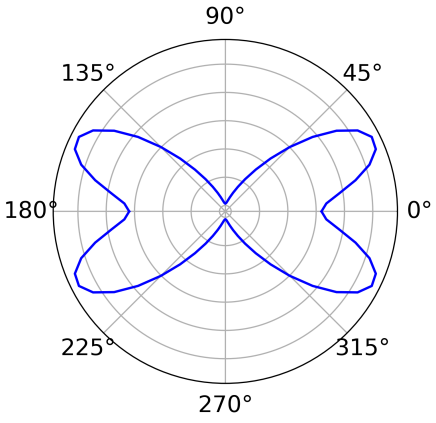

Figure 7.17: Calculated tunnel ionization rate of N_2O as a function of the angle between the molecular axis and the laser electric field. The intensity of the field is set to 2×10^{14} W/cm^2.

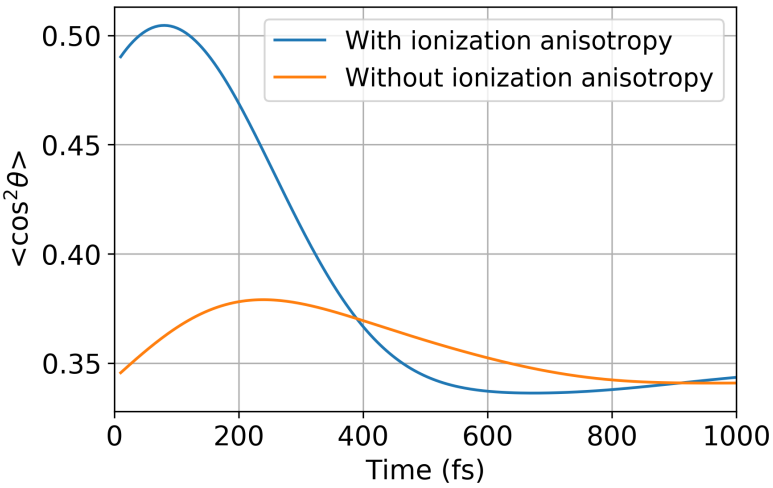

Figure 7.18: Calculated degrees of alignment of N_2O^+ at 300 K. Blue curve takes the ionization anisotropy into account while the orange curve ignores it.

From the calculated degree of alignment, the changes in the differential absorbance at the N_2O^+ N 1s-3π peak are calculated by using Eq. (6.16). Here, the overall height of the calculated absorbance is manually scaled to obtain the best fit to the experimental data. Figure 7.19 shows the result. The calculated data which incorporates the ionization anisotropy qualitatively agrees with the experiment. Meanwhile, if the ionization anisotropy is not taken into account, the polarization dependence of the transient absorbance is significantly underestimated. This result indicates that ionization anisotropy plays an important role in the molecular alignment process of molecular cations.

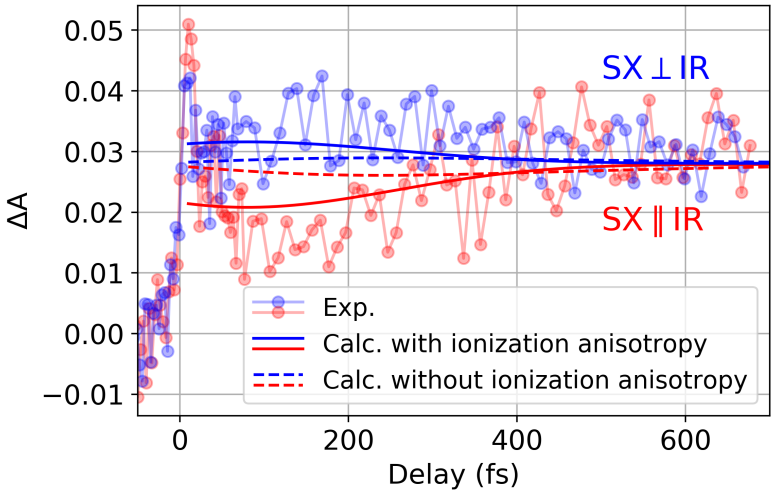

Figure 7.19: Comparison of the measured and the calculated changes in the differential absorbance at the N_2O^+ N 1s-3π peak. Circles are the measured data. Solid curves and dashed curves are the calculated data with and without incorporating the ionization anisotropy, respectively.

We note that around the delay origin of Fig. 7.19, there is a relatively large discrepancy

between the calculation and the experiment: in the experiment, ΔA is almost the same for the parallel and the perpendicular polarizations, but in the calculation, ΔA is smaller for the parallel polarization than the perpendicular polarization. The reason for this discrepancy is still under investigation. Some physics which is not considered in our calculation, such as quantum entanglement, might be a possible reason.

We also note that the alignment signal of NO^+ is smaller than that of N_2O^+. This can be explained by the ionization anisotropy of NO. As shown in Fig. E.1 in Appendix E, the ionization yield of NO is peaked at $\theta \sim 45°$, while that of N_2O is peaked at $\theta \sim 30°$. Therefore, the degree of alignment of NO^+ after tunnel ionization is closer to that of randomly oriented molecules compared to N_2O^+.

Molecular alignment signal at the N_2O^+ N_t1s-2π peak

Interestingly, the molecular alignment signal at the N_2O^+ N_t1s-2π peak and that at the N_2O^+ N 1s-3π peak are largely different, even though these two peaks originate from the same cation species. Figure 7.20 plots the temporal evolutions of the changes in the differential absorbance of the N_2O^+ N 1s-2π peak (averaged from 395.4 to 396.1 eV). It is visible that, for the perpendicular polarization, ΔA slowly increases for the first ~50 fs. This behavior is different from the N_2O^+ N_t1s-3π peak, where ΔA instantaneously increases around the delay zero (Fig. 7.14).

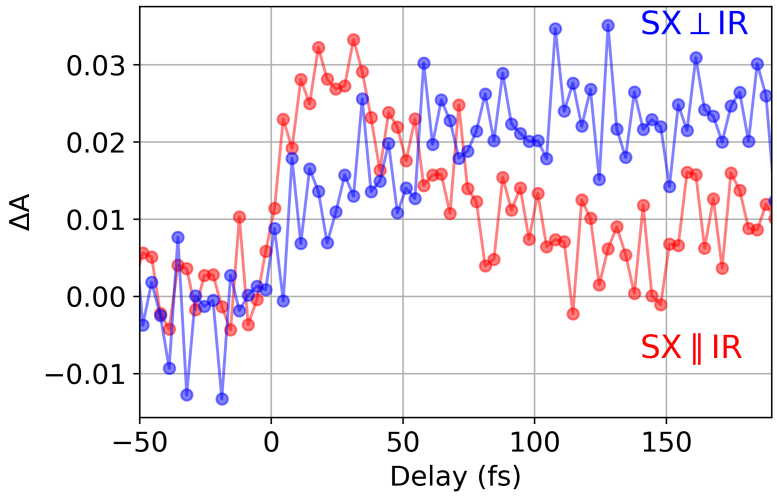

Figure 7.20: Measured temporal evolutions of the changes in the differential absorbance at the N_2O^+ N_t1s-2π peak (395.4-396.1 eV).

This phenomenon can be explained by the selective tunnel ionization and the following hole redistribution process as depicted in Fig. 7.21.

First, in the tunnel ionization process, an electron in the $2\pi_x$ orbital is selectively removed (Fig. 7.21(a)), where the $2\pi_x$ orbital is defined as an orbital whose wave function is symmetric with respect to the IR polarization. The reason for the selective ionization is that the robes of the $2\pi_y$ orbital are antisymmetric with respect to the polarization of the IR pulse and the tunnel-ionized electron wave packet from these robes destructively interferes, resulting in a complete suppression of ionization. Due to this selective ionization, at the delay origin, the electron excitation from the N_t1s to the

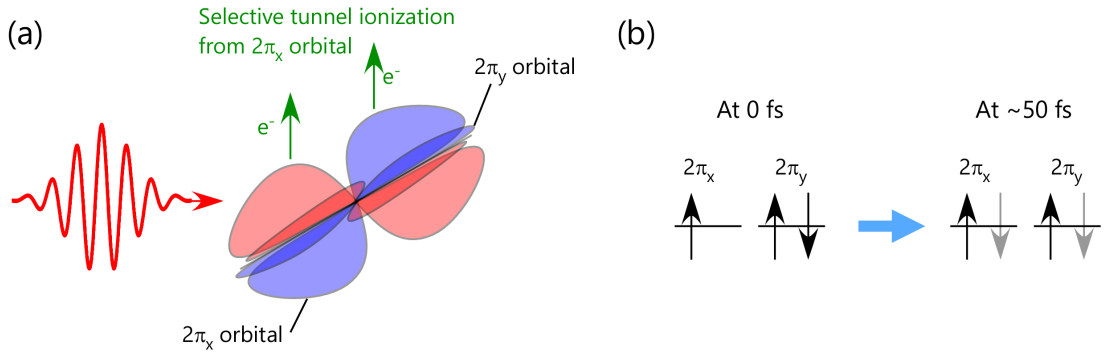

Figure 7.21: Possible mechanism which explains the temporal evolutions of the changes in the differential absorbance at the N_2O^+ N_t1s-2π peak. (a) An electron in the $2\pi_x$ orbital is selectively tunnel ionized. (b) After ionization, the hole in the $2\pi_x$ orbital partially hops to the $2\pi_y$ orbital, and the hole populations in the two orbitals become the same.

$2\pi_x$ orbital is allowed while the electron excitation from the N_t1s to the $2\pi_y$ orbital is completely suppressed. The SX absorbance A in such a situation can be formulated as follows. Let $(\sin\theta\cos\phi, \sin\theta\sin\phi, \cos\theta)$ be the molecular axis vector, and $(0, 0, 1)$ be the IR polarization vector. Again, note that the definition of the coordinates is different from that in Chapter 4. Here, it is assumed that the IR polarization axis is fixed to the z axis, and the laser propagation axis is fixed to the y axis. Then, the dipole moment of the N_t1s-$2\pi_x$ transition is $\boldsymbol{d} = |d|(-\cos\theta\cos\phi, -\cos\theta\sin\phi, \sin\theta)$. When the polarizations of the SX and the IR are parallel and perpendicular, the SX polarization vector $\boldsymbol{e}_{SX}$ can be written as $(0, 0, 1)$ and $(1, 0, 0)$, respectively. Therefore, the SX absorbance A is calculated to be

$$A \propto \begin{cases} |d|^2 \langle \sin^2\theta \rangle = |d|^2(1 - \langle \cos^2\theta \rangle) & (\text{SX} \parallel \text{IR}) \\ |d|^2 \langle \cos^2\theta \cos^2\phi \rangle = |d|^2 \dfrac{\langle \cos^2\theta \rangle}{2} & (\text{SX} \perp \text{IR}). \end{cases} \tag{7.3}$$

Compared to Eq. (6.16), the calculated absorbance in Eq. (7.3) is smaller for the perpendicular polarization, while it is the same for the parallel polarization. This is fully consistent with the observed behavior of the transient absorbance of the N_2O^+ N_t1s-2π peak around the delay origin (Fig. 7.20).

After tunnel ionization, the hole created in the $2\pi_x$ orbital can hop to the $2\pi_y$ orbital via, for example, electron-electron interaction. Because the $2\pi_x$ and the $2\pi_y$ orbitals are equivalent after the IR pulse is gone, the hole populations in these two orbitals are expected to become the same after a sufficient time (Fig. 7.21(b)). Once this hole redistribution process is completed, the SX absorption can be described by Eq. (6.16). Therefore, for the perpendicular polarization, it is expected that the SX absorption increases as the delay increases, which is consistent with the experimental observation.

7.5 Summary

In summary, we perform transient absorption spectroscopy of a triatomic molecule, N_2O, at the N K-edge. Electronic, vibrational, and rotational dynamics is simultaneously

observed as in the case of NO. Furthermore, to the best of our knowledge, we observe novel phenomena which have never been accessed by other techniques: intramolecular position-specific electronic dynamics and molecular alignment dynamics of ions. Although we still need further discussions and theoretical simulations, we believe these observations will contribute to deepen the understandings of ultrafast dynamics of molecules in strong laser fields.

Chapter 8

Conclusion and Outlook

8.1 Conclusion

In this study, we develop an SX beamline for HHG and transient absorption which is equipped with an efficient HHG system and an attosecond delay stabilization system. By using the developed beamline, we generate HHs in the water window region driven by long-wavelength IR pulses, and apply them to transient absorption spectroscopy of NO and N_2O molecules at the N K-edge (400 eV). The measured transient absorption spectra contain rich physics of ultrafast electron and nuclear motions. Especially, in N_2O, we observe novel phenomena such as intramolecular position-specific electronic dynamics and molecular alignment dynamics of ions. We believe that these results extend the frontier of attosecond science in the SX region, and will be a base to apply attosecond transient absorption measurements to more complex systems such as biomolecules and photocatalysis in liquid or solid phases.

8.2 Outlook

Improvement of the beamline

We plan two major upgrades of the HHG and the transient absorption beamline.

First, the X-ray spectrometer is planned to be replaced with a new one with a high energy resolution. Currently, the energy resolution is $\sim$400 at 400 eV and $\sim$150 at 460 eV. With this resolution, it is difficult to resolve fine absorption structures such as vibrational levels in molecules and crystal field splittings in metal complexes, thus dynamics in these structures cannot be investigated. Moreover, if the photon energy of HHs is increased in the future, the energy resolution becomes worse. Therefore, it is desirable to install a new X-ray spectrometer with a higher resolution. In the new spectrometer, we plan to use a high-resolution grating which is used in SPring-8 provided by Prof. Yoshihisa Harada [177]. The energy resolution of the new spectrometer is estimated to be over 1000 in the whole water window region.

Second, a photoelectron spectrometer for attosecond streaking is planned to be installed in the sample chamber. Attosecond streaking measurements provide fundamental information on the temporal shapes of the pump IR electric field and the probe SX pulse. By combining attosecond streaking with transient absorption spectroscopy, it will become

possible to obtain the absolute timing between the pump electric filed and the modulation of an SX absorption spectrum, which is important to understand sub-cycle dynamics of matter. As a photoelectron spectrometer, we plan to use a magnetic bottle time-of-flight spectrometer which has a high detection efficiency.

Extension of target samples

In this dissertation, diatomic and triatomic molecules are used as the target samples of the transient absorption experiments. However, to utilize element specificity, more complex systems such as polyatomic molecules, liquids, and solids should be used. Especially, liquids are suitable for our system because SX pulses in the water window can be transmitted through water. However, even in the water window region, the absorption length of water is a few micrometers. In order to realize such a thin liquid target, we plan to install a special liquid cell consisting of Si_3N_4 thin films [178].

Development of a new IR light source

Currently, the wavelength and the repetition rate of the BIBO-OPCPA system are 1.6 μm and 1 kHz, respectively. According to the scaling law, if the wavelength can be extended to, for example, 2 μm, the cutoff energy can reach 700 eV. Such HHs can cover the O K-edge (543 eV), V L-edge (515 eV), Cr L-edge (580 eV), and Mn L-edge (640 eV), and attosecond spectroscopy on various oxides and magnetic materials will become possible. However, at the same time, due to the scaling law, the photon flux of the HHs is expected to become low. Therefore, the repetition rate of the light source needs to be high. In order to realize such a long-wavelength, high-repetition rate light source, a degenerate OPCPA system pumped by a 1-μm Yb-based thin disk laser is planned. Another plan is femtosecond Cr-based lasers operating at 2.5 μm. Cr-based lasers can deliver MIR pulses without using OPA or OPCPA.

Appendix A

Details of the X-ray grating

In Appendix A, the details of the flat field X-ray grating employed in this study (Shimadzu 30-003) are described. Figure A.1 depicts the geometric setup and the parameters of the X-ray grating. The X-ray with a wavelength λ comes from the entrance slit at an angle α, is diffracted at an angle β, and reaches the detector at a position x.

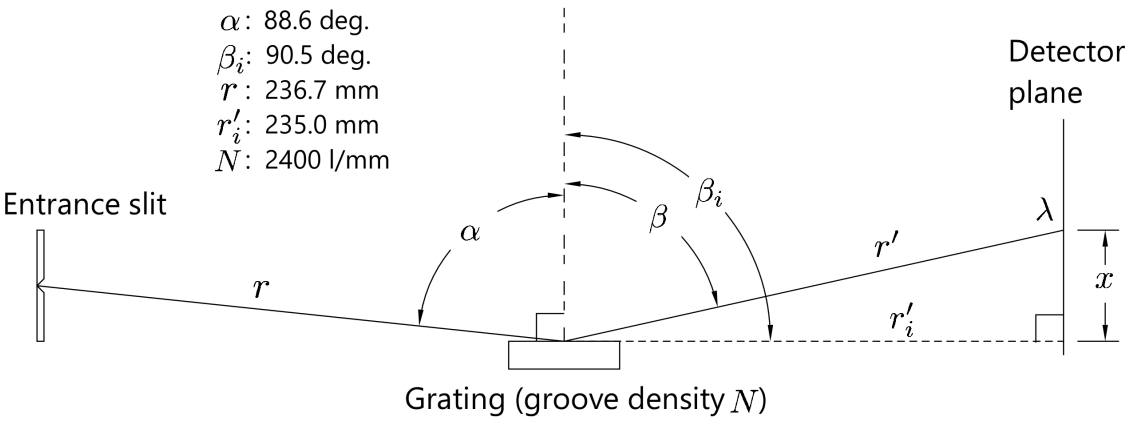

Figure A.1: Geometric setup of the X-ray grating.

The X-ray photon energy E can be calculated from the detector position x as follows. The first-order diffraction angle β and the X-ray wavelength λ is related by the following equation:

$$\sin\alpha + \sin\beta = N\lambda. \tag{A.1}$$

Here, because the grating has a variable line spacing, the groove density N depends on the position of the grating. However, within the designed wavelength range (1-7 nm), the groove density at the center of the grating (N = 2400 l/mm) can be used for calculation. Assuming that the detector plane is vertical to the grating surface, β can be calculated from x as

$$\sin\beta = \frac{r'_i}{\sqrt{r'^2_i + x^2}}. \tag{A.2}$$

Using Eqs. (A.1) and (A.2), λ can be calculated from x as

$$\lambda = \frac{1}{N}\left(\sin\alpha + \frac{r'_i}{\sqrt{r'^2_i + x^2}}\right). \tag{A.3}$$

The photon energy E can also be calculated as

$$E = \frac{hcN}{\sin\alpha + r'_i/\sqrt{r'^2_i + x^2}}, \tag{A.4}$$

where h and c are the Planck constant and the speed of light in vacuum, respectively.

Appendix B

Transient absorption spectroscopy of N_2 molecules

Besides NO and N_2O, we also tried N_2 as a target of transient absorption spectroscopy. The experimental setup is almost the same as the transient absorption experiments of NO and N_2O, but the target gas cell is filled with 0.15 bar of N_2. The pump intensity is set to 1×10^{14} W/cm^2. This pump intensity is estimated by the fact that the experimental setup of the pump beam is set to the same as that of NO. The polarizations of the pump IR and the probe SX pulses are set to parallel.

Figure B.1(a) presents the measured transient absorption spectrum of N_2. Figure B.1(b) plots the static absorbance spectrum measured in our beamline (gray circles) and in a synchrotron facility (gray curve) [155]. The strong peak around 401 eV corresponds to the transition from the N 1s orbital to the 2π orbital (LUMO). The weak peaks around 407 eV correspond to the transitions from the N 1s orbital to the Rydberg orbitals.

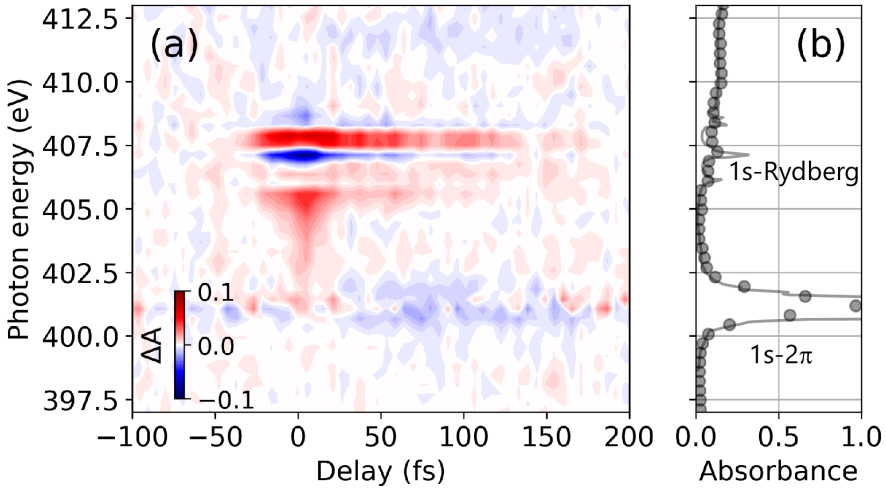

Figure B.1: (a) Measured transient absorption spectrum of N_2. (b) Static absorbance spectrum of N_2 measured in our beamline (circles) and in synchrotron (solid curve) [155].

The main feature in Fig. B.1(a) is the modulations of the 1s-Rydberg peaks. Such a feature is also observed in the transient absorption spectra of NO and N_2O, and can be explained by the emergence of laser-dressed states and AC Stark shift.

Appendix C

Noise source in transient absorption measurements

In order to obtain precise differential absorbance in a transient absorption measurement, it is important to reduce its noise as much as possible. Therefore, it is meaningful to specify the sources of the noise, or the limiting factor of the signal-to-noise ratio. In Appendix C, we show that the main limiting factor of the signal-to-noise ratio in our transient absorption measurements is the shot noise which originates from the low photon flux of the HHs.

First, we derive the formula to describe the the shot noise $\Delta A_{\mathrm{noise}}(E_j, \tau_i)$ in the corrected differential absorbance $\Delta A_{\mathrm{cor}}(E_j, \tau_i)$. Here, $\Delta A_{\mathrm{cor}}(E_j, \tau_i)$ is obtained from $\Delta A(E_j, \tau_i)$ by applying a background correction process (for the detailed definition, see Section 6.3.3).). $\Delta A(E_j, \tau_i)$ is calculated from the averaged HH intensity $I_{\mathrm{avg}}(E_j, \tau_i)$ at the delay τ_i and the reference HH intensity $I_{\mathrm{ref}}(E_j)$ as

$$\Delta A(E_j, \tau_i) = -\log_{10} \frac{I_{\mathrm{avg}}(E_j, \tau_i)}{I_{\mathrm{ref}}(E_j)}. \tag{C.1}$$

Because the background signal for the calculation of $\Delta A_{\mathrm{cor}}(E_j, \tau_i)$ is taken from the averaged differential absorbance of 10$\sim$20 CCD pixels, its shot noise is much smaller than that of $\Delta A(E_j, \tau_i)$. Therefore, $\Delta A_{\mathrm{noise}}(E_j, \tau_i)$ can be approximated by the shot noise of $\Delta A(E_j, \tau_i)$. Moreover, because $I_{\mathrm{ref}}(E_j)$ is obtained from the averaged HH intensity of several delay points, its shot noise is much smaller than that of $I_{\mathrm{avg}}(E_j, \tau_i)$. Therefore, $\Delta A_{\mathrm{noise}}(E_j, \tau_i)$ mainly originates from the noise in $I_{\mathrm{avg}}(E_j, \tau_i)$, and it can be written as

$$\Delta A_{\mathrm{noise}}(E_j, \tau_i) = \left| \Delta I_{\mathrm{avg}}(E_j, \tau_i) \frac{\partial}{\partial I_{\mathrm{avg}}(E_j, \tau_i)} \left[-\log_{10} \frac{I_{\mathrm{avg}}(E_j, \tau_i)}{I_{\mathrm{ref}}(E_j)} \right] \right| \tag{C.2}$$

$$= \frac{\Delta I_{\mathrm{avg}}(E_j, \tau_i)}{I_{\mathrm{avg}}(E_j, \tau_i)} \frac{1}{\log_e 10}, \tag{C.3}$$

where $\Delta I_{\mathrm{avg}}(E_j, \tau_i)$ is the shot noise of $I_{\mathrm{avg}}(E_j, \tau_i)$. Let $N_{\mathrm{total}}(E_j, \tau_i)$ be the number of total photons measured at a photon energy of E_j and a delay of τ_i. Its shot noise $\Delta N_{\mathrm{total}}(E_j, \tau_i)$ is obtained as $\sqrt{N_{\mathrm{total}}(E_j, \tau_i)}$. Then, $\Delta A_{\mathrm{noise}}(E_j, \tau_i)$ can be rewritten as

$$\Delta A_{\mathrm{noise}}(E_j, \tau_i) = \frac{\Delta N_{\mathrm{total}}(E_j, \tau_i)}{N_{\mathrm{total}}(E_j, \tau_i)} \frac{1}{\log_e 10} = \frac{1}{\sqrt{N_{\mathrm{total}}(E_j, \tau_i)}} \frac{1}{\log_e 10}. \tag{C.4}$$

Thus, $\Delta A_{\mathrm{noise}}(E_j, \tau_i)$ can be calculated from $N_{\mathrm{total}}(E_j, \tau_i)$. $N_{\mathrm{total}}(E_j, \tau_i)$ is calculated from the measured total CCD count in a CCD pixel $I_{\mathrm{count}}(E_j, \tau_i)$, the quantum efficiency of the CCD η, the well depth of the CCD N, the ADC resolution of the CCD $2^{n_{\mathrm{ADC}}}$, the number of electrons generated by one X-ray photon in the CCD n, and the preamp gain of the CCD g as $N_{\mathrm{total}}(E_j, \tau_i) = (I_{\mathrm{count}}(E_j, \tau_i)/\eta) \times (N/2^{n_{\mathrm{ADC}}})/n/g$. Here, $\eta = 0.8$, $N = 100000$, $2^{n_{\mathrm{ADC}}} = 65536$, $n = 0.267\times$(Photon energy (eV)), and $g = 4$.

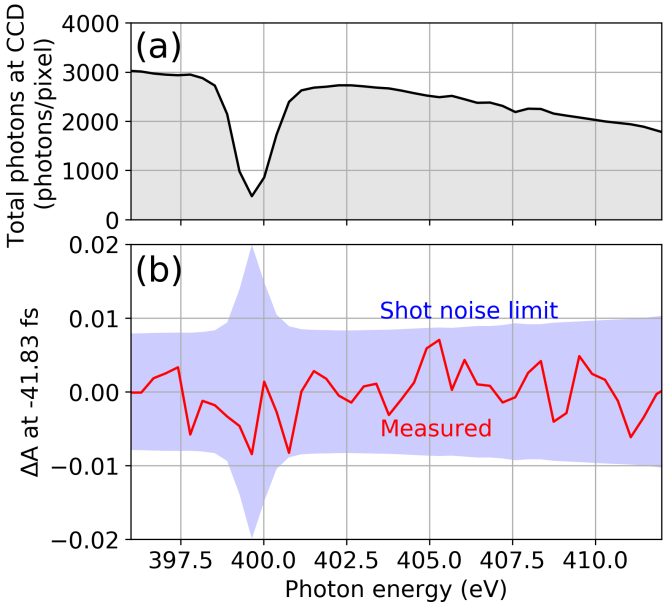

Figure C.1: Comparison between the calculated shot noise and the measured noise at τ = -41.83 fs in the transient absorption spectrum in Fig. 6.5. (a) Total number of photons recorded in each pixel in the CCD. (b) Calculated shot noise (blue shaded area) and measured noise (red curve) of the differential absorbance.

By using Eq. (C.4), we calculate the shot noise for actual experimental results. First, the shot noise for the transient absorption spectrum in Fig. 6.5 is calculated. We take a delay point of -41.83 fs. At this delay point, no absorbance change is induced by the pump pulse, thus the measured differential absorbance is purely dominated by noise. Figure C.1(a) shows the total number of photons in each CCD pixel recorded at this delay. A dip around 400 eV is the 1s-2π absorption peak of NO. From the total number of photons, the shot noise is calculated as shown in the blue shaded area in Fig. C.1(b). It is compared with the measured differential absorbance (red curve). The red curve falls within the blue shaded area, indicating that the noise in the measured differential absorbance is dominated by the shot noise.

Next, the shot noise for the attosecond transient absorption spectrum in Fig. 6.6 is calculated. We take a delay point of -11.0 fs, where no absorbance change is induced by the pump pulse. Figure C.2 shows the comparison between the calculated shot noise and the measured noise in the differential absorbance. Again, it can be seen that the measured noise is dominated by the shot noise. Compared to Fig. C.1, some part of the measured noise are out of the shot noise limit. This might be because the CEP is locked in the attosecond transient absorption measurement: when the CEP is locked, the HH spectrum

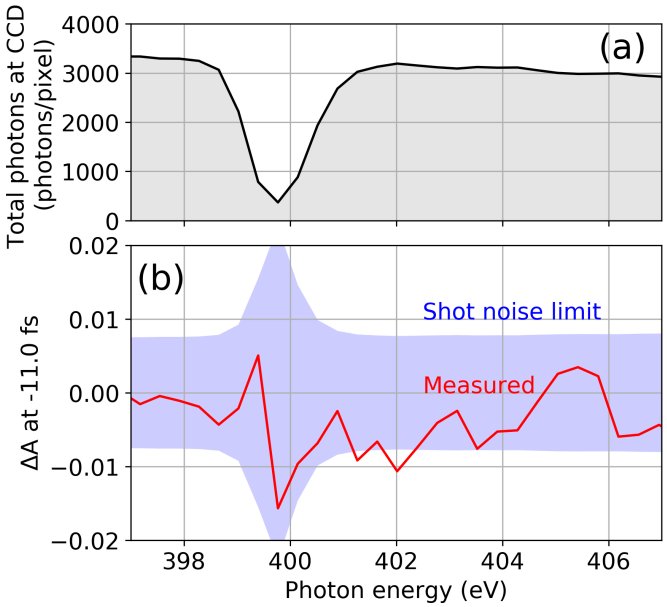

Figure C.2: Comparison between the calculated shot noise and the measured noise at τ = -11.0 fs in the transient absorption spectrum in Fig. 6.6. (a) Total number of photons recorded in each pixel in the CCD. (b) Calculated shot noise (blue shaded area) and measured noise (red curve) of the differential absorbance.

tends to have complex structures and the fluctuation of such structures deteriorates the signal-to-noise ratio.

In summary, it is shown that the main noise source in our transient absorption measurements is the shot noise. Therefore, in order to improve the signal-to-noise ratio, the photon flux of the HHs has to be increased.

Appendix D

Development of 400-nm pump light source

In the main chapters, the pump pulse of transient absorption spectroscopy is the IR pulse obtained from a BIBO-OPCPA system. However, to trigger photochemical reactions, short-wavelength pump pulses are more suitable. Therefore, we develop a 400-nm pump light source.

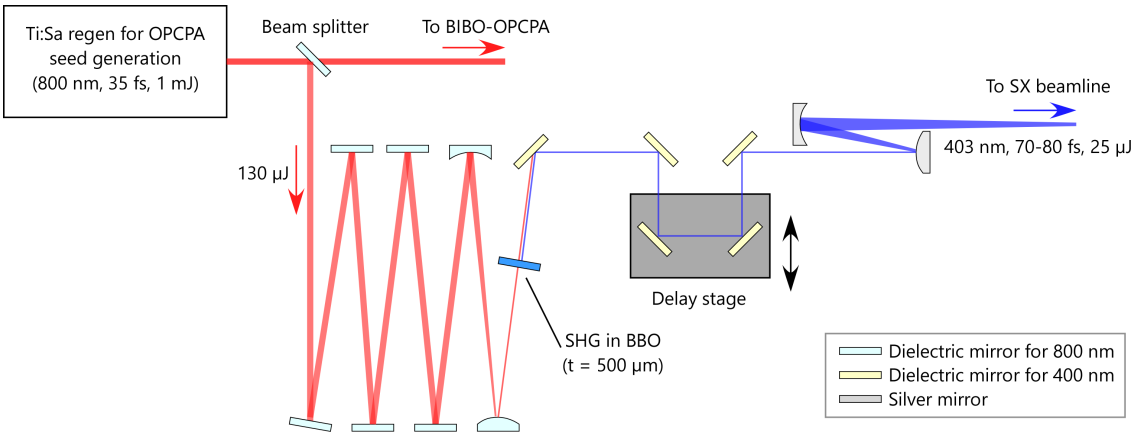

Figure D.1: Schematic of the setup for the generation of 400-nm pump pulses.

Figure D.1 depicts a schematic of the setup for the generation of 400-nm pump pulses. First, the output from a Ti:Sa regenerative amplifier (800 nm, 35 fs, 1 mJ) in the seed arm is split into two beams by a beam splitter. The transmitted beam (80%) goes to the seed generation for OPCPA. The reflected beam (20%) is used for the 400-nm pulse generation. The pulse energy of the reflected beam is 130 μJ. The Ti:Sa beam is then propagated for ∼10 m to compensate the delay, and the beam size is shrunk by a telescope consisting of a concave and a convex mirror. The beam passes through a BBO crystal (500-μmthick) to generate a 400-nm SH pulse. After that, the beam is reflected by dielectric mirrors for 400 nm for several times to remove the 800-nm component. A delay stage in the beam path (Sigma-tech, FS-1050PX) controls the pump-probe delay. Finally, a silver convex mirror magnifies the beam size and a silver concave mirror focuses the beam into the sample of transient absorption. Here, a hole-drilled mirror is not used for the recombination of the

pump and the probe beam. Instead, the two beams are noncollinearly recombined with an angle of 10 mrad. The pulse energy of the 400-nm pulse at the sample is 25 µJ.

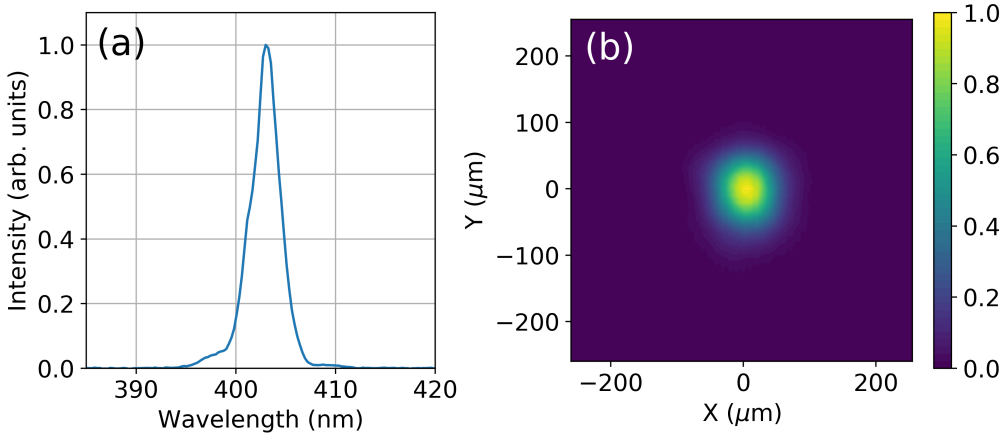

Figure D.2: (a) Spectrum and (b) spatial profile of the 400-nm beam.

Figure D.2(a) plots the spectrum of the generated 400-nm beam. The central wavelength is 403 nm. Figure D.2(b) shows the spatial profile at the sample position. The profile is nearly Gaussian, and its $1/e^2$ diameter is 150 µm.

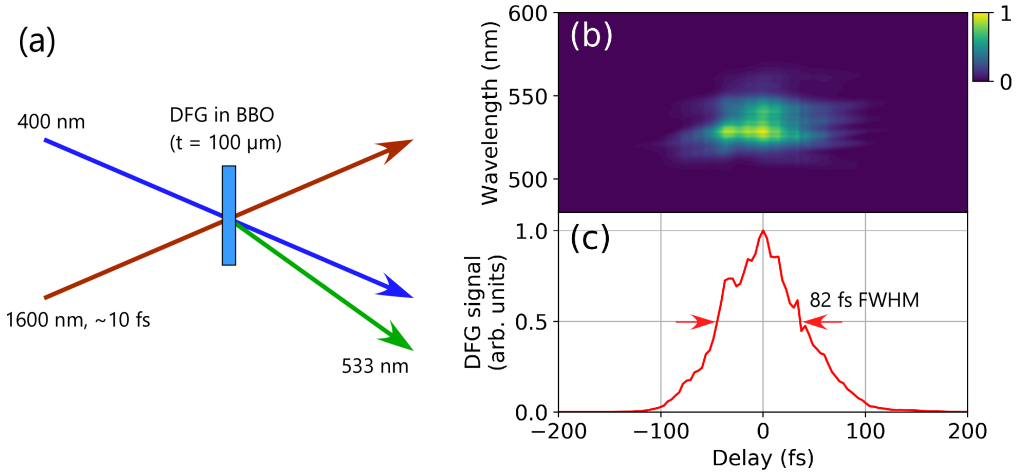

Figure D.3: (a) Schematic of the cross-correlation measurement. (b) Measured DFG cross correlation signal as a function of delay. (c) Integrated cross-correlation signal.

The duration of the 400-nm pulse is estimated by a cross-correlation measurement using the IR pulse from the BIBO-OPCPA system. Figure D.3(a) shows a schematic of the setup. The IR and the 400-nm pulses are focused into a BBO crystal (100-µm thick) which is placed at the sample position of transient absorption. In the BBO, a 533-nm pulse is generated by the DFG process. While scanning the delay between the IR and the 400-nm pulse, the spectrum of the 533-nm pulse is recorded by a spectrometer. Figures D.3(b, c) present the measured cross-correlation signal. The temporal width of the signal is 82 fs FWHM. Considering that the pulse duration of the IR pulse is 10 fs, the pulse duration of the 400-nm pulse is estimated to be 70∼80 fs.

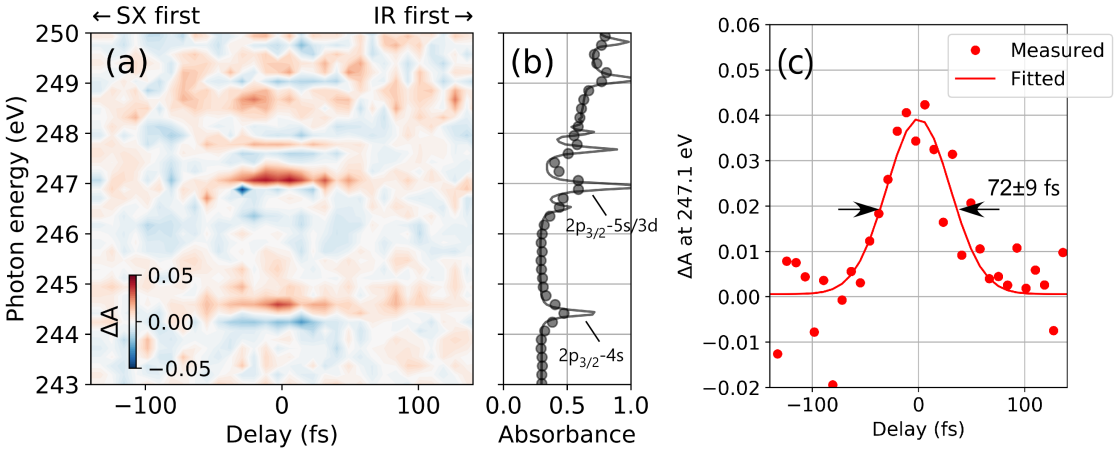

Figure D.4: (a) Measured transient absorption spectrum of Ar at the L-edge (250 eV) pumped by a 400-nm pulse. (b) Measured static absorbance spectrum of Ar (circles) and the reference curve from a synchrotron measurement (solid curve) [154]. (c) Measured temporal evolution of the differential absorbance at 247.1 eV (circles) and its Gaussian fitting (solid curve).

In order to test the 400-nm pump source in an actual transient absorption measurement, transient absorption spectroscopy of Ar at the L-edge (250 eV) is performed. Here, HHs from Ne are used as the probe pulses. 30 mbar of Ar is filled in a sample gas cell with a thickness of 4 mm. Note that this cell is different from that used in transient absorption spectroscopy of NO and N_2O. Considering the beam diameter, pulse energy, and the pulse duration, the peak intensity of the 400-nm pump pulse is estimated to be 3.8×10^{12} W/cm^2. The total measurement time is 1 hour. Figures D.4(a) and (b) show the measured transient absorption spectrum and the static absorbance spectrum, respectively. There are absorbance modulations at the $2p_{3/2}-4s$ and the $2p_{3/2}-5s/3d$ peaks around 0 fs. This is very similar to a previously reported UV-pump transient absorption spectrum of Ar [63], and it can be interpreted as the AC Stark shift induced by the strong 400-nm pulse. Figure D.4(c) plots the temporal evolution of the differential absorbance at 247.1 eV (circles). By fitting it with a Gaussian function, the temporal width of the absorbance change is calculated to be 72±9 fs FWHM. This value is consistent with the cross-correlation measurement in BBO.

In the future, we plan to use this setup to observe chemical reactions in molecules in gas or in liquid phases.

Appendix E

Molecular ADK theory

The molecular ADK theory [137] is employed several times in this dissertation. In Appendix E, the calculation procedure of the molecular ADK theory is briefly described.

First, the asymptotic wave function of the HOMO orbital of a molecule at a large distance from the nuclei is expanded as

$$\Psi^m(\boldsymbol{r}) = \sum_l C_l F_l(r) Y_{lm}(\hat{\boldsymbol{r}}). \tag{E.1}$$

Here, the molecular axis is assumed to be aligned with the laser polarization. m represents a magnetic quantum number, which is 1 for a π orbital and 0 for a σ orbital. l is an azimuthal quantum number. C_l is a coefficient. $F_l(r)$ is a radial distribution function which is defined as $F_l(r) = r^{Z_C/\kappa - 1} e^{-\kappa r}$, where Z_C is the effective Coulomb charge and $\kappa = \sqrt{2I_p}$. Z_C is 1 for tunnel ionization of a neutral molecule. I_p is the ionization potential. Y_{lm} is a spherical harmonic function. In order to obtain the coefficient C_l, the HOMO wave function is calculated by using a software such as GAMESS, and then its angular distribution $\Psi^m(\Omega)$ at a large r is extracted. Then, by calculating $\int \Psi^m(\Omega) Y_{lm}(\Omega) d\Omega$, $C_l F_l(r)$ is obtained.

Once the asymptotic expansion of the HOMO wave function is obtained, the ionization rate under a static electric field F can be calculated as

$$w_{\mathrm{stat}}(F, 0) = \frac{B(m)^2}{2^{|m|}|m|!} \frac{1}{\kappa^{2Z_C/\kappa - 1}} \left(\frac{2\kappa^3}{F} \right)^{2Z_C/\kappa - |m| - 1} e^{-2\kappa^3/3F}. \tag{E.2}$$

Here, $B(m)$ is defined as

$$B(m) = \sum_l C_l Q(l, m), \tag{E.3}$$

and $Q(l, m)$ is defined as

$$Q(l, m) = (-1)^m \sqrt{\frac{(2l+1)(l+|m|)!}{2(l-|m|)!}}. \tag{E.4}$$

If the molecular axis is tilted from the laser polarization with an arbitrary Euler angle $\boldsymbol{R}$, $B(m)$ is modified as

$$B(m') = \sum_l C_l D^l_{m',m}(\boldsymbol{R}) Q(l, m'), \tag{E.5}$$

where $D^l_{m',m}$ is the rotation matrix, which can be obtained by using a software such as SHTOOLS [179]. With $B(m')$, the ionization rate is calculated as

$$w_{\rm stat}(F,\boldsymbol{R}) = \sum_{m'} \frac{B(m')^2}{2^{|m'|}|m'|!} \frac{1}{\kappa^{2Z_C/\kappa-1}} \left(\frac{2\kappa^3}{F}\right)^{2Z_C/\kappa-|m'|-1} e^{-2\kappa^3/3F}. \tag{E.6}$$

This formula is intended for a static electric field. In the case of a low frequency AC electric field, the ionization rate is multiplied by $(3F/\pi\kappa^3)^{1/2}$.

In order to verify the validity of the molecular ADK theory, the ionization anisotropy of an NO molecule irradiated by a 1×10^{14}-W/cm^2 laser electric field is calculated and compared with a more accurate theory. In the calculation, the HOMO wave function of NO is obtained by using GAMESS (DFT, B3LYP/6-311+G(d)). Then, using Eq. (E.6), the ionization rate $w(\theta)$ for each angle between the molecular axis and the electric field θ is calculated. Because NO is an asymmetric molecule, the tunnel ionization rate is not symmetric; $w(\theta) \neq w(\pi-\theta)$. However, here, $w(\theta)$ is symmetrized as $(w(\theta)+w(\pi-\theta))/2$. The red curve in Fig. E.1 shows the result. The blue curve in Fig. E.1 plots the ionization anisotropy taken from ref. [180], which is obtained by the weak-field asymptotic theory (WFAT). WFAT is a more rigorous theory to describe tunnel ionization. The agreement between the two curves in Fig. E.1 indicates that the molecular ADK theory is, at least qualitatively, useful to understand the tunnel ionization process in molecules.

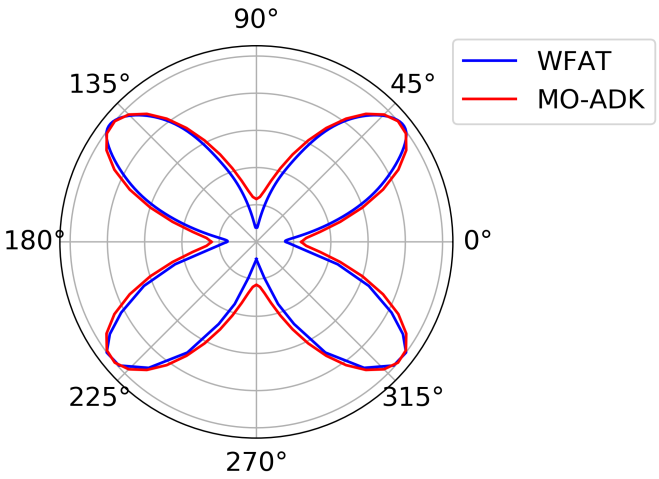

Figure E.1: Anisotropy of the tunnel ionization rate of NO irradiated by a 1×10^{14}-W/cm^2 laser electric field. The blue curve is obtained by WFAT, taken from ref. [180]. The red curve is calculated by the molecular ADK theory.

Bibliography

[1] T. H. Maiman, "Stimulated optical radiation in ruby," Nature (London) **187**, 493–494 (1960).

[2] A. H. Zewail, "Femtochemistry: Atomic-scale dynamics of the chemical bond," J. Phys. Chem. A **104**, 5660–5694 (2000).

[3] M. Ferray, A. L'Huillier, X. F. Li, L. A. Lompre, G. Mainfray, and C. Manus, "Multiple-harmonic conversion of 1064 nm radiation in rare gases," J. Phys. B **21**, 31–35 (1988).

[4] A. McPherson, G. Gibson, H. Jara, U. Johann, T. S. Luk, I. A. McIntyre, K. Boyer, and C. K. Rhodes, "Studies of multiphoton production of vacuum-ultraviolet radiation in the rare gases," J. Opt. Soc. Am. B **4**, 595–601 (1987).

[5] P. F. Moulton, "Spectroscopic and laser characteristics of Ti:Al_2O_3," J. Opt. Soc. Am. B **3**, 125–133 (1986).

[6] D. Strickland and G. Mourou, "Compression of amplified chirped optical pulses," Opt. Commun. **56**, 219 – 221 (1985).

[7] S. Backus, C. G. Durfee, M. M. Murnane, and H. C. Kapteyn, "High power ultrafast lasers," Rev. Sci. Instrm. **69**, 1207–1223 (1998).

[8] M. Nisoli, S. D. Silvestri, and O. Svelto, "Generation of high energy 10 fs pulses by a new pulse compression technique," Appl. Phys. Lett. **68**, 2793–2795 (1996).

[9] R. Szipöcs, C. Spielmann, F. Krausz, and K. Ferencz, "Chirped multilayer coatings for broadband dispersion control in femtosecond lasers," Opt. Lett. **19**, 201–203 (1994).

[10] D. J. Jones, S. A. Diddams, J. K. Ranka, A. Stentz, R. S. Windeler, J. L. Hall, and S. T. Cundiff, "Carrier-envelope phase control of femtosecond mode-locked lasers and direct optical frequency synthesis," Science **288**, 635–639 (2000).

[11] M. Hentschel, R. Kienberger, C. Spielmann, G. A. Reider, N. Milosevic, T. Brabec, P. Corkum, U. Heinzmann, M. Drescher, and F. Krausz, "Attosecond metrology," Nature (London) **414**, 509–513 (2001).

[12] P. M. Paul, E. S. Toma, P. Breger, G. Mullot, F. Augé, P. Balcou, H. G. Muller, and P. Agostini, "Observation of a train of attosecond pulses from high harmonic generation," Science **292**, 1689–1692 (2001).

[13] M. Drescher, M. Hentschel, R. Kienberger, M. Uiberacker, V. Yakovlev, A. Scrinzi, T. Westerwalbesloh, U. Kleineberg, U. Heinzmann, and F. Krausz, "Time-resolved atomic inner-shell spectroscopy," Nature (London) **419**, 803–807 (2002).

[14] M. Uiberacker, T. Uphues, M. Schultze, A. J. Verhoef, V. Yakovlev, M. F. Kling, J. Rauschenberger, N. M. Kabachnik, H. Schroder, M. Lezius, K. L. Kompa, H.-G. Muller, M. J. J. Vrakking, S. Hendel, U. Kleineberg, U. Heinzmann, M. Drescher, and F. Krausz, "Attosecond real-time observation of electron tunnelling in atoms," Nature (London) **446**, 627–632 (2007).

[15] M. Schultze, M. Fieß, N. Karpowicz, J. Gagnon, M. Korbman, M. Hofstetter, S. Neppl, A. L. Cavalieri, Y. Komninos, T. Mercouris, C. A. Nicolaides, R. Pazourek, S. Nagele, J. Feist, J. Burgdörfer, A. M. Azzeer, R. Ernstorfer, R. Kienberger, U. Kleineberg, E. Goulielmakis, F. Krausz, and V. S. Yakovlev, "Delay in photoemission," Science **328**, 1658–1662 (2010).

[16] A. Wirth, M. T. Hassan, I. Grguraš, J. Gagnon, A. Moulet, T. T. Luu, S. Pabst, R. Santra, Z. A. Alahmed, A. M. Azzeer, V. S. Yakovlev, V. Pervak, F. Krausz, and E. Goulielmakis, "Synthesized light transients," Science **334**, 195–200 (2011).

[17] Y. Nabekawa, Y. Furukawa, T. Okino, A. Amani Eilanlou, E. J. Takahashi, K. Yamanouchi, and K. Midorikawa, "Settling time of a vibrational wavepacket in ionization," Nat. Commun. **6**, 8197 (2015).

[18] M. Sabbar, H. Timmers, Y.-J. Chen, A. K. Pymer, Z.-H. Loh, S. Sayres, S. Pabst, R. Santra, and S. R. Leone, "State-resolved attosecond reversible and irreversible dynamics in strong optical fields," Nat. Phys. **13**, 472–478 (2017).

[19] F. Calegari, D. Ayuso, A. Trabattoni, L. Belshaw, S. De Camillis, S. Anumula, F. Frassetto, L. Poletto, A. Palacios, P. Decleva, J. B. Greenwood, F. Martín, and M. Nisoli, "Ultrafast electron dynamics in phenylalanine initiated by attosecond pulses," Science **346**, 336–339 (2014).

[20] C. Ott, A. Kaldun, L. Argenti, P. Raith, K. Meyer, M. Laux, Y. Zhang, A. Blattermann, S. Hagstotz, T. Ding, R. Heck, J. Madronero, F. Martin, and T. Pfeifer, "Reconstruction and control of a time-dependent two-electron wave packet," Nature (London) **516**, 374–378 (2014).

[21] M. Schultze, E. M. Bothschafter, A. Sommer, S. Holzner, W. Schweinberger, M. Fiess, M. Hofstetter, R. Kienberger, V. Apalkov, V. S. Yakovlev, M. I. Stockman, and F. Krausz, "Controlling dielectrics with the electric field of light," Nature (London) **493**, 75–78 (2013).

[22] M. Schultze, K. Ramasesha, C. Pemmaraju, S. Sato, D. Whitmore, A. Gandman, J. S. Prell, L. J. Borja, D. Prendergast, K. Yabana, D. M. Neumark, and S. R. Leone, "Attosecond band-gap dynamics in silicon," Science **346**, 1348–1352 (2014).

[23] H. Mashiko, K. Oguri, T. Yamaguchi, A. Suda, and H. Gotoh, "Petahertz optical drive with wide-bandgap semiconductor," Nat. Phys. **12**, 741–745 (2016).

[24] M. Lucchini, S. A. Sato, A. Ludwig, J. Herrmann, M. Volkov, L. Kasmi, Y. Shinohara, K. Yabana, L. Gallmann, and U. Keller, "Attosecond dynamical Franz-Keldysh effect in polycrystalline diamond," Science **353**, 916–919 (2016).

[25] M. Volkov, S. A. Sato, F. Schlaepfer, L. Kasmi, N. Hartmann, M. Lucchini, L. Gallmann, A. Rubio, and U. Keller, "Attosecond screening dynamics mediated by electron localization in transition metals," Nat. Phys. **15**, 1145–1149 (2019).

[26] T. Gaumnitz, A. Jain, Y. Pertot, M. Huppert, I. Jordan, F. Ardana-Lamas, and H. J. Wörner, "Streaking of 43-attosecond soft-X-ray pulses generated by a passively CEP-stable mid-infrared driver," Opt. Express **25**, 27506–27518 (2017).

[27] A. Fleischer, O. Kfir, T. Diskin, P. Sidorenko, and O. Cohen, "Spin angular momentum and tunable polarization in high-harmonic generation," Nat. Photon. **8**, 543–549 (2014).

[28] D. D. Hickstein, F. J. Dollar, P. Grychtol, J. L. Ellis, R. Knut, C. Hernández-García, D. Zusin, C. Gentry, J. M. Shaw, T. Fan, K. M. Dorney, A. Becker, A. Jaron-Becker, H. C. Kapteyn, M. M. Murnane, and C. G. Durfee, "Non-collinear generation of angularly isolated circularly polarized high harmonics," Nat. Photon. **9**, 743–750 (2015).

[29] T. Sekikawa, A. Kosuge, T. Kanai, and S. Watanabe, "Nonlinear optics in the extreme ultraviolet," Nature (London) **432**, 605–608 (2004).

[30] E. J. Takahashi, P. Lan, O. D. Mücke, Y. Nabekawa, and K. Midorikawa, "Attosecond nonlinear optics using gigawatt-scale isolated attosecond pulses," Nat. Commun. **4**, 2691 (2013).

[31] T. Fuji, N. Ishii, C. Y. Teisset, X. Gu, T. Metzger, A. Baltuska, N. Forget, D. Kaplan, A. Galvanauskas, and F. Krausz, "Parametric amplification of few-cycle carrier-envelope phase-stable pulses at 2.1 μm," Opt. Lett. **31**, 1103–1105 (2006).

[32] E. J. Takahashi, T. Kanai, Y. Nabekawa, and K. Midorikawa, "10mJ class femtosecond optical parametric amplifier for generating soft x-ray harmonics," Appl. Phys. Lett. **93**, 041111 (2008).

[33] O. D. Mücke, S. Ališauskas, A. J. Verhoef, A. Pugžlys, A. Baltuška, V. Smilgevičius, J. Pocius, L. Giniūnas, R. Danielius, and N. Forget, "Self-compression of millijoule 1.5 μm pulses," Opt. Lett. **34**, 2498–2500 (2009).

[34] K.-H. Hong, S.-W. Huang, J. Moses, X. Fu, C.-J. Lai, G. Cirmi, A. Sell, E. Granados, P. Keathley, and F. X. Kärtner, "High-energy, phase-stable, ultrabroadband kHz OPCPA at 2.1 μm pumped by a picosecond cryogenic Yb:YAG laser," Opt. Express **19**, 15538–15548 (2011).

[35] F. Silva, P. K. Bates, A. Esteban-Martin, M. Ebrahim-Zadeh, and J. Biegert, "High-average-power, carrier-envelope phase-stable, few-cycle pulses at 2.1 μm from a collinear BiB_3O_6 optical parametric amplifier," Opt. Lett. **37**, 933–935 (2012).

[36] N. Ishii, K. Kaneshima, K. Kitano, T. Kanai, S. Watanabe, and J. Itatani, "Sub-two-cycle, carrier-envelope phase-stable, intense optical pulses at 1.6 μm from a BiB_3O_6 optical parametric chirped-pulse amplifier," Opt. Lett. **37**, 4182–4184 (2012).

[37] Y. Yin, J. Li, X. Ren, K. Zhao, Y. Wu, E. Cunningham, and Z. Chang, "High-efficiency optical parametric chirped-pulse amplifier in BiB_3O_6 for generation of 3 mJ, two-cycle, carrier-envelope-phase-stable pulses at 1.7 μm," Opt. Lett. **41**, 1142–1145 (2016).

[38] Y. Fu, K. Midorikawa, and E. J. Takahashi, "Towards a petawatt-class few-cycle infrared laser system via dual-chirped optical parametric amplification," Sci. Rep. **8**, 7692 (2018).

[39] N. Bigler, J. Pupeikis, S. Hrisafov, L. Gallmann, C. R. Phillips, and U. Keller, "High-power OPCPA generating 1.7 cycle pulses at 2.5 μm," Opt. Express **26**, 26750–26757 (2018).

[40] M. Neuhaus, H. Fuest, M. Seeger, J. Schötz, M. Trubetskov, P. Russbueldt, H. Hoffmann, E. Riedle, Z. Major, V. Pervak, M. F. Kling, and P. Wnuk, "10 W CEP-stable few-cycle source at 2 μm with 100 kHz repetition rate," Opt. Express **26**, 16074–16085 (2018).

[41] B. Shan and Z. Chang, "Dramatic extension of the high-order harmonic cutoff by using a long-wavelength driving field," Phys. Rev. A **65**, 011804 (2001).

[42] E. J. Takahashi, T. Kanai, K. L. Ishikawa, Y. Nabekawa, and K. Midorikawa, "Coherent water window X ray by phase-matched high-order harmonic generation in neutral media," Phys. Rev. Lett. **101**, 253901 (2008).

[43] M.-C. Chen, P. Arpin, T. Popmintchev, M. Gerrity, B. Zhang, M. Seaberg, D. Popmintchev, M. M. Murnane, and H. C. Kapteyn, "Bright, coherent, ultrafast soft x-ray harmonics spanning the water window from a tabletop light source," Phys. Rev. Lett. **105**, 173901 (2010).

[44] N. Ishii, K. Kaneshima, K. Kitano, T. Kanai, S. Watanabe, and J. Itatani, "Carrier-envelope phase-dependent high harmonic generation in the water window using few-cycle infrared pulses," Nat. Commun. **5**, 3331 (2014).

[45] S. L. Cousin, F. Silva, S. Teichmann, M. Hemmer, B. Buades, and J. Biegert, "High-flux table-top soft x-ray source driven by sub-2-cycle, CEP stable, 1.85-μm 1-kHz pulses for carbon K-edge spectroscopy," Opt. Lett. **39**, 5383–5386 (2014).

[46] S. M. Teichmann, F. Silva, S. L. Cousin, M. Hemmer, and J. Biegert, "0.5-keV soft X-ray attosecond continua," Nat. Commun. **7**, 11493 (2016).

[47] G. J. Stein, P. D. Keathley, P. Krogen, H. Liang, J. P. Siqueira, C.-L. Chang, C.-J. Lai, K.-H. Hong, G. M. Laurent, and F. X. Kärtner, "Water-window soft x-ray high-harmonic generation up to the nitrogen K-edge driven by a kHz, 2.1 μm OPCPA source," J. Phys. B **49**, 155601 (2016).

[48] A. S. Johnson, L. Miseikis, D. A. Wood, D. R. Austin, C. Brahms, S. Jarosch, C. S. Strüber, P. Ye, and J. P. Marangos, "Measurement of sulfur $L_{2,3}$ and carbon K edge XANES in a polythiophene film using a high harmonic supercontinuum," Structural Dynamics **3**, 062603 (2016).

[49] C. Schmidt, Y. Pertot, T. Balciunas, K. Zinchenko, M. Matthews, H. J. Wörner, and J.-P. Wolf, "High-order harmonic source spanning up to the oxygen K-edge based on filamentation pulse compression," Opt. Express **26**, 11834–11842 (2018).

[50] A. S. Johnson, D. R. Austin, D. A. Wood, C. Brahms, A. Gregory, K. B. Holzner, S. Jarosch, E. W. Larsen, S. Parker, C. S. Strüber, P. Ye, J. W. G. Tisch, and J. P. Marangos, "High-flux soft x-ray harmonic generation from ionization-shaped few-cycle laser pulses," Sci. Adv. **4** (2018).

[51] J. Pupeikis, P.-A. Chevreuil, N. Bigler, L. Gallmann, C. R. Phillips, and U. Keller, "Water window soft x-ray source enabled by 25-W few-cycle mid-IR OPCPA at 100 kHz," arXiv 1910.03236 (2019).

[52] T. Popmintchev, M.-C. Chen, D. Popmintchev, P. Arpin, S. Brown, S. Ališauskas, G. Andriukaitis, T. Balčiunas, O. D. Mücke, A. Pugzlys, A. Baltuška, B. Shim, S. E. Schrauth, A. Gaeta, C. Hernández-García, L. Plaja, A. Becker, A. Jaron-Becker, M. M. Murnane, and H. C. Kapteyn, "Bright coherent ultrahigh harmonics in the keV X-ray regime from mid-infrared femtosecond lasers," Science **336**, 1287–1291 (2012).

[53] "SXR Specifications | Liniac Coherent Light Source," `https://lcls.slac.stanford.edu/instruments/sxr/specifications`. Accessed: 2019-12-13.

[54] T. Shintake, H. Tanaka, T. Hara, T. Tanaka, K. Togawa, M. Yabashi, Y. Otake, Y. Asano, T. Bizen, T. Fukui, S. Goto, A. Higashiya, T. Hirono, N. Hosoda, T. Inagaki, S. Inoue, M. Ishii, Y. Kim, H. Kimura, M. Kitamura, T. Kobayashi, H. Maesaka, T. Masuda, S. Matsui, T. Matsushita, X. Maréchal, M. Nagasono, H. Ohashi, T. Ohata, T. Ohshima, K. Onoe, K. Shirasawa, T. Takagi, S. Takahashi, M. Takeuchi, K. Tamasaku, R. Tanaka, Y. Tanaka, T. Tanikawa, T. Togashi, S. Wu, A. Yamashita, K. Yanagida, C. Zhang, H. Kitamura, and T. Ishikawa, "A compact free-electron laser for generating coherent radiation in the extreme ultraviolet region," Nat. Photon. **2**, 555–559 (2008).

[55] K. Holldack, J. Bahrdt, A. Balzer, U. Bovensiepen, M. Brzhezinskaya, A. Erko, A. Eschenlohr, R. Follath, A. Firsov, W. Frentrup, L. Le Guyader, T. Kachel, P. Kuske, R. Mitzner, R. Müller, N. Pontius, T. Quast, I. Radu, J.-S. Schmidt, C. Schüßler-Langeheine, M. Sperling, C. Stamm, C. Trabant, and A. Föhlisch, "FemtoSpeX: a versatile optical pump-soft X-ray probe facility with 100 fs X-ray pulses of variable polarization," J. Synchrotron Radiat. **21**, 1090–1104 (2014).

[56] S. Yamamoto, Y. Senba, T. Tanaka, H. Ohashi, T. Hirono, H. Kimura, M. Fujisawa, J. Miyawaki, A. Harasawa, T. Seike, S. Takahashi, N. Nariyama, T. Matsushita, M. Takeuchi, T. Ohata, Y. Furukawa, K. Takeshita, S. Goto, Y. Harada, S. Shin,

H. Kitamura, A. Kakizaki, M. Oshima, and I. Matsuda, "New soft X-ray beamline BL07LSU at SPring-8," J. Synchrotron Radiat. **21**, 352–365 (2014).

[57] N. Ishii, K. Kaneshima, T. Kanai, S. Watanabe, and J. Itatani, "Generation of sub-two-cycle millijoule infrared pulses in an optical parametric chirped-pulse amplifier and their application to soft x-ray absorption spectroscopy with high-flux high harmonics," J. Opt. **20**, 014003 (2017).

[58] J. Li, X. Ren, Y. Yin, K. Zhao, A. Chew, Y. Cheng, E. Cunningham, Y. Wang, S. Hu, Y. Wu, M. Chini, and Z. Chang, "53-attosecond X-ray pulses reach the carbon K-edge," Nat. Commun. **8**, 186 (2017).

[59] B. Buades, D. Moonshiram, T. P. H. Sidiropoulos, I. León, P. Schmidt, I. Pi, N. D. Palo, S. L. Cousin, A. Picón, F. Koppens, and J. Biegert, "Dispersive soft x-ray absorption fine-structure spectroscopy in graphite with an attosecond pulse," Optica **5**, 502–506 (2018).

[60] C. Kleine, M. Ekimova, G. Goldsztejn, S. Raabe, C. Strüber, J. Ludwig, S. Yarlagadda, S. Eisebitt, M. J. J. Vrakking, T. Elsaesser, E. T. J. Nibbering, and A. Rouzée, "Soft x-ray absorption spectroscopy of aqueous solutions using a table-top femtosecond soft x-ray source," J. Phys. Chem. Lett. **10**, 52–58 (2019).

[61] D. Popmintchev, B. R. Galloway, M.-C. Chen, F. Dollar, C. A. Mancuso, A. Hankla, L. Miaja-Avila, G. O'Neil, J. M. Shaw, G. Fan, S. Ališauskas, G. Andriukaitis, T. Balčiunas, O. D. Mücke, A. Pugzlys, A. Baltuška, H. C. Kapteyn, T. Popmintchev, and M. M. Murnane, "Near- and extended-edge x-ray-absorption fine-structure spectroscopy using ultrafast coherent high-order harmonic supercontinua," Phys. Rev. Lett. **120**, 093002 (2018).

[62] Y. Pertot, C. Schmidt, M. Matthews, A. Chauvet, M. Huppert, V. Svoboda, A. von Conta, A. Tehlar, D. Baykusheva, J.-P. Wolf, and H. J. Wörner, "Time-resolved x-ray absorption spectroscopy with a water window high-harmonic source," Science **355**, 264–267 (2017).

[63] A. R. Attar, A. Bhattacherjee, C. D. Pemmaraju, K. Schnorr, K. D. Closser, D. Prendergast, and S. R. Leone, "Femtosecond x-ray spectroscopy of an electrocyclic ring-opening reaction," Science **356**, 54–59 (2017).

[64] S. L. Cousin, N. Di Palo, B. Buades, S. M. Teichmann, M. Reduzzi, M. Devetta, A. Kheifets, G. Sansone, and J. Biegert, "Attosecond streaking in the water window: A new regime of attosecond pulse characterization," Phys. Rev. X **7**, 041030 (2017).

[65] B. Buades, A. Picón, I. León, N. D. Palo, S. L. Cousin, C. Cocchi, E. Pellegrin, J. H. Martin, S. Mañas-Valero, E. Coronado, T. Danz, C. Draxl, M. Uemoto, K. Yabana, M. Schultze, S. Wall, and J. Biegert, "Attosecond-resolved petahertz carrier motion in semi-metallic TiS_2," arXiv 1808.06493 (2018).

[66] P. B. Corkum, "Plasma perspective on strong field multiphoton ionization," Phys. Rev. Lett. **71**, 1994–1997 (1993).

[67] L. V. Keldysh, "Ionization in the field of a strong electromagnetic wave," J. Exp. Theor. Phys. **20**, 1307 (1965).

[68] A. M. Perelomov, V. S. Popov, and M. V. Terent'ev, "Ionization of atoms in an alternating electric field," J. Exp. Theor. Phys. **23**, 924 (1966).

[69] M. V. Ammosov, N. B. Delone, and V. P. Krainov, "Tunnel ionization of complex atoms and of atomic ions in an alternating electromagnetic field," J. Exp. Theor. Phys. **64**, 1191 (1986).

[70] M. Lewenstein, P. Balcou, M. Y. Ivanov, A. L'Huillier, and P. B. Corkum, "Theory of high-harmonic generation by low-frequency laser fields," Phys. Rev. A **49**, 2117–2132 (1994).

[71] A. Baltuska, T. Udem, M. Uiberacker, M. Hentschel, E. Goulielmakis, C. Gohle, R. Holzwarth, V. S. Yakovlev, A. Scrinzi, T. W. Hansch, and F. Krausz, "Attosecond control of electronic processes by intense light fields," Nature (London) **421**, 611–615 (2003).

[72] C. A. Haworth, L. E. Chipperfield, J. S. Robinson, P. L. Knight, J. P. Marangos, and J. W. G. Tisch, "Half-cycle cutoffs in harmonic spectra and robust carrier-envelope phase retrieval," Nat. Phys. **3**, 52–57 (2007).

[73] J. Tate, T. Auguste, H. G. Muller, P. Salières, P. Agostini, and L. F. DiMauro, "Scaling of wave-packet dynamics in an intense midinfrared field," Phys. Rev. Lett. **98**, 013901 (2007).

[74] A. D. Shiner, C. Trallero-Herrero, N. Kajumba, H.-C. Bandulet, D. Comtois, F. Légaré, M. Giguère, J.-C. Kieffer, P. B. Corkum, and D. M. Villeneuve, "Wavelength scaling of high harmonic generation efficiency," Phys. Rev. Lett. **103**, 073902 (2009).

[75] T. Pfeifer, C. Spielmann, and G. Gerber, "Femtosecond x-ray science," Rep. Prog. Phys. **69**, 443–505 (2006).

[76] A. Paul, E. A. Gibson, Xiaoshi Zhang, A. Lytle, T. Popmintchev, Xibin Zhou, M. M. Murnane, I. P. Christov, and H. C. Kapteyn, "Phase-matching techniques for coherent soft X-ray generation," IEEE J. Quantum Electron. **42**, 14–26 (2006).

[77] T. Popmintchev, M.-C. Chen, A. Bahabad, M. Gerrity, P. Sidorenko, O. Cohen, I. P. Christov, M. M. Murnane, and H. C. Kapteyn, "Phase matching of high harmonic generation in the soft and hard X-ray regions of the spectrum," Proc. Natl. Acad. Sci **106**, 10516–10521 (2009).

[78] C. Zhang, G. G. Brown, K. T. Kim, D. M. Villeneuve, and P. B. Corkum, "Full characterization of an attosecond pulse generated using an infrared driver," Sci. Rep. **6**, 26771 (2016).

[79] T. Matsushita and R. P. Phizackerley, "A fast x-ray absorption spectrometer for use with synchrotron radiation," Jpn. J. Appl. Phys. **20**, 2223–2228 (1981).

[80] J. Stöhr, *NEXAFS Spectroscopy* (Springer, 1992).

[81] F. Sette, J. Stöhr, E. B. Kollin, D. J. Dwyer, J. L. Gland, J. L. Robbins, and A. L. Johnson, "Na-induced bonding and bond-length changes for CO on Pt(111): A near-edge x-ray-absorption fine-structure study," Phys. Rev. Lett. **54**, 935–938 (1985).

[82] A. P. Hitchcock, "Core excitation and ionization of molecules," Phys. Scr. **T31**, 159–170 (1990).

[83] J. Stöhr, K. Baberschke, R. Jaeger, R. Treichler, and S. Brennan, "Orientation of chemisorbed molecules from surface-absorption fine-structure measurements: CO and NO on Ni(100)," Phys. Rev. Lett. **47**, 381–384 (1981).

[84] E. Goulielmakis, Z.-H. Loh, A. Wirth, R. Santra, N. Rohringer, V. S. Yakovlev, S. Zherebtsov, T. Pfeifer, A. M. Azzeer, M. F. Kling, S. R. Leone, and F. Krausz, "Real-time observation of valence electron motion," Nature (London) **466**, 739–743 (2010).

[85] Y. Kobayashi, K. F. Chang, T. Zeng, D. M. Neumark, and S. R. Leone, "Direct mapping of curve-crossing dynamics in IBr by attosecond transient absorption spectroscopy," Science **365**, 79–83 (2019).

[86] M. Chini, X. Wang, Y. Cheng, Y. Wu, D. Zhao, D. A. Telnov, S.-I. Chu, and Z. Chang, "Sub-cycle oscillations in virtual states brought to light," Sci. Rep. **3**, 1105 (2013).

[87] E. R. Hosler and S. R. Leone, "Characterization of vibrational wave packets by core-level high-harmonic transient absorption spectroscopy," Phys. Rev. A **88**, 023420 (2013).

[88] Z. Wei, J. Li, L. Wang, S. T. See, M. H. Jhon, Y. Zhang, F. Shi, M. Yang, and Z.-H. Loh, "Elucidating the origins of multimode vibrational coherences of polyatomic molecules induced by intense laser fields," Nat. Commun. **8**, 735 (2017).

[89] H. Timmers, X. Zhu, Z. Li, Y. Kobayashi, M. Sabbar, M. Hollstein, M. Reduzzi, T. J. Martínez, D. M. Neumark, and S. R. Leone, "Disentangling conical intersection and coherent molecular dynamics in methyl bromide with attosecond transient absorption spectroscopy," Nat. Commun. **10**, 3133 (2019).

[90] Z.-H. Loh and S. R. Leone, "Ultrafast strong-field dissociative ionization dynamics of CH_2Br_2 probed by femtosecond soft x-ray transient absorption spectroscopy," J. Chem. Phys. **128**, 204302 (2008).

[91] M.-F. Lin, D. M. Neumark, O. Gessner, and S. R. Leone, "Ionization and dissociation dynamics of vinyl bromide probed by femtosecond extreme ultraviolet transient absorption spectroscopy," J. Chem. Phys. **140**, 064311 (2014).

[92] Y. Cheng, M. Chini, X. Wang, A. González-Castrillo, A. Palacios, L. Argenti, F. Martín, and Z. Chang, "Reconstruction of an excited-state molecular wave packet with attosecond transient absorption spectroscopy," Phys. Rev. A **94**, 023403 (2016).

[93] E. R. Warrick, W. Cao, D. M. Neumark, and S. R. Leone, "Probing the dynamics of Rydberg and valence states of molecular nitrogen with attosecond transient absorption spectroscopy," J. Phys. Chem. A **120**, 3165–3174 (2016).

[94] H. Wang, M. Chini, S. Chen, C.-H. Zhang, F. He, Y. Cheng, Y. Wu, U. Thumm, and Z. Chang, "Attosecond time-resolved autoionization of argon," Phys. Rev. Lett. **105**, 143002 (2010).

[95] Y. Kobayashi, M. Reduzzi, K. F. Chang, H. Timmers, D. M. Neumark, and S. R. Leone, "Selectivity of electronic coherence and attosecond ionization delays in strong-field double ionization," Phys. Rev. Lett. **120**, 233201 (2018).

[96] L. M. Carneiro, S. K. Cushing, C. Liu, Y. Su, P. Yang, A. P. Alivisatos, and S. R. Leone, "Excitation-wavelength-dependent small polaron trapping of photoexcited carriers in α-Fe_2O_3," Nat. Mater. **16**, 819–825 (2017).

[97] A. Bhattacherjee and S. R. Leone, "Ultrafast x-ray transient absorption spectroscopy of gas-phase photochemical reactions: A new universal probe of photoinduced molecular dynamics," Acc. Chem. Res. **51**, 3203–3211 (2018).

[98] A. Chew, N. Douguet, C. Cariker, J. Li, E. Lindroth, X. Ren, Y. Yin, L. Argenti, W. T. Hill, and Z. Chang, "Attosecond transient absorption spectrum of argon at the $L_{2,3}$ edge," Phys. Rev. A **97**, 031407 (2018).

[99] N. Kosugi, J. Adachi, E. Shigemasa, and A. Yagishita, "High-resolution and symmetry-resolved N and O K-edge absorption spectra of NO," J. Chem. Phys. **97**, 8842–8849 (1992).

[100] J. Adachi, N. Kosugi, and A. Yagishita, "Symmetry-resolved soft x-ray absorption spectroscopy: its application to simple molecules," J. Phys. B **38**, R127–R152 (2005).

[101] O. Ghafur, A. Rouzée, A. Gijsbertsen, W. K. Siu, S. Stolte, and M. J. J. Vrakking, "Impulsive orientation and alignment of quantum-state-selected NO molecules," Nat. Phys. **5**, 289–293 (2009).

[102] P. M. Kraus, S. B. Zhang, A. Gijsbertsen, R. R. Lucchese, N. Rohringer, and H. J. Wörner, "High-harmonic probing of electronic coherence in dynamically aligned molecules," Phys. Rev. Lett. **111**, 243005 (2013).

[103] S. G. Walt, N. Bhargava Ram, M. Atala, N. I. Shvetsov-Shilovski, A. von Conta, D. Baykusheva, M. Lein, and H. J. Wörner, "Dynamics of valence-shell electrons and nuclei probed by strong-field holography and rescattering," Nat. Commun. **8**, 15651 (2017).

[104] X. Zhou, P. Ranitovic, C. W. Hogle, J. H. D. Eland, H. C. Kapteyn, and M. M. Murnane, "Probing and controlling non-Born-Oppenheimer dynamics in highly excited molecular ions," Nat. Phys. **8**, 232–237 (2012).

[105] M. Huppert, I. Jordan, D. Baykusheva, A. von Conta, and H. J. Wörner, "Attosecond delays in molecular photoionization," Phys. Rev. Lett. **117**, 093001 (2016).

[106] R. Schoenlein, T. Elsaesser, K. Holldack, Z. Huang, H. Kapteyn, M. Murnane, and M. Woerner, "Recent advances in ultrafast X-ray sources," Phil. Trans. R. Soc. A **377**, 20180384 (2019).

[107] L. Young, K. Ueda, M. Gühr, P. H. Bucksbaum, M. Simon, S. Mukamel, N. Rohringer, K. C. Prince, C. Masciovecchio, M. Meyer, A. Rudenko, D. Rolles, C. Bostedt, M. Fuchs, D. A. Reis, R. Santra, H. Kapteyn, M. Murnane, H. Ibrahim, F. Légaré, M. Vrakking, M. Isinger, D. Kroon, M. Gisselbrecht, A. L'Huillier, H. J. Wörner, and S. R. Leone, "Roadmap of ultrafast x-ray atomic and molecular physics," J. Phys. B **51**, 032003 (2018).

[108] J. Weisshaupt, V. Juvé, M. Holtz, S. Ku, M. Woerner, T. Elsaesser, S. Alisauskas, A. Pugzlys, and A. Baltuska, "High-brightness table-top hard X-ray source driven by sub-100-femtosecond mid-infrared pulses," Nat. Photon. **8**, 927–930 (2014).

[109] A. Jonas, H. Stiel, L. Glöggler, D. Dahm, K. Dammer, B. Kanngießer, and I. Mantouvalou, "Towards Poisson noise limited optical pump soft X-ray probe NEXAFS spectroscopy using a laser-produced plasma source," Opt. Express **27**, 36524–36537 (2019).

[110] H. Öström, H. Öberg, H. Xin, J. LaRue, M. Beye, M. Dell'Angela, J. Gladh, M. L. Ng, J. A. Sellberg, S. Kaya, G. Mercurio, D. Nordlund, M. Hantschmann, F. Hieke, D. Kühn, W. F. Schlotter, G. L. Dakovski, J. J. Turner, M. P. Minitti, A. Mitra, S. P. Moeller, A. Föhlisch, M. Wolf, W. Wurth, M. Persson, J. K. Nørskov, F. Abild-Pedersen, H. Ogasawara, L. G. M. Pettersson, and A. Nilsson, "Probing the transition state region in catalytic CO oxidation on Ru," Science **347**, 978–982 (2015).

[111] T. J. A. Wolf, R. H. Myhre, J. P. Cryan, S. Coriani, R. J. Squibb, A. Battistoni, N. Berrah, C. Bostedt, P. Bucksbaum, G. Coslovich, R. Feifel, K. J. Gaffney, J. Grilj, T. J. Martinez, S. Miyabe, S. P. Moeller, M. Mucke, A. Natan, R. Obaid, T. Osipov, O. Plekan, S. Wang, H. Koch, and M. Gühr, "Probing ultrafast $\pi\pi^*$/nπ^* internal conversion in organic chromophores via K-edge resonant absorption," Nat. Commun. **8**, 29 (2017).

[112] Y. Obara, H. Ito, T. Ito, N. Kurahashi, S. Thürmer, H. Tanaka, T. Katayama, T. Togashi, S. Owada, Y.-i. Yamamoto, S. Karashima, J. Nishitani, M. Yabashi, T. Suzuki, and K. Misawa, "Femtosecond time-resolved X-ray absorption spectroscopy of anatase TiO_2 nanoparticles using XFEL," Struct. Dyn. **4**, 044033 (2017).

[113] A. Cavalleri, M. Rini, H. H. W. Chong, S. Fourmaux, T. E. Glover, P. A. Heimann, J. C. Kieffer, and R. W. Schoenlein, "Band-selective measurements of electron dynamics in VO_2 using femtosecond near-edge x-ray absorption," Phys. Rev. Lett. **95**, 067405 (2005).

[114] I. Radu, K. Vahaplar, C. Stamm, T. Kachel, N. Pontius, H. A. Dürr, T. A. Ostler, J. Barker, R. F. L. Evans, R. W. Chantrell, A. Tsukamoto, A. Itoh, A. Kirilyuk, T. Rasing, and A. V. Kimel, "Transient ferromagnetic-like state mediating ultrafast reversal of antiferromagnetically coupled spins," Nature (London) **472**, 205–208 (2011).

[115] N. Pontius, T. Kachel, C. Schüßler-Langeheine, W. F. Schlotter, M. Beye, F. Sorgenfrei, C. F. Chang, A. Föhlisch, W. Wurth, P. Metcalf, I. Leonov, A. Yaresko, N. Stojanovic, M. Berglund, N. Guerassimova, S. Düsterer, H. Redlin, and H. A. Dürr, "Time-resolved resonant soft x-ray diffraction with free-electron lasers: Femtosecond dynamics across the Verwey transition in magnetite," Appl. Phys. Lett. **98**, 182504 (2011).

[116] M. P. Minitti, J. M. Budarz, A. Kirrander, J. S. Robinson, D. Ratner, T. J. Lane, D. Zhu, J. M. Glownia, M. Kozina, H. T. Lemke, M. Sikorski, Y. Feng, S. Nelson, K. Saita, B. Stankus, T. Northey, J. B. Hastings, and P. M. Weber, "Imaging molecular motion: Femtosecond X-ray scattering of an electrocyclic chemical reaction," Phys. Rev. Lett. **114**, 255501 (2015).

[117] S. Minemoto, H. Shimada, K. Komatsu, W. Komatsubara, T. Majima, S. Miyake, T. Mizuno, S. Owada, H. Sakai, T. Togashi, M. Yabashi, P. Decleva, M. Stener, S. Tsuru, and A. Yagishita, "Time-resolved photoelectron angular distributions from nonadiabatically aligned CO_2 molecules with SX-FEL at SACLA," J. Phys. Commun. **2**, 115015 (2018).

[118] N. Hartmann, G. Hartmann, R. Heider, M. S. Wagner, M. Ilchen, J. Buck, A. O. Lindahl, C. Benko, J. Grünert, J. Krzywinski, J. Liu, A. A. Lutman, A. Marinelli, T. Maxwell, A. A. Miahnahri, S. P. Moeller, M. Planas, J. Robinson, A. K. Kazansky, N. M. Kabachnik, J. Viefhaus, T. Feurer, R. Kienberger, R. N. Coffee, and W. Helml, "Attosecond time-energy structure of X-ray free-electron laser pulses," Nat. Photon. **12**, 215–220 (2018).

[119] J. Duris, S. Li, T. Driver, E. G. Champenois, J. P. MacArthur, A. A. Lutman, Z. Zhang, P. Rosenberger, J. W. Aldrich, R. Coffee, G. Coslovich, F.-J. Decker, J. M. Glownia, G. Hartmann, W. Helml, A. Kamalov, J. Knurr, J. Krzywinski, M.-F. Lin, J. P. Marangos, M. Nantel, A. Natan, J. T. O'Neal, N. Shivaram, P. Walter, A. L. Wang, J. J. Welch, T. J. A. Wolf, J. Z. Xu, M. F. Kling, P. H. Bucksbaum, A. Zholents, Z. Huang, J. P. Cryan, and A. Marinelli, "Tunable isolated attosecond X-ray pulses with gigawatt peak power from a free-electron laser," Nat. Photon. **14**, 30–36 (2020).

[120] A. Dubietis, G. Jonusauskas, and A. Piskarskas, "Powerful femtosecond pulse generation by chirped and stretched pulse parametric amplification in BBO crystal," Opt. Commun. **88**, 437–440 (1992).

[121] C. C. Wang and G. W. Racette, "Measurement of parametric gain accompanying optical difference frequency generation," Appl. Phys. Lett. **6**, 169–171 (1965).

[122] C. Zhou, T. Seki, T. Kitamura, Y. Kuramoto, T. Sukegawa, N. Ishii, T. Kanai, J. Itatani, Y. Kobayashi, and S. Watanabe, "Wavefront analysis of high-efficiency, large-scale, thin transmission gratings," Opt. Express **22**, 5995–6008 (2014).

[123] M. Zimmermann, C. Gohle, R. Holzwarth, T. Udem, and T. W. Hänsch, "Optical clockwork with an offset-free difference-frequency comb: accuracy of sum- and difference-frequency generation," Opt. Lett. **29**, 310–312 (2004).

[124] C. Manzoni, G. Cerullo, and S. D. Silvestri, "Ultrabroadband self-phase-stabilized pulses by difference-frequency generation," Opt. Lett. **29**, 2668–2670 (2004).

[125] P. Tournois, "Acousto-optic programmable dispersive filter for adaptive compensation of group delay time dispersion in laser systems," Opt. Comm. **140**, 245–249 (1997).

[126] T. R. Schibli, J. Kim, O. Kuzucu, J. T. Gopinath, S. N. Tandon, G. S. Petrich, L. A. Kolodziejski, J. G. Fujimoto, E. P. Ippen, and F. X. Kaertner, "Attosecond active synchronization of passively mode-locked lasers by balanced cross correlation," Opt. Lett. **28**, 947–949 (2003).

[127] R. Trebino, *Frequency-Resolved Optical Gating* (Kluwer Academic, Boston, 2000).

[128] J. Itatani, F. Quéré, G. L. Yudin, M. Y. Ivanov, F. Krausz, and P. B. Corkum, "Attosecond streak camera," Phys. Rev. Lett. **88**, 173903 (2002).

[129] K. T. Kim, C. Zhang, A. D. Shiner, B. E. Schmidt, F. Legare, D. M. Villeneuve, and P. B. Corkum, "Petahertz optical oscilloscope," Nat. Photon. **7**, 958–962 (2013).

[130] A. S. Wyatt, T. Witting, A. Schiavi, D. Fabris, P. Matia-Hernando, I. A. Walmsley, J. P. Marangos, and J. W. G. Tisch, "Attosecond sampling of arbitrary optical waveforms," Optica **3**, 303–310 (2016).

[131] P. Carpeggiani, M. Reduzzi, A. Comby, H. Ahmadi, S. Kühn, F. Calegari, M. Nisoli, F. Frassetto, L. Poletto, D. Hoff, J. Ullrich, C. D. Schröter, R. Moshammer, G. G. Paulus, and G. Sansone, "Vectorial optical field reconstruction by attosecond spatial interferometry," Nat. Photon. **11**, 383–389 (2017).

[132] Y. Nomura, H. Shirai, and T. Fuji, "Frequency-resolved optical gating capable of carrier-envelope phase determination," Nat. Commun. **4**, 2820 (2013).

[133] S. B. Park, K. Kim, W. Cho, S. I. Hwang, I. Ivanov, C. H. Nam, and K. T. Kim, "Direct sampling of a light wave in air," Optica **5**, 402–408 (2018).

[134] A. Schiffrin, T. Paasch-Colberg, N. Karpowicz, V. Apalkov, D. Gerster, S. Mühlbrandt, M. Korbman, J. Reichert, M. Schultze, S. Holzner, J. V. Barth, R. Kienberger, R. Ernstorfer, V. S. Yakovlev, M. I. Stockman, and F. Krausz, "Optical-field-induced current in dielectrics," Nature (London) **493**, 70–74 (2012).

[135] T. Paasch-Colberg, S. Y. Kruchinin, Özge Sağlam, S. Kapser, S. Cabrini, S. Muehlbrandt, J. Reichert, J. V. Barth, R. Ernstorfer, R. Kienberger, V. S. Yakovlev, N. Karpowicz, and A. Schiffrin, "Sub-cycle optical control of current in a semiconductor: from the multiphoton to the tunneling regime," Optica **3**, 1358–1361 (2016).

[136] J. Liu and X.-C. Zhang, "Terahertz-radiation-enhanced emission of fluorescence from gas plasma," Phys. Rev. Lett. **103**, 235002 (2009).

[137] X. M. Tong, Z. X. Zhao, and C. D. Lin, "Theory of molecular tunneling ionization," Phys. Rev. A **66**, 033402 (2002).

[138] A. Lofthus and P. H. Krupenie, "The spectrum of molecular nitrogen," J. Phys. Chem. Ref. Data **6**, 113–307 (1977).

[139] I. H. Malitson, "Interspecimen comparison of the refractive index of fused silica," J. Opt. Soc. Am. **55**, 1205–1209 (1965).

[140] N. Saito, N. Ishii, T. Kanai, and J. Itatani, "All-optical characterization of the two-dimensional waveform and the Gouy phase of an infrared pulse based on plasma fluorescence of gas," Opt. Express **26**, 24591–24601 (2018).

[141] J. R. Sutherland, E. L. Christensen, N. D. Powers, S. E. Rhynard, J. C. Painter, and J. Peatross, "High harmonic generation in a semi-infinite gas cell," Opt. Express **12**, 4430–4436 (2004).

[142] J.-P. Brichta, M. C. H. Wong, J. B. Bertrand, H.-C. Bandulet, D. M. Rayner, and V. R. Bhardwaj, "Comparison and real-time monitoring of high-order harmonic generation in different sources," Phys. Rev. A **79**, 033404 (2009).

[143] M. Huppert, I. Jordan, and H. J. Wörner, "Attosecond beamline with actively stabilized and spatially separated beam paths," Rev. Sci. Instrum. **86**, 123106 (2015).

[144] "CXRO X-ray interactions with matter," `http://henke.lbl.gov/optical_constants`. Accessed: 2019-12-13.

[145] M. Chini, H. Mashiko, H. Wang, S. Chen, C. Yun, S. Scott, S. Gilbertson, and Z. Chang, "Delay control in attosecond pump-probe experiments," Opt. Express **17**, 21459–21464 (2009).

[146] M. Sabbar, S. Heuser, R. Boge, M. Lucchini, L. Gallmann, C. Cirelli, and U. Keller, "Combining attosecond XUV pulses with coincidence spectroscopy," Rev. Sci. Instrum. **85**, 103113 (2014).

[147] M. Fieß, M. Schultze, E. Goulielmakis, B. Dennhardt, J. Gagnon, M. Hofstetter, R. Kienberger, and F. Krausz, "Versatile apparatus for attosecond metrology and spectroscopy," Rev. Sci. Instrum. **81**, 093103 (2010).

[148] J. Vaughan, J. Bahder, B. Unzicker, D. Arthur, M. Tatum, T. Hart, G. Harrison, S. Burrows, P. Stringer, and G. M. Laurent, "Design of an optically-locked interferometer for attosecond pump-probe setups," Opt. Express **27**, 30989–31000 (2019).

[149] Z. Chang, *Fundamentals of Attosecond Optics* (CRC Press, 2011).

[150] S. M. Teichmann, F. Silva, S. L. Cousin, and J. Biegert, "Importance of intensity-to-phase coupling for water-window high-order-harmonic generation with few-cycle pulses," Phys. Rev. A **91**, 063817 (2015).

[151] G. Sansone, E. Benedetti, F. Calegari, C. Vozzi, L. Avaldi, R. Flammini, L. Poletto, P. Villoresi, C. Altucci, R. Velotta, S. Stagira, S. De Silvestri, and M. Nisoli, "Isolated single-cycle attosecond pulses," Science **314**, 443–446 (2006).

[152] T. H. Dinh, Y. Kondo, T. Tamura, Y. Ono, H. Hara, H. Oikawa, Y. Yamamoto, M. Ishino, M. Nishikino, T. Makimura, P. Dunne, G. O'Sullivan, S. Ohta, K. Kitano, T. Ejima, T. Hatano, and T. Higashiguchi, "Evaluation of a flat-field grazing incidence spectrometer for highly charged ion plasma emission in soft x-ray spectral region from 1 to 10 nm," Rev. Sci. Instrum. **87**, 123106 (2016).

[153] C. A. MacDonald, *An Introduction to X-ray Physics, Optics, and Applications* (Princeton University Press, 2017).

[154] O. Schwarzkopf, F. Eggenstein, U. Flechsig, C. Kalus, H. Lammert, U. Menthel, G. Reichardt, P. Rotter, F. Senf, T. Zeschke, and W. B. Peatman, "High-resolution constant length rowland circle monochromator at BESSY," Rev. Sci. Instrum. **69**, 3789–3793 (1998).

[155] C. T. Chen, Y. Ma, and F. Sette, "K-shell photoabsorption of the N_2 molecule," Phys. Rev. A **40**, 6737–6740 (1989).

[156] K. Kidena, M. Endo, H. Takamatsu, M. Niibe, M. Tagawa, K. Yokota, Y. Furuyama, K. Komatsu, H. Saitoh, and K. Kanda, "Resistance of hydrogenated titanium-doped diamond-like carbon film to hyperthermal atomic oxygen," Metals **5**, 1957–1970 (2015).

[157] G. Akgül, "Effects of thickness on electronic structure of titanium thin films," Bull. Mater. Sci. **37**, 41–45 (2014).

[158] V. N. Strocov, T. Schmitt, U. Flechsig, L. Patthey, and G. S. Chiuzbăian, "Numerical optimization of spherical variable-line-spacing grating X-ray spectrometers," J. Synchrotron Radiat. **18**, 134–142 (2011).

[159] G. Ghiringhelli, A. Piazzalunga, C. Dallera, G. Trezzi, L. Braicovich, T. Schmitt, V. N. Strocov, R. Betemps, L. Patthey, X. Wang, and M. Grioni, "SAXES, a high resolution spectrometer for resonant x-ray emission in the 400–1600 eV energy range," Rev. Sci. Instrum. **77**, 113108 (2006).

[160] P. Antoine, A. L'Huillier, and M. Lewenstein, "Attosecond pulse trains using high-order harmonics," Phys. Rev. Lett. **77**, 1234–1237 (1996).

[161] D. G. Lee, H. J. Shin, Y. H. Cha, K. H. Hong, J.-H. Kim, and C. H. Nam, "Selection of high-order harmonics from a single quantum path for the generation of an attosecond pulse train," Phys. Rev. A **63**, 021801 (2001).

[162] N. Kosugi and H. Kuroda, "Efficient methods for solving the open-shell SCF problem and for obtaining an initial guess. the "one-Hamiltonian" and the "partial SCF" methods," Chem. Phys. Lett. **74**, 490 – 493 (1980).

[163] N. Kosugi, "Strategies to vectorize conventional SCF-Cl algorithms," Theor. Chim. Acta **72**, 149–173 (1987).

[164] W. C. Ho, I. Ozier, D. T. Cramb, and M. C. L. Gerry, "Diode laser spectroscopy of the vibrational fundamental of NO^+," J. Mol. Spectrosc. **149**, 559–561 (1991).

[165] J. Ortigoso, M. Rodriguez, M. Gupta, and B. Friedrich, "Time evolution of pendular states created by the interaction of molecular polarizability with a pulsed nonresonant laser field," J. Chem. Phys. **110**, 3870–3875 (1999).

[166] H. Sakai, C. P. Safvan, J. J. Larsen, K. M. Hilligsøe, K. Hald, and H. Stapelfeldt, "Controlling the alignment of neutral molecules by a strong laser field," J. Chem. Phys. **110**, 10235–10238 (1999).

[167] C. Amiot, "The infrared emission spectrum of NO: Analysis of the Δv = 3 sequence up to v = 22," J. Mol. Spectrosc. **94**, 150 – 172 (1982).

[168] N. J. Bridge, A. D. Buckingham, and J. W. Linnett, "The polarization of laser light scattered by gases," Proc. Royal Soc. A **295**, 334–349 (1966).

[169] M. Schmidt, K. Baldridge, J. Boatz, S. Elbert, M. Gordon, J. Jensen, S. Koseki, N. Matsunaga, K. Nguyen, S. Su, T. Windus, M. Dupuis, and J. Montgomery, "General atomic and molecular electronic structure system," J. Computat. Chem. **14**, 1347–1363 (1993).

[170] G. W. Luther, *Inorganic Chemistry for Geochemistry and Environmental Sciences: Fundamentals and Applications* (Wiley, 2016).

[171] T. Shimanouchi, *Tables of molecular vibrational frequencies. Consolidated volume I* (National Bureau of Standards, 1972).

[172] T. Ergler, B. Feuerstein, A. Rudenko, K. Zrost, C. D. Schröter, R. Moshammer, and J. Ullrich, "Quantum-phase resolved mapping of ground-state vibrational D_2 wave packets via selective depletion in intense laser pulses," Phys. Rev. Lett. **97**, 103004 (2006).

[173] E. R. Hosler, "Ultrafast strong-field vibrational dynamics studied by femtosecond extreme-ultraviolet transient absorption spectroscopy," Ph.D. thesis, UC Berkeley (2013).

[174] O. Tolstikhin, T. Morishita, and L. Madsen, "Theory of tunneling ionization of molecules: Weak-field asymptotics including dipole effects," Phys. Rev. A **84**, 053423 (2011).

[175] L. H. Scharpen, J. S. Muenter, and V. W. Laurie, "Electric polarizability anisotropies of nitrous oxide, propyne, and carbonyl sulfide by microwave spectroscopy," J. Chem. Phys. **53**, 2513–2519 (1970).

[176] H. Gritli, Z. B. Lakhdar, G. Chambaud, and P. Rosmus, "Ro-vibronic spectrum of the N_2O^+ ion in the $X^2\Pi$ state," Chem. Phys. **178**, 223–233 (1993).

[177] Y. Harada, M. Kobayashi, H. Niwa, Y. Senba, H. Ohashi, T. Tokushima, Y. Horikawa, S. Shin, and M. Oshima, "Ultrahigh resolution soft x-ray emission spectrometer at BL07LSU in SPring-8," Rev. Sci. Instrum. **83**, 013116 (2012).

[178] M. Nagasaka, H. Yuzawa, T. Horigome, and N. Kosugi, "In operando observation system for electrochemical reaction by soft X-ray absorption spectroscopy with potential modulation method," Rev. Sci. Instrum. **85**, 104105 (2014).

[179] "Spherical Hamronic Tools | SHTOOLS - Tools for working with spherical harmonics," `https://shtools.oca.eu/shtools/public/`. Accessed: 2019-12-13.

[180] T. Endo, A. Matsuda, M. Fushitani, T. Yasuike, O. I. Tolstikhin, T. Morishita, and A. Hishikawa, "Imaging electronic excitation of NO by ultrafast laser tunneling ionization," Phys. Rev. Lett. **116**, 163002 (2016).

Author's contributions

The BIBO-OPCPA system was mainly developed by Dr. Nobuhisa Ishii. Dr. Keisuke Kaneshima, Dr. Teruto Kanai, Prof. Jiro Itatani, and Prof. Shuntaro Watanabe also contributed to the development. The measurement of the timing drift between the pump and the seed arms, the *f*-to-*2f* measurement, and the waveform measurement using plasma fluorescence were conducted by the author.

The HHG and the transient absorption beamline was mainly developed by the author, with the help of many people. The HHG chamber and the differential pumping system were designed by Hiroki Sannohe, advised by Dr. Nobuhisa Ishii. The semi-infinite gas cell scheme was developed by Prof. Zenghu Chang, Dr. Yi Wu, Mr. Andrew Chew, and Dr. Seunghwoi Han, and constructed by the author. The toroidal chamber was originally designed by Dr. Nobuhisa Ishii, and later redesigned and constructed by the author. The sample chamber, the X-ray spectrometer, the pump-probe optics, and the delay stabilization system were designed by the author. They were constructed with the help of Hiroki Sannohe.

The transient absorption measurements of NO and N_2O were performed and analyzed by the author. The ab initio calculation of the potential energy curves of the core-excited states and the ground tate of NO was performed by Prof. Nobuhiro Kosugi.

The overall project was supervised by Prof. Jiro Itatani.

Acknowledgements

First of all, I am grateful to Prof. Jiro Itatani for supervising the entire research. He gave me the opportunity to work on this exciting project and always gave me kind support.

Second, I would like to thank Dr. Nobuhisa Ishii for teaching me experimental techniques, for developing the amazing light source and a part of the beamline, and for giving me insightful advice. Without him, I would not have been able to accomplish this work.

I would like to thank the ALPS course and the DC2 fellowship program by JSPS for their financial support. Especially, I am grateful to Prof. Katsumi Midorikawa for his kind support as my secondary supervisor in the ALPS course.

Special thanks go to the members of Itatani group. Especially, I would like to thank Hiroki Sannohe for developing the differential pumping system in the HHG chamber, and for helping me construct the beamline. I would like to thank Dr. Teruto Kanai for his contribution to the light source development, and for providing excellent lab environments. I would like to thank Mr. Tianqi Yang for measuring the pumping speed of the dry pumps and calculating the energy resolution of the new X-ray spectrometer. I would like to thank Dr. Tomoya Mizuno, Mr. Peiyu Xia, and other members for discussions and for creating a warm atmosphere.

This work was supported by many collaborators. I would like to thank Prof. Zenghu Chang, Dr. Yi Wu, Mr. Andrew Chew, Dr. Seunghwoi Han, and Dr. Jie Li for developing the semi-infinite gas cell scheme and for giving me the opportunity to conduct collaborative research in UCF. I would like to thank Dr. Bruno E. Schmidt and Prof. François Légaré for sharing us their knowledge about differential pumping. I would like to thank Prof. Nobuhiro Kosugi for calculating the energy levels of the core-excited states of NO. I would like to thank Prof. Akiyoshi Hishikawa, Dr. Mizuho Fushitani, Dr. Akitaka Matsuda, Dr. Hirofumi Yanagisawa, and Mr. Kazma Komatsu for fruitful discussions on the transient absorption spectra of NO. I would like to thank Prof. Luca Argenti, Dr. Nicolas Douguet, Dr. Barry Schneider and Dr. Jeppe Olsen for performing simulations on the attosecond transient absorption spectrum of N_2O. I would like to thank Prof. Yoshihisa Harada and his group members for sharing us the knowledge of SX spectroscopy in synchrotron facilities and providing us a high-resolution X-ray grating. I would like to thank Prof. Chihiro Ito, Prof. Masaki Hada, and Prof. Shinya Koshihara for supporting me in the project of transient absorption spectroscopy of polydiacetylene, although I could not include it in this dissertation. I would like to thank Prof. Matthias Kling and his group members for giving me the opportunity to conduct collaborative research in LMU and MPQ.

I would like to thank Prof. Hirofumi Sakai, Prof. Kenichi L. Ishikawa, Prof. Ryusuke Matsunaga, Prof. Hiroki Wadati, and Prof. Katsumi Midorikawa for reviewing this

dissertation as committee members.

Finally, I would like to thank my friend Tetsuya Sugimoto and my family.